MODEL AIDED OBSERVATIONAL STUDY OF PHYSICAL PROCESSES IN FRESH WATER RESERVOIRS

A Thesis

by

FAHAD AL SENAFI

Submitted to the Office of Graduate Studies of
Texas A&M University
in partial fulfillment of the requirements for the degree of

MASTER OF SCIENCE

August 2012

Major Subject: Physical Oceanography

Model Aided Observational Study of Physical Processes in Fresh Water Reservoirs

MODEL AIDED OBSERVATIONAL STUDY OF PHYSICAL PROCESSES IN FRESH WATER RESERVOIRS

A Thesis

by

FAHAD AL SENAFI

Submitted to the Office of Graduate Studies of
Texas A&M University
in partial fulfillment of the requirements for the degree of

MASTER OF SCIENCE

Approved by:

Chair of Committee,	Ayal Anis
Committee Members,	Timothy Dellapenna
	John Sweetman
Head of Department,	Piers Chapman

August 2012

Major Subject: Physical Oceanography

ABSTRACT

Model Aided Observational Study of Physical Processes in Fresh Water Reservoirs.

(August 2012)

Fahad Al Senafi, B.S., Plymouth University

Chair of Advisory Committee: Dr. Ayal Anis

The aim of this study is to compare observational data to data simulated by a one dimensional model. Observational data collected from January to July 2006 at Lake Whitney, Texas, included water current velocities from an Acoustic Doppler Current Profiler, and an Acoustic Doppler Velocimeter from which shear stress, turbulent kinetic energy dissipation rates, and turbulence kinetic energy were computed using several methods. Numerical model experiments, forced by the surface heat and momentum fluxes, velocity profiles, and temperature profiles were conducted to simulate the development of the turbulence parameters. Two equation models, k-ϵ and k-kl, were used to find which model best describes the observed physical processes (turbulence kinetic energy, turbulent kinetic energy dissipation rate and velocity variances).

The combined observational and simulated results show a change in stratification levels that consequently leads to variations in turbulent kinetic energy dissipation rate, turbulent kinetic energy, and the velocity variances. In order to investigate the accuracy of the model, we quantitatively compared these parameters to estimates from the observed data in the bottom boundary layer. In general, the model and observational data

agree well for the three parameters, with the exception of some time periods, during which the model prediction differed from the observed. This was at times when the Acoustic Doppler Velocimeter measurements were at the noise level of the instrument. Overall, the *k-kl* model simulation results appear to be closer to the observational results during the weakly and strongly stratified periods than the *k*-ϵ model.

ACKNOWLEDGEMENTS

I would like to thank my committee chair, Dr. Ayal Anis, and my committee members, Dr. Timothy Dellapenna, and Dr. Bert Sweetman for their guidance and support throughout the course of this research. I would also like to thank Mrs. Ruthy Anis for her warm welcome and making my stay at Galveston cheerful with her great personality and unforgettable lovely cooking.

A thanks also goes to my friends, colleagues, department faculty and staff for making my time at Texas A&M University a great experience. I would also like to give a special thanks to my colleague in the microstructure lab, Mr. Zhang Zheng, for his help and support.

Finally, thanks to my mother and father for their encouragement and to my lovely wife Amal and daughter Leemar for their patience and love.

NOMENCLATURE

ADCP	Acoustic Doppler Current Profiler	
ADV	Acoustic Doppler Velocimeter	
BBL	Bottom boundary layer	
SBL	Surface boundary layer	
c	Sound speed	ms^{-1}
C	Constant	dimensionless
c_d	Empirical constant	dimensionless
C_D	Drag coefficient	dimensionless
C_e	Transfer coefficient	dimensionless
$c_\in$	Empirical constant	dimensionless
c_μ	Stability function	dimensionless
C_p	Specific heat capacity	$m^2s^{-2}k^{-1}$
D	Depth	m
D_K	Sum of the gradient term (advection and diffusion)	m^2s^{-3}
$D_\in$	Sum of the gradient term (advection and diffusion)	m^2s^{-4}
d	Grain diameter	m
$E(f)$	Frequency spectra	m^3s^{-2}
$E(k)$	Wavenumber spectra	m^3s^{-2}
E_{10}	Wind power input	Wm^{-2}

f	Frequency	Hz
f	Coriolis parameter	s^{-1}
g	Gravitational acceleration force (9.81)	ms^{-2}
I	Irradiance	Wm^{-2}
J_b^0	Net buoyancy flux	WKg^{-1}
J_q^l	Net latent heat flux	Wm^{-2}
J_q^{lw}	Net longwave radiation	Wm^{-2}
J_q^o	Net heat flux	Wm^{-2}
J_q^s	Net sensible heat flux	Wm^{-2}
J_d^{sw}	Downward shortwave radiation	Wm^{-2}
J_q^{sw}	Net short wave radiation	Wm^{-2}
k	Wave number	m^{-1}
K	Turbulent Kinetic Energy	m^2s^{-2}
K	Secant bulk module	bars
K_o	Vertical eddy diffusivity during homogenous conditions	m^2s^{-1}
K_z	Vertical eddy diffusivity	m^2s^{-1}
l	Turbulent macro length scale	m
l_{lk}	Kolmogorov length scale	m
L	Monin-Obukov length scale	m
L_e	Latent heat coefficient	$m^2s^{-2}K^{-1}$
M	Shear frequency	s^{-1}

N	Buoyancy frequency	s^{-1}
P	Pressure	Nm^{-2}
P	Rate of production by the mean flow	m^2s^{-3}
q	Humidity	%
Ri	Richardson number	dimensionless
Ri_c	Critical Richardson number (0.25)	dimensionless
Re	Reynolds number	dimensionless
Re_c	Critical Reynolds number (10^4)	dimensionless
S_l	Solar constant (1368)	Wm^{-2}
t	Time	s
T	Temperature	^oC
T_k	Transmittance	dimensionless
TKE	Turbulent Kinetic Energy	m^2s^{-2}
u	Velocity in the X direction	ms^{-1}
u^*	Frictional velocity	ms^{-1}
u_E	Ekman velocity component	ms^{-1}
U	Mean velocity	ms^{-1}
U_r	Mean wind speed at 10m	ms^{-1}
v	Velocity in the Y direction	ms^{-1}
v	Viscosity	m^2s^{-1}
v_E	Ekman velocity component	ms^{-1}

v_g	Geostrophic velocity component	ms^{-1}
v_t	Eddy viscosity	m^2s^{-1}
v_t'	Eddy diffusivity	m^2s^{-1}
z	Vertical distance	m
α	Albedo	dimensionless
α_s	Shear parameter	dimensionless
α_N	Buoyancy parameter	dimensionless
α_T	Thermal expansion	$Kgm^{-3}K^{-1}$
ε	TKE dissipation rate	m^2s^{-3}
ϵ_{ss}	Longwave emissivity (0.985)	Wm^{-2}
κ	Von Karman constant (0.4)	dimensionless
σ_k	Schmidt number	dimensionless
σ_{SB}	Stefan-Boltzmann constant ($5.67x10^{-8}$)	$Wm^{-2}K^{-4}$
ρ	Water density	Kgm^{-3}
ρ_o	Surface water density	Kgm^{-3}
ρ_a	Air density	Kgm^{-3}
Γ	Mixing efficiency ratio	dimensionless
τ	Wind stress	Nm^{-2}
θ	Suns declination	^{o}
θ	Potential temperature	^{o}C
ζ	Attenuation length	m

TABLE OF CONTENTS

Page

LIST OF FIGURES

LIST OF TABLES

1. INTRODUCTION

'*Turbulence is the dominant physical process in the transfer of momentum and heat, and in dispersing solutes and small organic and inorganic particles*'

[*Thorpe*, 2007]

1.1 Turbulence

1.1.1 Turbulent flows

Turbulence is a process that incites the change of a fluid flow from laminar to an irregular state of vortical motions called eddies. Such motions have a variety of length and time scales (Fig 1.1). Turbulence has a capability of transferring kinetic, potential and heat energy from one form to another and from place to place. This transfer of energy is the primary driver of transport and mixing in the water column [*Pope*, 2000]. The effect of turbulent flows in our environment is significant making them important to understand. For example, these flows control a variety of factors, such as mixing rates, spreading of pollutants, transport of sediments, and in addressing factors contributing to fish kill and harmful algae blooms [*Wolfgang*, 1987].

This thesis follows the style of Journal of Geophysical Research.

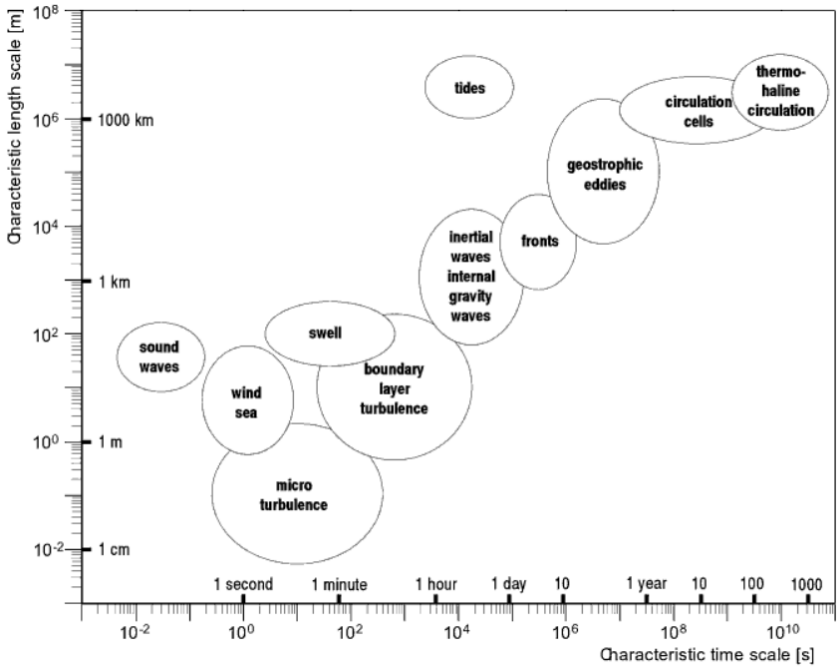

Fig 1.1. Time and Length Scale of Physical Processes in Oceans [*von Storch and Zwiers*, 1999].

1.1.2 Turbulent dynamics

There are two processes in a turbulent flow that cause mixing and dispersion. The first is the mechanical process of stirring, which is where advection produces and increases a gradient in the water properties [*Aref*, 2002]. This process creates an eddy and becomes narrower and longer over time (Fig. 1.2). The increase in gradient is followed by the process of diffusion or conduction, which decreases the gradient. Unlike stirring, diffusion is molecular and not mechanical [*Thorpe*, 2007].

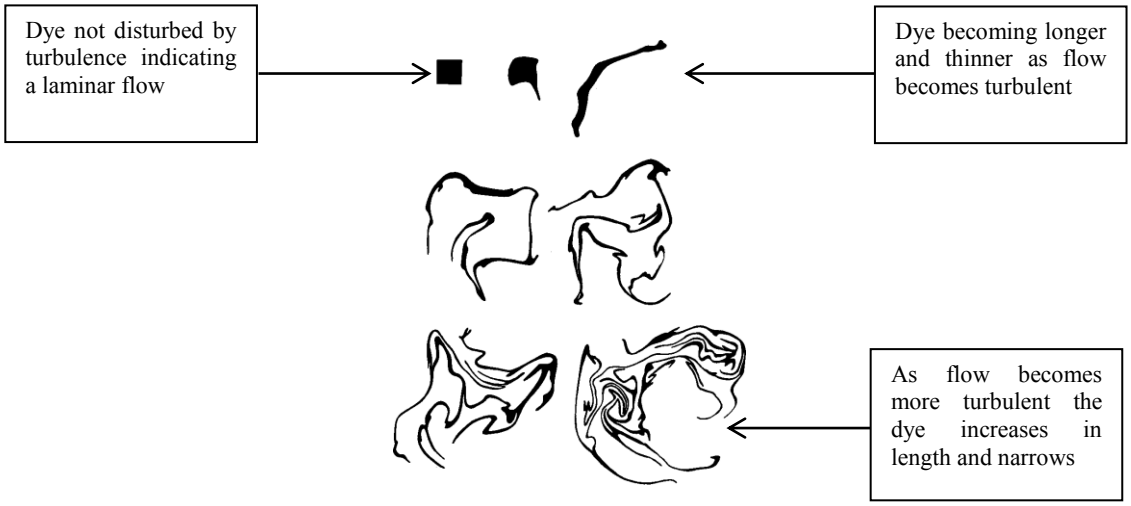

Fig 1.2. Behavior of a Laminar Flow Becoming Turbulent [*Welander*, 1955].

1.2 Turbulence in oceanic boundary layers

To understand turbulence, it is essential to observe physical processes on a range of temporal and spatial scales. Further, to understand the pathways of energy, one should know the sources of energy, and the amount of energy supplied to and from various processes. In relatively shallow aquatic bodies such as Lake Whitney (average depth 5m), most of the energetic processes take place in the surface boundary layer (SBL) and bottom boundary layer (BBL). As a result, these two layers strongly influence the water column structure, and the physical and biochemical properties.

1.2.1 Surface boundary layer (SBL)

The surface boundary layer is the part of the aquatic system that is directly influenced by the atmosphere so that momentum, heat and gas are exchanged. It is at this layer where the most biological activity occurs due to presence of solar energy [*Burchard et al.*, 2008]. The SBL's depth extends from the surface to a depth where the water layer is no longer uniform [*Anis and Singhal*, 2006]. Due to the layer being energetic through external atmospheric forcing in terms of heat flux and surface wind stress, the layer tends to be turbulent. The result of this turbulence generates the uniform mixed surface layer. On top of the surface boundary layer is a thin layer typically 1mm known as the skin layer. The properties of the thin skin layer are what controls the rate of heat fluxes, gas exchange, and momentum transfer [*Burchard et al.*, 2008].

1.2.1.1 Wind stress

The wind stress transfers momentum from the atmosphere into the SBL through frictional force. When wind stress is high enough, waves generate and therefore disrupt the skin layer by the breaking waves. This disruption in the skin layer increases gas exchange from atmosphere to the sea and increases momentum transfer. The increase in momentum adds to the turbulent kinetic energy at the SBL. This additional energy dissipates and diffuses to deeper waters, causing vertical transport of the water properties [*Thorpe*, 1995]. The wind stress can be numerically expressed using bulk parameterization of air-sea fluxes as:

$$[Nm^{-2}] \qquad \tau = \rho_a C_D U_r^2 \qquad (1)$$

where τ is stress due to wind, $\rho_a$is air density, C_D is the drag coefficient and U_r is the mean wind speed at a reference height from sea level [*Fairall et al.*, 2003] typically 10m.

1.2.1.2 Heat flux

Heat fluxes are driven by solar radiation and exchanged through the air-sea interface through molecular conduction. Once in the water, turbulence and molecular conductivity distribute the heat deeper in the water column [*Stull,* 1988].

The heat flux budget in the surface boundary layer is the sum of the heat fluxes:

$$[Wm^{-2}] \qquad J_q^o = J_q^{sw} + J_q^{lw} + J_q^l + J_q^s \qquad (2)$$

where J_q^o is the net surface heat flux, $J_q^{sw}$is the net shortwave radiation, J_q^{lw} is the net longwave radiation, J_q^l is the net latent heat, and J_q^s is the net sensible heat flux [*Anis and Singhal*, 2006].

(i) Shortwave radiation:

Shortwave radiation is the radiation generated by the sun with wave lengths of 0.3-3μm. Due to its wavelength being short, these waves are easily absorbed, scattered and reflected by clouds and particles in the atmosphere before reaching the surface. The fraction of shortwave radiation reaching the Earth's surface is called transmittance (T_k) [*Stull,* 1988] and is numerically defined as:

$$T_k = \frac{J_d^{sw}}{(\frac{S_l sin\theta}{\gamma^2})} \quad (3)$$

where J_d^{sw} is the net downward shortwave radiation at the surface after atmospheric loss, S_l is the solar constant, θ is the sun's angle during the day, and γ is the ratio of actual to mean distance between the sun and earth taking into account the ecliptic path of the sun during the year.

When the short wave radiation reaches the SBL, some radiation can be reflected back into the atmosphere or absorbed depending on the surface albedo[*Payne*, 1972]. The J_q^{sw} absorbed into the SBL is given by:

$$[Wm^{-2}] \qquad J_q^{sw} = (1-\alpha)J_d^{sw} \quad (4)$$

where α is the albedo.

Once the shortwave radiation is in the SBL, it is absorbed exponentially and reduces with depth:

$$[Wm^{-2}] \qquad I = J_q^{sw} e^{z/\zeta} \quad (5)$$

where I is the downward irradiance, z is depth, and ζ is the attenuation length [*Paulson and Simpson*, 1977].

(ii) Longwave radiation:

Longwave radiation is the greybody emission from atmospheric gases, clouds, and sea surface with wavelengths of 3-50μm (infrared). In aquatic systems where the atmosphere is cooler, the loss of longwave flux or so called the upward longwave flux

(J_u^{lw}) is always more than the downward longwave flux (J_d^{lw}). This overall loss results in a negative J_q^{lw} [*Dickey et al.*, 1994].

The longwave radiation loss by the sea varies depending on three parameters. The first is the relative humidity of the atmosphere directly above the sea surface. The increase in water vapor due to humidity adds to the J_d^{lw} by losing longwave radiation that is gained by the sea surface. The second is the absolute sea surface temperature, which controls the amount of energy flow from the sea to atmosphere. An increase in temperature will also lead to an increase in the water vapor, which will decrease J_u^{lw}. The third is by cloud cover. As cloud cover increases, the surface radiates more heat and J_u^{lw} increases. These parameters can be expressed using Lonnquist formula:

$$[Wm^{-2}] \qquad J_q^{lw} = (143 - 0.9T_s - 0.46q)(1 - 0.1C_l) \qquad (6)$$

where T_s is the surface water temperature, q is the relative humidity above the water and C_l is cloud cover [*Pickard,* 1990].

(iii) Latent heat:

Latent heat flux is directly influenced by the rate of evaporation. For water molecules in the sea water to change state from liquid to gas to become water vapor, energy is required. Therefore, the molecules consume the heat energy in the SBL, which allows heat energy to transfer into kinetic energy to transport from the sea to the atmosphere [*Pickard,* 1990].

The SBL does not gain any latent heat but only loses latent heat. The rate at which the J_q^l is lost depends on the rate of evaporation. Controlling the evaporation is

wind speed, sea surface temperature, air density and humidity. These controlling factors can be expressed using the bulk parameterization equation:

$$[Wm^{-2}] \qquad J_q^l = \rho_a L_e C_e U_r (q_s - q_r) \qquad (7)$$

where J_q^l is the net latent heat flux not taking into account the "Webb effect" (see *Webb et al*, 1980 for details), L_e is the latent heat coefficient, C_e is transfer coefficient, q_s is humidity at sea surface and q_r is the humidity at 10m from sea surface [*Fairall et al.*, 1996].

(iv) Sensible heat:

Sensible heat flux is the loss or gain of heat through conduction due to the temperature gradient between the air and sea interface. The rate of heat exchange is a function of temperature gradient, air density, air's specific heat and heat conductivity [*Pickard*, 1990]. The J_q^s can be numerically calculated using the bulk flux formula:

$$[Wm^{-2}] \qquad J_q^s = \rho_a c_p C_h S (T_s - \theta) \qquad (8)$$

where c_p is the heat capacity of air at constant pressure, C_h is the heat exchange coefficient and θ is the air potential temperature [*Fairall et al.*, 1996].

1.2.1.3 Buoyancy flux

Buoyancy flux (J_b^0) is the vertical movement of a fluid parcel to satisfy its density fluctuation with the surrounding water. The J_b^0 in a fresh water aquatic body is a function of density and net heat flux where salinity is not a controlling factor of density [*Dorrestein*, 1979]. Buoyancy flux can be shown as:

$$[Wkg^{-1}] \qquad J_b^0 = \frac{g\alpha_T J_q^0}{C_p \rho} \tag{9}$$

where g is gravitational acceleration, α_T is thermal expansion coefficient, C_p is the specific heat capacity and ρ is the density for fresh water calculated using Chen and Millero (1986):

$$[kgm^{-3}] \qquad \rho = \rho_o \left(1 - \frac{P}{K}\right)^{-1} \tag{10}$$

where ρ_o is the surface density, *P* is pressure and *K* is the secant bulk module.

1.2.1.4 Monin-Obukov length scale

Monin-Obukov length scale (*L*) describes the depth of the convective boundary layer driven by surface forcing. It indicates the depth in the water column where turbulence produced by wind stress and buoyancy flux are equal and is expressed as:

$$[m] \qquad L = -\frac{(\tau/\rho_o)^{3/2}}{(\kappa J_b^0)} \tag{11}$$

where κ is the von Karman constant (~0.4) [*Thorpe*, 2007].

The scale provides an indication of the stability conditions in the water column and gives better understanding of the distribution of seawater properties through the

motion of eddies [*Csanady*, 2001]. A positive *L* would indicate stable conditions, while negative indicates unstable convective conditions.

1.2.2 Bottom boundary layer

The bottom boundary layer (BBL) is the layer above the seabed that can extend, on rare occasions, to the surface when turbulent motion is high enough in shallow waters. This layer is where transportation and resuspension of sediments and nutrients occur. Such processes make the physical dynamics of this layer important for coastal engineers, sedimentologists and marine biologists.

The BBL can be broken down into three sub layers describing the force being induced (Fig 1.3). The first layer closest to the seabed is the viscous layer. In this thin layer (typically a few millimeters) is molecular friction and pressure gradient are the dominating forces due to the close distance from the sea floor. The layer above the viscous layer is the logarithmic layer. Due to the layer being close to the seabed, it will be subjected to shear stress while staying in equilibrium with the pressure gradient force. The top layer is the bottom Ekman layer where all three forces (Coriolis force, frictional force, and pressure gradient) are at equilibrium.

With the absence of direct atmospheric input of energy, the BBL gains its energy through currents that flow near the seabed. The strong shear stress generated by the seabed causes the flow to be zero at the bed surface and increases to the mean flow velocity logarithmically as a function of the height above the seabed (Fig 1.3). At this height is the top boundary of the BBL.

The disruption in flow caused by the seabed results in the dissipation of energy through the irregular motion of eddies and as a result enhances mixing in the BBL. It can be stated that the BBL physical processes are influenced by the near seabed flow and the nature of the sea floor [*Salon et al*., 2008].

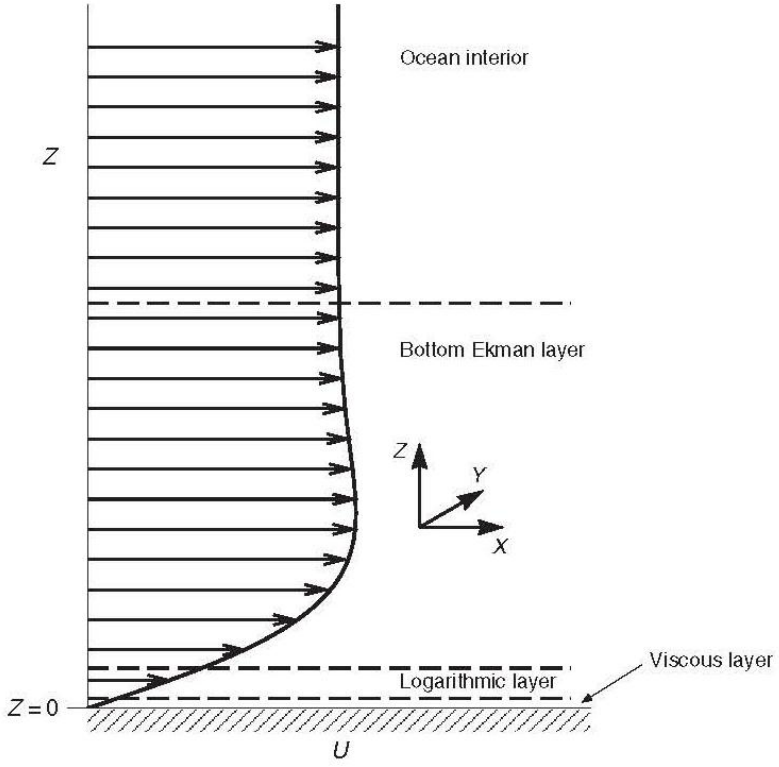

Fig 1.3. BBL Current Velocity Profile with the Layers Associated [*Salon et al.*, 2008].

1.2.2.1 Near bottom current flow

The near bottom current flow is subjected to different forcing at each sub-layer as explained in section 1.2.2. In order to obtain a valid flow equation that takes into account the different forces applied, assumptions must be made. The elite equation used to describe the bottom boundary flow is the Ekman equations (eqns. 12, 13). Ekman

assumed the sea floor is stationary, and the velocity at the surface of the seabed is zero. He also assumed as the distance from the seabed increases, friction decreases and is overcome by the geostrophic force.

$$u = u_E = -v_g e^{-\frac{\pi z}{D}} \sin(\pi z/D) \quad [ms^{-1}] \tag{12}$$

$$v = v_E + v_g = v_g(1 - e^{-\frac{\pi z}{D}} \cos(\pi z/D)) \quad [ms^{-1}] \tag{13}$$

where u_E and v_E are the Ekman components, v_g is the geostrophic component and D is the depth where the Ekman component is not considered due to geostrophic dominance over the frictional force [*Pond*, 1983].

It should be noted that Ekman theory is only applicable in large scale systems where the effect of Coriolis force is significant.

1.2.2.2 Seabed and current flow

Using Ekman's equations (eqns. 12, 13) have its disadvantages. The equation does not consider the seabed nature in terms of roughness and bathymetry. Therefore, corrections should be applied when studying close bottom current layer, specifically where friction is substantial at the viscous and logarithmic layers. At these two sub-layers, the momentum flux is dependent on viscosity (ν) and friction velocity (u^*). These components can be quantified to best describe the seabed roughness by the use of Reynolds number (Re_d):

$$Re_d = \frac{u^* d}{v} \tag{14}$$

where d is the grain diameter.

The velocity component near seabed at the logarithmic sub-layer can be measured using an Acoustic Doppler Velocimeters (ADV) or calculated using the Von Karman-Prandtl equation where the seabed characteristics are taken into consideration:

$$u(z) = \frac{u^*}{\kappa} \ln\left(\frac{Z}{Z_o}\right) + u(Z_o) \quad [ms^{-1}] \tag{15}$$

where κ is a Von Karman-Prandtl constant, Z is the vertical distance from the sea floor and Z_o is the vertical length of the BBL [*Salon et al*., 2008].

1.3 Turbulence observation

Understanding turbulence starts by observing the transition of the flow from laminar to turbulent. This can be done using three different techniques: field observations, numerical modeling and a combination of observation and numerical modeling.

1.3.1 Field observation

1.3.1.1 Turbulent flows

Most naturally occurring flows tend to be turbulent. The intensity and nature of these turbulent flows can be quantified based on their characteristic length scale (L), velocity (U) and kinematic viscosity (v). Furthermore, these characteristics portray how energy evolves in a flow and how energy is distributed, e.g. as a function of length scale, or more commonly as a function of wavenumber.

1.3.1.2 Reynolds number

Contributing to the stability/instability of a flow are three characteristics (U, L and v). The significance of these characteristics was first introduced by *Reynolds* [1894], where he quantified the stability of a flow in a pipe as the flow transitioned from laminar to turbulent by the use of a dimensionless number (Re number):

$$Re = \frac{UL}{v} \tag{16}$$

where the critical Re number (Re_c) is commonly 10^4 based on laboratory experiments by Reynolds and verified by field measurements at a strong tidal channel Seymour, Canada by *Grant et al.* [1962]. A turbulent flow is characterized by a high Re number ($Re > Re_c$), where the momentum terms (U and L) dominate over the friction term (v), resulting in a turbulent flow.

1.3.1.3 Richardson number (Ri)

The second number used to quantify the stability/instability of a flow is the Ri number. It is a ratio of the buoyancy frequency (N^2) and vertical shear (S^2):

$$Ri = \frac{N^2}{S^2} \tag{17}$$

where empirically the critical value (Ri_c) is 0.25 [*Stull*,1988]. When the vertical shear dominates ($Ri < Ri_c$), the kinetic energy from the shear is sufficient enough to lift the denser fluid over the lighter fluid causing instability and leading to mixing.

1.3.1.4 Energy cascade

Richardson [1922] introduced the theory of an energy cascade from large to smaller eddies. Richardson's intuition was that a large eddy consists of many smaller eddies, which through straining of the small eddies are stretched and cause instability by the increasing vorticity. This instability causes the large eddies to break up, transferring their energy to the smaller scale eddies [*Tennekes and Lumley*, 1972]. Breaking up of the large eddies continues until the effect of viscosity is significant enough to make the flow stable ($Re < Re_c$). Richardson's intuition is summarized in the now famous expression:

"*Big whirls have little whirls that feed on their velocity, and little whirls have lesser whirls and so on to viscosity*" [*Richardson*, 1922]

Kolmogorov [1941] proposed a length scale l_{lk} (eqn. 18) where the effect of viscosity becomes significant to make the flow stable. As the energy is transferred to smaller scales, it reaches scale l_{lk} where the energy is dissipated (ϵ) to the internal energy (cheat) of the fluid by viscosity. Kolmogorov used dimensional (length, L, and time, T,) arguments and the use of turbulence quantities, (ϵ with dimensions L^2T^{-3} and v with dimensions L^2T^{-1}) to represent the l_{lk} [*Kolmogorov*, 1962].

$[m]$

$$l_{lk} = \left(\frac{v^3}{\epsilon}\right)^{\frac{1}{4}} \tag{18}$$

1.3.1.5 Kolmogorov hypothesis

Kolmogorov [1941] theory was the first to suggest how energy, represented as power spectrum density (PSD) (Fig. 1.4), is distributed as a function of wavenumber. This theory is applicable only when Re number is high enough ($Re > Re_c$), the flow is turbulent, and small scale eddies are isotropic. Kolmogorov proposed that large scale eddies (small wavenumber) gain energy from the mean flow much more than they lose, this is called turbulence production (energy-containing range). Energy transfers into heat energy and potential energy feeding on the TKE of the flow through straining, until eventually all that TKE energy is dissipated by viscosity (dissipation range). Between the energy-containing range and dissipation range lies a subrange where turbulence production rate equals the dissipation rate and in which the PSD follows the well-known -5/3 slope (inertial subrange) (eqn. 53) [*Baumert et al*, 2005]. Separating the energy-containing range and inertial subrange is length scale l_{EI}(l_{EI}≈1/6 of the largest eddy). Separating the inertial subrange and dissipation range is length scale l_{DI} (l_{DI}≈60l_{lk})[*Pope*, 2000].

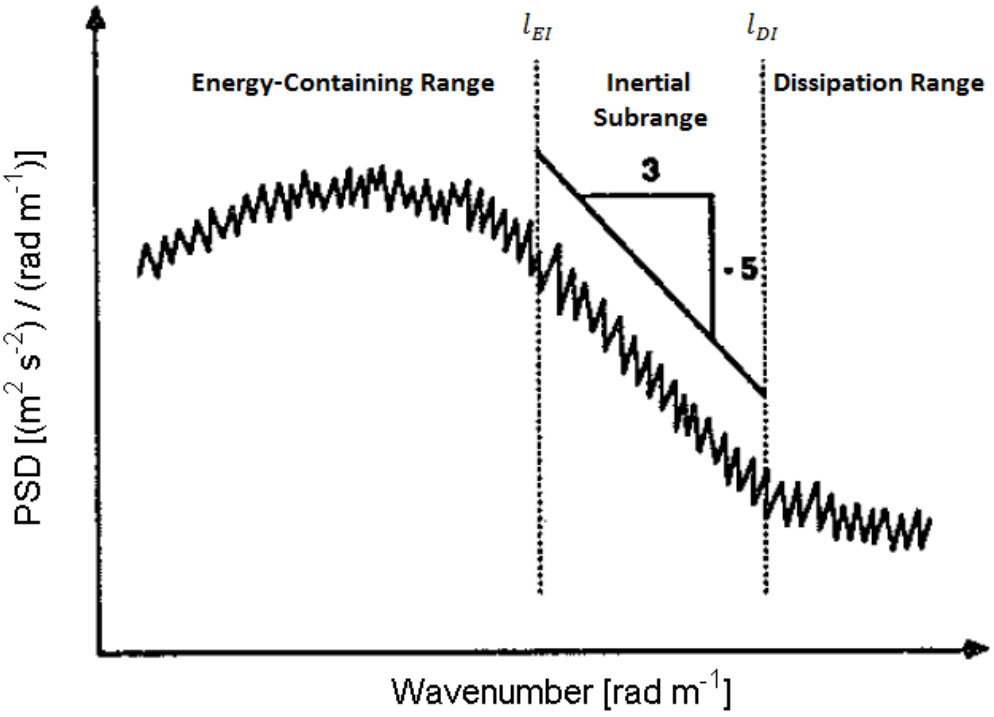

Fig 1.4. PSD Plot. The plot shows the inertial subrange aligned with the -5/3 slope and the length scales of l_{EI} and l_{DI} where the energy production rate and dissipation rate changes are significant [Stull, 1988].

1.3.2 Numerical modeling

Observing physical processes of turbulence in water bodies is challenging due to their irregular and random motion. To assist with this task, a numerical model, forced by the available observations (heat fluxes, momentum fluxes, temperatures profiles and velocity profiles), may elucidate the turbulence processes through the use of suitable mathematical models of the flow field [*Bolding et al.*, 2002]. The difficult part in numerical models is choosing the correct model that best describes the region of study in terms of its dynamics. For the study of small scale mixing in an aquatic body, a statistical turbulence closure model is more convenient, where the Navier-stokes

equation and the continuity equation are used to deduce the mean properties (salinity, temperature and velocity) of large scale flows using Reynolds averaging (for details see section 3.2.2) [*Sander*, 1998].

1.3.2.1 Statistical approach to turbulence

Most geophysical flows tend to be turbulent ($Re > Re_c$), and it would be difficult to look at each individual turbulent fluctuation, so in this work, statistical tools are used to describe the macroscopic properties of turbulence following *Reynolds* [1894]. The starting point is Reynolds averaging of the relevant continuity, momentum (Navier-Stokes) and heat equations. The first step is to "break down" the velocity and other quantities into mean and fluctuating components (Reynolds decomposition):

$$[ms^{-1}] \qquad u = \langle u \rangle + u' \tag{19.1}$$

$$[ms^{-1}] \qquad v = \langle v \rangle + v' \tag{19.2}$$

$$[ms^{-1}] \qquad w = \langle w \rangle + w' \tag{19.3}$$

where square brackets, $\langle u \rangle, \langle v \rangle, \langle w \rangle$, represent an average and the primes, u', v', w', represent fluctuations (u, v, w, are the x, y and z velocity components). It follows that:

$$0 = \langle u' \rangle \quad , \quad 0 = \langle v' \rangle \quad , \quad 0 = \langle w' \rangle$$

Beginning with the momentum (Navier-Stokes) equation for rotating fluids:

$$\frac{\partial u}{\partial t} + \frac{\partial}{\partial x}(uu) + \frac{\partial}{\partial y}(uv) + \frac{\partial}{\partial z}(uw) - fv = -\frac{1}{\rho}\frac{\partial p}{\partial x} + \nu\left(\frac{\partial^2 u}{\partial x^2} + \frac{\partial^2 u}{\partial y^2} + \frac{\partial^2 u}{\partial z^2}\right) \tag{20.1}$$

$$\frac{\partial v}{\partial t}+\frac{\partial}{\partial x}(vu)+\frac{\partial}{\partial y}(vv)+\frac{\partial}{\partial z}(vw)+fu= \\ -\frac{1}{\rho}\frac{\partial p}{\partial y}+\nu\left(\frac{\partial^2 v}{\partial x^2}+\frac{\partial^2 v}{\partial y^2}+\frac{\partial^2 v}{\partial z^2}\right) \tag{20.2}$$

$$\frac{\partial w}{\partial t}+\frac{\partial}{\partial x}(wu)+\frac{\partial}{\partial y}(wv)+\frac{\partial}{\partial z}(ww)= \\ -\frac{1}{\rho}\frac{\partial p}{\partial z}-g+\nu\left(\frac{\partial^2 w}{\partial x^2}+\frac{\partial^2 w}{\partial y^2}+\frac{\partial^2 w}{\partial z^2}\right) \tag{20.3}$$

where f is the Coriolis parameter, ν is the kinematic viscosity and the last term on the RHS is the frictional term.

Averaging equation (20) and using equation (19) results in:

$$\frac{\partial\langle u\rangle}{\partial t}+\frac{\partial}{\partial x}(\langle u\rangle\langle u\rangle)+\frac{\partial u}{\partial y}(\langle u\rangle\langle v\rangle)+\frac{\partial}{\partial z}(\langle u\rangle\langle w\rangle)-f\langle v\rangle= \\ -\frac{1}{\rho}\frac{\partial\langle p\rangle}{\partial x}+\nu\left(\frac{\partial^2\langle u\rangle}{\partial x^2}+\frac{\partial^2\langle u\rangle}{\partial y^2}+\frac{\partial^2\langle u\rangle}{\partial z^2}\right)-\boldsymbol{\frac{\partial\langle u'u'\rangle}{\partial x}}-\boldsymbol{\frac{\partial\langle u'v'\rangle}{\partial y}}-\boldsymbol{\frac{\partial\langle u'w'\rangle}{\partial z}} \tag{21.1}$$

$$\frac{\partial\langle v\rangle}{\partial t}+\frac{\partial}{\partial x}(\langle v\rangle\langle u\rangle)+\frac{\partial u}{\partial y}(\langle v\rangle\langle v\rangle)+\frac{\partial}{\partial z}(\langle v\rangle\langle w\rangle)+f\langle u\rangle= \\ -\frac{1}{\rho}\frac{\partial\langle p\rangle}{\partial y}+\nu\left(\frac{\partial^2\langle v\rangle}{\partial x^2}+\frac{\partial^2\langle v\rangle}{\partial y^2}+\frac{\partial^2\langle v\rangle}{\partial z^2}\right)-\boldsymbol{\frac{\partial\langle v'u'\rangle}{\partial x}}-\boldsymbol{\frac{\partial\langle v'v'\rangle}{\partial y}}-\boldsymbol{\frac{\partial\langle v'w'\rangle}{\partial z}} \tag{21.2}$$

$$\frac{\partial\langle w\rangle}{\partial t}+\frac{\partial}{\partial x}(\langle w\rangle\langle u\rangle)+\frac{\partial u}{\partial y}(\langle w\rangle\langle v\rangle)+\frac{\partial}{\partial z}(\langle w\rangle\langle w\rangle)= \\ -\frac{1}{\rho}\frac{\partial\langle p\rangle}{\partial z}-g+\nu\left(\frac{\partial^2\langle w\rangle}{\partial x^2}+\frac{\partial^2\langle w\rangle}{\partial y^2}+\frac{\partial^2\langle w\rangle}{\partial z^2}\right)-\boldsymbol{\frac{\partial\langle w'u'\rangle}{\partial x}}-\boldsymbol{\frac{\partial\langle w'v'\rangle}{\partial y}}-\boldsymbol{\frac{\partial\langle w'w'\rangle}{\partial z}} \tag{21.3}$$

By comparing the full equation (20) and averaged equation (21), it can be noticed that the terms indicated in bold font in equation (21) appear. These terms in bold $-\langle u'u'\rangle, -\langle u'v'\rangle, -\langle w'u'\rangle, -\langle v'v'\rangle, -\langle v'w'\rangle, -\langle w'w'\rangle,$ (9 terms in total with 3 redundant terms) as described by Reynolds, are the second moment terms, which represent the frictional stresses in the fluid due to turbulence and are called Reynolds stresses [*Cushman-Roisin*, 2011]. Reynolds stresses quantify the rate of momentum transfer across a surface due to turbulence [*Thorpe*, 2007]. A similar approach presented by Reynolds can be used to obtain various fluxes such as heat flux $\langle u'T'\rangle$ and salinity flux $\langle u'S'\rangle$.

1.3.2.2 GOTM

The turbulence model used for this study is the general ocean turbulence model (GOTM) (For details see [*Burchard and Bolding*, 2001; *Burchard et al.*, 2006; *Burchard et al.*, 2008; *Umlauf and Burchard*, 2003]). The GOTM simulates vertical mixing in the water column, turbulence parameters such as (TKE, TKE dissipation rate, eddy viscosity, eddy diffusivity) as well as other parameters (buoyancy frequency, velocity shear and *Ri* number).

It should be noted that this one dimensional model has disadvantages that need to be taken into consideration. Using a one dimensional numerical simulation model leads to a dimensional problems as the behavior is in three dimensions, not one. This causes an inaccurate increase in kinetic energy that increases the mixing rate above what is

observed in reality as suggested by *Mellor* [2001]. This challenge allows us to test the model by comparing the simulated results with the observation results.

A unique feature of GOTM is the option to choose a number of state-of-the-art closure models for simulations and turbulence models with different types and levels (zero-, one- and two-equation models, K-profile parameterization bulk model, algebraic models, empirical models) that have been extensively tested. Two of these models are the most widely used in geophysical flows, namely the two equation k-ϵ model [*Launder and Spalding*, 1972], and the level 2.5 *k-kl* model [*Mellor and Yamada*, 1982]. Each of these is investigated in this study for critical comparison with each other and with field data.

Both models use similar boundary layer approximations; both neglect the effect of Coriolis force since its small compared to the turbulent length scale. Also neglecting the horizontal pressure gradient since the model is one dimensional and all the advection terms can be neglected, as they are accounted for by the option of relaxing to the velocity and density profiles [*Burchard*, 2002].

The first part of the k-ϵ and *k-kl* models is to obtain two equations for calculating the TKE and TKE dissipation rate. From these values, eddy viscosity and diffusivity can be calculated for closure of the model.

1.3.2.3 The Ƙ-equation:

When the boundary layer approximations are applied (section 1.3.2.2), the transport equation for TKE in two-equation models is derived from Reynolds averaged equations (eqn. 21) and is given by:

$$Ƙ^{*} = D_{Ƙ} + P + B - \epsilon \tag{22}$$

where $Ƙ^{*}$is the derivative of Ƙ (eqn. 23) with time and space, $D_{Ƙ}$ is the sum of the gradient terms (advection and diffusion)(eqn. 25), P is rate of turbulence production by the mean flow (eqn. 26), B is the buoyancy flux (eqn. 27) and ϵ is the TKE dissipation rate (eqn. 28) [*Anis and Singhal*, 2006].

$$Ƙ = \frac{1}{2}(\langle u'^{2}\rangle + \langle v'^{2}\rangle + \langle w'^{2}\rangle) \tag{23}$$

where,

$$\langle v_j'^{2}\rangle = \frac{1}{N}\sum_{i=1}^{N}\left(v_{ij-}\langle v_j\rangle\right)^{2} \tag{24}$$

$$D_{Ƙ} = \frac{\partial}{\partial z}\left(\frac{v_t}{\sigma_{Ƙ}}\frac{\partial Ƙ}{\partial z}\right) \tag{25}$$

where σ_k is the Schmidt-number constant (Table 1 and 2) and v_t is the eddy diffusivity

(i) Production rate, *P*

The production rate is the TKE generated as a result of the mean flow. This rate is the product of the mean shear and Reynolds stress expressed as:

$$P = -\langle w'u' \rangle \frac{\partial U}{\partial z} - \langle w'v' \rangle \frac{\partial V}{\partial z} \quad (26)$$

(ii) Buoyancy flux, *B*

Buoyancy flux can be expressed as the turbulent potential energy. This type of energy adds to the turbulent kinetic energy by transfer of energy from potential to kinetic. Buoyancy flux is given by:

$$B = \left(-\frac{g}{\rho}\right) \langle w'\rho' \rangle \quad (27)$$

(iii) Dissipation rate, ∈

Dissipation rate is the turbulent kinetic energy lost as a result of viscosity. This term is negative in equation (22) indicating loss. Dissipation rate is expressed as:

$$\in = \upsilon \left\langle \left(\frac{\partial u}{\partial z}, \frac{\partial v}{\partial z}\right)^2 \right\rangle \quad (28)$$

1.3.2.4 The ϵ and Kl equations:

Both models use a different equation and constants to calculate the dissipation rate (eqn. 29 and 33).The *k*-ϵ model method takes the derivative of ∈ (eqn. 28) with time and space, a similar approach to what has been done with the K-equation (eqn. 22). Therefore resulting in the closed form of ϵ-equation:

$$\in^* = D_\in + \left(\frac{\in}{\mathrm{K}}\right)(c_{\in 1} P + c_{\in 3} B - c_{\in 2} \in) \quad (29)$$

where $\in^*$ is the derivative of $\in$ (eqn. 28) with time and space, $D_\in$ is the sum of the gradient terms (advection and diffusion) (eqn. 30) and $c_{\in 1}, c_{\in 2}$ are the empirical constants [*Anis and Singhal*, 2006]. $c_{\in 3}$ is a computed value that is dependent on the stratification level, and in stable conditions the value of $c_{\in 3}$ is near zero and in unstable conditions its near 1 (Table 1) [*Umlauf and Burchard*, 2003].

$$D_\epsilon = \frac{\partial}{\partial z}\left(\frac{\nu_t}{\sigma_\epsilon}\frac{\partial \epsilon}{\partial z}\right) \tag{30}$$

where σ_ϵ is the Schmidt-number for $\in$.

Table 1. *k-ϵ* Model Empirical Constants [*Rodi,* 1987].

σ_K	$\sigma_\in$	$c_{\in 1}$	$c_{\in 2}$	$c_{\in 3}$
1.0	1.3	1.44	1.92	See text 1.3.2.3

The *k-kl* model method in obtains $\in$ following *Rotta* [1951] by applying the integral of the two point correlation function that leads to a turbulent macro length scale equation (l). *Mellor and Yamada* [1982] suggested an equation for $\in$ by combining the product of K and l leading to:

$$Kl^* = D_l + \left(\frac{l}{2}\right)[E_1 P + E_3 B - E_2 F \in] \tag{31}$$

where Kl^* is the derivative of Kl with time and space, D_l is the sum of the gradient terms (advection and diffusion) (eqn. 32), F is the wall function (eqn. 33) and E_1, E_2 and E_3 are empirical constants (Table 2).

$$D_l = \frac{\partial}{\partial z}\left(KlS_l\frac{\partial Kl}{\partial z}\right) \tag{32}$$

where S_l is a constant Table 2.

$$F = 1 + E_2 \left(\frac{l}{\kappa l_z} \right)^2 \tag{33}$$

where κ is the Von Karman constant and $l_z$is the distance from the wall.

Table 2. *k-kl* Model Empirical Constants [*Mellor and Yamada,* 1982]

σ_K	S_l	E_1	E_2	E_3
1.96	0.2	1.8	1.33	1.8

1.3.2.5 Eddy viscosity and diffusivity

The challenging part about second momentum equations is the closure problem. There are more unknown parameters than equations. The unknown parameters include 14 Reynolds stress terms:

$$-\langle u'u' \rangle, -\langle u'v' \rangle, -\langle w'u' \rangle, -\langle v'v' \rangle, -\langle v'w' \rangle, -\langle w'w' \rangle, -\langle u'S' \rangle,$$

$$-\langle v'S' \rangle, -\langle w'S' \rangle, -\langle S'S' \rangle, -\langle u'T' \rangle, -\langle v'T' \rangle, -\langle w'T' \rangle, -\langle T'T' \rangle$$

while only four equations are known; the continuity and the three momentum equations. The solution to this challenge is to parameterize by approximation using the stability function (section 1.3.2.6). There are multiple techniques in closing the second order moments. All methods are derived from Reynolds averaging equation and based on the Reynolds stress and heat flux equation (section 1.3.2.1) [*Burchard and Bolding*, 2001]. These equations are related to eddy viscosity, v_t, and eddy diffusivity, $v_t{}'$, in terms of:

$$\langle w'u' \rangle = -v_t(\frac{\partial U}{\partial z}) \tag{34.1}$$

$$\langle w'v' \rangle = -v_t(\frac{\partial V}{\partial z}) \tag{34.2}$$

$$\langle w'T' \rangle = -v_t'(\frac{\partial T}{\partial z}) \tag{34.3}$$

Eddy viscosity is for the momentum flux and eddy diffusivity is for the temperature flux. v_t is related to K and $\in$ through equation (37). This is done by combining the relationship of v_t to K from equation (35) and the relationship of K with $\in$ from equation (36).

$$v_t = c_\mu \sqrt{\mathrm{K}} l \tag{35}$$

c_μ is stability function that depends on the stability of the flow in terms of shear number and buoyancy-number (section 1.3.2.6) [*Umlauf and Burchard*, 2003].

$$\in = c_d \frac{\mathrm{K}^{3/2}}{l} \tag{36}$$

where c_d is am empirical constant.

$$v_t = c_\mu \frac{\mathrm{K}^2}{\in} \tag{37}$$

Similar to eddy viscosity eddy diffusivity v'_t is given as:

$$v'_t = c'_\mu \frac{\mathrm{K}^2}{\in} \tag{38}$$

where c'_μ is a stability function. [*Rodi*, 1982].

1.3.2.6 Stability functions

All stability functions in GOTM, including the ones used by the *k*-ϵ and *k*-*kl* models (section 1.3.2.3) that contain the second momentum equations, are non-dimensional. These functions depend on two parameters:

(i) Shear number α_S:

$$\alpha_S = \frac{\mathrm{K}^2}{\epsilon^2} S^2 \tag{39}$$

where S^2 being the shear frequency expressed as:

$$S^2 = \left(\frac{\partial U}{\partial z}\right)^2 + \left(\frac{\partial V}{\partial z}\right)^2 \tag{40}$$

(ii) Buoyancy number α_N:

$$\alpha_N = \frac{\mathrm{K}^2}{\epsilon^2} N^2 \tag{41}$$

There are a number of methods to calculate the c'_μ and c_μ stability functions used in the GOTM. Some of these methods are:

(i) *Kantha and Clayson* [1994]:

$$c_\mu = \frac{0.1682 + 0.03263\alpha_N}{1 + 0.4679\alpha_N + 0.07372\alpha_S + 0.01761\alpha_N\alpha_S + 0.003371\alpha_N^2} \tag{42}$$

$$c'_\mu = \frac{0.1783 + 0.01586\alpha_N + 0.003173\alpha_N}{1 + 0.4679\alpha_N + 0.07372\alpha_S + 0.01761\alpha_N\alpha_S + 0.003371\alpha_N^2} \tag{43}$$

(ii) *Canuto et. al* [2001] version A:

$$c_\mu = \frac{0.1070 + 0.01741\alpha_N - 0.00012\alpha_S}{1 + 0.2555\alpha_N + 0.02872\alpha_S + 0.008677\alpha_N^2 + 0.005222\alpha_N\alpha_S - 0.0000337\alpha_S^2} \quad (44)$$

$$c'_\mu = \frac{0.1120 + 0.004519\alpha_N + 0.00088\alpha_S}{1 + 0.2555\alpha_N + 0.02872\alpha_S + 0.008677\alpha_N^2 + 0.005222\alpha_N\alpha_S - 0.0000337\alpha_S^2} \quad (45)$$

(iii) *Canuto et. al* [2001] version B:

$$c_\mu = \frac{0.1270 + 0.01526\alpha_N - 0.00016\alpha_S}{1 + 0.1977\alpha_N + 0.03154\alpha_S + 0.005832\alpha_N^2 + 0.004127\alpha_N\alpha_S - 0.000042\alpha_S^2} \quad (46)$$

$$c'_\mu = \frac{0.1190 + 0.00429\alpha_N - 0.00066\alpha_S}{1 + 0.1977\alpha_N + 0.03154\alpha_S + 0.005832\alpha_N^2 + 0.004127\alpha_N\alpha_S - 0.000042\alpha_S^2} \quad (47)$$

(For more detail about stability functions see [*Burchard and Bolding*, 2001])

(iv) *Cheng et. al* [2002]

$$c_\mu = \frac{0.107 + 0.019\alpha_N - 0.00018\alpha_S}{1 + 0.2826\alpha_N + 0.02816\alpha_S + 0.008927\alpha_N^2 + 0.0055\alpha_N\alpha_S - 0.00005\alpha_S^2} \quad (48)$$

$$c'_\mu = \frac{0.1208 + 0.004376\alpha_N + 0.00058\alpha_S}{1 + 0.2826\alpha_N + 0.02816\alpha_S + 0.008927\alpha_N^2 + 0.0055\alpha_N\alpha_S - 0.00005\alpha_S^2} \quad (49)$$

1.3.3 Combination of observation and numerical modeling

A combination of observation and numerical model techniques are used in this study. Limitations in the field measurement technique may be alleviated by using numerical modeling. The numerical model is forced by observational measurements wind stress, heat flux, momentum flux and relaxed with the observed currents and the thermal structure of the water column. The relaxation of the models allows it to look back at the observation profiles of parameters such as temperature and velocity to reassess its simulations accordingly.

The combination of observations and numerical modeling also allows for validating the model and testing its accuracies.

1.4 Study region

Located in the state of Texas, in the United States of America, Lake Whitney Reservoir (Fig 1.5) is part of the Brazos River Basin with a surface area of ~95Km² [*Schwierzke et. al,2010*]. The lake's main source of inflow is from Granbury Lake and rainfall from a catchment area of 45,644km². The average depth of the lake is ~5m with a total volume of $467 \times 10^6 m^3$ [*Roelke et. al, 2010*]. In 1951, Whitney Dam was built to provide hydropower, agriculture purposes and water level control [*Seth, 2011*].

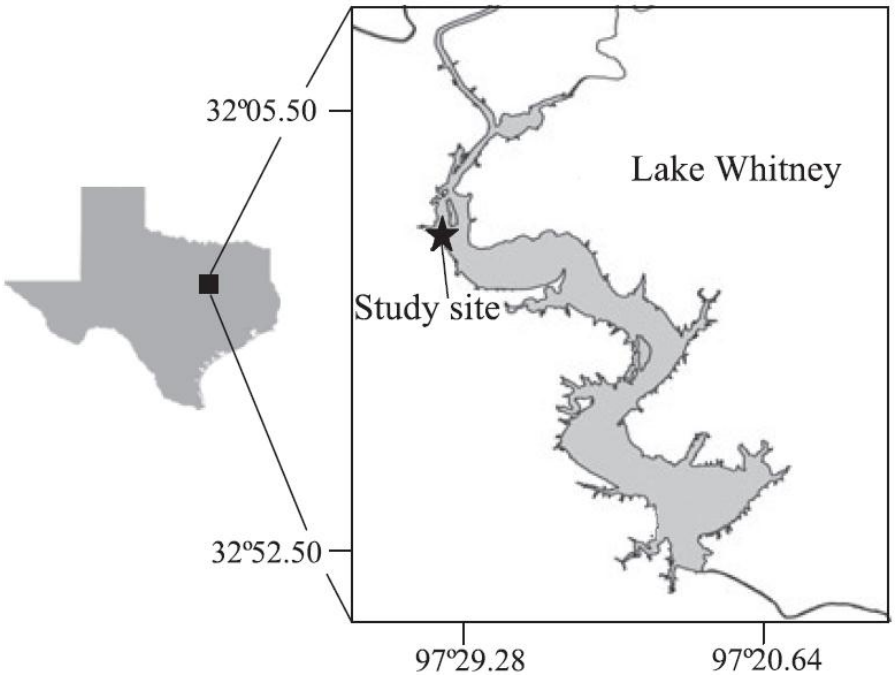

Fig 1.5. Study Site [*Schwierzke et al.*, 2010].

Major fish kill caused by toxic blooms, mainly *Prymnesium parvum*, in the past 30 years have been reported by studies on Lake Whitney. These blooms generated as a result of stratification level controlling the nutrients concentrations in the water column, resulting in the fish kill. Studies of Lake Whitney suggest that the blooms commonly occur during the winter season when specific conditions are met [*Roelke et al.*, 2010; *Roelke et al.*, 2011; *Schwierzke et al.*, 2010].

2. METHODS

'Turbulence is a three dimensional time dependent motion in which vortex stretching causes velocity fluctuations to spread to all wavelengths between a minimum determined by viscous forces and a maximum determined by the boundary conditions. It is the usual state of fluid motion except at low Reynolds numbers' [*Bradshaw*,1972]

Data collection was conducted at two stations (A) and (B) in Lake Whitney, Texas from January to July 2006. Station (A) measured hydrographic data and station (B) measured meteorological data (Fig 2.1).

Fig 2.1. Hydrographic Station (A) and Meteorological Station (B).

Fig 2.2. ADCP & ADV on the Bottom Mount (Photograph courtesy Dr. Ayal Anis).

2.1 Station (A)

Field observation is the measurement of turbulence to observe the nature of a fluid flow at the field. This is done by measuring the changes in the water structure with time in terms of parameters, such as velocity and temperature. There are two types of classes for field measurements: Lagrangian and Eulerian. Lagrangian measurements are done at multiple locations, therefore provides data over a path. Eulerian measurements are done at a fixed location, as done in this study using an Acoustic Doppler Current Profiler (ADCP) and Acoustic Doppler Velocimeter (ADV) (Fig 2.2) [*Pond,* 1983]. The use of these techniques are common due to their advantages, such as cost when compared to other instruments, high sampling rate, small sampling volume and the instruments ability to measure water velocity in three directions (X, Y, Z).

Both the ADCP and ADV consist of sound transmitters and receivers (Fig 2.3 and 2.4). The transmitted sound pulses are reflected off of any reflectors in the water column such as suspended sediments or air bubbles and through the Doppler phase shift the flow velocity is calculated using:

$$[ms^{-1}] \qquad U = \frac{c(d\emptyset/dt)}{4\pi f} \qquad (50)$$

where c is the sound speed in the medium, $\emptyset$ is the signal phase, and f is the operating frequency.

Fig 2.3. Nortek Aquadopp Current Profiler [*Nortek*, 2008].

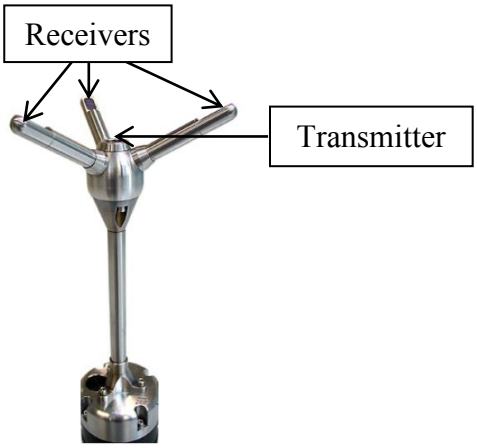

Fig 2.4. Nortek Vector Current Meter [*Nortek*, 2005].

ADV's sampling resolution also allows the observation of the TKE, TKE dissipation rate and Reynolds stresses.

Station (A), located at 32.018^{0}N, 97.487^{0}W, consisted of a vertical mooring line instrumented to measure the vertical thermal structure, using a string of temperature loggers, and water-currents, using an ADCP and an ADV mounted at the bottom (Fig 2.5). The water depth at station (A) was about 9m.

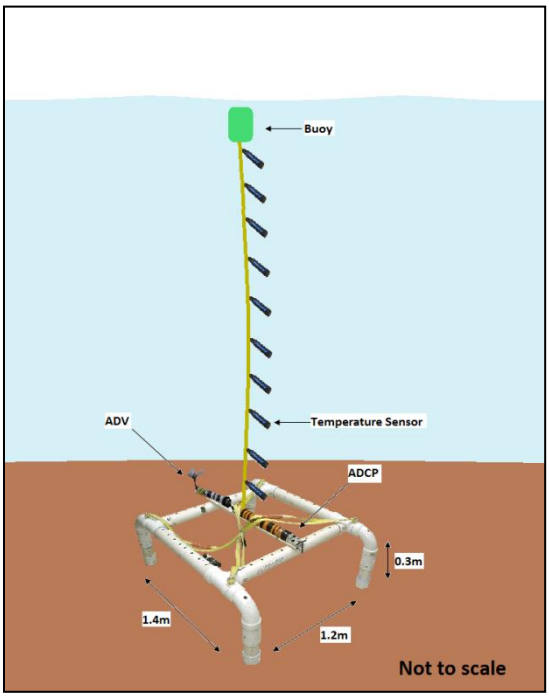

Fig 2.5. Sketch of Mooring at Station (A).

(i) Thermal structure

The vertical thermal structure of the water column was measured using 10 to 32 temperature loggers (ONSET Water Temp Pro: accuracy ±0.2 ^{0}C and resolution 0.02

^{0}C) with more loggers used during high stratification conditions. The loggers were set to take measurements at two minutes intervals.

(ii) Water-currents

Mounted at the bottom of the mooring (~8.6m depth) the ADCP and ADV (Fig 2.2) measured the velocity profile and velocity at single point at the BBL (0.73m from the bottom), respectively.

The ADCP (Nortek 1 MHz; accuracy 1% of the measured value ±0.5 cms^{-1}; [*Nortek*, 2008]) measured profiles of water-currents in bins of vertical length of 0.3m. Profiles were averaged over four minute intervals. The measurements were then rotated from earth coordinates (North-South and East-West) into cross channel (246°) and along channel (336°) directions following the bathymetry of Lake Whitney.

The ADV (Nortek; accuracy ±0.5% of the measured value ±0.1cms^{-1}; [*Nortek*, 2005]) measured water-currents at a single point in the BBL in bursts. Each burst included 1024 samples, sampled at a rate of 16Hz [*Nortek*, 2005]. Time interval between bursts was 450 seconds. Similar to the ADCP, the measurements were oriented from earth coordinates to match the bathymetry of Lake Whitney.

Using the ADV time series of velocity fluctuations, it is possible to estimate the PSD of the three velocity components u (along-channel), v (cross-channel) and w (vertical) (Fig 2.6) [*Press et al.,* 2007] from which the TKE and TKE dissipation rates can then be obtained. The measured velocity fluctuations represent a wide range of eddies at different wave numbers [*Thorpe*, 2005]. To show the contribution of energy

from these eddies at different scales Taylor hypothesis [*Taylor*, 1938] was applied to convert the time series from frequency space to wave number space:

$$[\frac{m^2 s^{-2}}{rad\ m^{-1}}] \qquad E(k) = \frac{E(f)\langle U\rangle}{2\pi} \tag{51}$$

where $E(k)$ is the wavenumber spectra, $E(f)$ is the frequency spectra and $\langle U\rangle$ is the mean horizontal velocity.

TKE dissipation rates were estimated by first selecting a range of wavenumbers in the PSD where it follows a -5/3 slope and fitting the selection by the robust regression algorithm. The robust regression fitting is based on the least square regression (eqn. 52). However, unlike the least square regression, it reduces the influence of outlier data with the use of the bi-square function [*Hubber*, 1964].

$$S = \sum_{i=1}^{N} (y_i - y'_i)^2 \tag{52}$$

where y_i is the value of y at the *i*th element and y'_i is the corresponding value of y at the *i*th element [*Emery and Thomson*, 1997]. The value of y in this study is $E(k)$ and the *i*th element represents the wavenumber (k).

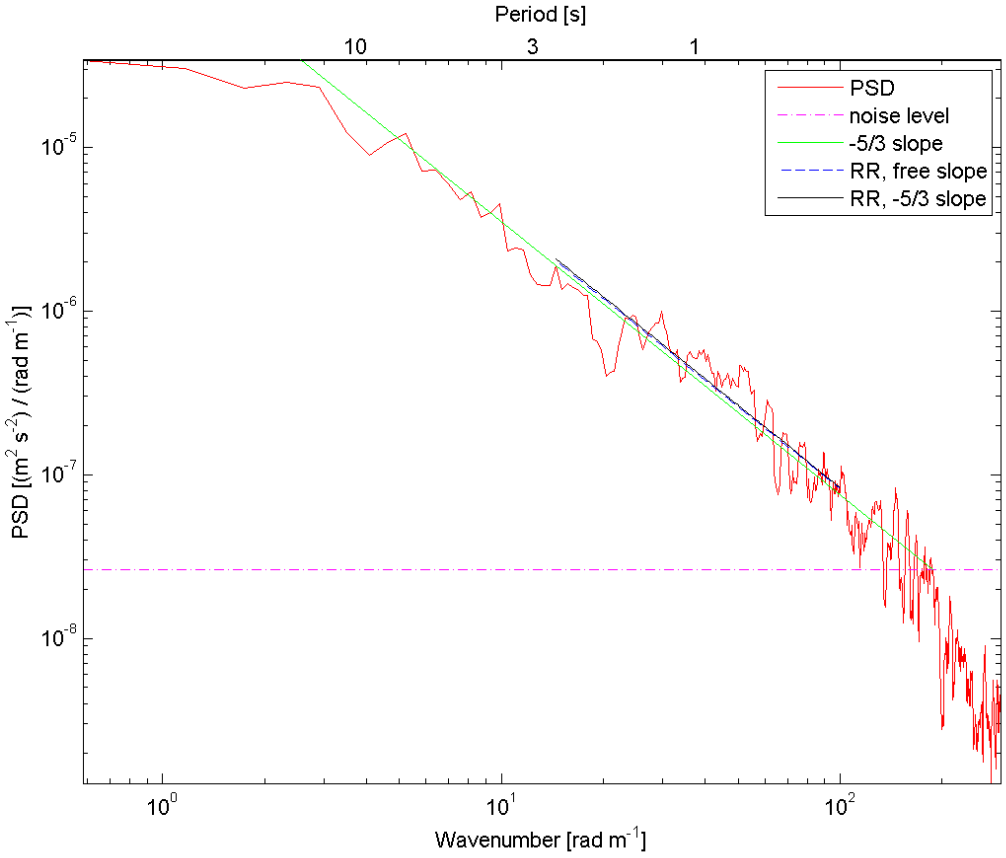

Fig 2.6. Example of PSD of the Vertical Velocity Component. The plot shows the -5/3 free slope is within 95% confidence interval of the robust regression. Noise level line is set as the 10% of the lowest *E(k)*.

In the example shown in Figure 2.6, the selected range was 13-195 rad m⁻¹. The range selection shows a good fit to a -5/3 slope within the 95% confidence interval. After selecting the region on the PSD, the TKE dissipation rate was obtained by equation (53). This was carried out for 2217 bursts in which only slopes fitting within the 95% confidence interval were used.

$$[\frac{m^2 s^{-2}}{rad\ m^{-1}}] \qquad E(k) = C\varepsilon^{\frac{2}{3}}k^{-\frac{5}{3}} \qquad (53)$$

where C is a universal Kolmogorov constant with a value of:

(i)For a longitudinal spectrum, $\mathrm{C} = \mathrm{C}_1 \approx 0.9$ [*Pope*, 2000], where the direction of the velocity component is aligned with the wavenumber direction [*Tennekes and Lumley*, 1972].

(ii)For a transverse spectrum, $C = C_2 \approx 0.65$ [*Pope*, 2000], where the direction of the velocity component is perpendicular to the wavenumber. [*Tennekes and Lumley*, 1972]. In this study the value of C_2 was used since the vertical component of velocity in the PSD was used, which is perpendicular to the wavenumber.

The vertical velocity component was chosen and not the horizontal is because the ADV is more sensitive to the vertical velocity changes. This is due to the vertical component being parallel to the transmitting beam, unlike the horizontal component where the reflection is at an angle (Fig 2.7) (For details see [*Nortek*, 2005]). This also allows the vertical component to have a lower noise level threshold.

A second turbulent parameter that can be estimated from the PSD is the TKE in the inertial subrange:

$$[m^2 s^{-2}] \qquad \mathrm{K} = \int_{2\pi/l_{EI}}^{2\pi/l_{DI}} E(k)dk - \int_{2\pi/l_{EI}}^{2\pi/l_{DI}} N dk \qquad (54)$$

where N is the noise spectrum (for the ADV the noise spectrum is white)

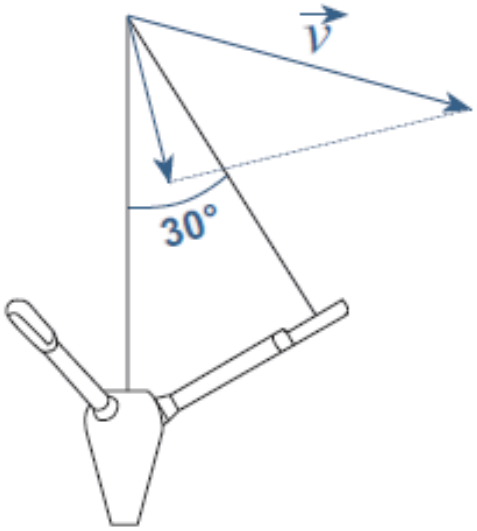

Fig 2.7. ADV's Angle of Reflection [*Nortek*, 2005].

2.2 Station (B)

Surface meteorological parameters were measured at station (B) (location 32.019^0N and 97.487^0W). The station consisted of a tripod (Fig 2.8) with sensors to measure air temperature and humidity (Campbell model CS500 housed in a Davis solar powered fan aspirated radiation shield), wind speed (Campbell wind-anemometer model 03101-5) and direction (Campbell wind vane model 03301-5), incoming solar radiation (Kipp & Zonen silicon pyranometer model SP Lite), long wave radiation (Kipp & Zonen CG3 Pyrgeometer), barometric pressure (Vaisala model PTA427), and rainfall rate (Texas Electronics tipping bucket rain gage model TE525). Sensors sampled every five seconds and data was then averaged over a 10 minute period and stored. These meteorological parameters were measured to obtain the net surface heat flux (J_q^o) and momentum flux into the SBL. The calculated parameters of J_q^o and momentum flux will

be used to explain the physical processes in the water column and also to force the model.

Fig 2.8. Station B Meteorological Measurement Tripod (Photograph courtesy Dr. Ayal Anis).

(i) Contributing to the thermal structure of the water column is net surface heat flux which is the sum of the following four components:

$$J_q^o = J_q^{sw} + J_q^{lw} + J_q^l + J_q^s \quad [Wm^{-2}] \tag{55}$$

where $J_q^{sw}$is the measured net shortwave radiation after applying *Payne* [1972] correction for albedo, J_q^{lw} is the measured net longwave radiation after applying *Dickey et al.* [1994] formulation, J_q^l is the latent heat flux and J_q^s is the sensible heat flux. Both the sensible and latent heat fluxes were calculated using *Fairall et al.* [1996] and *Fairall et al.* [2003] parameterization [*Anis and Singhal*, 2006].

For the surface heat flux calculations, the measured surface water temperatures were corrected using *Fairall et al.*[1996] to account for the cool skin layer. The cool skin layer is a ~1mm layer on top of the SBL in which temperature changes faster than the SBL due to its interaction with the air interface. This difference in cooling and warming rate between the cool skin and SBL is caused by J_q^{lw}, J_q^l and J_q^s [*Fairall et al.*, 1996].

(ii) Momentum flux (wind stress) (eqn. 56) transfer at the air-sea interface was calculated using:

$$[Nm^{-2}] \qquad \tau^2 = \sqrt{\tau^x + \tau^y} = C_D \rho_w U_r^2 \qquad (56)$$

where τ is the rate per unit area at which horizontal momentum is transferred vertically, C_D is the drag coefficient, ρ_w is the water density and U_r is the wind speed at a reference point, commonly taken at a height of 10m above the surface.

(iii) In addition to wind stress, the wind power was also computed as:

$$[Wm^{-2}] \qquad E_{10} = \tau * U_r \qquad (57)$$

(iv) To indicate convective conditions the surface buoyancy flux (J_b^0) and Monin-Obukov length (L) (section 1.2.1.4) were calculated using:

$$[Wkg^{-1}] \qquad J_b^0 = \frac{g \alpha_T J_q^0}{C_p \rho} \qquad (58)$$

$$[m] \qquad L = -\frac{(\tau/\rho_o)^{3/2}}{\kappa J_b^0} \qquad (59)$$

3. RESULTS

3.1 Observational results

3.1.1 Overview of Lake Whitney's meteorological observations

Continued sampling of meteorological data at station (B) starting February and ending mid-July 2006 provided data time series for late winter (February to mid-March), spring (mid-March to May) and summer seasons (May to July). Overall, the atmospheric pressure observations follow the general seasonal global pressure systems pattern (Fig 3.1), where the impact of the seasonal pressure systems on the local weather is significant. The presence of a dominant high pressure system during winter results in north-westerly winds (continental polar air mass) and the presence of a dominant low pressure system during summer results in south-easterly winds (tropical maritime air mass). These two major wind patterns (Fig 3.2) have shown to bring different weather characteristic to the region. A north-westerly wind is characterized to cause relatively colder and drier conditions, while the south-easterly winds cause relatively warmer and humid conditions.

During the winter, the dominant high pressure system (atmospheric pressure≥1000mb) in the region is a result of the cold continental land mass causing the air mass in the Hadley cell to descend. The presence of the high pressure system can be noticed from the atmospheric pressure measurements during winter (Fig 3.3 panel F). The high pressure system resulted in north-westerly winds bringing dry and relatively colder conditions to Lake Whitney (Fig 3.3 panels B, C and D). The dominant winter high pressure is often interfered by a low pressure system (atmospheric

pressure<1000mb) moving to Texas and causing winds to veer and become south-westerly as seen on February 1st and 15th. Warm and humid conditions are associated with the south-westerly winds (Fig 3.3 panels B, C and D). However, these conditions do change to extreme cold conditions whenever a cold front is pushed south by the low pressure system. An example of the passing of a cold front over Lake Whitney can be noticed on February 17th-18th and resulted in a steep drop in air temperature from 29°C to a minimum recorded value of -4.9°C and wind speed of 11ms^{-1} with gusts up to 16ms^{-1}. Similar conditions were observed on March 18th-20th, when a total of 72mm of rainfall was measured, a drop in air temperature from 19°C to 10°C and relatively high wind speed were recorded up, to 10 ms^{-1}, as a cold front passed over the area.

In summer, the warm continental land mass radiates heat resulting in a dominant low pressure system over the region. This can be noticed from the recorded atmospheric pressure observations during summer being mostly lower than 1000mb (Fig 3.3 panel F). Similar to the winter period associated with the low pressure system are south-westerly winds. These winds caused relatively high humilities, up to 95%, and air temperatures up to 38°C as seen during July. Summer storm events passing Lake Whitney caused peak values of rainfall and wind velocities. The storm on June 18th resulted in the maximum recorded rainfall of 17.3mm. The storm event on April 22nd caused a maximum recorded wind speed of 14.1 ms^{-1} for the duration of this study.

(Monthly meteorological observations are in the appendix section).

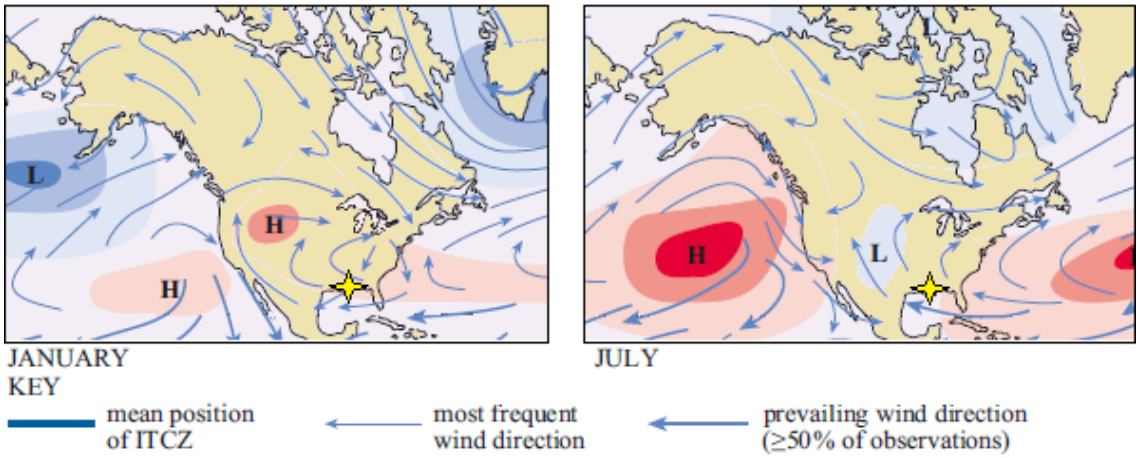

Fig 3.1. Regional Seasonal Pressure Systems with the Prevailing Winds. (left) Northern hemisphere winter period, (right) Northern hemisphere summer period [*Colling et. al*, 2001].

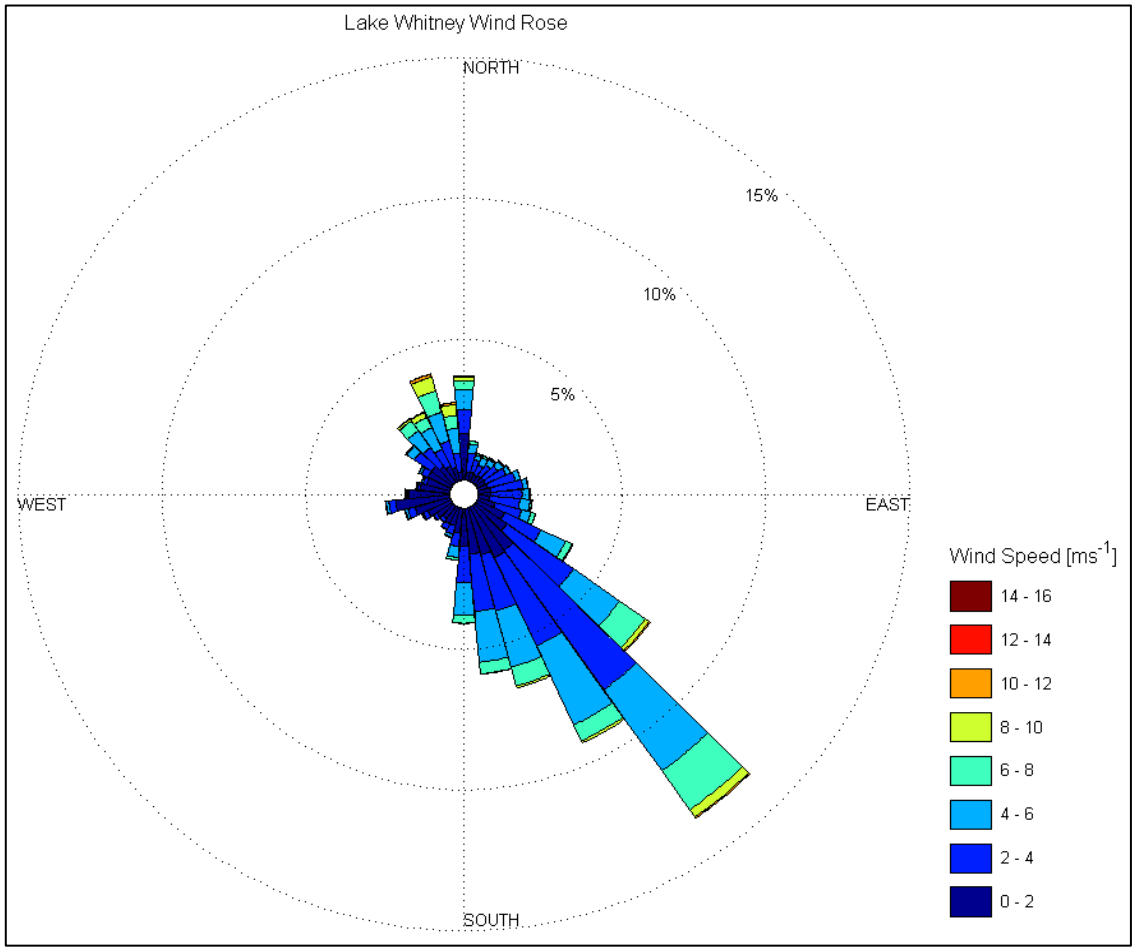

Fig 3.2. Wind Rose Plot of Wind Speed and Direction for the Periods of February to Mid-July.

Table 3. Basic Monthly Statistics of Meteorological Parameters from February to Mid-July. The negative heat flux represents flux into the lake surface.

	Mean wind stress			**Net heat flux**			**Rainfall**
	Magnitude (Nm^{-2})	Direction (^{o})	Max (Nm^{-2})	Mean (Wm^{-2})	Max gain (Wm^{-2})	Max loss (Wm^{-2})	Total (mm)
Feb.	0.023	287	0.29	1.74	866	420	30
Mar.	0.021	169	0.25	-41	843	431	76
Apr.	0.018	143	0.39	-59	851	604	58
May	0.02	150	0.2	-54	819	602	65
June	0.017	146	0.23	-32	779	505	67
July	0.012	137	0.18	-45	852	512	11

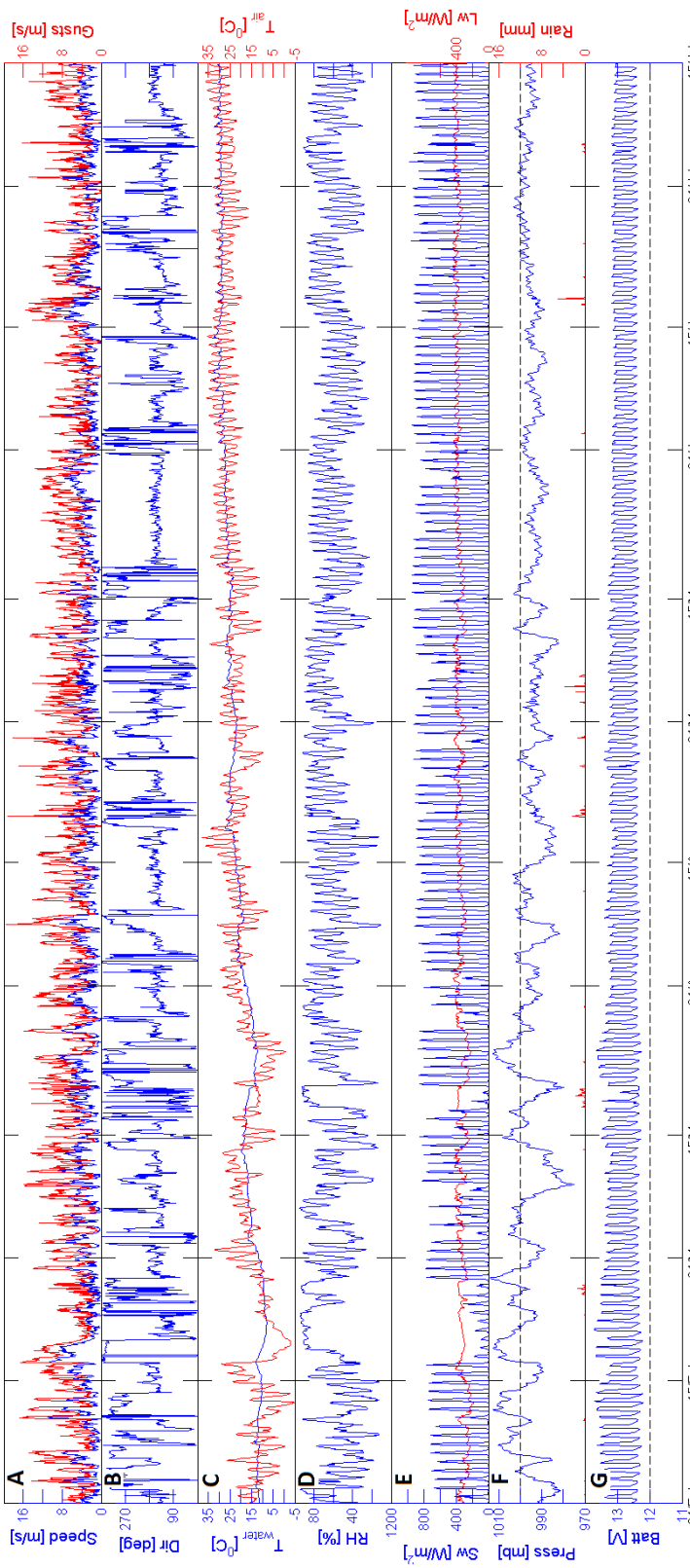

Fig 3.3. Hourly Averaged Measured Meteorological Data from February to Mid-July. (A) wind speed and gusts, (B) wind direction, (C) water surface temperature and air temperature, (D) relative humidity, (E) short and longwave radiation, (F) atmospheric pressure and rainfall,(G) battery voltage. Time axis is UTC.

3.1.2 Overview of Lake Whitney's momentum and heat fluxes observations

The momentum and heat fluxes are based on the meteorological conditions. The wind stress and wind power followed the same trend as wind speed. Both parameters were higher during the winter and spring periods than summer (Table 3). Also, relatively higher computed values of wind stress and wind power were observed during summer storm events, e.g. on May 3rd-5th and June 18th. The highest recorded value of wind stress was 0.39 Nm^{-2}, recorded on April 22nd (Fig 3.4 panel A).

The net shortwave radiation changed between the seasons (Fig 3.4 panel B), with maximum observed values during the summer as the earth reached its aphelion point in July. The maximum computed value for the net shortwave radiation absorbed by the lake was 1014Wm^{-2} on the afternoon of the July 14th on a clear and low wind speed day. The net shortwave radiation can be an indicator of cloud cover conditions, as the incoming solar radiation gets absorbed resulting in low values as observed on Feb 17th-26th, March 18th-20th, April 20th and 29th, May 3rd-5th, June 18th and July 6th.

The net longwave radiation fluctuated more during winter and spring periods, while following a more regular pattern in summer (Fig 3.4 panels B and C). The irregular pattern of the net longwave radiation during winter and spring was a result of the large fluctuation in air-water temperature differences (Fig 3.3 panel C). In summer the air-water temperatures differences followed a more conspicuous trend with a diurnal cycle resulting in a less fluctuating longwave radiation. In addition to the air-water temperature difference, cloudy condition periods blocking the direct solar radiation have shown to contribute to the amount of longwave radiation loss from the lake as well. The

sensible and latent heat fluxes followed a similar seasonal pattern as the net longwave radiation.

The second largest contributing parameter to the net surface heat flux after the shortwave radiation is latent heat flux. The latter varied with air-sea temperature difference, humidity and wind speed. High recorded values of latent heat fluxes up to 438Wm^{-2} were calculated during periods of high air-sea temperature difference and high wind velocity as seen on 17th February and May 11th (Fig 3.3 panel A and C). The sensible heat flux values followed a similar pattern to that of the latent heat flux, with values up to 187Wm^{-2} during the same period of high latent heat fluxes (Fig 3.4 panel C).

The net surface heat flux and buoyancy flux both are a function of the meteorological conditions. Periods when the lake cools as observed during the passage of a cold front, storm systems and cloudy conditions resulted in more positive net heat flux (heat loss from lake body) (Fig 3.4 panel D). As a result of this net cooling, the lake surface water became negatively buoyant. Similarly, when the water column is being heated during the day or when air temperature is warmer than the surface water temperature, this results in a more negative net heat flux (heat gained by the lake body). The result of this heating causes positively buoyant conditions. Overall, the values varied between -866Wm^{-2} and 604Wm^{-2} for the net heat flux (Table 3) and -6x$10^{-7}Wkg^{-1}$ and 3.7x$10^{-7}Wkg^{-1}$ for the buoyancy flux.

The Monin-Obukov length scales are dependent on the wind stress and buoyancy flux (Fig 3.4 panels A, D and E). In the absence of wind stress L=0 and will increase with increasing wind stress, at times reaching lengths larger than the actual lake depth, e.g. as observed on February 17th. The more energetic wind system during the winter period and negatively buoyant surface waters resulted in an average L=-0.33m. This suggests that convective conditions were strong during the winter period and at times homogenized the water column, as seen on the evening of March 14th. The relatively weak wind systems and positively buoyant surface waters during summer resulted in a positive average L=3.52m, indicating stable conditions.

The temperature difference between the cool skin layer (section 2.2) and SBL, indicated by dT_{cool}, was high when the air-sea temperature gradient was steep. Steeper air-sea temperature gradients were observed mostly in the winter (Fig 3.4 panel E). The maximum calculated value of dT_{cool}=1.13°C was observed during February 12th.

(Monthly heat and momentum fluxes observations are in the appendix section).

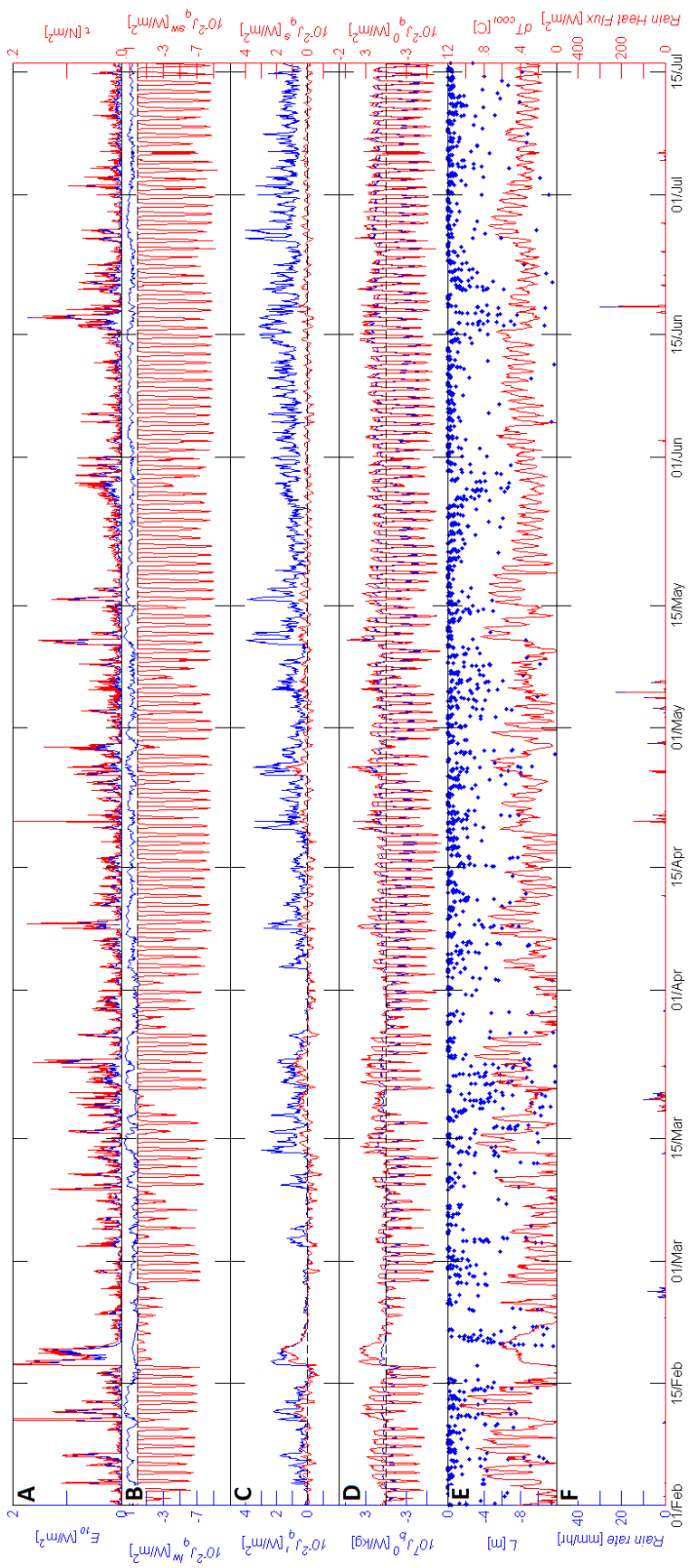

Fig 3.4. Hourly Averaged Surface Heat and Momentum Fluxes from February to Mid-July. (A) wind power and stress, (B) longwave and shortwave radiations, negative heat flux represents heat into water column, (C) latent and sensible heat fluxes, (D) buoyancy flux and net heat flux, (E) Monin-Obukov length scale and cool skin temperature, (F) rainfall and rainfall heat flux. Time axis is UTC.

3.1.3 Overview of Lake Whitney's hydrographic observations

Lake Whitney is an artificial reservoir constructed to provide flood control and other uses (section 1.4). Two rain events took place that allowed the lake's water level to rise substantially. The first event on March 18th to 22nd was followed by a water level increase of 0.87m. The second event started on May 5th and ended on May 15th resulting in a water level rise of 0.59m (Fig 3.5 panel A). Both events resulted in noticeable abrupt changes in the thermal and current structures of the water column (Fig 3.5 panels C, D and E).

The thermal structure of Lake Whitney followed a general heating trend as seasons progressed from winter to summer (Fig 3.5 panel C). The water column was well mixed during the winter period with temperature differences between surface and bottom layers were no more than 3°C. The minimum recorded temperature of 6.8°C occurred on February 20th in the BBL, shortly after the passage of a cold front. During spring the temperature gradient in the water column started to increase rapidly becoming more stratified as a result of the net heat flux. Maximum increase of water temperatures in spring were during periods of calm winds and clear skies as seen on April 3rd and 16th. The homogenizing effect of night convection became apparent in mid-spring (2nd April) and onwards. The summer season revealed a more pronounced diurnal trend, with the water column being strongly stratified during the day, with temperature differences between surface and bottom layers up to 7°C. The daytime heating of the water column was often interfered by strong wind events (>6ms^{-1}) inducing vigorous mixing capable of homogenizing the water column as observed on March 9th 24th, April 8th 20th 29th,

May 4th and June 17th. The maximum recorded temperature was 33°C at the SBL on June 3rd when winds were calm and the skies were clear.

The horizontal velocity components, u and v, were rotated to match Lake Whitney's bathymetry to reflect the along and cross channel flow directions. It should be noted that no velocity measurements were recorded during the periods of Februray15th to March 8th due to ADCP technical problems. These were resolved on March 8th.

The measurements show that the flow was stronger in the along-channel direction with velocities up to $0.3ms^{-1}$ (Fig 3.5) due to the bathymetry and wind velocity. The current at Lake Whitney is influenced by the meteorological conditions, primarily wind velocity. The wind velocity fluctuated more during the winter and spring periods than summer. The irregular wind pattern observed during the winter and spring periods were reflected in the current velocity, with strong wind events forcing the currents in the same direction as the wind. This is observed on February 11th when the northwesterly winds caused a downstream current and on March 27th when the southeasterly winds caused an upstream current. The result of a one directional flow of the water column is a buildup of a pressure gradient in the opposite direction of the wind. As wind relaxes, the pressure gradient forces a current at the BBL in the opposite direction of the previous wind event as observed on the February 12th and March 28th (section 4.1.1). In summer, the wind speed followed a more diurnal pattern, with winds stronger during day than night. During the day, the wind forced the current in the same direction as the wind building up a pressure gradient opposite to the wind direction. As the wind relaxed during the evening the pressure gradient forced a current in the opposite direction

(section 4.2.1). This summer diurnal pattern in current velocity was often interfered by storm events e.g. as observed on June 18th.

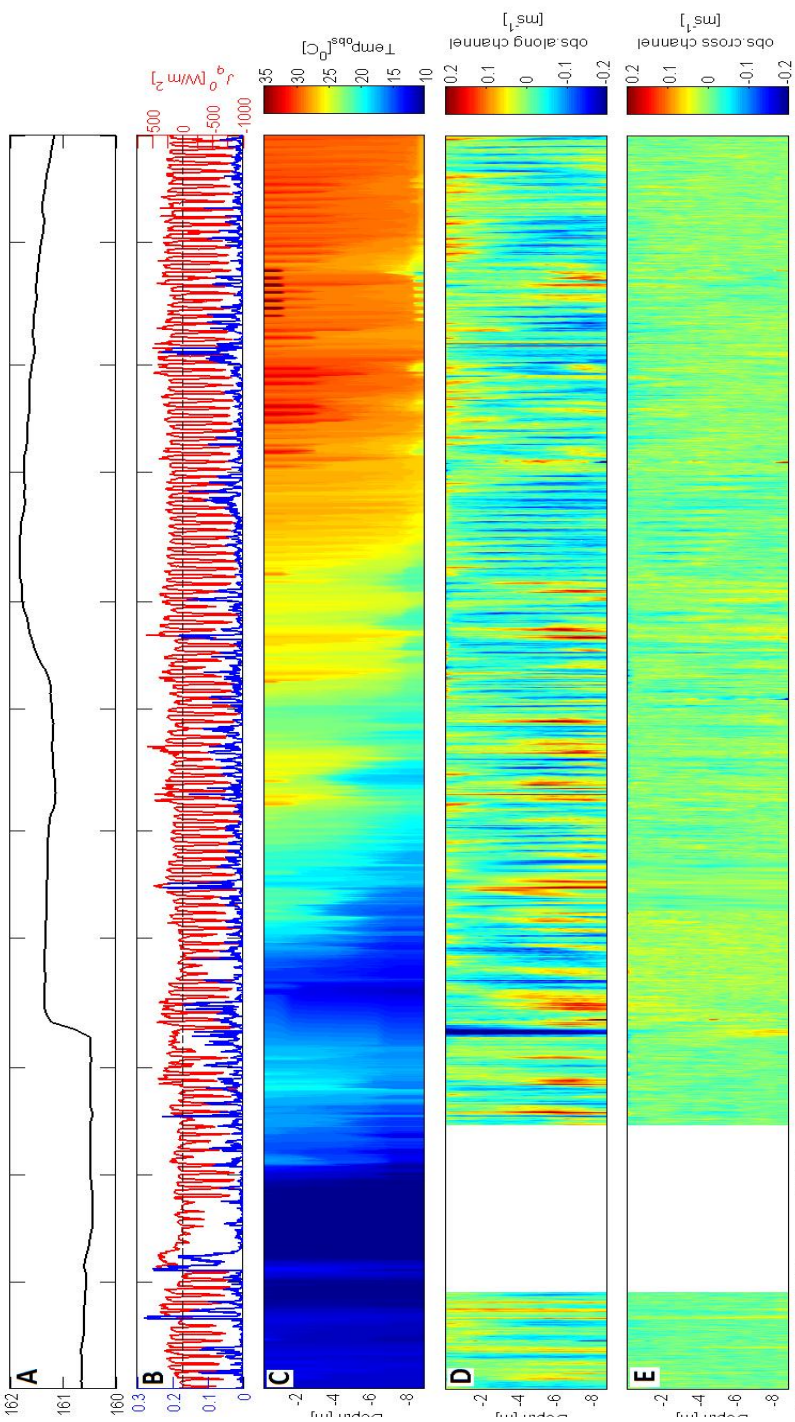

Fig 3.5. Meteorological and Hydrographical Observations from February to Mid-July. (A) Lake Whitney surface elevation above mean sea level, (B) surface momentum and heat fluxes, negative heat flux represents heat into water column, (C) thermal structure, (D) observed along channel velocity, where negative values represent a flow upstream, (E) observed cross channel velocity. Time axis is UTC.

3.2 Simulation results

Forced by surface heat and momentum fluxes only, i.e. no relaxation to thermal or current fields (Fig 3.6 panel B), the *k-kl* and *k-ϵ* models were used to simulate the thermal structure, TKE, and TKE dissipation rate throughout the period of the study (Feb 1st-July 15th) (Figs 3.6 and 3.7). Qualitatively, both model simulations show a similar pattern for these parameters.

3.2.1 Simulation results of the thermal structure

Overall, simulations of the thermal structure showed the progressive warming of the water column as the time progressed from winter to summer (Figs 3.6 and 3.7 panel D). During winter (February to March 15th), both models show a well-mixed thermal structure similar to the observed structure. As spring (March 15th to May) started, the water column began to heat up and become more stratified. The simulations results did underestimate the temperature by (<4.7°C) during spring as seen on March 15th to 18th, April 3rd to 8th, and April 20th to 26th. This was possibly caused by the runoff from rain events on March 13th, March 30th, and April 19th (Fig 3.3 panel F) which are not accounted for by the models. Similarly, during May the rainfall runoff between 2nd and 7th, in addition to dam flood control, could have been the reason for the underestimated heating of the water column by both models. During summer, the diurnal heating and cooling of the SBL was simulated well by both models. The simulated results of the thermal structure did not do well at the BBL (Fig 3.8), where a return flow caused by the

pressure gradient resulted in abrupt changes in water temperature making it cooler through advection as observed on May 11th, 17th and June 3rd, 9th, 14th, 26th-July 15th.

3.2.2 Simulation results of TKE and TKE dissipation

The TKE and TKE dissipation rate simulation results of both models follow a similar trend (Figs 3.6 and 3.7 panels E and F). The magnitude of both quantities varied primarily as a function of the surface forcing creating instability indicated by low Ri numbers ($Ri < Ri_c$) (Fig 3.6 and 3.7 panel G). During the winter and spring seasons, the atmospheric conditions were more energetic. As a result, the simulated TKE and TKE dissipation rate values were simulated higher throughout the water column than in the summer (Table 4). The simulated values of TKE and TKE dissipation rate during summer followed a diurnal pattern as the wind was more energetic during the day and calm during the night. The summer diurnal pattern was often disrupted by storm and strong wind events causing high mixing intensities, as observed on May 27-31st, June 18th 25th and July 5th.

Table 4. Mean Seasonal Values of Simulated TKE and TKE Dissipation Rate of the Water Column

	Mean TKE [m^2s^{-2}]			Mean TKE dissipation rate [m^2s^{-3}]		
	Winter	Spring	Summer	Winter	Spring	Summer
k-kl mod.	5.63×10^{-5}	4.81×10^{-5}	3.99×10^{-5}	4.81×10^{-7}	3.44×10^{-7}	2.75×10^{-7}
k-ϵ mod.	5.63×10^{-5}	4.80×10^{-5}	3.91×10^{-5}	4.82×10^{-7}	3.44×10^{-7}	2.75×10^{-7}

Table 5. Maximum Values of Simulated TKE and TKE Dissipation Rate of the Water Column

	TKE Max [m^2s^{-2}]	TKE dissipation Max [m^2s^{-3}]
k-kl mod.	1.4×10^{-3}	2.89×10^{-4}
k-ϵ mod.	1.6×10^{-3}	2.89×10^{-4}

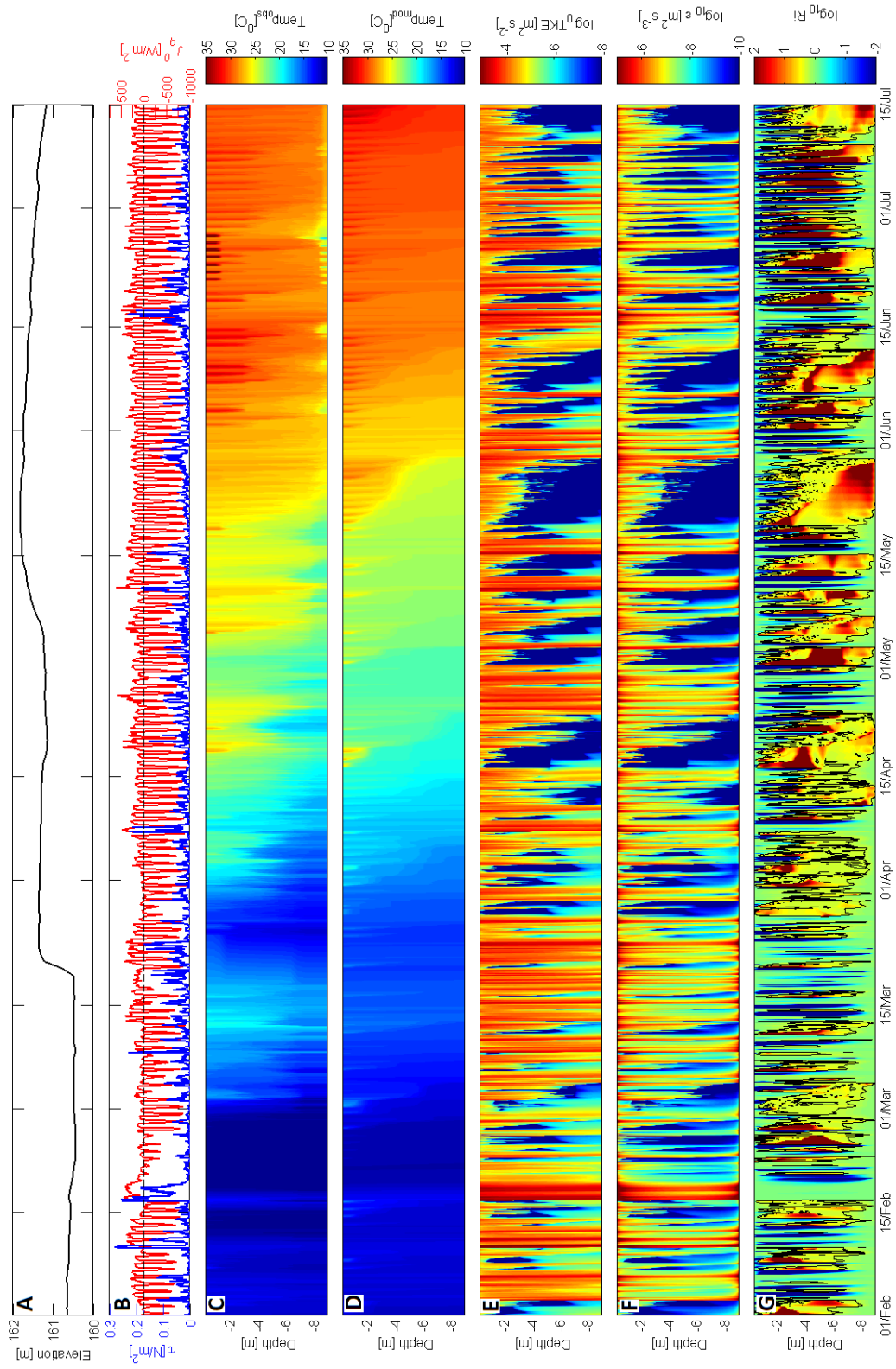

Fig 3.6. Simulation Results Using the *k-kl* Model Forced by Surface Momentum and Heat Fluxes. (A) Lake Whitney surface elevation above mean sea level, (B) surface momentum and heat fluxes, negative heat flux represents heat into water column, (C) observed thermal structure, (D) simulated thermal structure, (E) simulated TKE, (F) simulated TKE dissipation rate, (G) simulated Ri number with line=Ri^c. Time axis is UTC.

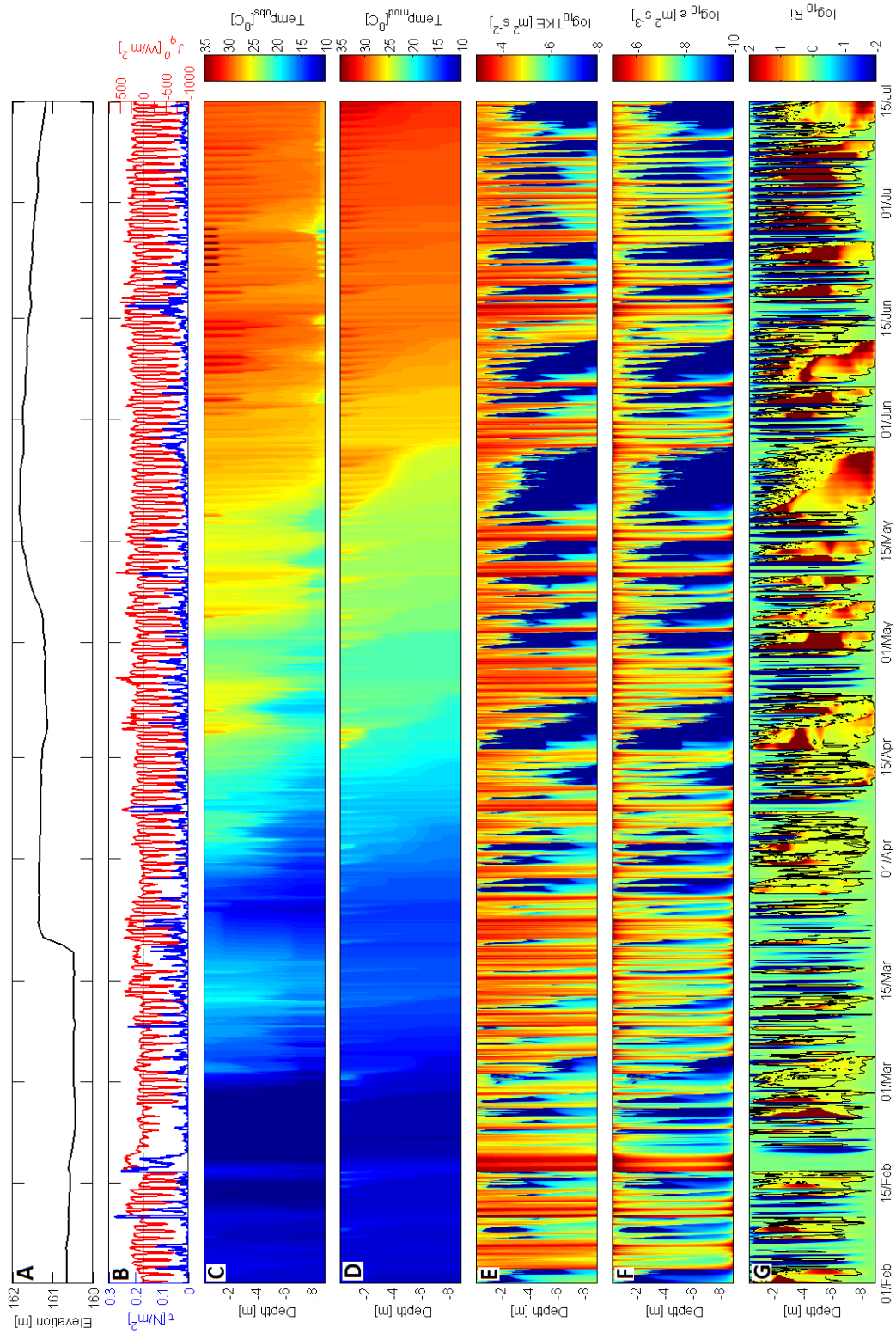

Fig 3.7. Simulation Results Using the *k-ε* model Forced by Surface Momentum and Heat Fluxes from February to Mid-July. (A) Lake Whitney surface elevation above mean sea level, (B) surface momentum and heat fluxes, negative heat flux represents heat into water column, (C) observed thermal structure,(D) simulated thermal structure,(E) simulated TKE,(F) simulated TKE dissipation rate,(G) Simulated Ri number with line=Ri$_c$. Time axis is UTC.

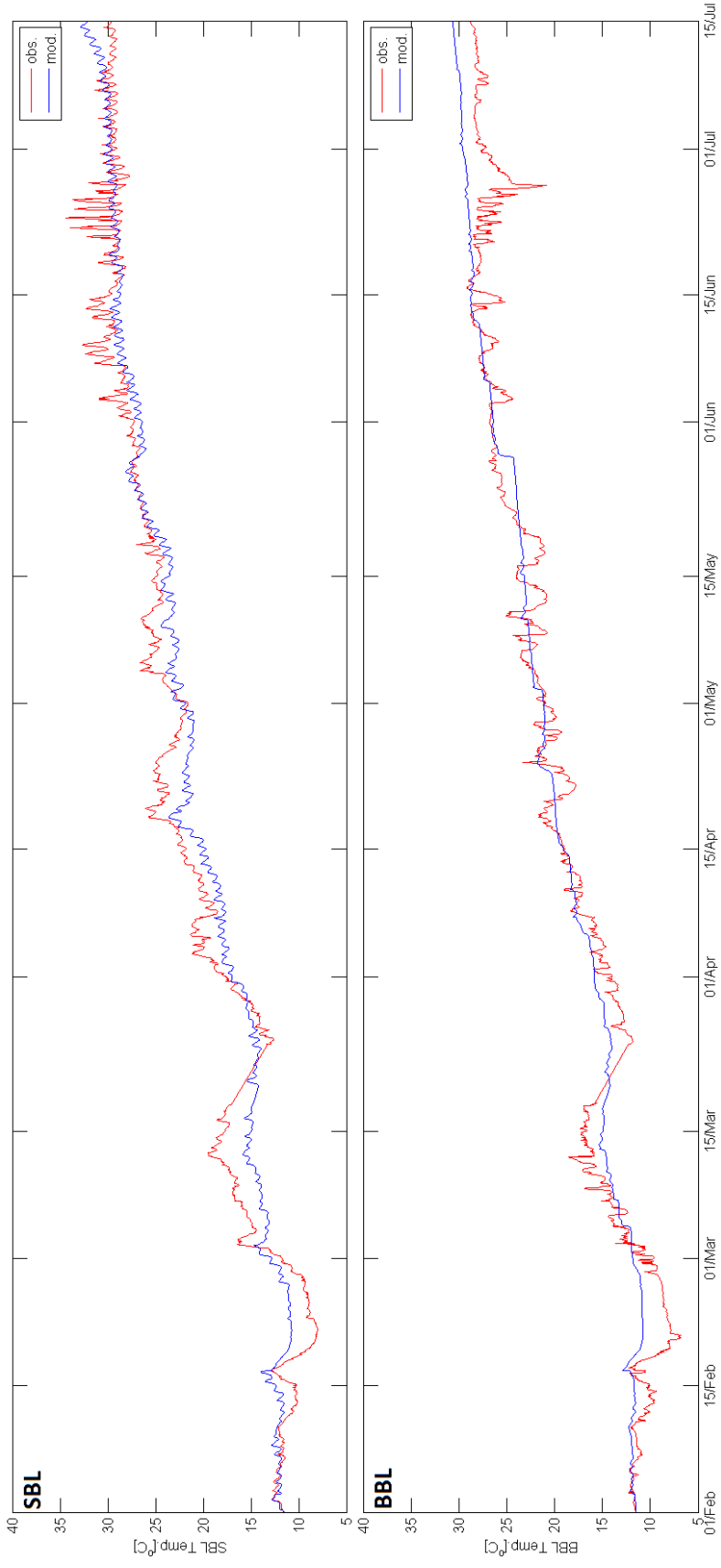

Fig 3.8. Observed and Simulated Temperatures at the SBL and BBL Throughout the Study Period (Feb-July). Since the simulated results by the *k-ϵ* and *k-kl* models were identical one line was used to represent them.

4. DISCUSSION

The selected parameters of velocity variances, TKE, and TKE dissipation are compared over a four day time series, during two different time periods: a) when the lake was strongly stratified (3-7 June); b) weakly stratified (11-15 March). This allows testing of the model for accuracy and comparison to the observations during periods with different environmental conditions.

4.1 Weakly stratified conditions (11-15 March)

4.1.1 General observed conditions

The surface forcing (heat and momentum fluxes) associated with meteorological conditions (Figs 4.1 and 4.2) were the primary driving forces of the thermal and current fields in the water column during this period (Fig 4.3 panels B, D and E). Based on the observations, it is suggested that the winds during this period were dominantly from the north-west (continental polar air mass) and the south-east (tropical maritime air mass) directions (Fig 4.1 panel B) (section 3.1.1). The different characteristics of these two air masses appear to have significant impact on the lake, which is mainly observed in the thermal structure.

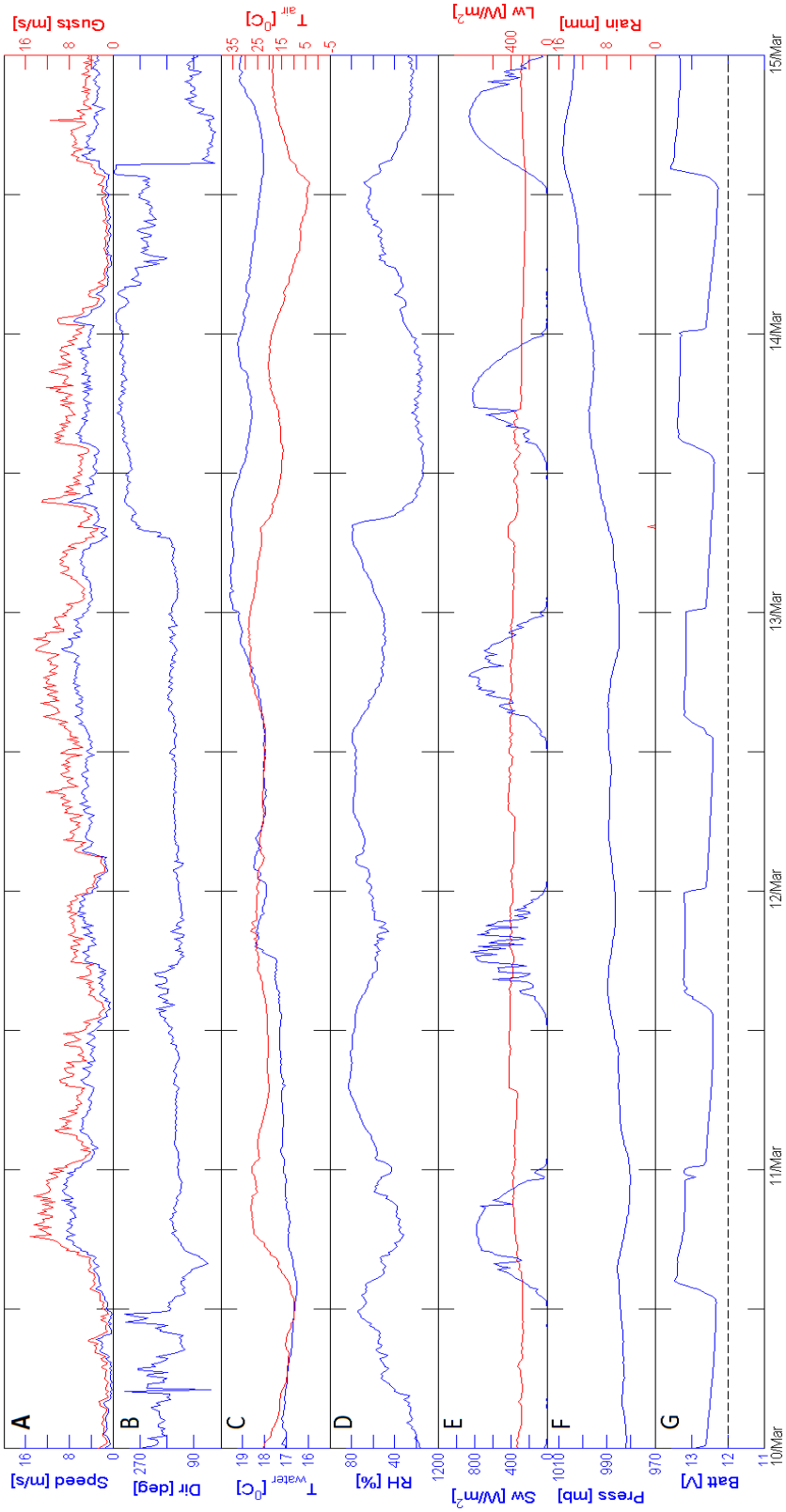

Fig 4.1. Measured Meteorological Data. (A) wind speed and gust, (B) wind direction, (C) water surface temperature and air temperature, (D) relative humidity, (E) short and long wave radiation, (F) atmospheric pressure and rainfall,(G) battery voltage. Time axis is UTC.

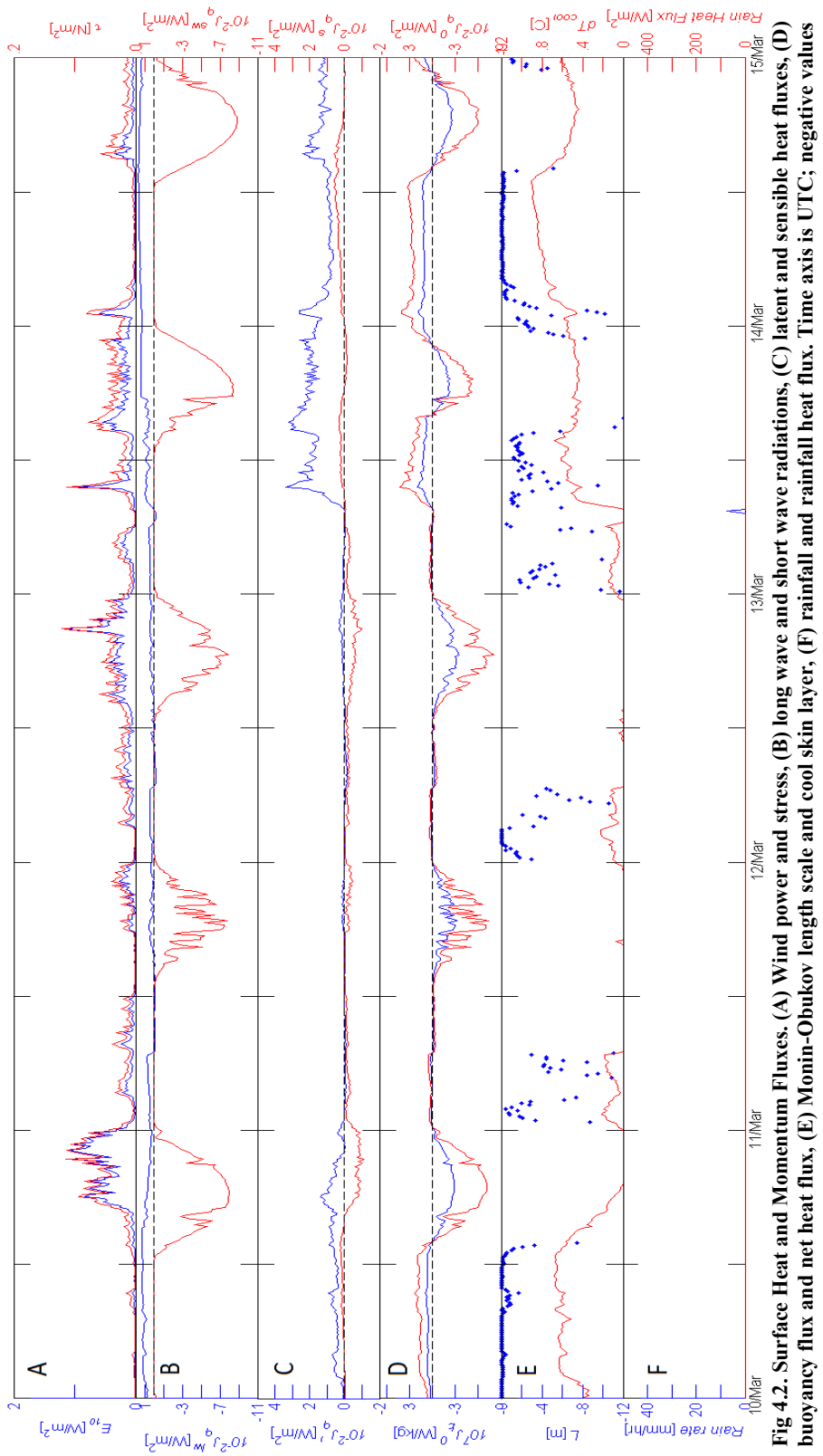

Fig 4.2. Surface Heat and Momentum Fluxes. (A) Wind power and stress, (B) long wave and short wave radiations, (C) latent and sensible heat fluxes, (D) buoyancy flux and net heat flux, (E) Monin-Obukov length scale and cool skin layer, (F) rainfall and rainfall heat flux. Time axis is UTC; negative values indicate a flux into the water.

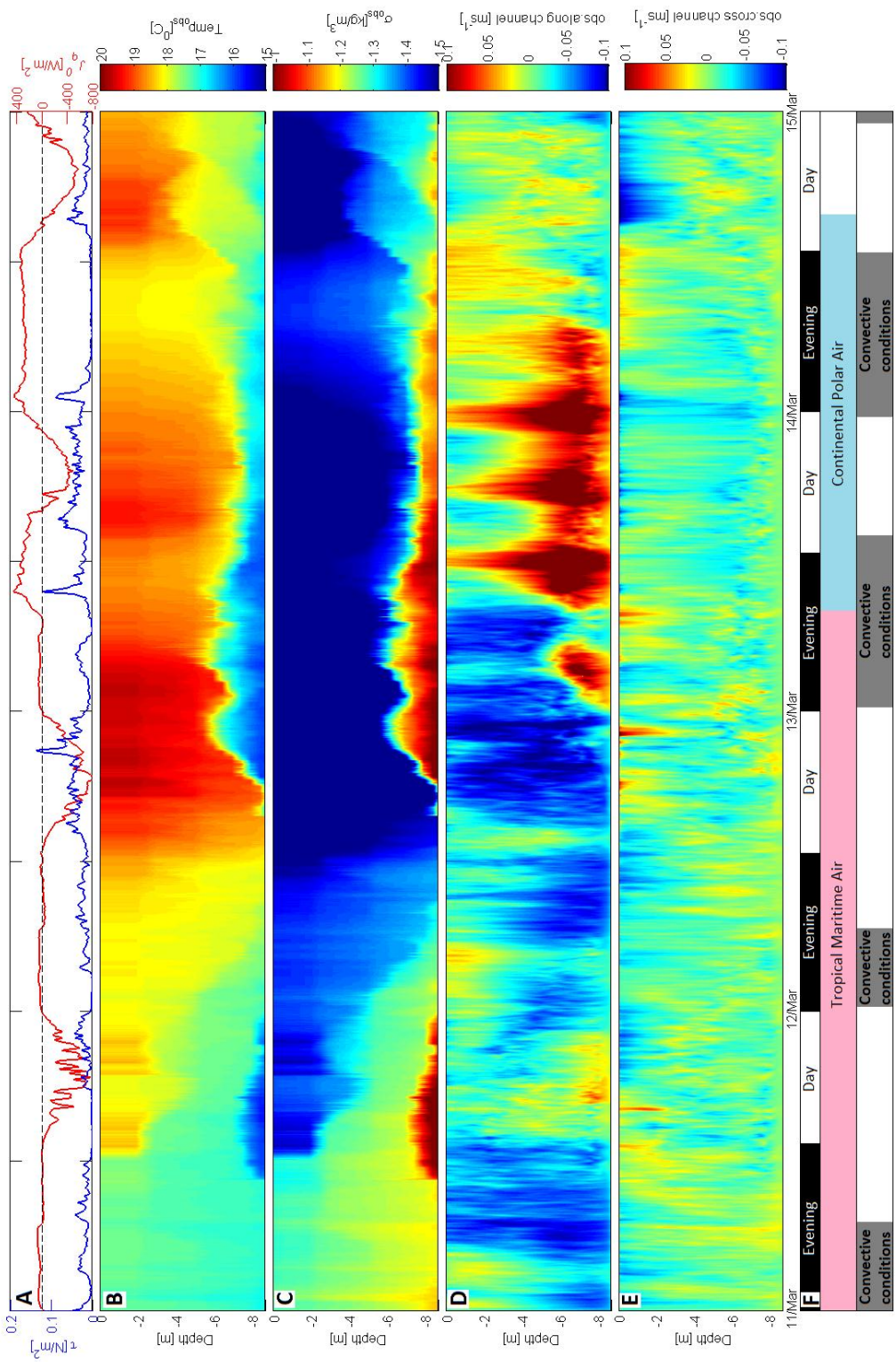

Fig 4.3. Observational Results. (A)Momentum and heat fluxes; negative heat flux represents heat into water column,(B) observed temperature,(C) observed σ_θ (σ_θ= potential density-1000), (D) observed along channel velocity; negative values represent a flow upstream, (E) observed cross channel velocity, (F) description of day/evening times, air masses and convective conditions based on the buoyancy flux. Time axis is UTC.

The tropical maritime air (March 11th-13th 10:00) induces a net heating of the SBL due to an increase in sensible heat flux and a relatively low loss of latent heat flux from the lake's surface (Fig 4.2 panels C and D). The net heating of the SBL resulted in an overall increase of temperature in the water column as observed during the periods of March 11th-13th (Fig 4.3 panel B). In addition to the heating due to the gained sensible and low loss of latent heat fluxes, superposed on the general heating trend, there was a diurnal cycle with waters becoming warmer and increasingly stratified during the daytime, as observed on March 11th 13:00-23:00 and 12th 13:00- 13th 00:00 (Fig 4.2 panel B and 4.3 panel B).

The clear skies, and dry and cooler air associated with the continental polar air, caused higher losses of latent, sensible and longwave heat fluxes from the lake surface, thus increasing the net heat loss from the lake (March 13th 10:00- 14th 14:00) (Fig 4.2 panels B, C and D). This increased net heat loss, predominately at night when shortwave radiation was absent, and resulted in a decrease of buoyancy at the surface, and, thus, in convective conditions (Fig 4.2 panel D). This is consistent with the Monin-Obukov length scale values of ($-2m \leq L < 0m$), as observed on March 11th 01:00-03:00, 12th 01:00-08:00, 13th 01:00-15:00 and 14th 00:30-14:00 (Fig 4.2 panel E). Nighttime convective conditions were more pronounced during continental polar air than tropical maritime air due to the associated larger heat loss from the lake, which was mainly driven by the latent heat flux loss.

The current structure varied with wind direction and magnitude. As specified previously, winds were dominant in the north-west and south-east directions. Due to the

lake's weak stratification, the momentum flux of a high wind speed (>6ms^{-1}) was sufficient to penetrate to the BBL and force the flow of the water column in the same direction as the wind. On March 11th-13th 10:00, the scattered strong south-easterly winds (Fig 4.1 panels A and B) forced the current structure of the water column in the same direction as the wind (upstream) (Fig 4.3 panel D and Fig 4.4 boxes with Roman numeral I, III and V). A pressure gradient in the opposite direction of the wind built up during this event. When the wind weakened (<3ms^{-1}), as seen on March 11th 12:00-19:00 and 13th 00:00-03:00, this pressure gradient forced a return flow at the BBL in a direction opposite to the wind (downstream) (Fig 4.4 boxes with roman numeral II and IV). This return flow (downstream) did bring cooler water to the BBL as seen on March 11th 12:00-22:00 (Fig 4.3 B).

As the winds veered to become north-westerly on March 13th 10:00-14th 14:00, the surface current was forced downstream (Fig 4.3 panel D), while the pressure gradient from the recent south-easterly event continued to force a downstream return flow in the BBL (Fig 4.3 and Fig 4.4 box with roman numeral VI). The combination of the two forces acting in the same direction resulted in maximum recorded velocities during this weakly stratified period. The water column flowing in an upstream direction caused a buildup of a pressure gradient in the opposite direction. As the north-westerly wind weakened on March 14th 02:00-14:00, the pressure gradient forced a return downstream flow in the BBL (Fig 4.4 box with Roman numeral VII) bringing warmer water (Fig 4.3 B). On March 14th 14:00-15th winds veered to become easterly causing the along channel

velocity to reduce (Fig 4.3 panel D) and the cross channel velocity to increase (4.3 panel E).

A summary of the source of forcing that induced the flow in the BBL is shown in Figure 4.5. A significant north-westerly wind resulted in positive velocities (downstream). As the north-westerly wind weakened, the flow became negative due to the pressure gradient force. A significant south-easterly wind did result in a negative velocity (upstream). As the south-easterly wind weakened, the flow became positive (downstream) due to the pressure gradient force.

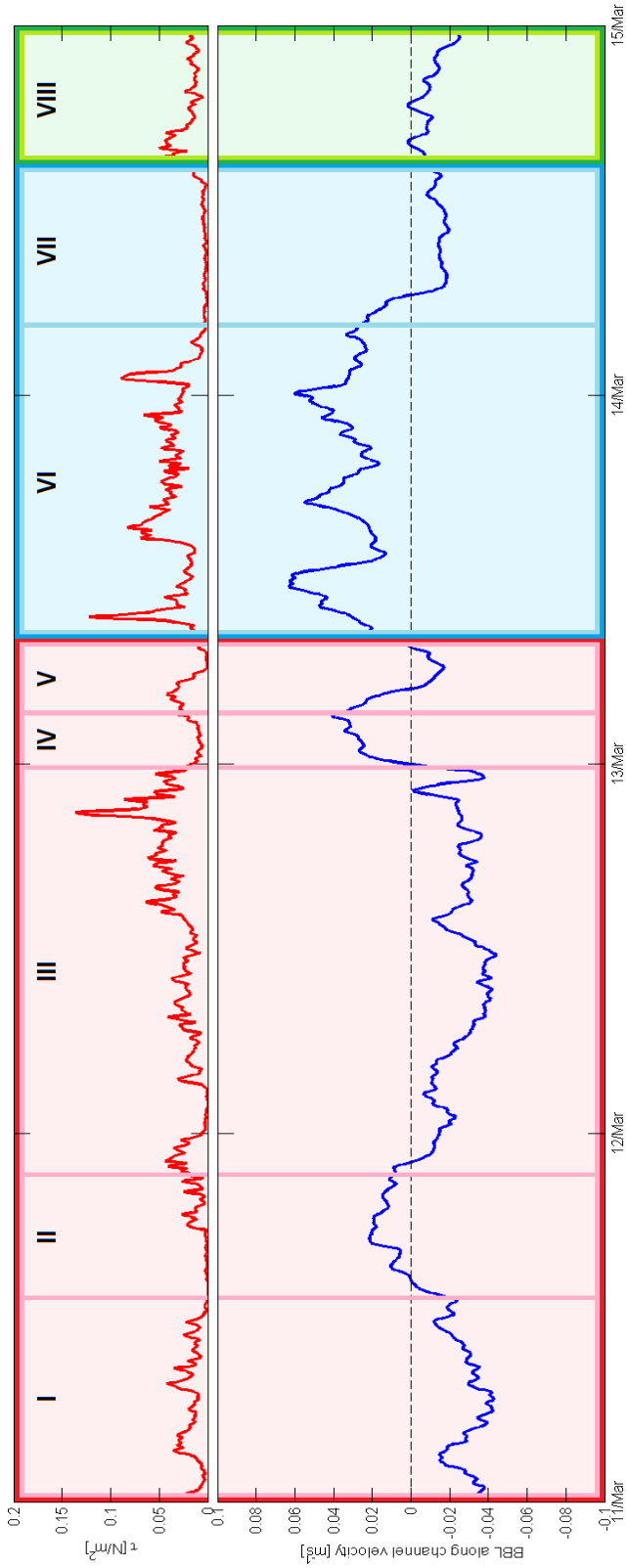

Fig 4.4. BBL Forced Flow. Wind stress (top) and averaged over 0.5m bin in the BBL (7.8m-8.3m depth) along channel current velocity (bottom) during several event stages. The red box (I-V) represents a period of south-easterly winds, the blue box (VI and VII) a period of north-westerly winds, and the green box (VIII) a period of easterly winds. Each wind event is separated into sub-stages defined in roman numerals. Positive velocities represent a downstream flow, while negative velocities represent an upstream flow. Time axis is UTC.

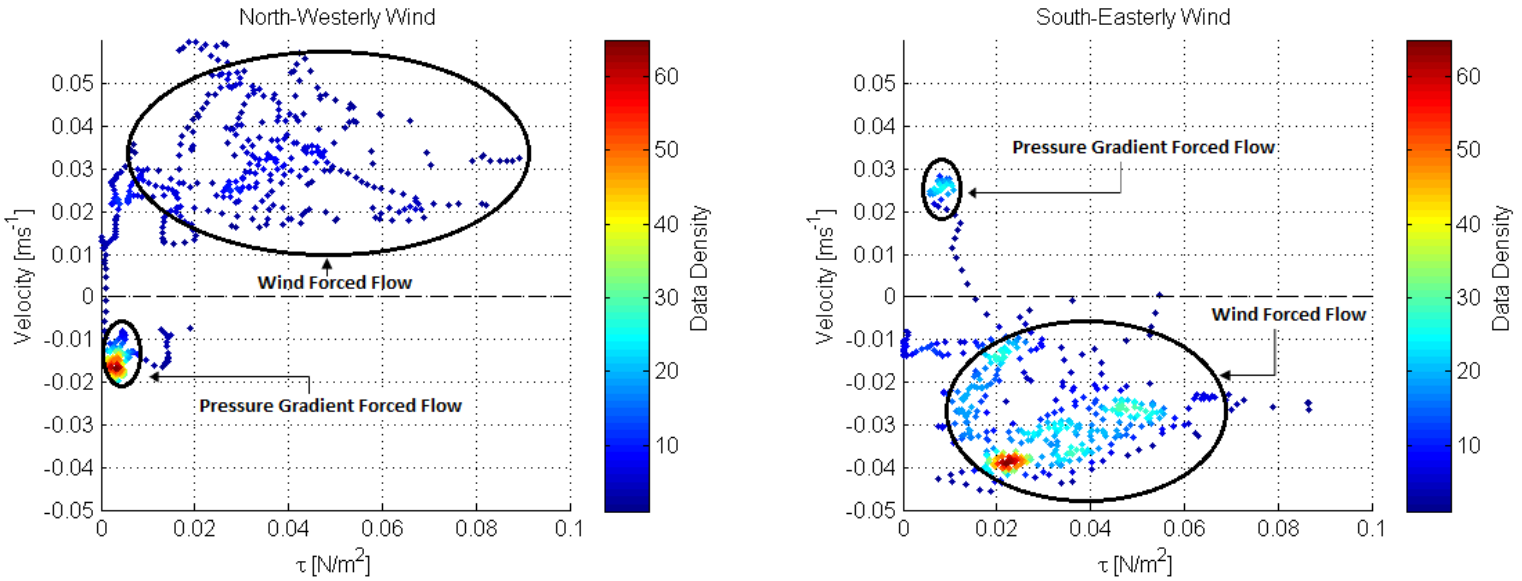

Fig 4.5. Scatter Plot of Wind Stress and BBL Along Channel Velocity. Data distribution is indicated in colors, during two wind events. The source of forcing is indicated outlined with a black circle.

In models such as GOTM, it is often assumed that conditions are isotropic. In isotropy the mean properties such as velocity variances of an eddy are equal in all directions. To test whether in the lake conditions were isotropic during the period of weak stratification, a variance plot was constructed that included all three velocity variance components (Fig 4.6). Qualitatively, the plot shows all three components being on the same order of magnitude during most of the time. The time periods where the horizontal and vertical components were at the instruments noise level was cut-off, e.g. March 11th 22:00-12th 03:00. The noise thresholds for the horizontal and vertical components were estimated to be $1.1 \times 10^{-6} m^2 s^{-2}$ and $3.59 \times 10^{-8} m^2 s^{-2}$, respectively (For details on how the threshold values were estimated see section 4.2.1).

The significant velocity gradient in the BBL (section 1.2.2) causes eddies to follow a 'pancake' like structure, where the vertical parameters are smaller compared to the horizontal [*Davidson*, 2004]. This effect resulted in the w-variance to be lower than the u-variance and v-variance throughout the time period (Fig 4.6). Furthermore, to quantify the relation between the variance components, a scatter plot with correlation values using 1000 bootstrap samples was made, where only data above the noise level was used (Fig 4.7, 4.8 and 4.9). It can be concluded from the correlation values (>0.71) that all three components are in a strong relation and near isotropic.

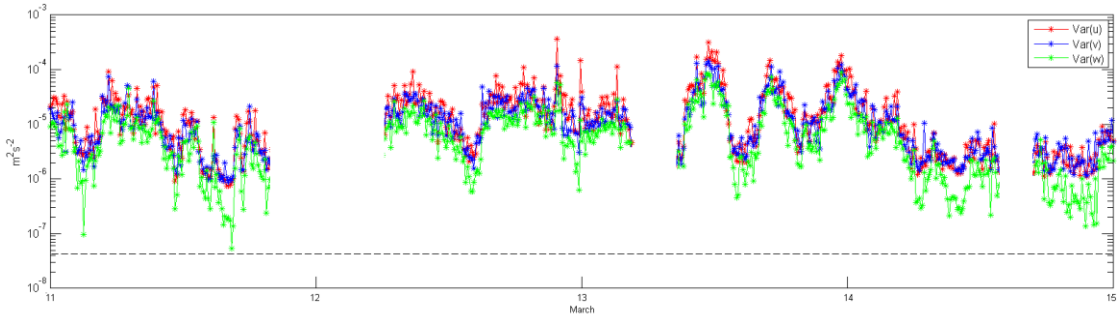

Fig 4.6. Observed Velocity Variances at 8.3m Depth. The noise level for the w velocity component indicated in black dashed line.

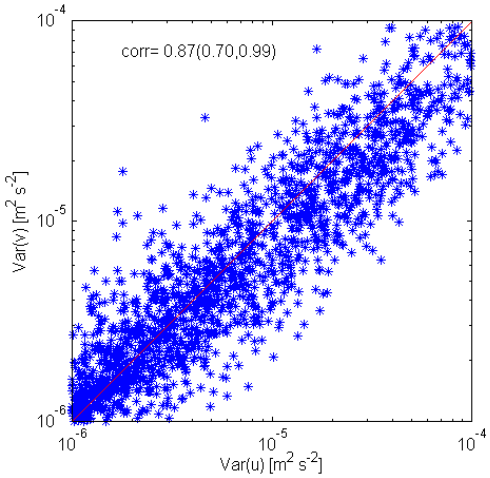

Fig 4.7. Scatter Plot of Variances in the u and v Components at 8.3m Depth. The correlation value and 95% confidence intervals in parenthesis.

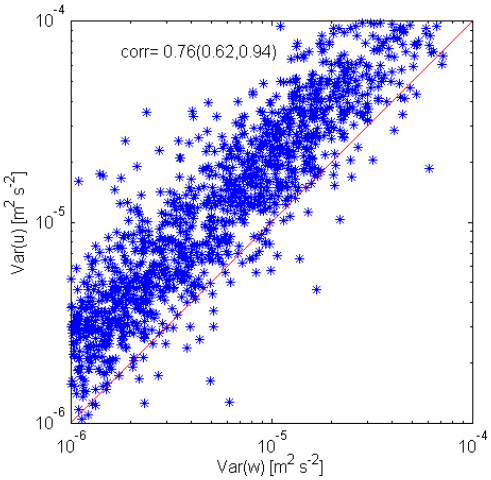

Fig 4.8. Scatter Plot of Variances in the w and u Components at 8.3m Depth. The correlation value and 95% confidence intervals in parenthesis.

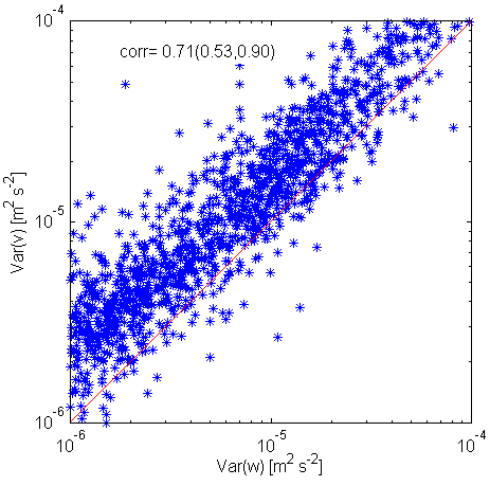

Fig 4.9. Scatter Plot of Variances in the w and v Components at 8.3m Depth. The correlation value and 95% confidence intervals in parenthesis.

4.1.2 *k-ϵ* model and *k-kl* model simulations

4.1.2.1 *k-ϵ* model vs *k-kl* model

As specified in the methods section, simulations were conducted using the *k-ϵ* and *k-kl* models. Both models show a similar trend but slightly vary in magnitudes of the physical processes as seen in the figure on page (74), where the *k-kl* model simulated higher mean values of TKE and TKE dissipation during this time period (Table 5). A quantitative comparison between the models was made using Pearson's correlation function [*Press et al.*, 2007]. With correlation values above 0.9 (Fig 4.10 and 4.11) for the simulated values of TKE and TKE dissipation rate it can be stated that both models strongly simulate similar simulations.

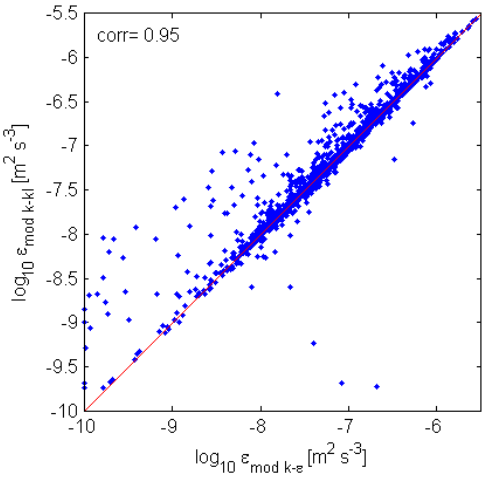

Fig 4.10. Comparison between Models' TKE Dissipation Rate.

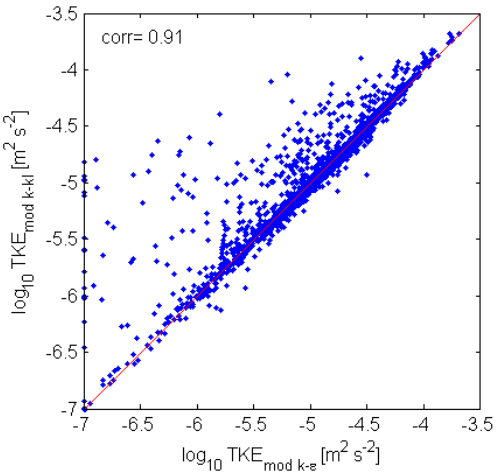

Fig 4.11. Comparison between Models' TKE.

4.1.2.2 General features of the simulated parameters in the water column

From the observations it has been suggested that the surface momentum flux induced by the wind stress, night convection generated by the heat fluxes, and return flow forced by pressure gradient were the primary drivers of the physical properties in the water column during this period.

The simulated mixing intensity of the water column indicated by the TKE dissipation rate followed a diurnal trend (Fig. 4.12). Net heating during daytime would result in relatively low simulated TKE and TKE dissipation rates. With the progression of night, the heat gets radiated from the lake body, causing the water column to become unstable through convection. During convection, the simulated values of TKE and TKE dissipation rate were high and capable of penetrating to the BBL (Fig 4.12 panel F).

Contributing to the turbulence production is surface momentum flux. The simulated turbulence production by the momentum flux penetrated to the BBL only during weak stratification. Such conditions only occurred during the evenings of this period, due to convection, as seen on March 11th 00:00-10:00, 12th 07:00-12:00, 13th 10:00-12:00 and 14th 00:00-01:00 (Fig 4.12). Although, surface momentum flux was significant during some periods of the daytime, it was not sufficient to produce turbulence that would penetrate to the BBL, as seen during the period of maximum wind stress (momentum flux) on March 12th 22:00 (Fig 4.12) and the enhanced stratification during daytime.

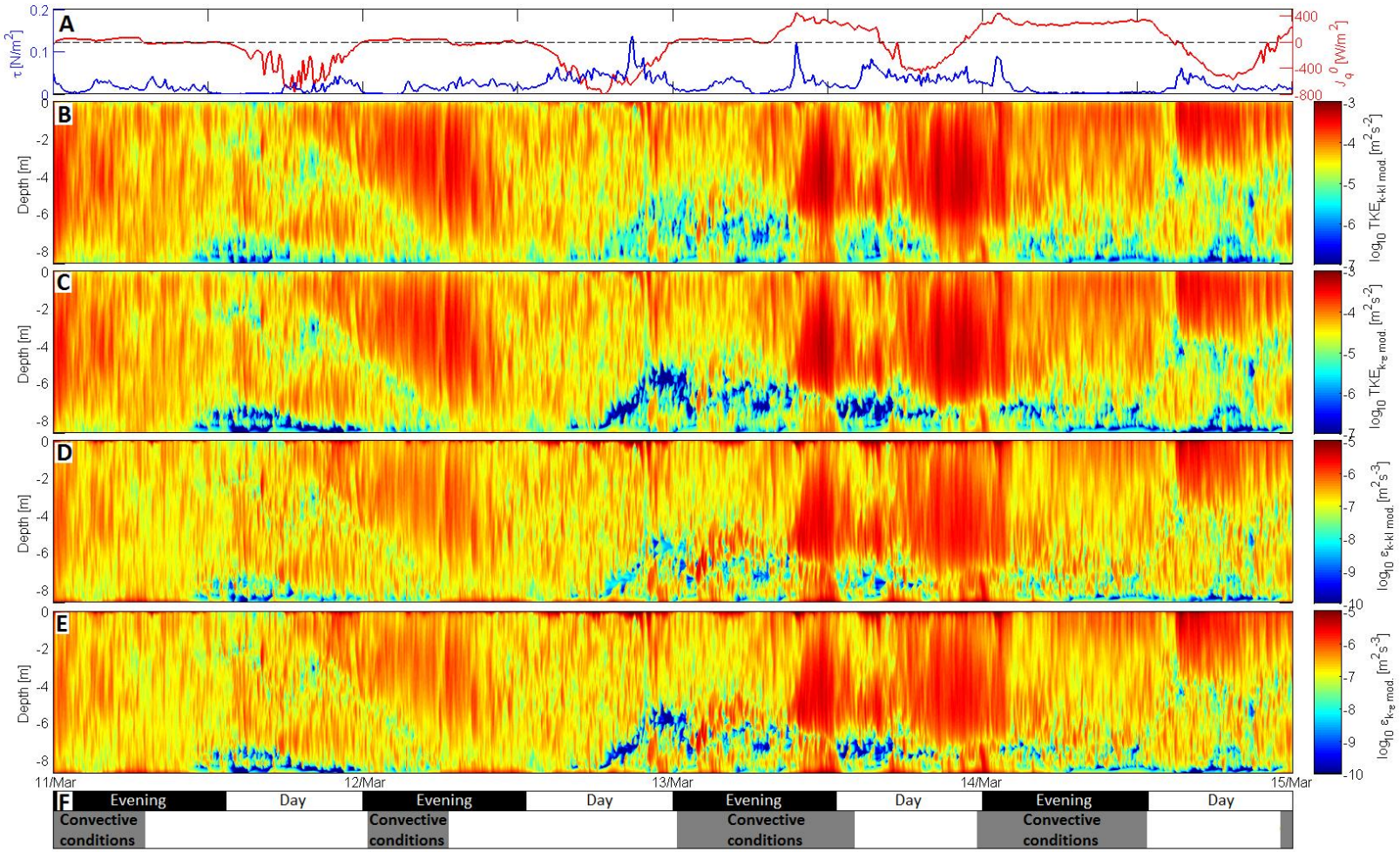

Fig 4.12. Simulated TKE and TKE Dissipation Rates. (A)Observed momentum and heat flux where negative heat flux represents heat into water column, (B) simulated TKE by k-kl model, (C) simulated TKE by k-ϵ model, (D) simulated TKE dissipation rate by k-kl model, (E) simulated TKE dissipation rate by k-ϵ model, (F) description of day/evening times and convective conditions. Time axis is UTC.Fig 4.12.(A)Observed momentum and heat flux where negative heat flux represents heat into water column, (B) simulated TKE by k-kl model, (C) simulated TKE by k-ϵ model, (D) simulated TKE dissipation rate by k-kl model, (E) simulated TKE dissipation rate by k-ϵ model, (F) description of day/evening times and convective conditions. Time axis is UTC.

4.1.2.3 Qualitative comparison of select observed and simulated parameters in the BBL

Focusing on the BBL, a qualitative comparison was made by plotting the simulated and observed values of TKE, TKE dissipation and velocity variances (Figs 4.13-4.16). The simulated and observed data from these plots were smoothed by a 15 and 5 points running average, respectively (both including the same time period of 45 minutes).

Overall, the model simulations followed the observed mixing dynamics well during this time period. The simulations of TKE, TKE dissipation and velocity variances in the BBL by both models during this period followed a diurnal trend (Figs 4.13-4.16). The net heating during the daytime caused higher values of buoyancy frequency and therefore resulting in a more stable water column indicated by an overall higher Ri number ($Ri > Ri_c$) as seen on the 11th, 12th and 14th. Due to such conditions the simulated TKE and TKE dissipation rates in the BBL were relatively low during daytime, following well the observed values. However, during daytime on March 12th the simulated values of TKE and TKE dissipation rates were lower than the observed. This was during a period of high surface wind stress that may have not been accounted for by the simulated values in the BBL. As specified in section 4.1.2.2, during daytime when the water was more stratified, the simulated turbulence production by the surface momentum flux did not penetrate to the BBL, contradicting the observational results (section 4.1.1.) that show the surface wind stress during daytime of March 12th penetrating to the BBL.

As night progressed, the surface net heat loss from the lake caused low buoyancy frequency and nighttime convection. The unstable conditions associated with nighttime convection are indicated by a low Ri number ($Ri < Ri_c$) as seen on the 11th, 12th and 14th. Nighttime mixing events were captured well by both models throughout this period. Both models did simulate high values of TKE and TKE dissipation rates that followed the observations well.

The diurnal trend was interrupted on March 13th, a period when the wind veered to northwesterly (cold and dry) (section 4.1.1), causing less heat gain by the lake during day and larger loss during night. As a result, the water column became less stratified due to vertical mixing. Such weakly stratified conditions have caused the wind stress and vertical mixing to penetrate to the BBL, resulting in maximum simulated and observed values of TKE and TKE dissipation rates in the BBL.

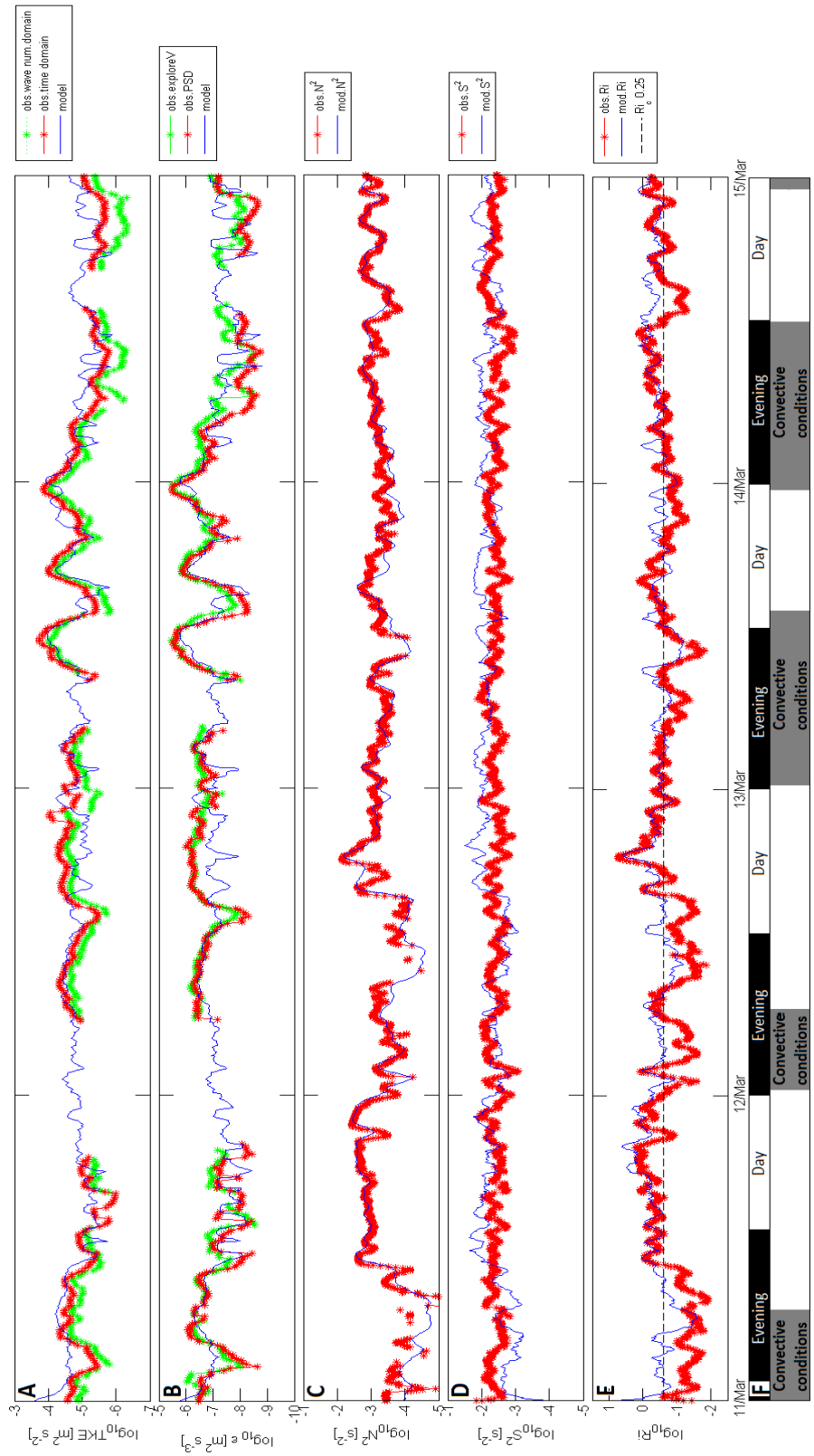

Fig 4.13. *k-kl* Modeled vs Observed Turbulence Parameters at 8.3m Depth. (A) TKE, (B) TKE dissipation rate, (C) buoyancy frequency, (D) shear frequency, (E) Ri number, (F) description of day/evening times, air masses and convective conditions. Time axis is UTC.

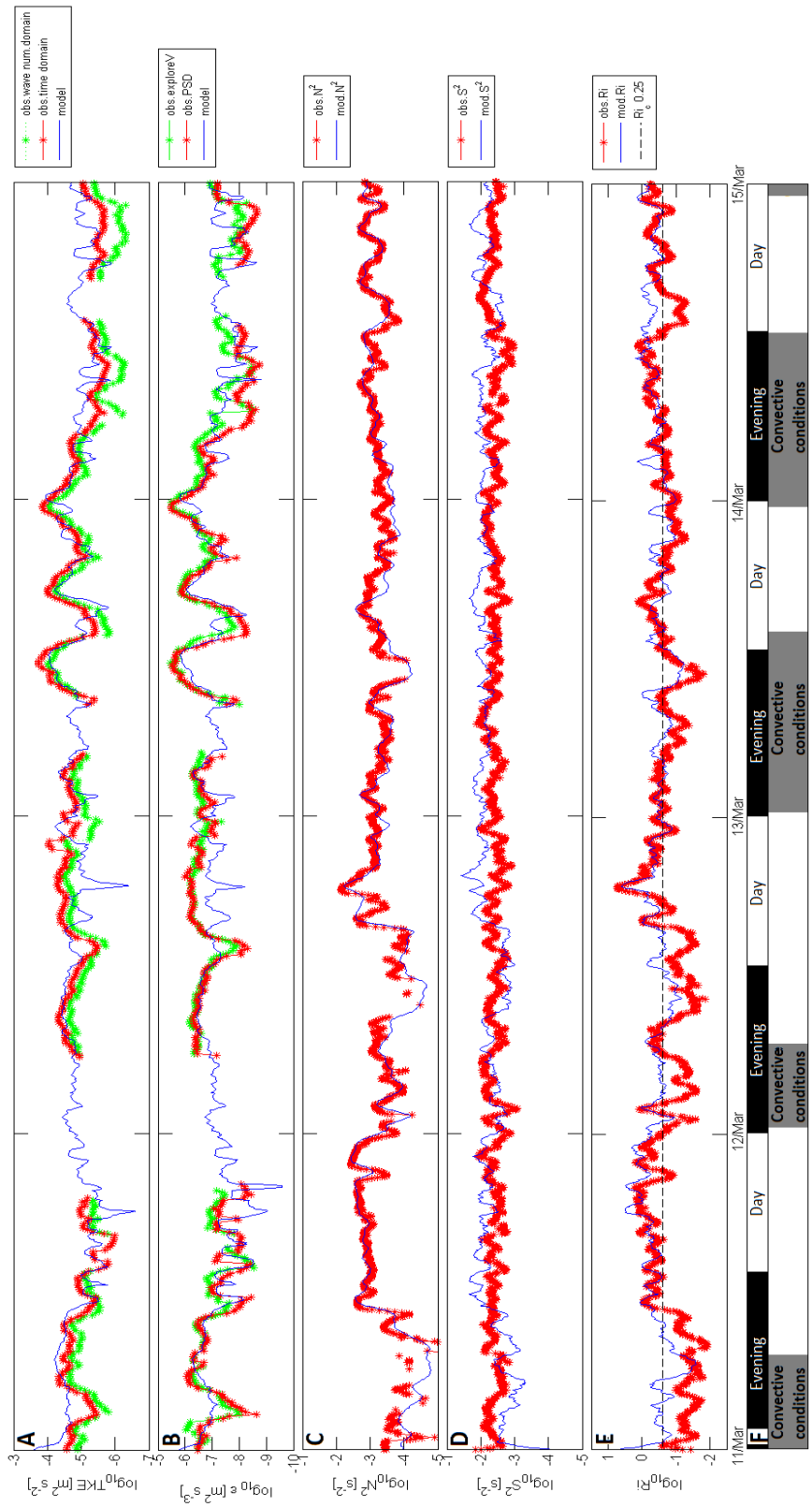

Fig 4.14. *k-ε* Modeled vs Observed Turbulence Parameters at 8.3m Depth. (A) TKE, (B) TKE dissipation rate, (C) buoyancy frequency, (D) shear frequency, (E) Ri number, (F) description of day/evening times, air masses and convective conditions. Time axis in UTC.

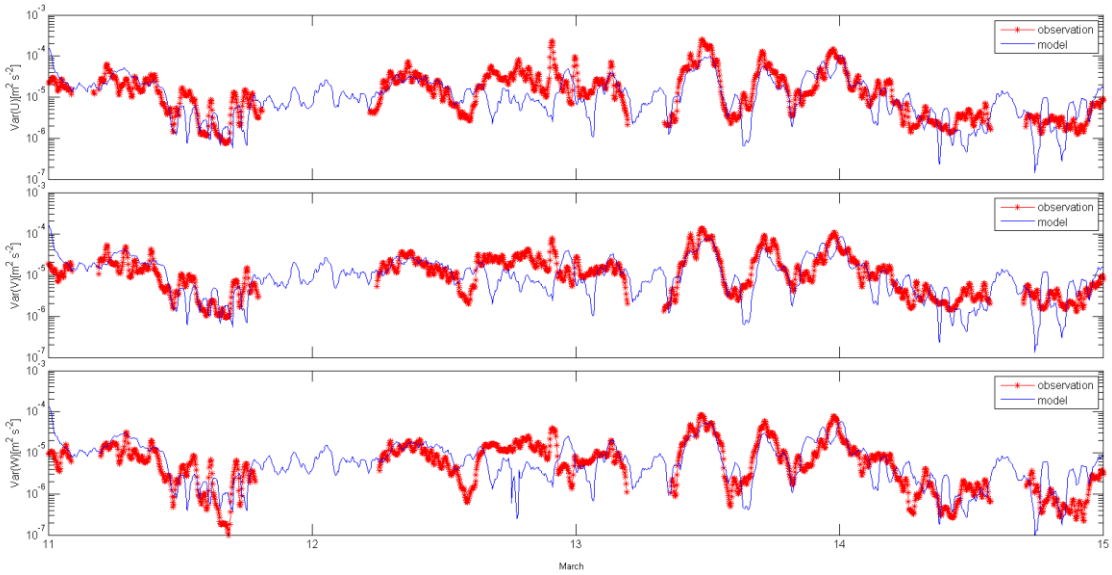

Fig 4.15. *k-kl* Modeled vs Observed Velocity Variances at 8.3m Depth. (top) U-component, (middle) V-component, (bottom) W-component.

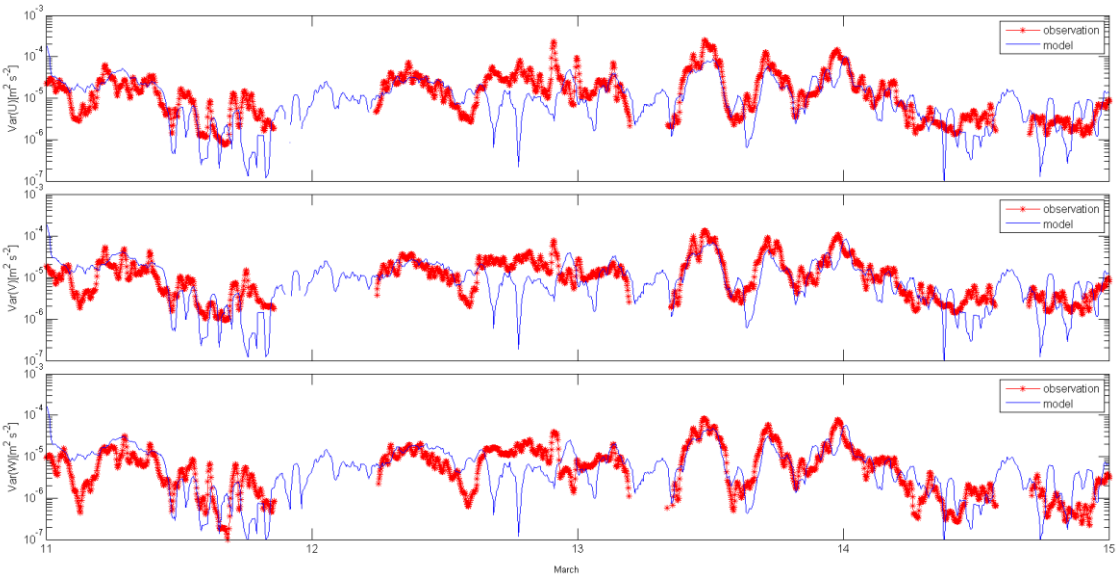

Fig 4.16. *k-ϵ* Modeled vs Observed Velocity Variances at 8.3m Depth. (top) U-component, (middle) V-component, (bottom) W-component.

4.1.2.4 Quantitative comparison of observed and simulated parameters in the BBL

Quantitatively, the comparisons between simulated and observed values of TKE and TKE dissipation was done using multiple statistical tools (Maximum Likelihood Estimator (MLE), arithmetic sample mean, and correlation). Statistical functions were computed using the bootstrap method.

(i) MLE:

Due to the intermittent nature of turbulence, the values of velocity fluctuations vary considerably both temporally and spatially [*Baker and Gibson*, 1987]. In intermittent turbulence where the Re number is high ($Re > Re_c$), the TKE dissipation rate follows an approximate lognormal distribution as proposed by *Kolmogorov* [1962], *Obukhov* [1962] and *Yaglom* [1966]. This is similar to what has been observed in this study (Fig 4.17) and is compared to simulation values later in this section.

In lognormally distributed data, using the arithmetic mean may provide a "misleading" lower value of the true expected value. *Baker and Gibson* [1987] suggested that for lognormally distributed data, X, the MLE is given by:

$$MLE = \exp(m + \frac{s^2}{2}) \tag{60}$$

where m is the arithmetic mean of $\ln(X)$ (eqn. 61) and s is the variance of $\ln(X)$ (eqn. 62). X represent either the observed or simulated values of TKE dissipation rate.

$$m = \frac{1}{N}\sum_{i=1}^{N} lnX \tag{61}$$

$$s^2 = \frac{1}{N}\sum_{i=1}^{N}(lnX - \langle m \rangle)^2 \tag{62}$$

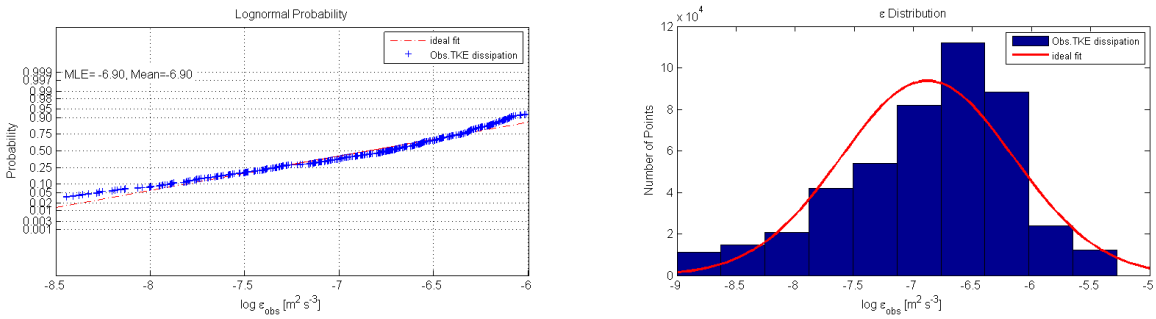

Fig 4.17. TKE Data Distribution Test. (left) Lognormal probability distribution of TKE dissipation rates using 1000 bootstrap samples. The red dashed line represents an ideal fit to the lognormal probability distribution. The MLE value was computed using equation (60) and mean using equation (61). (right) A histogram showing the distribution using 1000 bootstrap samples of the TKE dissipation rate. The red line represents an ideal fit to the lognormal distribution.

(ii) Pearson's product-moment correlation:

Using Pearson's correlation (eqn. 63) [*Press et al.*, 2007] we will quantify how well the observed and simulated values of TKE and TKE dissipation rate are related.

$$Corr(x,y) = \sum_{i=1}^{N}\frac{(x_i - \langle x \rangle)(y_i - \langle y \rangle)}{(n-1)\sigma_x\sigma_y} \tag{63}$$

where σ is the sample standard deviation. x and y represents the observed and simulated results, respectively, of TKE and TKE dissipation rates.

Statistics values during this weakly stratified period are shown in Table 6. The mean values of TKE dissipation rates as suggested by *Baker and Gibson* [1987] underestimate the expected MLE value in a lognormally distributed data. Both the

simulated and observed datasets in Table 6 show a good agreement with Baker and Gibson's results. A study at Lake Maggiore, Italy, by *Stip et al.*[2002], shows the mean value of the simulated TKE dissipation rates being equal to the MLE and therefore providing a good estimator of the expected MLE, unlike the findings of this study. However, a study by *Anis and Singhal* [2006] at Valle de Bravo fresh water reservoir, Mexico, shows the simulated mean values being smaller than the MLE as found in this study.

Table 6. Observed and Modeled Simulation (*k-ϵ* and *k-kl*) Values of TKE and TKE Dissipation Rate. The mean and MLE values and the 95% confidence intervals in brackets were computed using 1000 bootstrap samples for the periods of 11 March to 15 March.

	11-Mar to 15-Mar		
	Maximum	Mean	MLE
TKE [m^2s^{-2}]			
k-ϵ	4.72×10^{-4}	2.22×10^{-5}	2.54×10^{-5}
(Simulated)		(2.12, 2.35)	(2.22, 3.32)
k-kl	3.74×10^{-4}	2.31×10^{-5}	2.66×10^{-5}
(Simulated)		(2.20, 2.44)	(2.38, 3.15)
Wavenumber domain	1.35×10^{-4}	1.53×10^{-5}	1.92×10^{-5}
(Observed)		(1.36, 1.74)	(1.64, 2.32)
Time domain	2.7×10^{-4}	2.42×10^{-5}	3.32×10^{-5}
(Observed)		(2.18, 2.75)	(2.81, 4.04)
ϵ [m^2s^{-3}]			
k-ϵ	3.63×10^{-6}	1.83×10^{-7}	2.99×10^{-7}
(Simulated)		(1.70, 1.98)	(2.68, 3.50)
k-kl	3.06×10^{-6}	1.86×10^{-7}	3.14×10^{-7}
(Simulated)		(1.72, 2.02)	(2.80, 3.53)
Eqn. (53)	5.03×10^{-6}	3.28×10^{-7}	6.22×10^{-7}
(Observed)		(2.77, 3.92)	(5.02, 7.68)

Further correlation testing was conducted to conclude which model better follows the observation results (Table 7). From the correlation values, both models follow the observational estimates of TKE and TKE dissipation rate well, with *k-kl* model following the observational results closer.

Table 7. Correlation Values of the Observed vs Modeled Simulation (*k-ϵ* and *k-kl*) of TKE and TKE Dissipation Rates. The correlation values and the 95% confidence intervals in brackets were computed using 1000 bootstrap samples for the periods of 11 March to 15 March.

		Simulated			
		TKE		*ϵ*	
		k-kl	*k-ϵ*	*k-kl*	*k-ϵ*
Observed	ϵ	-	-	0.63	0.61
		-	-	(0.52, 0.74)	(0.48, 0.71)
	TKE wavenumber domain	0.5	0.46	-	-
		(0.39. 0.60)	(0.34, 0.56)	-	-
	TKE time domain	0.52	0.49	-	-
		(0.37, 0.63)	(0.36, 0.60)	-	-

In general, both models do follow the observed estimates of the TKE and TKE dissipation rate well during weakly stratified periods. This relation between the observed and simulated can be seen qualitatively from plots 4.13-4.16 and quantitatively from the statistics values in Tables 6 and 7.

4.2 Strongly stratified conditions (3-7 June)

4.2.1 General observed conditions

During this period of summer, the winds were weak to moderate blowing from southwest (tropical maritime air mass) (Fig 4.18 panel B), with two events of relatively high wind speed on June 4th 23:00 and 5th 22:00 (Fig 4.18 panel A). With no frontal systems passing over the region during this period, the wind speed was higher during day than night. This diurnal wind pattern is a response to shortwave radiation warming of the continental land mass leading to a buildup of a pressure gradient between the land mass (Texas State) and sea (Gulf of Mexico) resulting in a sea breeze during the day.

Conditions show a diurnal pattern where the surface heat fluxes were the primary controlling factor of the thermal structure conditions (Fig 4.19 panel A and B). During daytime, shortwave and sensible heat fluxes transferred heat to the SBL (Fig 4.19 panels B and C), therefore increasing the water temperature of the SBL significantly and enhancing stratification. This heating was followed by heat loss (latent and longwave heat fluxes) during the nights (Fig 4.19 panel B and C). The heat loss decreased the surface water buoyancy resulting in night convection (Fig 4.19 panels D and E). Unlike the weakly stratified period, night convection during this strongly stratified period was not able to penetrate to the BBL and was confined to ~7.8m depth, e.g. the night of June 3rd and 6th. On June 4th, the calm winds and clear skies resulted in the water becoming strongly stratified and night convection was confined in shallow depths ~3m (Fig 4.20 panel B and F).

The current velocity throughout the water column was relatively weak and dominant in the along channel direction (Figs 4.20 panels D and E). The SBL current was primarily downstream but changed direction to upstream when the south-easterly wind gusted up to $8ms^{-1}$ as seen on the 3rd 12:00-23:00, 4th 23:00-23:59 and 5th 23:00-23:59 (Figs 4.18 panel A, Fig 4.20 panel D and Fig 4.21 ellipses with roman numeral II). Due to the lakes topography, the dominant downstream current in the SBL resulted in a buildup of a pressure gradient in the opposite direction of the flow. This buildup of pressure gradient forced an upstream BBL return flow (Fig 4.21 boxes with Roman numeral I).

Similar to what has been done in the weakly stratified period, a plot was constructed to check for isotropic conditions (Fig 4.22). Qualitatively, Figure 4.22 shows the three components being on one order of magnitude during most of the time period. From the correlation values on the scatter plots, which ranged between 0.85 and 0.9 (Figs 4.24-4.26), it is suggested that conditions were nearly isotropic.

The periods when the variances for the u and v components "flat out" at $1.1x10^{-6}$ m^2s^{-2} is when the instrument noise level for these two components is reached. The noise level was estimated by integrating the area below the PSD of the horizontal velocity components where the noise level is reached (Fig 4.23). A similar approach was used to estimate the noise level threshold for the vertical component. Section 2.1 part (ii) includes the reasons why the threshold in the vertical components is lower than the horizontal.

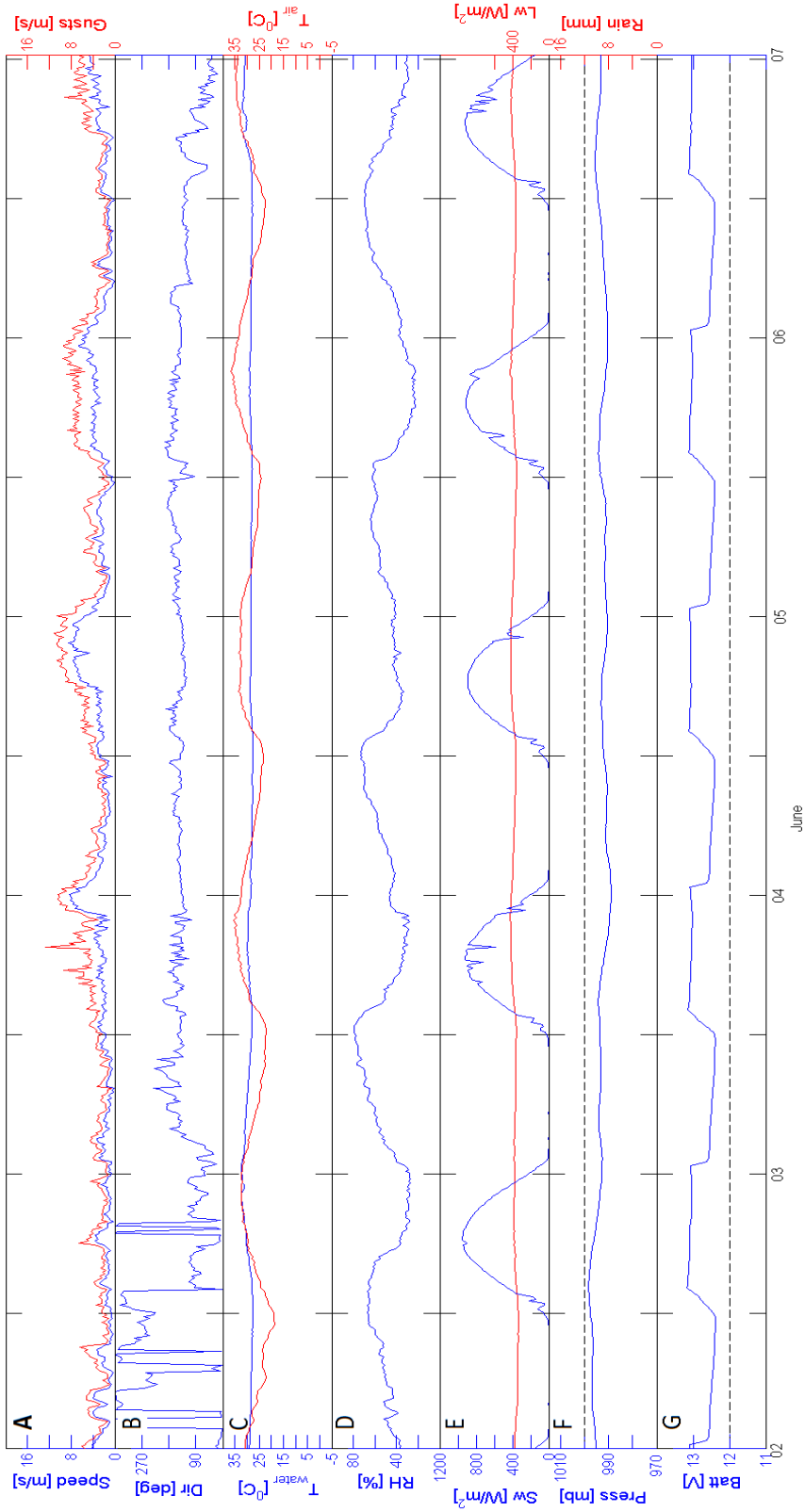

Fig 4.18. Measured Meteorological Data. (A) wind speed and gust, (B) wind direction, (C) water surface temperature and air temperature, (D) relative humidity, (E) short wave and longwave radiations, (F) atmospheric pressure and rainfall,(G) battery voltage. Time axis is UTC.

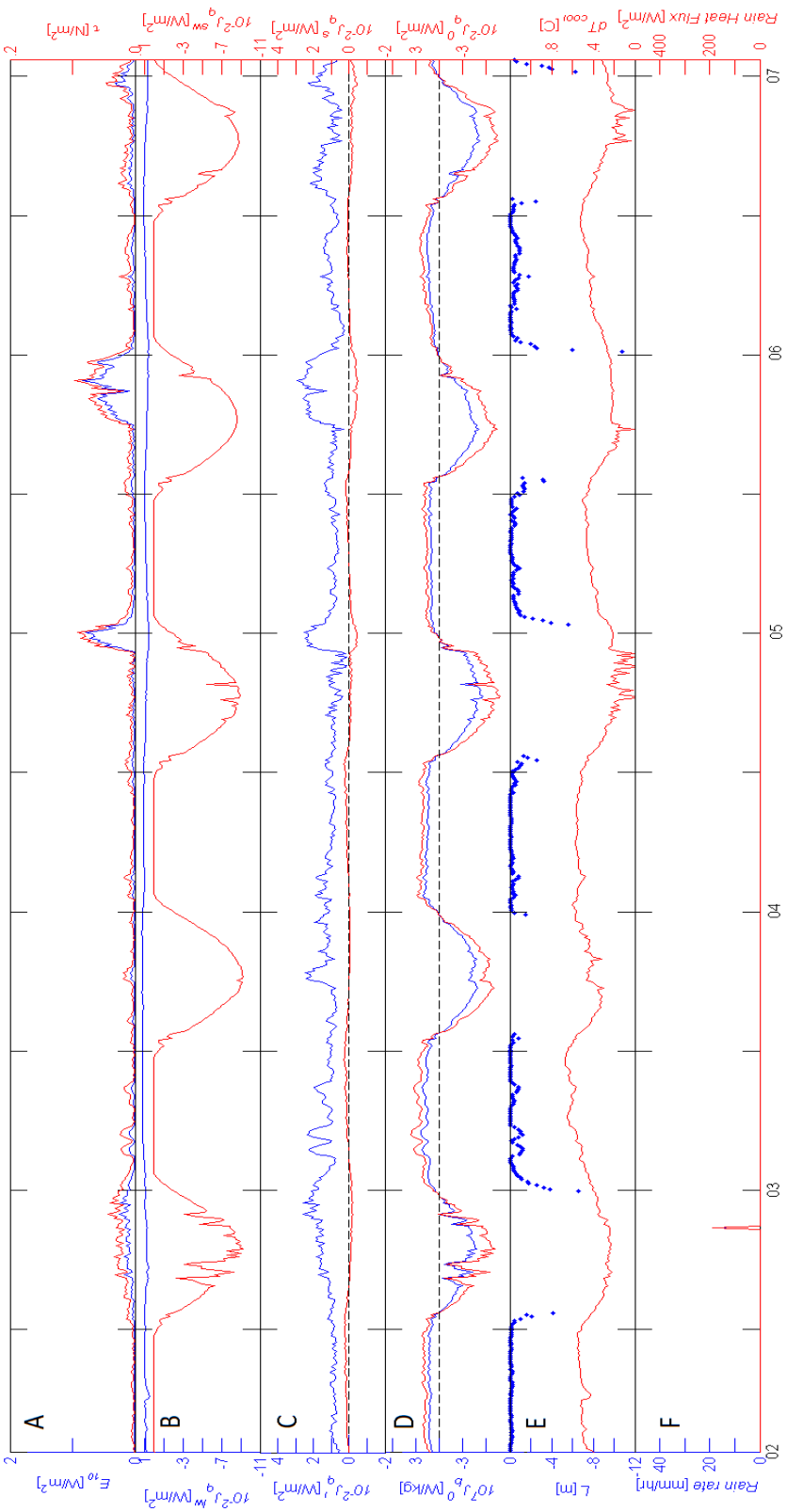

Fig 4.19. Surface Heat and Momentum Fluxes. (A) wind power and stress, (B) longwave and shortwave radiations , (C) latent and sensible heat fluxes, (D) buoyancy flux and net heat flux, (E) Monin-Obukov length scale and cool skin layer, (F) rainfall and rainfall heat flux; negative values indicate a flux into the water column. Time axis is UTC.

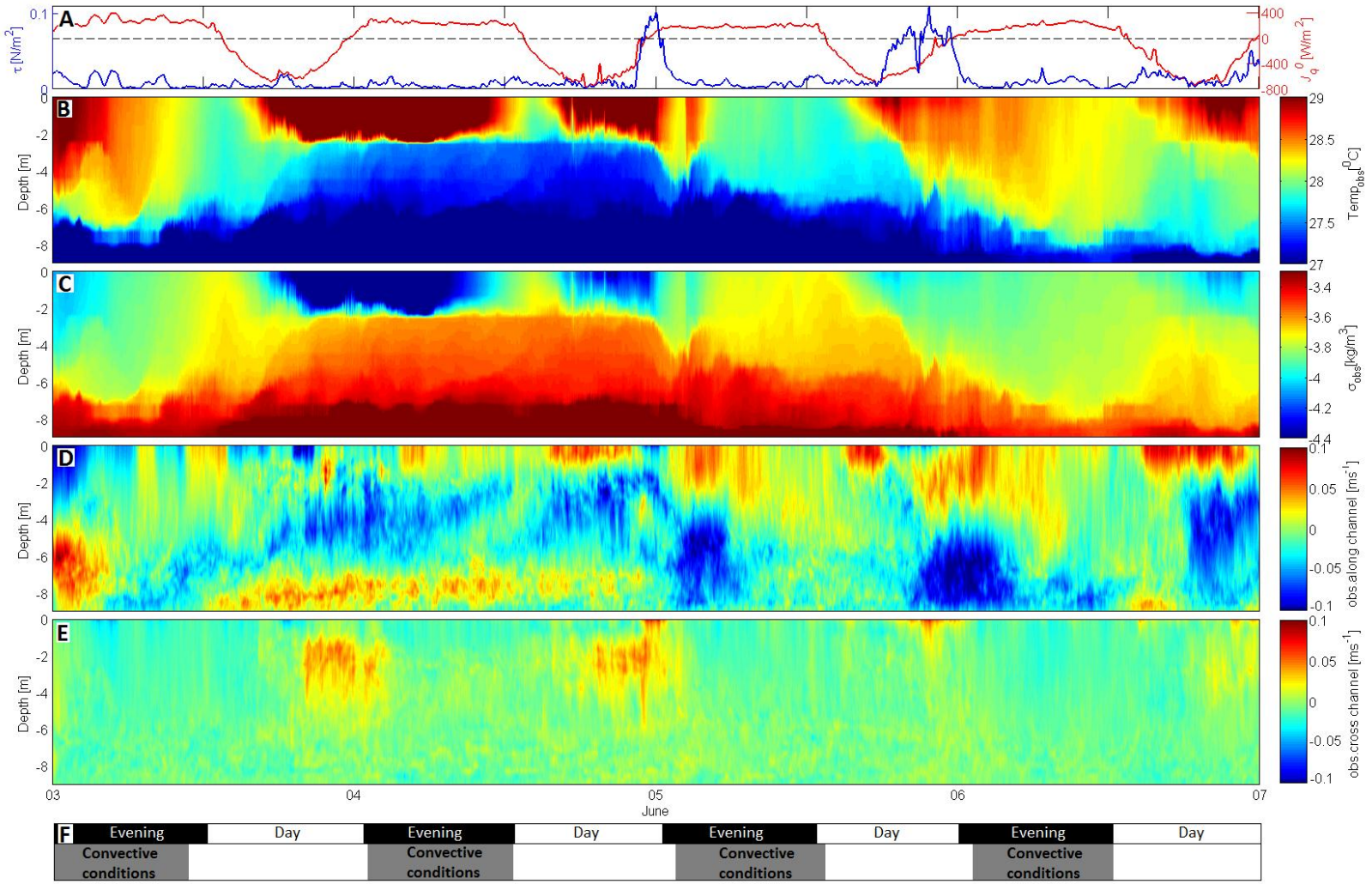

Fig 4.20. Observational Results. (A)Momentum and heat flux; negative heat flux represents heat into water column,(B) observed temperature,(C) observed σ_θ (σ_θ= potential density-1000), (D) observed along channel velocity, where negative values represent a flow upstream, (E) observed cross channel velocity, (F) description of day/evening times and convective conditions based on the buoyancy flux. Time axis is UTC.

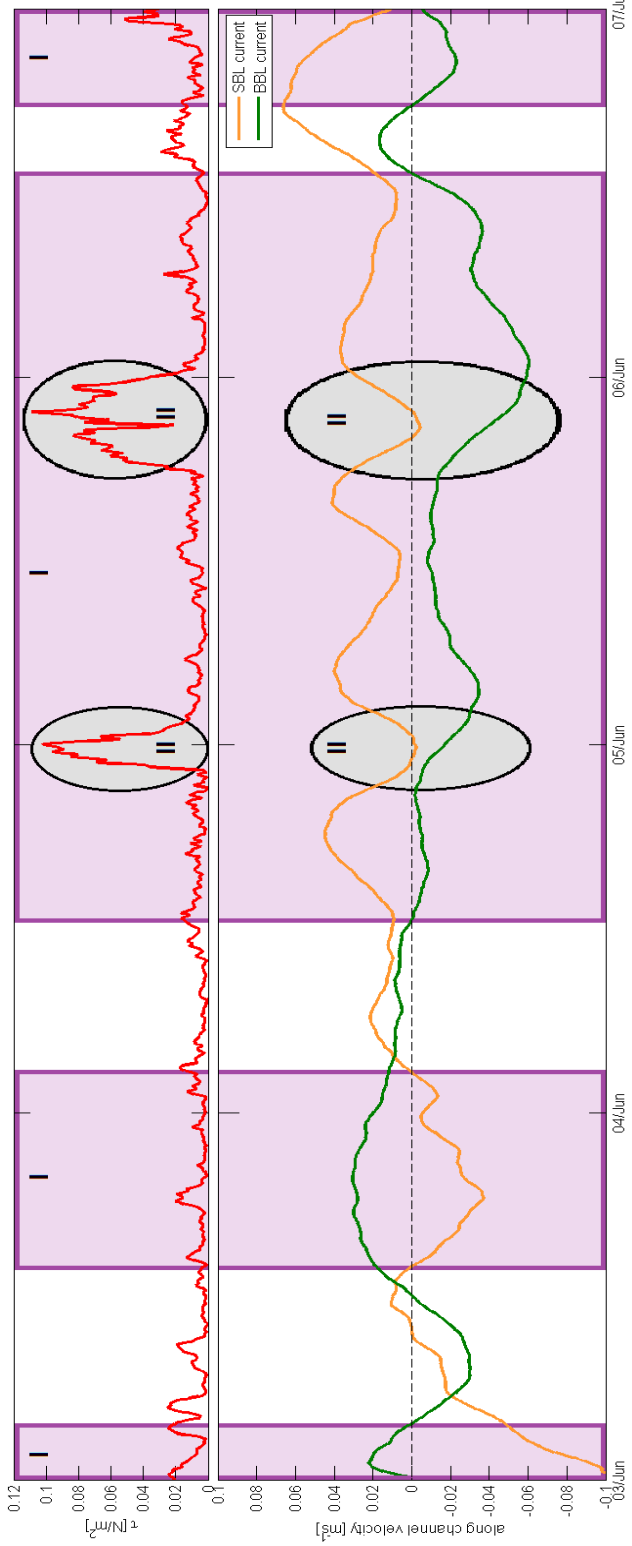

Fig 4.21. BBL Forced Flow. Wind stress (top) and along channel current velocities averaged over 0.5m bin in the SBL (0m-0.5m depth) and BBL (8.2m-8.7m depth) (lower) during several event stages. The purple boxes allocated with a roman numeral I represents a period when the currents are in opposite directions, the black ellipses with roman numeral II shows the effect of wind stress on velocity magnitude. Time axis is UTC.

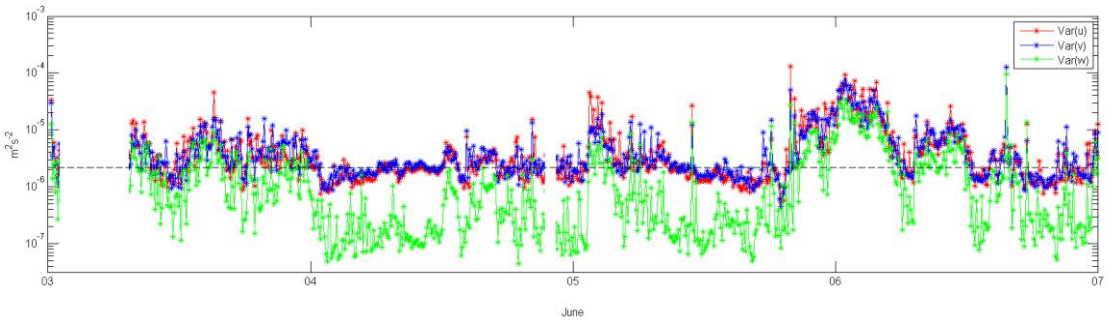

Fig 4.22. Observed Velocity Variances at 8.7m Depth. The noise level for the u and v velocity components indicated in a black dashed line.

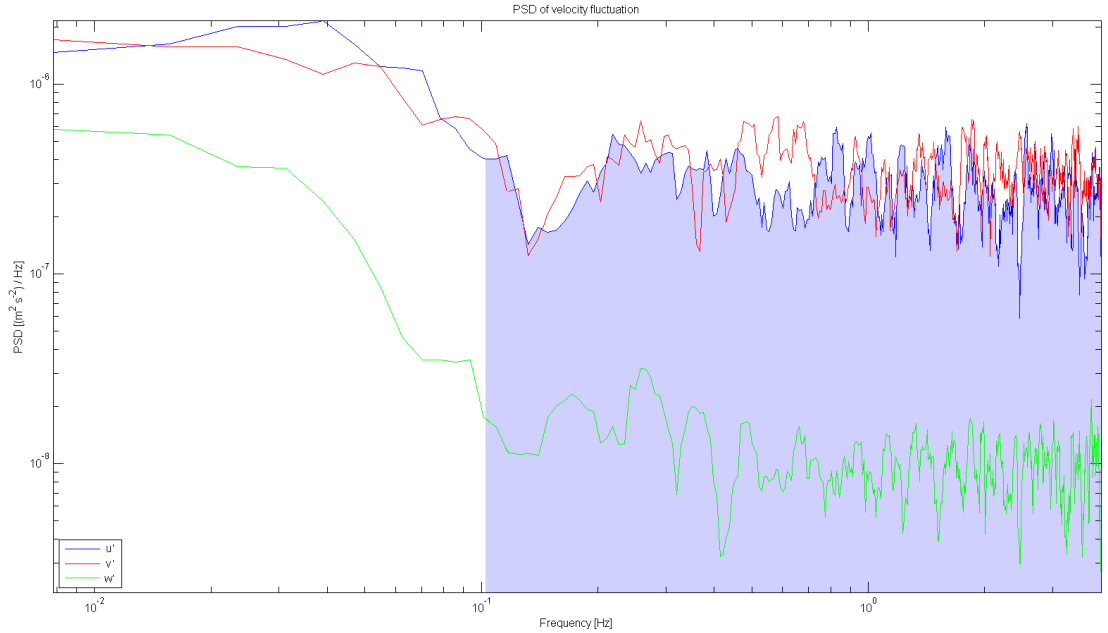

Fig 4.23. PSD of the Velocity Fluctuation Components. The area shaded blue is noise level of component u and v.

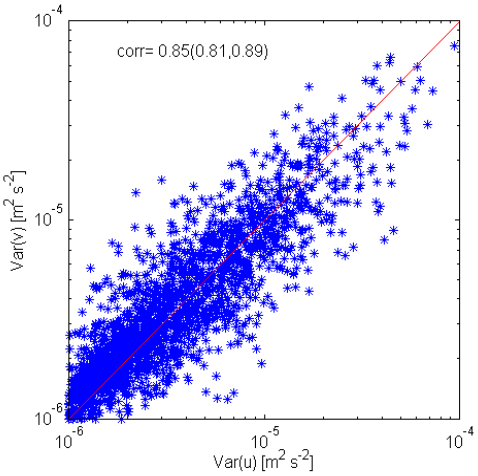

Fig 4.24. Scatter Plot of Variances in the u and v Components at 8.7m Depth. The correlation value and 95% confidence intervals in parenthesis.

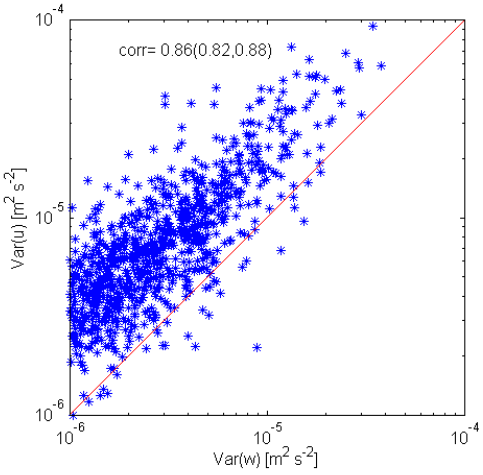

Fig 4.25. Scatter Plot of Variances in the w and u Components at 8.7m Depth. The correlation value and 95% confidence intervals in parenthesis.

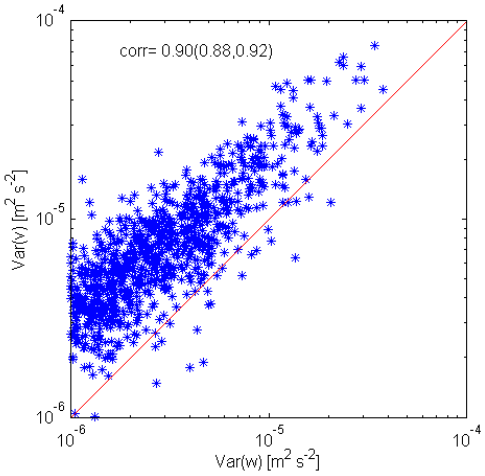

Fig 4.26. Scatter Plot of Variances in the w and v Components at 8.7m Depth. The correlation value and 95% confidence intervals in parenthesis.

4.2.2 *k-ϵ* model and *k-kl* model simulations

4.2.2.1 *k-ϵ* model vs *k-kl* model

The two models (*k-ϵ* and *k-kl*) follow the same trend in simulating turbulence processes at the BBL but vary in magnitude (Fig 4.29); similar to what has been observed during the weakly stratified period. Both the mean and MLE values of the simulated turbulence parameters by the *k-ϵ* model were lower than the *k-kl* model (Table 9), similar to what has been observed during the previous period. A test of correlation to quantify the strength of the relation between the models was made. Correlation values higher than 0.9 (Figs 4.27 and 4.28), which are similar to what has been observed in the weakly stratified period; show that both models are not significantly different.

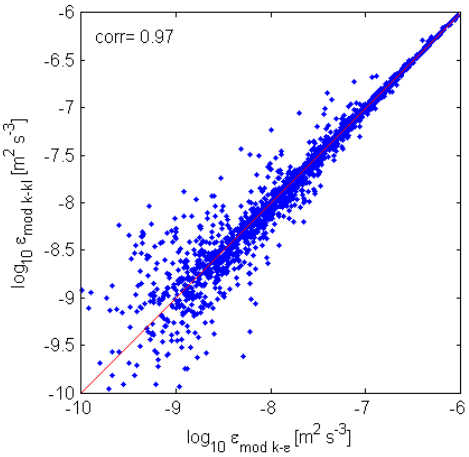

Fig 4.27. Comparison between Models TKE Dissipation Rate.

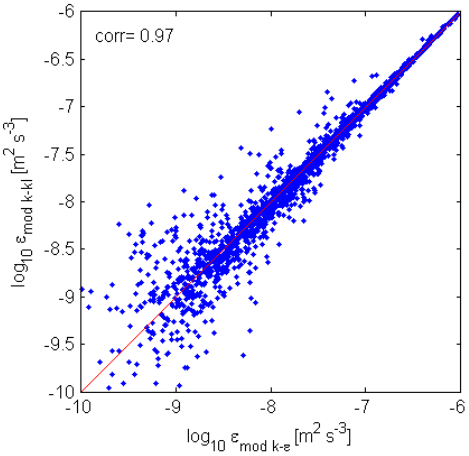

Fig 4.28. Comparison between Models TKE.

4.2.2.2 General features of the simulated parameters in the water column

The observations suggested that the water column followed a pronounced diurnal pattern, and was strongly stratified during day and relatively weakly stratified during night. Both models simulated the TKE and TKE dissipation rate to follow this diurnal pattern (Fig 4.29). The strong stratified period during daytime was associated with relatively low values of TKE and TKE dissipation rates throughout the water column. During nights, the simulated values of TKE and TKE dissipation rates were relatively high and extended deeper, reflecting the effect of convection. However, the turbulence produced by the surface forcing was unable to penetrate to the BBL. Because wind stress was relatively high during the daytime, a period of high stratification, the simulated effect of wind stress on turbulence processes was confined to the top 2m. On July 4th, the trend was not diurnal as specified in section 4.2.1 and the water was highly stratified during the night unlike the other 3 days. The simulated parameters reflected this well and values of TKE and TKE dissipation rate were relatively low throughout the water column.

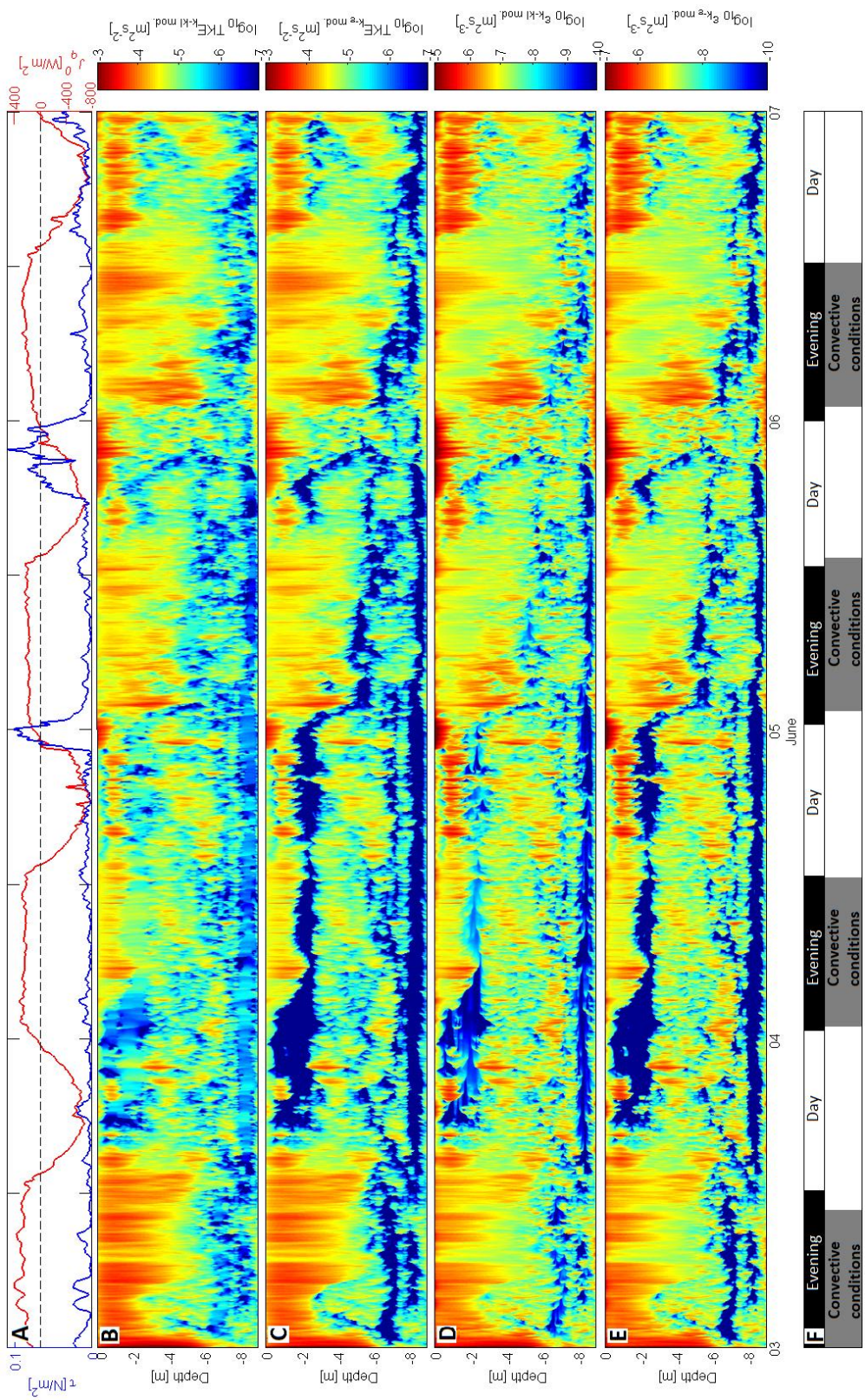

Fig 4.29. Simulated TKE and TKE Dissipation Rates. (A)Observed momentum and heat flux where negative heat flux represents heat into water column, (B) simulated TKE by k-kl model, (C) simulated TKE by k-ε model, (D) simulated TKE dissipation rate by k-kl model, (E) simulated TKE dissipation rate by k-ε model, (F) description of day/evening times and convective conditions. Time axis is UTC.

4.2.2.3 Qualitative comparison of observed and simulated selected parameters in the BBL

Similar to the weakly stratified period, the focus was on the BBL for a detailed comparison between the selected parameters (TKE and TKE dissipation rate). Data were first smoothed to reduce fluctuations in a similar approach and intervals as before (section 4.1.2.3).

As specified previously (section 4.2.1), the highly stratified conditions during this period confined convection and wind stress effects to the upper mixed layer only, and were unable to penetrate to the BBL. Therefore, the return flow magnitude in the BBL, forced by the pressure gradient, was expected to be a main controlling factor of the turbulence parameters in the BBL (Fig 4.21).

Qualitatively, both model simulations follow the observations well, with exception of some periods (June 4th 14:00-1500, 19:00-5th 01:00 and 5th 9:00-10:00) where both models have simulated low values for TKE, TKE dissipation rates and velocity variances (Figs 4.30-4.33). At this same time, the observed horizontal velocity components were at the instruments noise level (section 4.2.1). This suggests the models did not simulate the values of the turbulence parameters well because it was forced by noise affected velocity profiles (section 1.3.3).

With the absence of surface forcing effects at the BBL during this period, the modeled turbulence parameters (TKE and TKE dissipation rate) followed the BBL current velocity magnitude. A faster BBL current velocity causes an increase in shear and as a result turbulence production increases (section 1.2.2) (Figs 4.30, 4.31 panels A and B).

Periods when the BBL along channel current velocity was higher than $0.02ms^{-1}$, they were followed by increase in turbulence production and mixing intensity as seen on June 3rd, 5th 01:00-05:00 and 5th 19:00-7th (Figs 4.21, 4.30-4.33). Both models reflected well the TKE and TKE dissipation rates associated with the high BBL current ($>0.02ms^{-1}$). When the BBL current weakened ($<0.02ms^{-1}$) stability was enhanced, it was followed by an increase in Ri number ($Ri>Ri_c$) as seen on June 4th and 5th 05:00-19:00. The *k-kl* model captured these stable conditions well, which resulted in relatively low simulated values of TKE and TKE dissipation rates, following the observational results well. However, the *k-ϵ* model overestimated the TKE, TKE dissipation rates and velocity variances during these stable conditions.

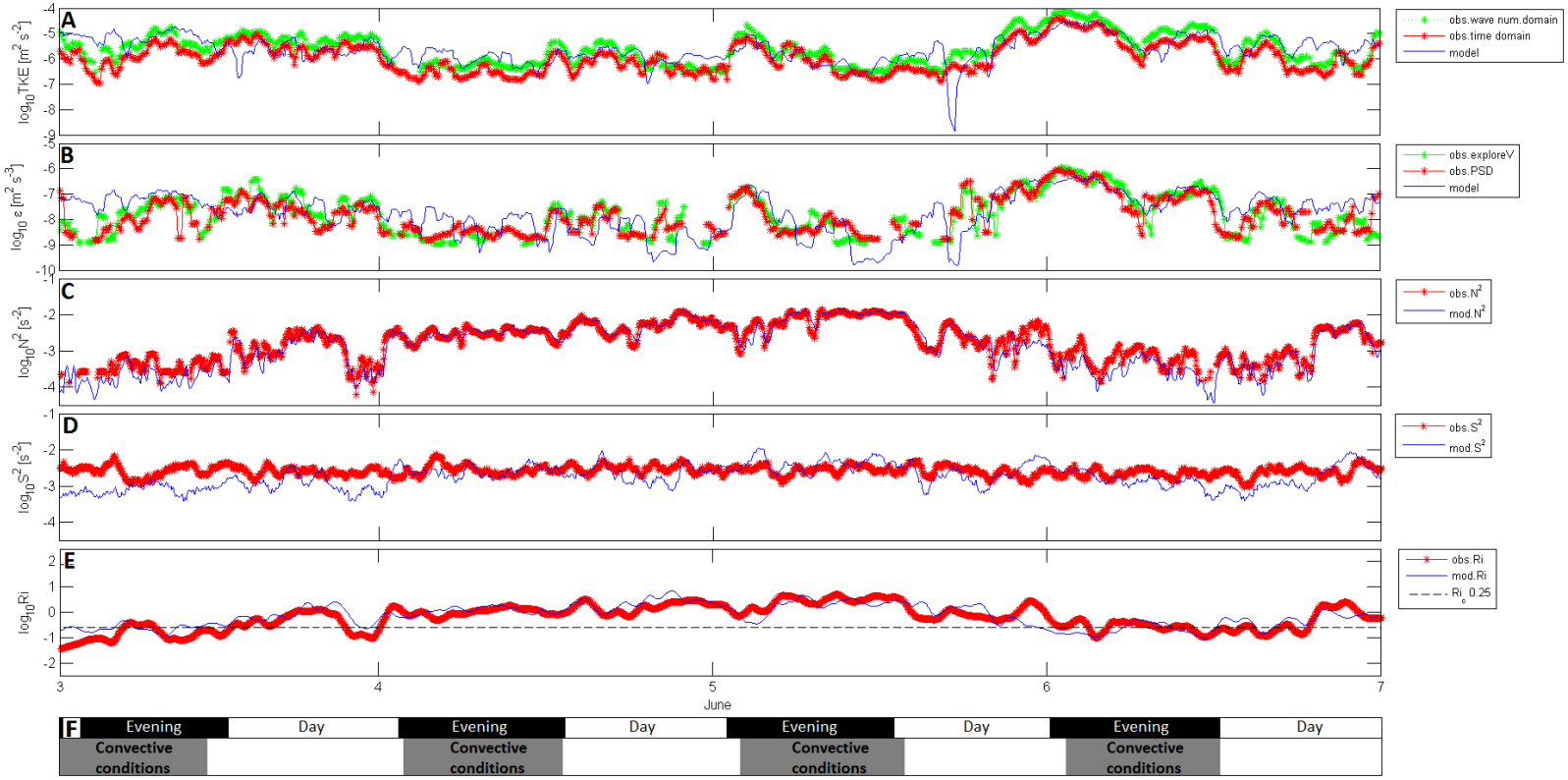

Fig 4.30. *k-kl* Modeled vs Observed Turbulence Parameters at 8.7m. (A) TKE, (B) TKE dissipation rate, (C) buoyancy frequency, (D) shear frequency, (E) Ri number, (F) description of day/evening times, air masses and convective conditions. Time axis is UTC.

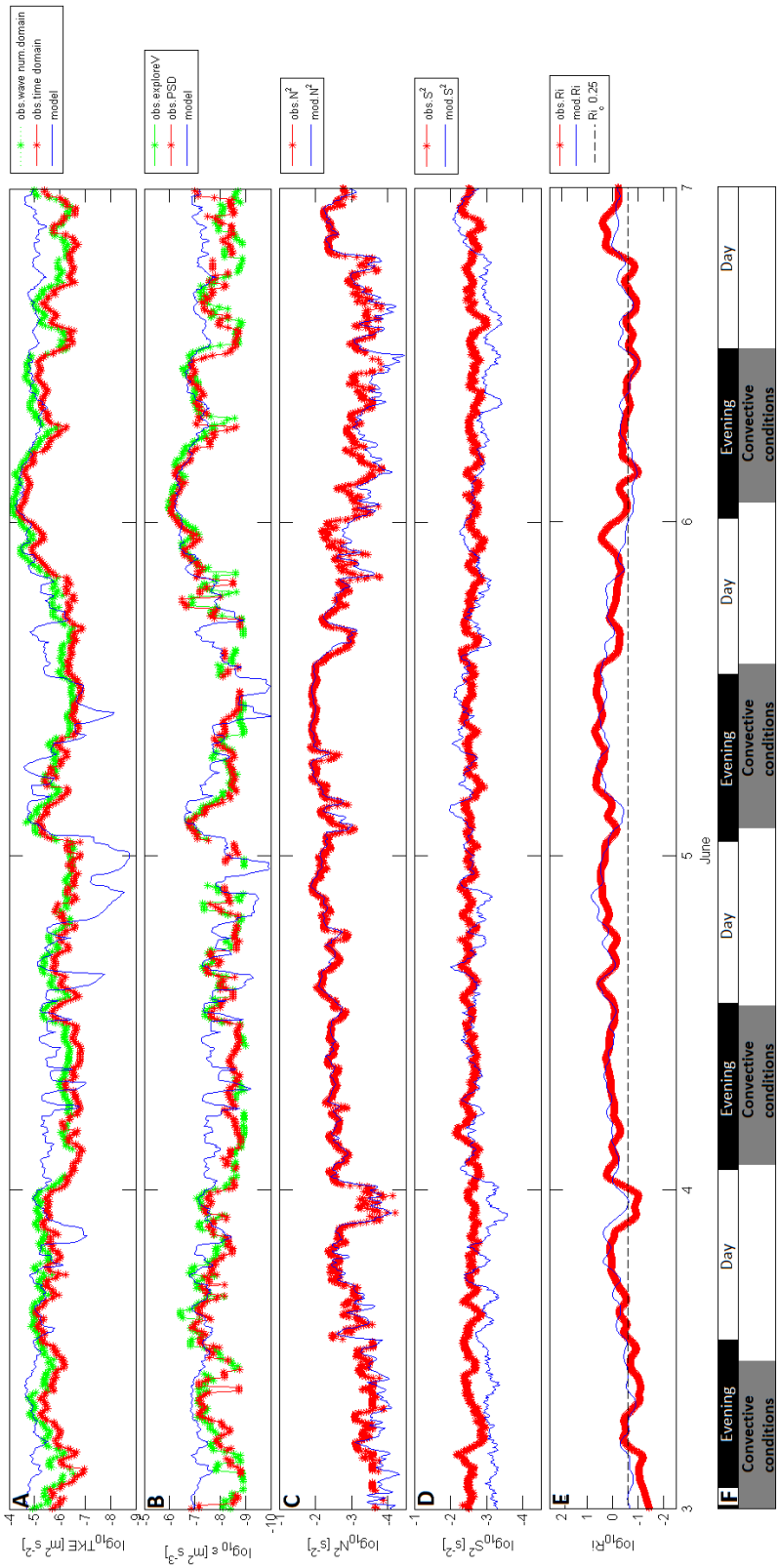

Fig 4.31. *k-ϵ* Modeled vs Observed Turbulence Parameters at 8.7m. (A) TKE, (B) TKE dissipation rate, (C) buoyancy frequency, (D) shear frequency, (E) Ri number, (F) description of day/evening times, air masses and convective conditions. Time axis is UTC.

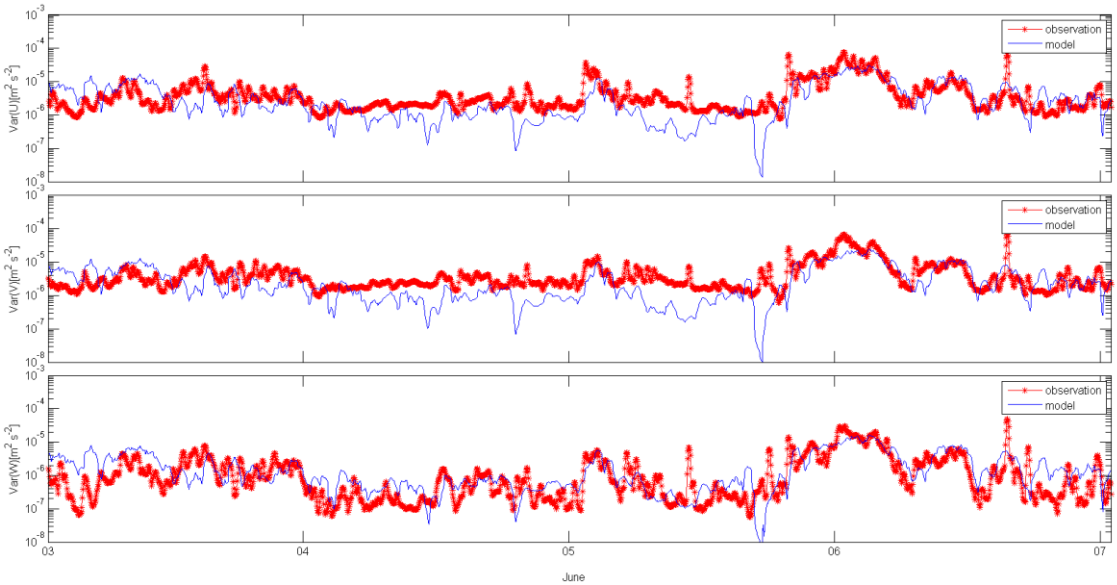

Fig 4.32. *k-kl* Modeled vs Observed Velocity Variances at 8.7m. (top) U-component, (middle) V-component, (bottom) W-component.

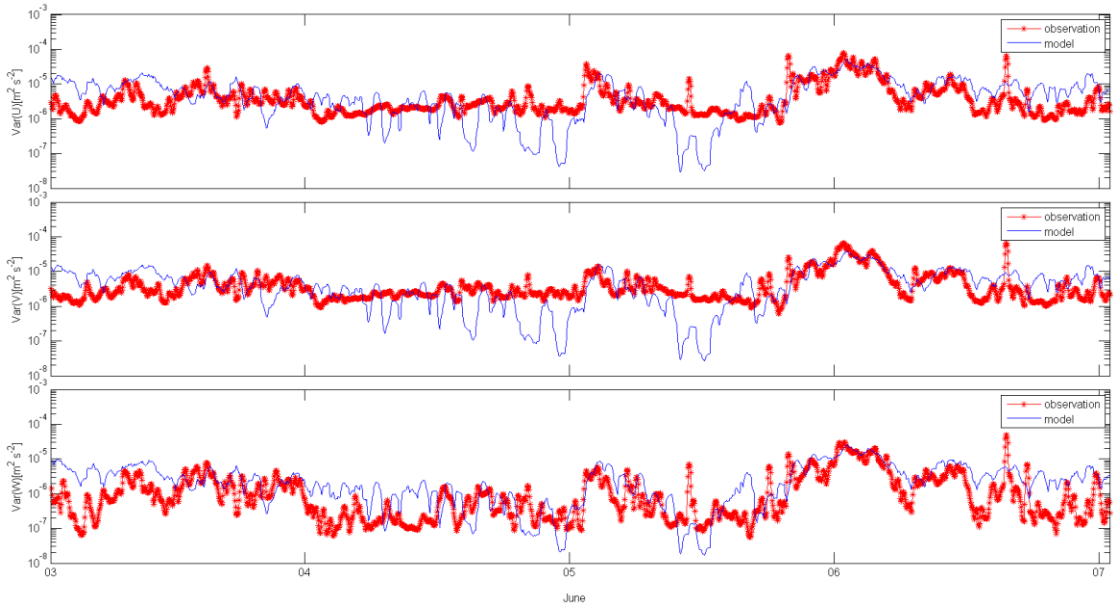

Fig 4.33. *k-ϵ* Modeled vs Observed Velocity Variances at 8.7m. (top) U-component, (middle) V-component, (bottom) W-component.

4.2.2.4 Quantitative comparison of observed and simulated selected parameters in the BBL

It was emphasized in the previous section 4.2.2.3 that the magnitude of the BBL along channel current velocity was a main driver of turbulence production during this strongly stratified period due to current shear. A correlation test was made to quantify the significance of this relation. The correlation values for the effect of the BBL current on the simulated turbulence parameters for both models have shown that there is a strong relation supporting the arguments in section 4.2.2.3, with correlation values above 0.7 (Table 8).

Table 8. Correlation Values of the BBL Current Velocity vs Simulated (*k-ϵ* and *k-kl*) TKE and TKE Dissipation Rates for the Periods of 3 June to 7 June.

	Simulated			
	TKE		*ϵ*	
	k-kl	k-ϵ	*k-kl*	k-ϵ
Along channel current magnitude at the BBL	0.72	0.70	0.73	0.72

Basic statistical (maximum, minimum, mean and MLE) values for the simulated and observed turbulence parameters are presented in Table 9. Similar to the weakly stratified period, the mean values for the dissipation rates did underestimate the MLE values as suggested by *Baker and Gibson* [1987].

To conclude which model better follows the observation results of the turbulence parameters, a correlation test was made between the observation and simulation results. Similar to the weakly stratified period, the *k-kl* model has shown follow the observations

closer than the *k*-ϵ model (Fig 4.30). The correlation values show that the *k*-*kl* model better follows the observations with values of 0.61 and 0.6 for the TKE and 0.58 for the dissipation rate. The correlation values were 0.56 for the *k*-ϵ model, 0.57 for the TKE, and 0.53 for the TKE dissipation rate (Table 10).

Table 9. Observed and Models Simulated (*k*-ϵ and *k*-*kl*) Values of TKE and TKE Dissipation Rate. The mean and MLE values and the 95% confidence intervals in brackets were computed using 1000 bootstrap samples for the periods of 3 June to 7 June.

	3-Jun to 7-Jun		
	Maximum	Mean	MLE
TKE [m^2s^{-2}]			
k-ϵ	9.24×10^{-4}	2.41×10^{-6}	5.61×10^{-6}
(Simulated)		(2.13, 2.76)	(4.88, 7.59)
k-*kl*	9.15×10^{-4}	3.02×10^{-6}	5.69×10^{-6}
(Simulated)		(2.76, 3.35)	(4.84, 7.47)
Wavenumber. domain	3.50×10^{-5}	3.34×10^{-6}	4.67×10^{-6}
(Observed)		(2.94, 3.80)	(4.06, 5.57)
Time. domain	1.87×10^{-5}	1.46×10^{-6}	2.20×10^{-6}
(Observed)		(1.30, 1.67)	(1.91, 2.69)
ϵ [m^2s^{-3}]			
k-ϵ	1.27×10^{-6}	3.01×10^{-8}	6.88×10^{-8}
(Simulated)		(2.66, 3.41)	(5.55, 10.06)
k-*kl*	1.27×10^{-6}	3.08×10^{-8}	7.04×10^{-8}
(Simulated)		(2.74, 3.51)	(6.53, 11.78)
Equation (53)	6.46×10^{-7}	2.92×10^{-8}	6.11×10^{-8}
(Observed)		(2.38, 3.72)	(4.55, 9.12)

Table 10. Observed vs Models Simulated (*k-ϵ* and *k-kl*) Correlation values of TKE and TKE Dissipation Rates. The 95% confidence intervals in brackets were computed using 1000 bootstrap samples for the periods of 3 June to June.

		Simulated			
		TKE		*ϵ*	
		k-kl	*k-ϵ*	*k-kl*	*k-ϵ*
Observed	ϵ	-	-	0.58	0.53
		-	-	(0.48, 0.68)	(0.41, 0.65)
	TKE wavenumber domain	0.61	0.56	-	-
		(0.52, 0.70)	(0.46. 0.67)	-	-
	TKE time domain	0.60	0.57	-	-
		(0.50, 0.69)	(0.47, 0.67)	-	-

Overall, the simulated parameters of velocity variances, TKE and TKE dissipation rate during this strongly stratified period followed the observational values well, both qualitatively (Figs 4.30-4.33) and quantitatively (Tables 9 and 10). The correlation values signify a positive relation between the simulated and observed estimates of TKE and TKE dissipation rates with the *k-kl* model following the observational results slightly closer.

4.3 Vertical eddy diffusivity (K_z)

Several events of fish kill have been reported in Lake Whitney (section 1.4) [*Roelke et al.*, 2010; *Roelke et al.*, 2011]. These events are directly influenced by the vertical mixing in the SBL, where the vertical transport of nutrients, air-sea interface exchange (gas, heat and momentum), and the vertical migration of phytoplankton are affected [*MacIntyre*, 1993]. The magnitude of the vertical mixing is dependent on the stratification level and turbulence intensity. This section looks at how temporal changes in stratification and turbulence affect the vertical eddy diffusivity. Furthermore, we compare the observational results with simulated by *k*-ϵ and *k*-*kl* and also with K-Profile Parameterization (*KPP*) [*Large et al.*, 1994] and *Loewen et al*. [2007] equations (eqn. 64 and 65, respectively), to conclude which method best reflects the observational conditions.

The vertical eddy diffusivity for the observed and simulated (*k*-ϵ and *k*-*kl*) datasets was estimated using *Osborn's* [1980] formula:

$$K_z = \Gamma \frac{\epsilon}{N^2} \tag{63}$$

where Γ is the mixing efficiency, which is the ratio of change in potential energy and kinetic energy ($\frac{\Delta PE}{\Delta KE}$) taken as 0.25 based on Joint Air-Sea Interaction experiment (JASIN) (see [*Oakey*, 1985]).

Two other methods were used to compute the vertical eddy diffusivity. The first, is the *KPP* method (eqn. 23), which is based on field experiments in deep ocean environments (see [*Large et al.*, 1994]).

$$K_z = K_o(1 + 3.33 * Ri)^{-\frac{3}{2}} \quad (64)$$

where K_o is the value of vertical eddy diffusivity during homogenous conditions (unstratified water column) estimated from the observational results as ~9x10^{-4} m^{2}s^{-1}. K_o was obtained by first averaging the simulated (*k*-ϵ and *k*-*kl*) Ri number over four days at multiple depth levels (300). Levels where the Ri number is below the critical number was assumed to be unstratified. From the simulated (*k*-ϵ and *k*-*kl*) results of heat diffusivity at the levels where Ri number was below the critical number were averaged to obtain K_o.

The second, is the *Loewen et al* [2007] method (eqn. 65), which is based on field experiments in a shallow lake (~8-11m).

$$K_z = K_o\left(1 - \left(\frac{Ri}{Ri_o}\right)^2\right)^3 \quad (65)$$

Ri_o is a Ri critical value of 0.7 [*Large et al.*, 1994].

As seen previously in this section, the effect of surface forcing (heat and momentum) on Lake Whitney is significant, causing conditions to become weakly stratified during winter (section 4.1) and strongly stratified during summer (section 4.2). The temporal changes in stratification conditions reflected on the magnitude of the vertical eddy diffusivity (Figs 4.3). During winter, the relatively high turbulence production from surface forcing extended to the BBL causing the Ri number to be lower overall than in summer. Both the observational and all simulated results during both periods follow a similar trend and show that the vertical eddy diffusivity decreases rapidly when Ri number is small ($Ri_c < Ri$). Because the *KPP* method was based on

ocean conditions, it simulated higher values than the observations and not reflecting lake conditions well (Table 11). The *Loewen et al.* [2007] method was based on an experiment at a Lake, which is similar to this study; and therefore provided closer simulated values to the observations than the *KPP* during both periods. The simulated results by the *k*-ϵ and *k*-*kl* models were about the same and both followed the observations well.

Table 11. Observed and Model Simulated (*k*-ϵ, *k*-*kl*, *KPP* and *Loewen et al.* [2007]) Log Mean Values of the Vertical Eddy Diffusivity During Weakly (March 11-15) and Strongly (June 3-7) Stratified Periods.

	Mean K_z 10^{-4}[m²s⁻¹]	
	Weakly Stratified	Strongly Stratified
Observed	2.81 (1.30,6.32)	0.66 (0.53,0.91)
k-ϵ	3.79 (3.21,4.45)	0.74 (0.64,0.85)
k-*kl*	4.66 (4.06,5.47)	0.77 (0.68,0.89)
KPP	5.45 (5.22, 5.68)	5.20 (5.09, 5.44)
Loewen et al. [2007]	2.93 (2.81,3.05)	2.73 (2.60,2.87)

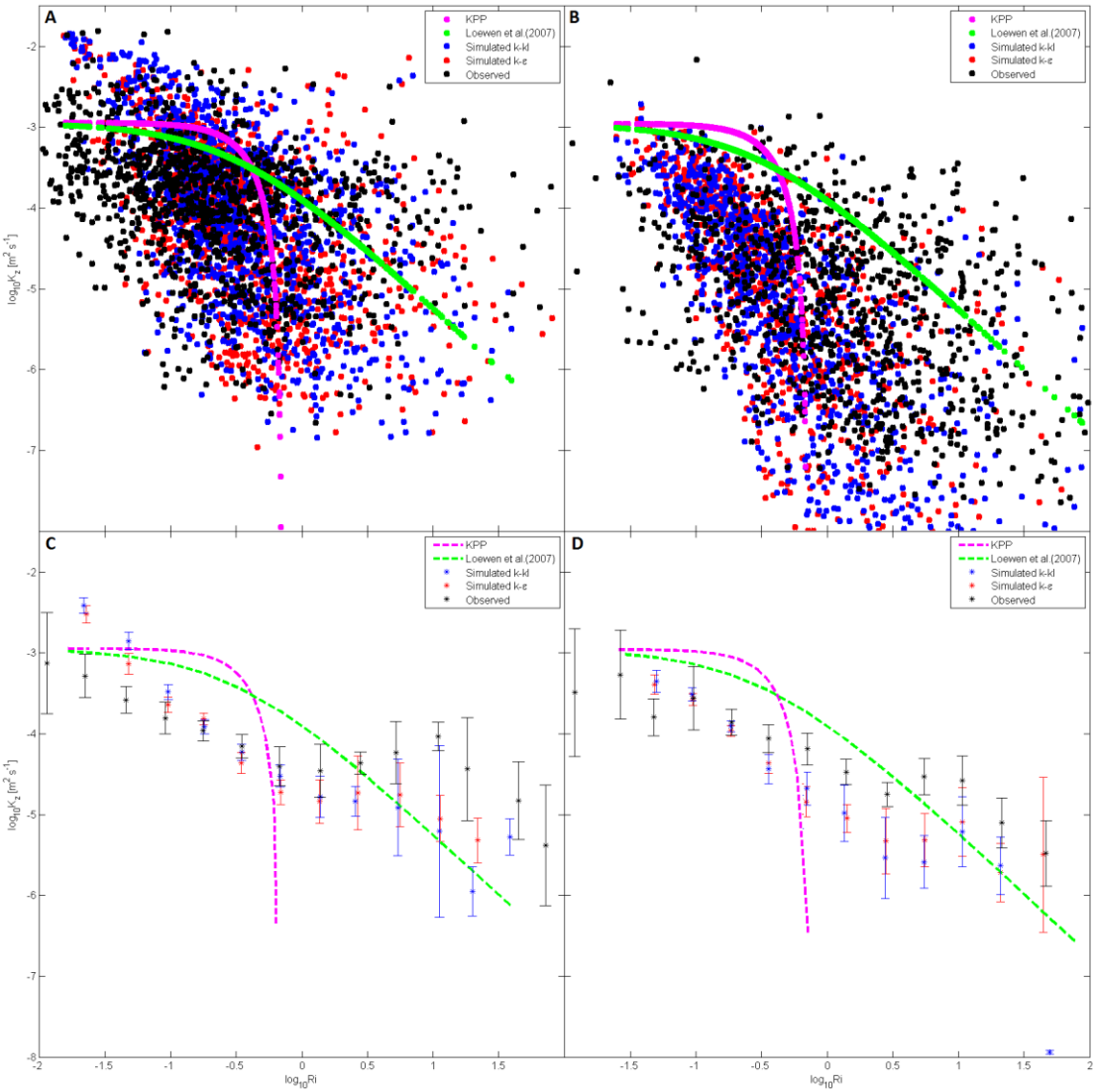

Fig 4.34. Observed and model simulations (*k-kl*, *k-ϵ*, *KPP* and *Loewen*) of K_z and Ri number. (A and B) Raw data during weakly stratified (11-15 March) and strongly stratified (June 3-7) periods, respectively. (C and D) Raw data smoothed by Ri number bin averaging (bin size 0.3) during weakly and strongly stratified periods, respectively. All data is taken from the BBL.

5. CONCLUSIONS

The simulated turbulence parameters of TKE and TKE dissipation rate by both models (*k-kl* and *k-*ϵ) in the BBL were found to be in agreement with the observations during both weakly and strongly stratified periods. Both models produced similar simulation results indicating a strong relation between the two models throughout the study period, with correlation values up to 0.97.

During the weak stratified period, the meteorological surface forcing (momentum and heat fluxes) were the primary drivers of the physical processes throughout the water column. Nighttime convection extended to the BBL when wind speed was at least 6ms^{-1} and the BBL return flow forced by the pressure gradient caused the turbulence parameters to change accordingly. These physical processes were captured well by both models as observed when quantitatively tested using Parson's correlation with values up to 0.63. The *k-kl* model has shown to follow the observational results slightly closer than the *k-*ϵ model during this period.

During the strong stratified period of summer, the diurnal influence of wind stress and net heat flux caused the physical processes to follow a pronounced diurnal pattern in the surface layers. The strong stratified conditions during this period prevented convection cells and turbulence produced by wind stress to penetrate to the BBL. Because the surface forcing did not extend deep, the BBL current alone was the primary driver of the simulated turbulence production in a good agreement with the observational results with correlation values up to 0.61. Similar to the weakly stratified period, the *k-kl* model followed the observational results closer than the *k-*ϵ model.

In summary, it is suggested that two equation models reflect well the TKE and TKE dissipation rate that are associated with convection, return flows and other physical processes in a fresh water reservoir. Similar conclusions have been reached by *Stip's et al.*[2002] and by *Anis and Singhal* [2006]. Finally, it can be stated that the *k-kl* model has provided slightly closer simulation results to the observations and therefore might have a slight advantage in simulating a fresh water reservoir than the k-ϵ model.

REFERENCES

Anis, A., and G. Singhal (2006), Mixing in the surface boundary layer of a tropical freshwater reservoir, *Journal of Marine Systems*, *63*(3-4), 225-243.

Aref, H. (2002), The development of chaotic advection, *Physics of Fluids*, *14*(4), 1315-1325.

Baker M.A., C.H. Gibson (1987), Sampling turbulence in the startified ocean: statistical consequences of strong intermittency. *Journal of Physical Oceanography*, 17: 1817-1836.

Baumert H.Z., Simpson, J.H., Sundermann, J. (eds.) (2005) *Marine Turbulence.* 2 ed., Cambridge: Cambridge University Press.

Bolding, K., H. Burchard, T. Pohlmann, and A. Stips (2002), Turbulent mixing in the Northern North Sea: a numerical model study, *Continental Shelf Research*, *22*(18-19), 2707-2724.

Bradshaw, P. (1972). *An Introduction to Turbulence and its Measurment*. Oxford: Pergamon Press.

Burchard, H. (2002) *Applied Turbulence Modelling in Marine Waters,* Berlin: Springer-verlag.

Burchard, H., and K. Bolding (2001), Comparative analysis of four second-moment turbulence closure models for the oceanic mixed layer, *Journal of Physical Oceanography*, *31*(8), 1943-1968.

Burchard, H., K. Bolding, W. Kühn, A. Meister, T. Neumann, and L. Umlauf (2006), Description of a flexible and extendable physical–biogeochemical model system for the water column, *Journal of Marine Systems*, *61*(3-4), 180-211.

Burchard, H., et al. (2008), Observational and numerical modeling methods for quantifying coastal ocean turbulence and mixing, *Progress In Oceanography*, *76*(4), 399-442.

Canuto, V. M., A. Howard, Y. Cheng, and M. S. Dubovikov, (2001): Ocean turbulence. Part I: One-point closure model momentum and heat vertical diffusivities. *J. Phys. Oceanogr.*, 31**,** 1413–1426.

Chen, C. T. A., and F. J. Millero (1986), Precise thermodynamics poperties For natural-waters covering only the limnological range, *Limnol. Oceanogr.*, *31*(3), 657-662.

Cheng, Y., V. M. Canuto, and A. M. Howard (2002), An improved model for the turbulent PBL, *Journal of the Atmospheric Sciences*, *59*(9), 1550-1565.

Colling, A., and O. U. O. C. Team (2001), *Ocean Circulation*, Oxford: Butterworth-Heinemann.

Csanady G.T., (2001) *Air-Sea Interaction,* Cambridge: Cambridge University Press.

Cushman-Roisin B., Beckers, J.M. (2011) *Introduction to Geophysical Fluid Dynamics,* San Diego: Academic Press.

Davidson., P.A, (2004) *Turbulence an Introduction for Scientists and Engineers,* New York: Oxford University Press.

Dickey, T. D., D. V. Manov, R. A. Weller, and D. A. Siegel (1994), Determination of longwave heat flux at the air-sea Interface using measurements from buoy platforms, *Journal of Atmospheric and Oceanic Technology*, *11*(4), 1057-1078.

Dorrestein, R. (1979), On the vertical buoyancy flux below the sea surface as induced by atmospheric factors, *Journal of Physical Oceanography*, *9*(1), 229-231.

Emery, W. J., and R.E. Thomson (1997), *Data Analysis Methods in Physical Oceanography,*Kent: Gray Publishing.

Fairall, C. W., E. F. Bradley, J. S. Godfrey, G. A. Wick, J. B. Edson, and G. S. Young (1996), Cool-skin and warm-layer effects on sea surface temperature, *J. Geophys. Res.*, *101*(C1), 1295-1308.

Fairall, C. W., E. F. Bradley, D. P. Rogers, J. B. Edson, and G. S. Young (1996), Bulk parameterization of air-sea fluxes for Tropical Ocean-Global Atmosphere Coupled-Ocean Atmosphere Response Experiment, *J. Geophys. Res.*, *101*(C2), 3747-3764.

Fairall, C. W., E. F. Bradley, J. E. Hare, A. A. Grachev, and J. B. Edson (2003), Bulk parameterization of air–sea fluxes: updates and verification for the COARE algorithm, *Journal of Climate*, *16*(4), 571-591.

García, C. M., M. I. Cantero, Y. Niño, and M. H. García (2005), Turbulence measurements with acoustic doppler velocimeters, *Journal of Hydraulic Engineering*, *131*(12),1062-1073.

Grant, H. L., R. W. Stewart, and A. Moilliet (1962), Turbulence spectra from a tidal channel, *Journal of Fluid Mechanics*, *12*(02), 241–268, doi:10.1017/S002211206200018X.

Huber, P. J. 1964. Robust estimation of a location parameter. *Annals of Mathematical Statistics* 35:73-101.

Kantha, L. H., and C. A. Clayson, 1994: An improved mixed layer model for geophysical applications. *J. Geophys. Res.,* 99, 25 235–25 266.

Kolmogorov, A. N. (1941), Dissipation of energy in the locally isotropic turbulence, *Dok. Akad. Nauk SSSR*, *31*, 538–540.

Kolmogorov, A.N. (1962), A refinement of previous hypothesis concerning the local structure of turbulence in a viscous incompressible fluid at high Reynolds number. *J. Fluid Mech. 13, 82-85.*

Large, W. G., J. C. McWilliams, and S. C. Doney (1994), Oceanic vertical mixing: A review and a model with a nonlocal boundary layer parameterization, *Rev. Geophys.*, *32*(4), 363-403

Launder, B., and D. Spalding (1972), Mathematical models of turbulence. London: Academic Press Inc. (London) Limited. Paper, 169pp., *Journal of sound and vibration*, *25*(4), 651.

Loewen, M. R., J. D. Ackerman, and P. F. Hamblin (2007), Environmental implications of stratification and turbulent mixing in a shallow lake basin, *Canadian Journal of Fisheries & Aquatic Sciences*, *64*(1), 43-57.

Mellor, G. L., and T. Yamada (1982), Development of a turbulence closure model for geophysical fluid problems, *Rev. Geophys.*, *20*(4), 851-875.

MacIntyre, S. (1993), Vertical mixing in a shallow, eutrophic lake: possible consequences for the light climate of phytoplankton, *Limnol. Oceanogr.*, *38*(4), 798-817.

Navier, L. M. (1822), Memoire sur les lois du mouvement des fluids. *Memoires de l'Academie des Sciences de l'Institut de* France 6: 389-440 Annee 1823.

Nortek AS, (2000) *ExploreV Software Manual*. Rev H, Rud: Nortek AS.

Nortek AS, (2005) *Vector Current Meter User Manual*. Rev H, Rud: Nortek AS.

Nortek AS, (2008) *Aquadopp Current Profiler User Guide*. Rud: Nortek AS.

Oakey, N. S. (1985), Statistics of mixing parameters in the upper ocean during JASIN phase 2, *Journal of Physical Oceanography*, *15*(12), 1662-1675.

Obukhov, A. M. (1962), Some specific features of atmospheric turbulence, *J. Geophys. Res.*, *67*(8), 3011-3014.

Osborn, T. R. (1980), Estimates of the local rate of vertical diffusion from dissipation measurements, *Journal of Physical Oceanography*, *10*(1), 83-89.

Paulson, C. A., and J. J. Simpson (1977), Irradiance measurements in the upper ocean, *Journal of Physical Oceanography*, *7*(6), 952-956.

Payne, R. E. (1972), Albedo of the sea surface, *Journal of the Atmospheric Sciences*, *29*(5), 959-970.

Pickard G., Emery W., (1990) *Descriptive Physical Oceanography.* 5 ed, Oxford: Butterworth Heinemann.

Pond S., Pickard G., (1983) *Introduction Dynamical Oceanography*. 2 ed., Elmsford: Pergamon Press.

Pope S., (2000) *Turbulent Flow,* Cambridge: Cambridge University Press.

Rotta, J. C., (1951) Statistische theorie nichthomogener turbulenz. *Z. Phys*., 129, 542-572.

Press, W. H., S. A. Teukolsky, W. T. Vetterling, and B. P. Flannery (Eds.) (2007), *Numerical Recipes: The Art of Scientific Computing*, 3rd ed., 1235 pp., Cambridge University Press, NY.

Reynolds, O. (1894), On the dynamical theory of incompressible viscous fluids and the determination of the criterion, *Proceedings: Mathematical and Physical Sciences*, *451*(1941), 5-47.

Richardson, L.F. (1922) *Weather Prediction by Numerical Processes.* Cambridge: Cambridge University Press

Rodi, W. (1982), Examples of turbulence models for incompressible flows, *AIAA journal*, *20*(7), 872-879.

Roelke, D. L., G. M. Gable, T. W. Valenti, J. P. Grover, B. W. Brooks, and J. L. Pinckney (2010), Hydraulic flushing as a Prymnesium parvum bloom-terminating mechanism in a subtropical lake, *Harmful Algae*, *9*(3), 323-332.

Roelke, D. L., et al. (2011), A decade of fish-killing Prymnesium parvum blooms in Texas: roles of inflow and salinity, *Journal of Plankton Research*, *33*(2), 243-253.

Salon, S., A. Crise, et al. (2008). Dynamics of the Bottom Boundary Layer. Developments in Sedimentology, *Elsevier*, *60*, 83-97.

Schwierzke, L., D. L. Roelke, B. W. Brooks, J. P. Grover, T. W. Valenti, M. Lahousse, C. J. Miller, and J. L. Pinckney (2010), Prymnesium parvum population dynamics during bloom development: a role assessment of grazers and viruses, *JAWRA Journal of the American Water Resources Association*, *46*(1), 63-75.

Sreenivasan, K. R. (1995), *On the universality of the Kolmogorov constant*, *Phys. Rev. E*, *7*, 2778.

Stull R.B, (1988) *An Introduction to Boundary Layer Meteorology,* Norwell: Kluwer Academic Publisher.

Taylor, G.I., (1938). *The Spectrum of Turbulence*. Proc. R. Soc. London Ser. A 164, 476-490.

Tennekes, H., and J.L. Lumley (1972) *A First Course in Turbulence*, Cambridge: The MIT Press.

Thorpe, S. A. (1995), Dynamical processes of transfer at the sea surface, *Progress In Oceanography*, *35*(4), 315-352.

Thorpe S.A., (2005) *The Turbulent Ocean,* Cambridge: Cambridge University Press.

Thorpe S.A., (2007) *An Introduction to Ocean Turbulence,* Cambridge: Cambridge University Press.

Umlauf, L., and H. Burchard (2003), A generic length-scale equation for geophysical turbulence models, *Journal of Marine Research*, *61*(2), 235-265.

Webb, E. K., Pearman, G. I. and Leuning, R. (1980), Correction of flux measurements for density effects due to heat and water vapour transfer. *Quarterly Journal of the Royal Meteorological Society*, 106: 85–100. doi: 10.1002/qj.49710644707

Welander, P. (1955), Studies On The General Development Of Motion In a 2-Dimensional, Ideal Fluid, *Tellus*, *7*(2), 141-156.

Wolfgang, R. (1987), Examples of calculation methods for flow and mixing in stratified fluids, *Journal of Geophysical Research, 92(C5):5305-5328*, *34*(11), 934-934.

von Storch, H., and F. W. Zwiers, (1999) *Statistical Analysis in Climate Research,* Cambridge: Cambridge University Press.

Yaglom. A.M (1966), The influence of the fluctuation in energy dissipation on the shape of turbulent characteristics in the inertial interval, *Soviet Physics-Doklady*, 2, 26-29.

APPENDIX A OBSERVATIONAL RESULTS

A.1 Lake Whitney Basic Meteorological Data

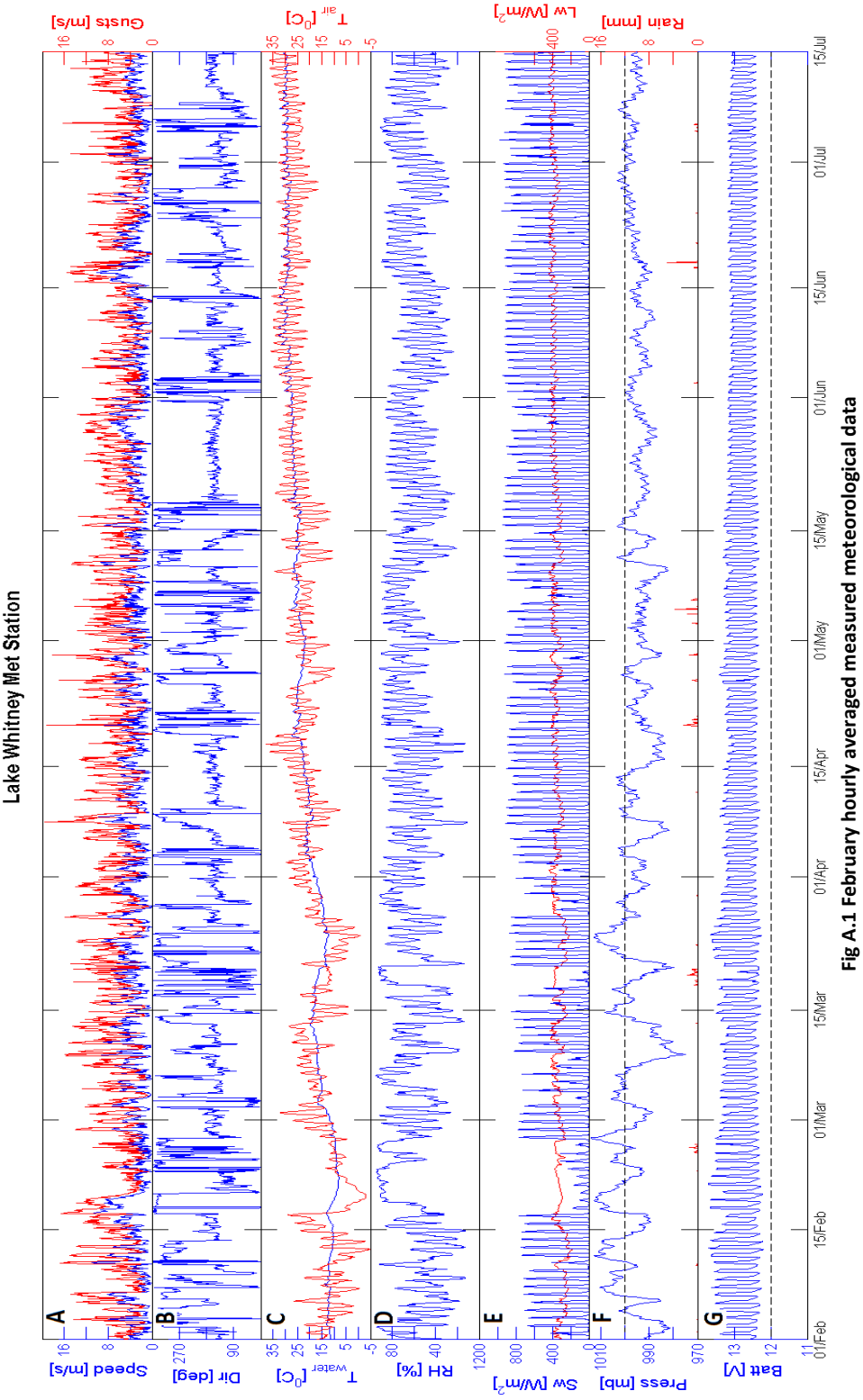

Fig A.1 February hourly averaged measured meteorological data

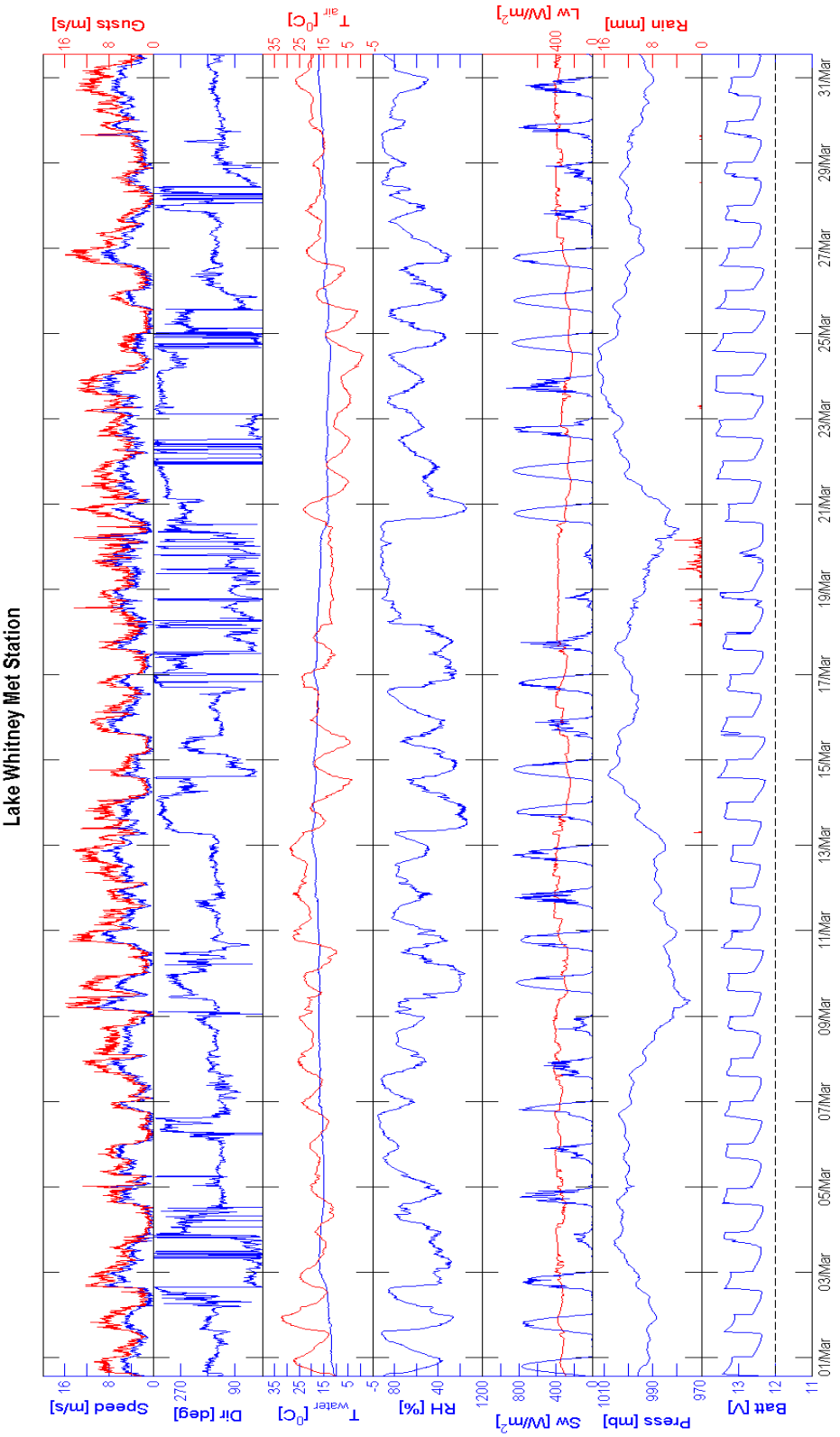

Fig A.2 March hourly averaged measured meteorological data

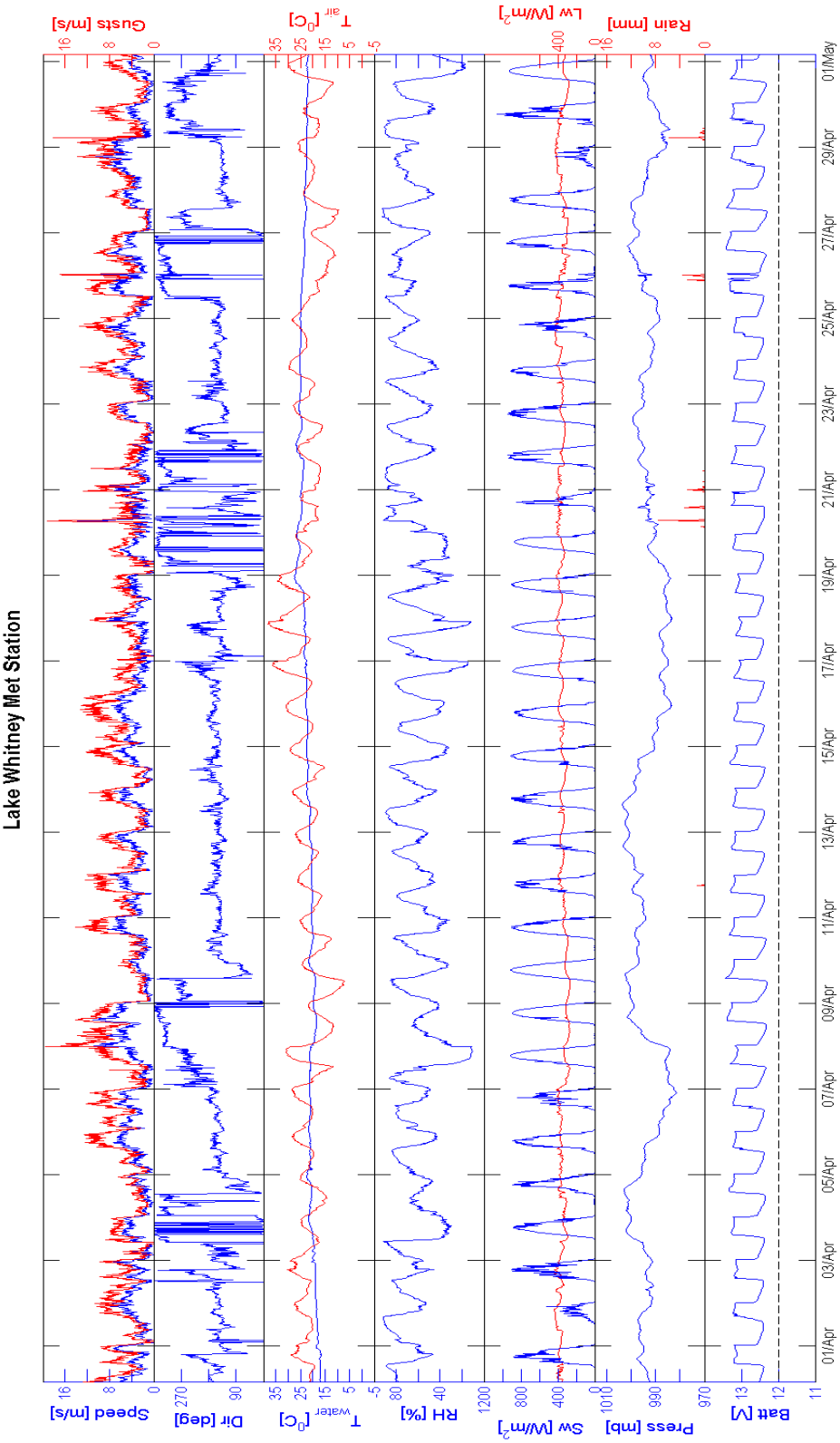

Fig A.3 April hourly averaged measured meteorological data

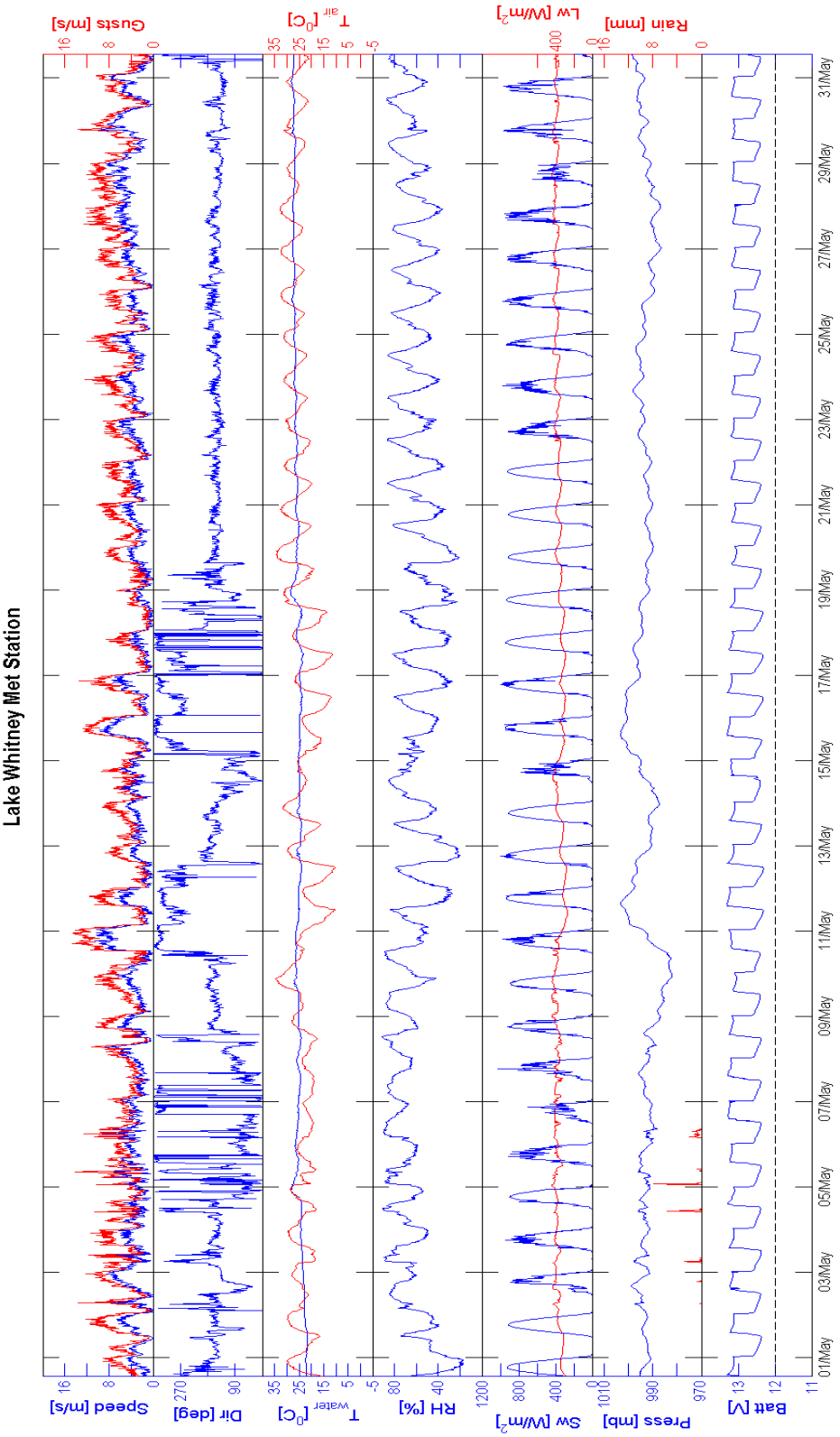

Fig A.4 May hourly averaged measured meteorological data

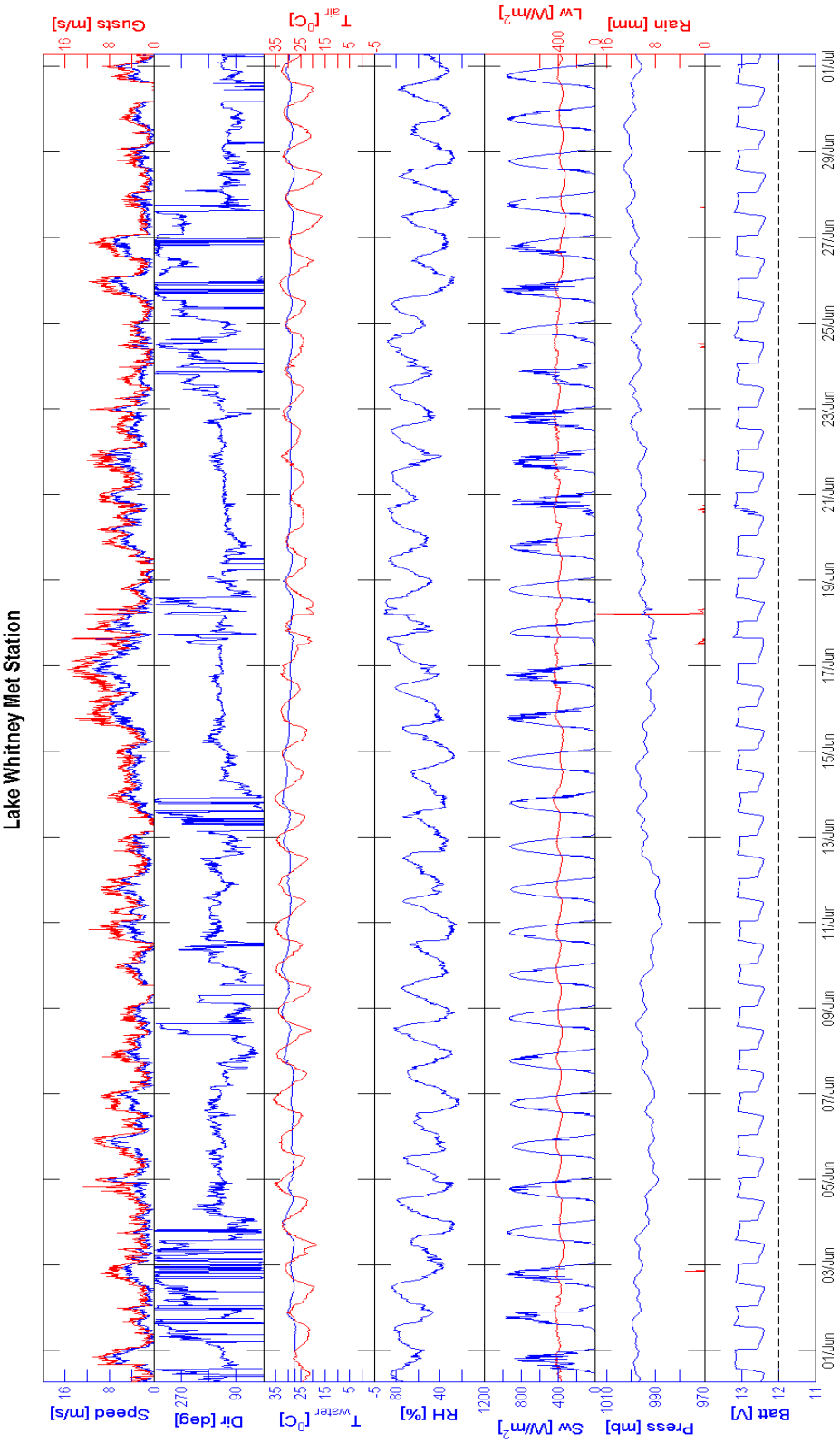

Fig A.5 June hourly averaged measured meteorological data

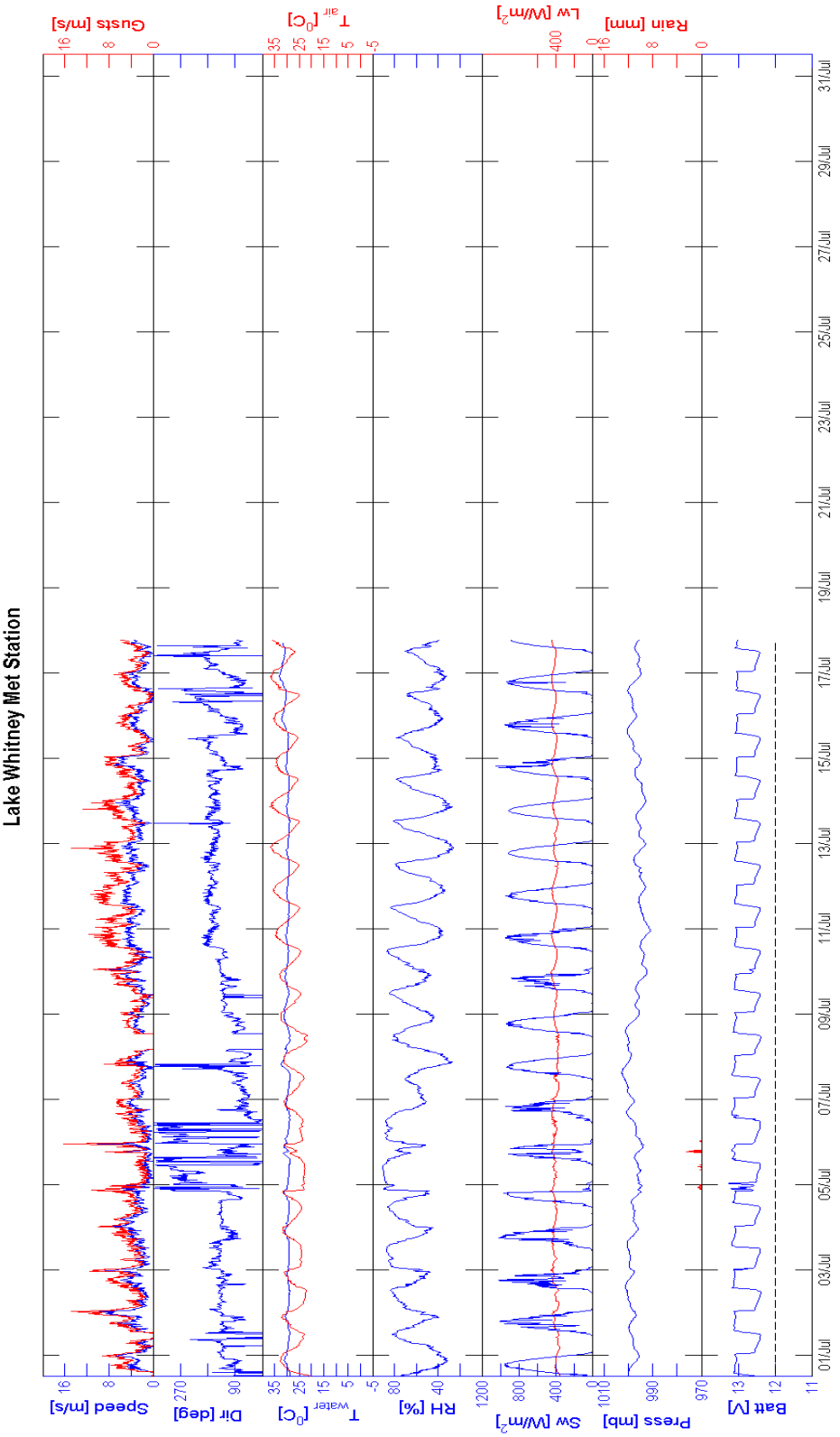

Fig A.6 July hourly averaged measured meteorological data

A.2 Lake Whitney Heat & Momentum Flux Data

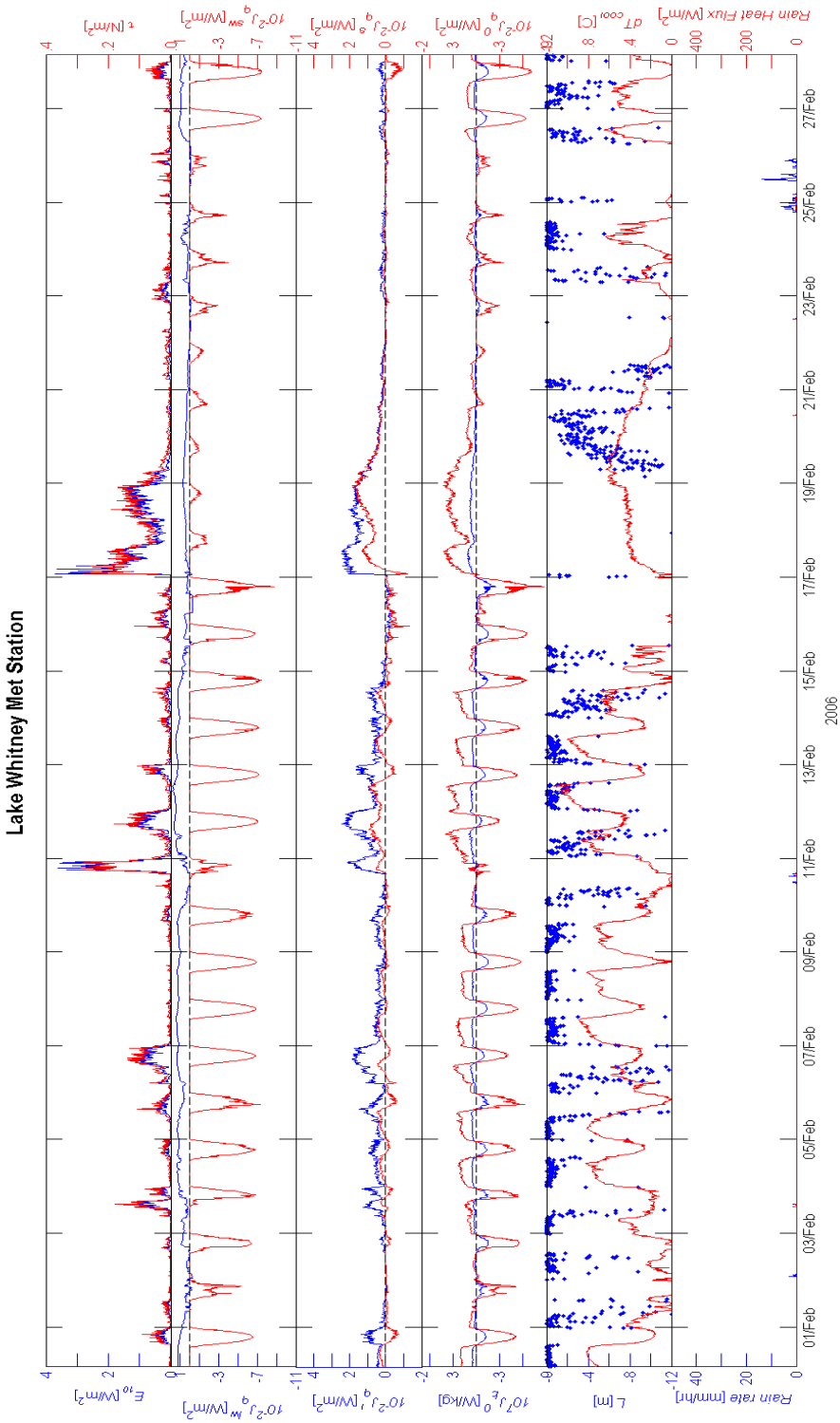

Fig A.7 February hourly averaged surface momentum and heat fluxes

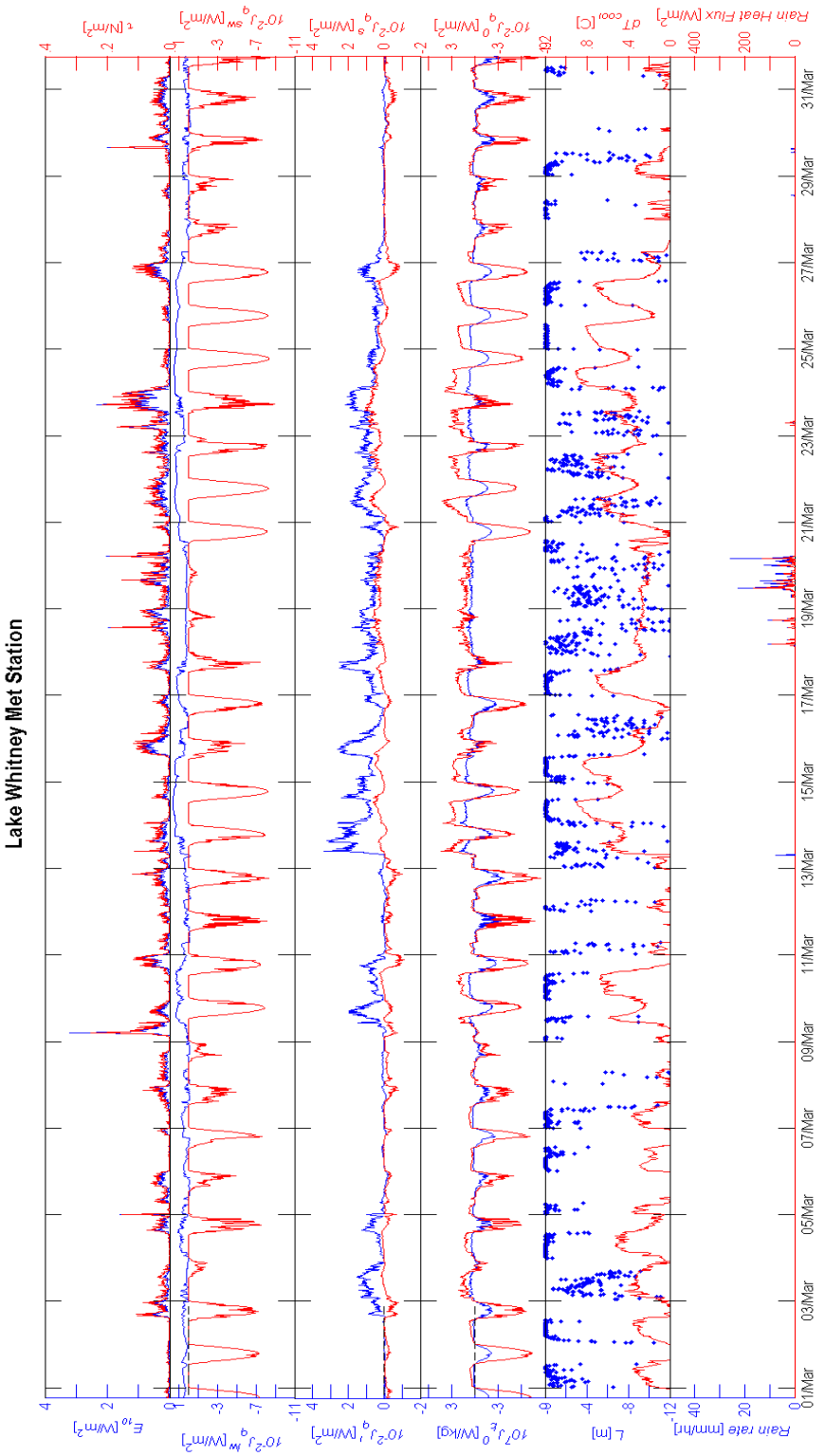

Fig A.8 March hourly averaged surface momentum and heat fluxes

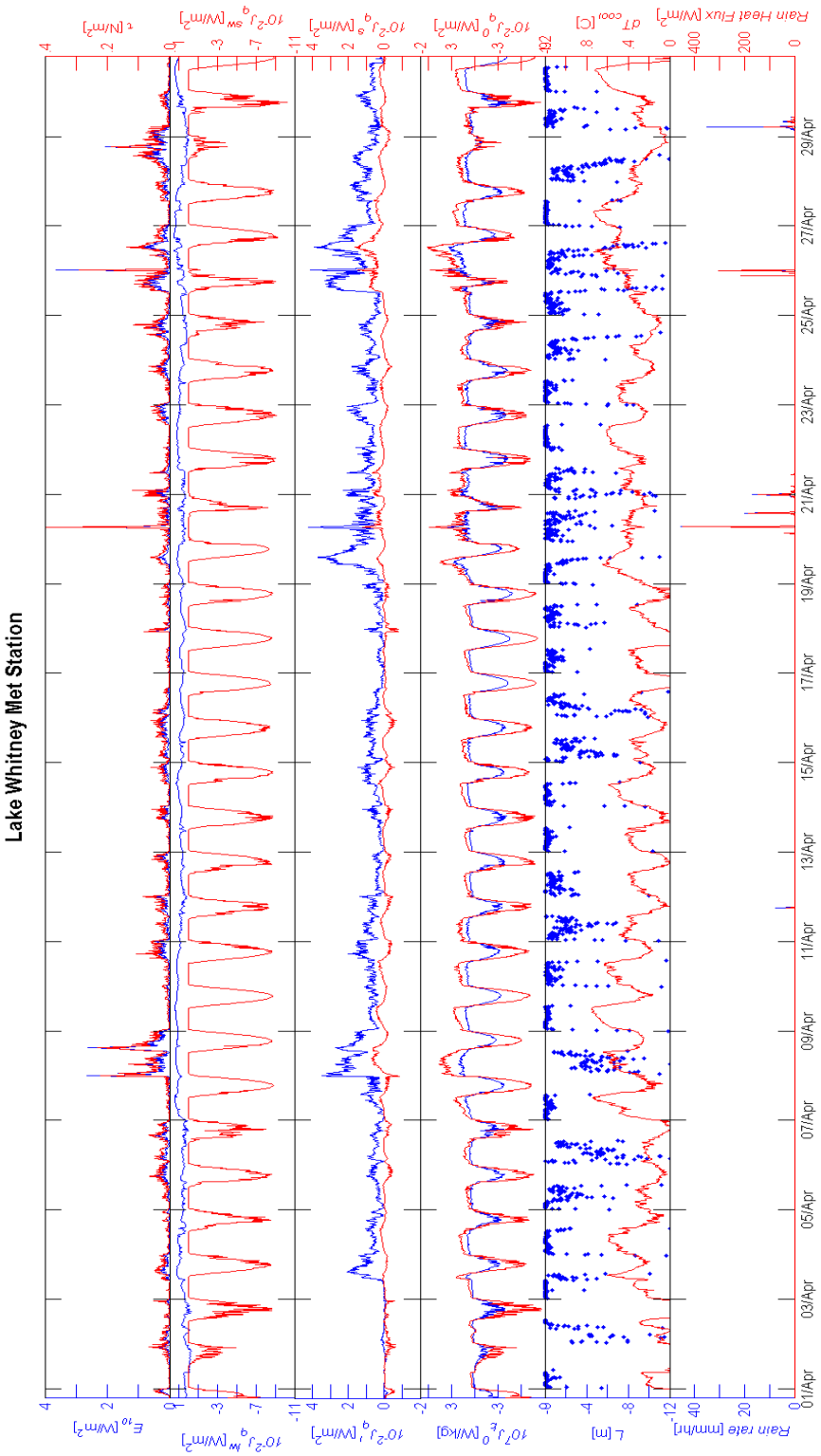

Fig A.9 April hourly averaged surface momentum and heat fluxes

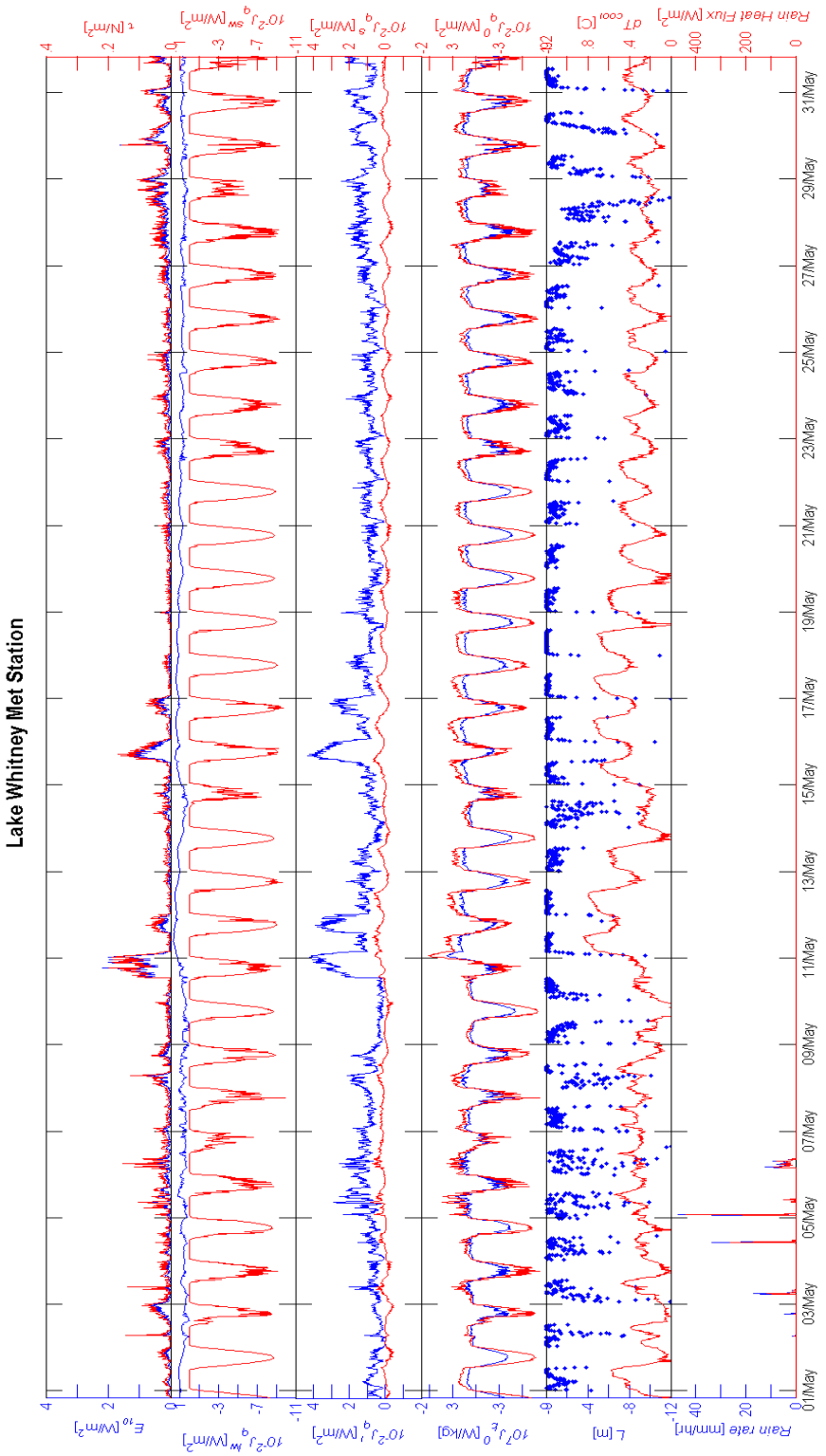

Fig A.10 May hourly averaged surface momentum and heat fluxes

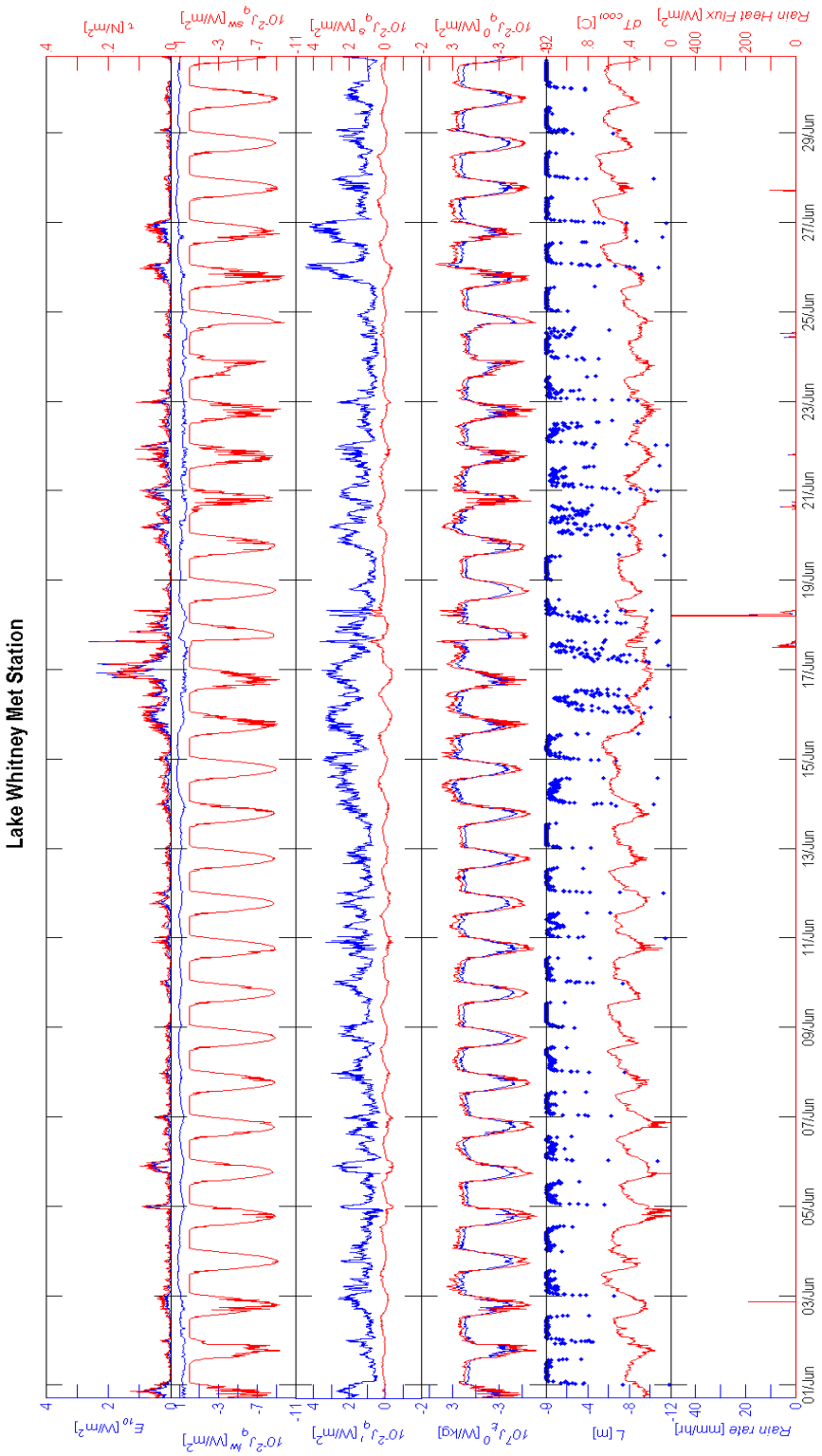

Fig A.11 June hourly averaged surface momentum and heat fluxes

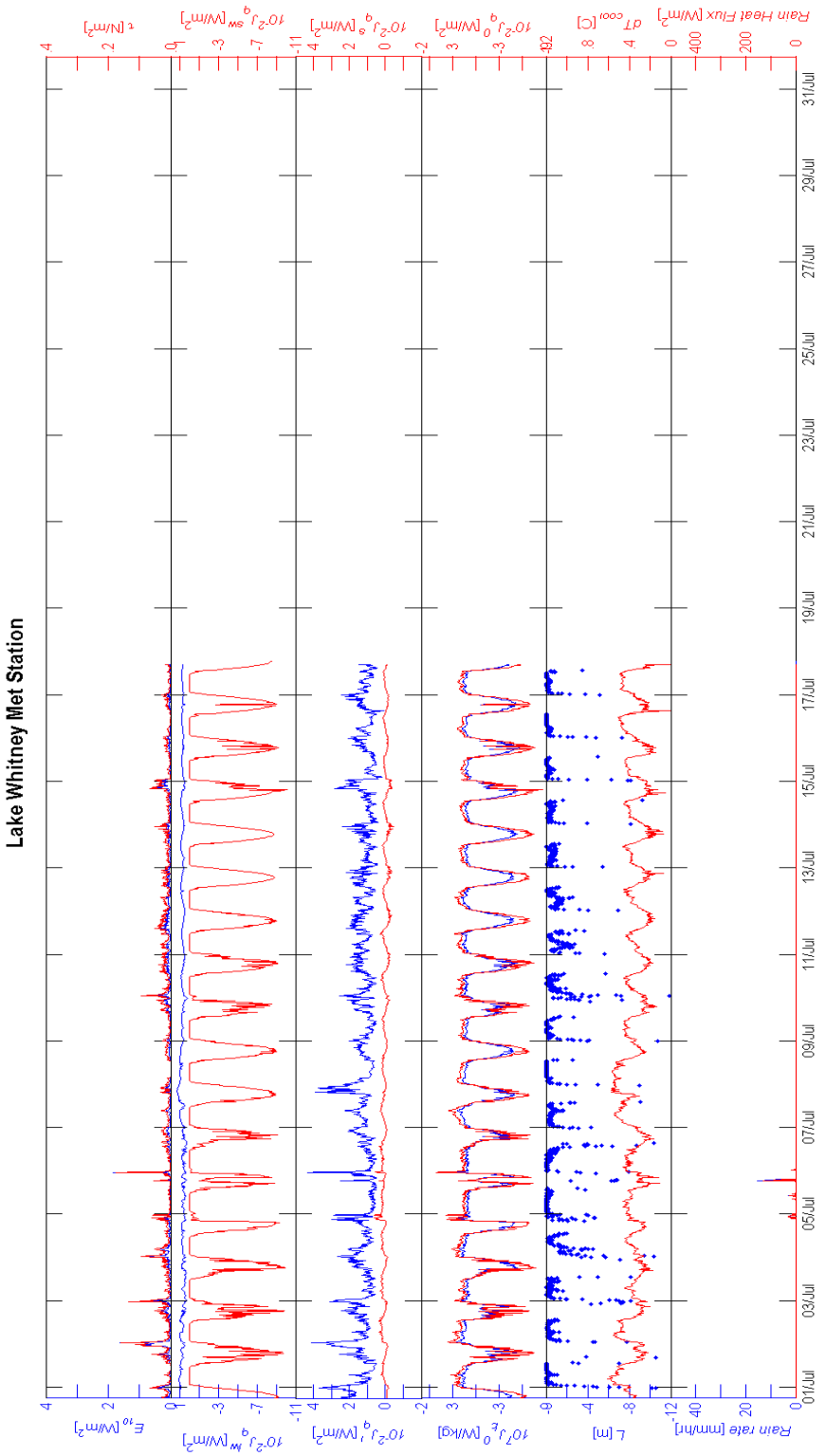

Fig A.12 July hourly averaged surface momentum and heat fluxes

A.3 Lake Whitney Thermal Structure

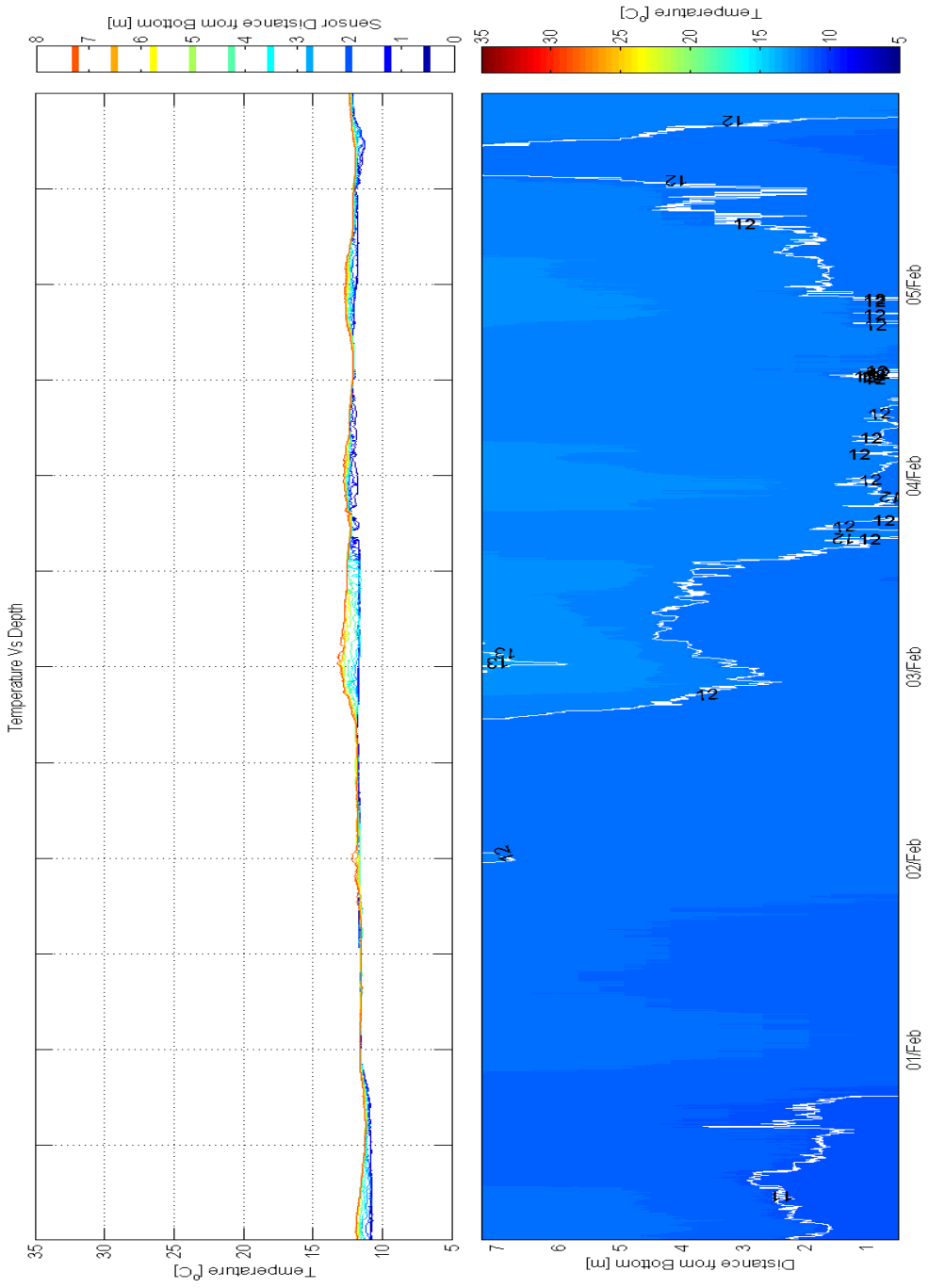

Fig A.13 Vertical thermal structure for week one of the study. Top panel is the temperature tracer at multiple depths. Bottom panel is a contour plot of the thermal structure

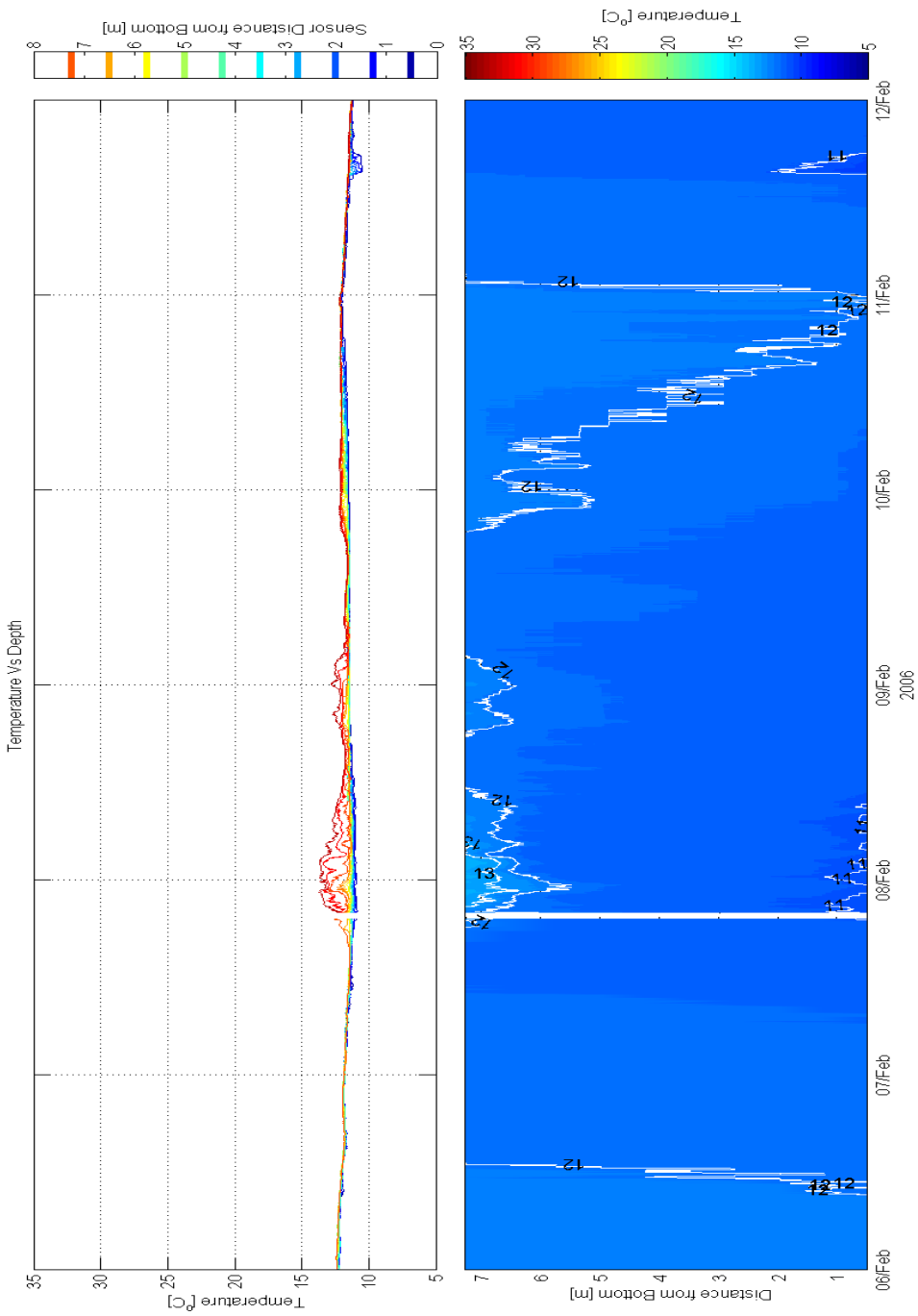

Fig A.14 Vertical thermal structure for week two of the study. Top panel is the temperature tracer at multiple depths. Bottom panel is a contour plot of the thermal structure

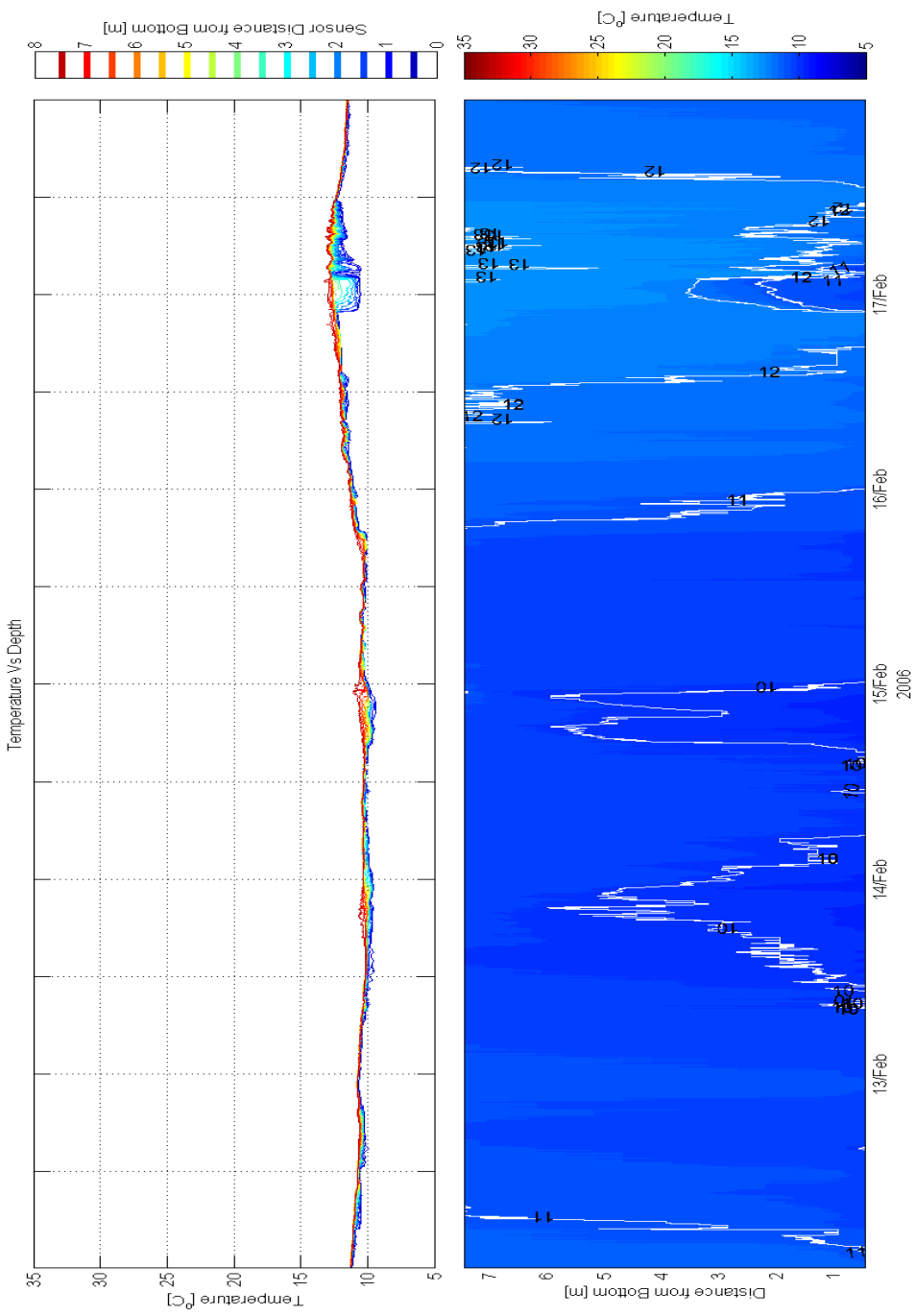

Fig A.15 Vertical thermal structure for week three of the study. Top panel is the temperature tracer at multiple depths. Bottom panel is a contour plot of the thermal structure

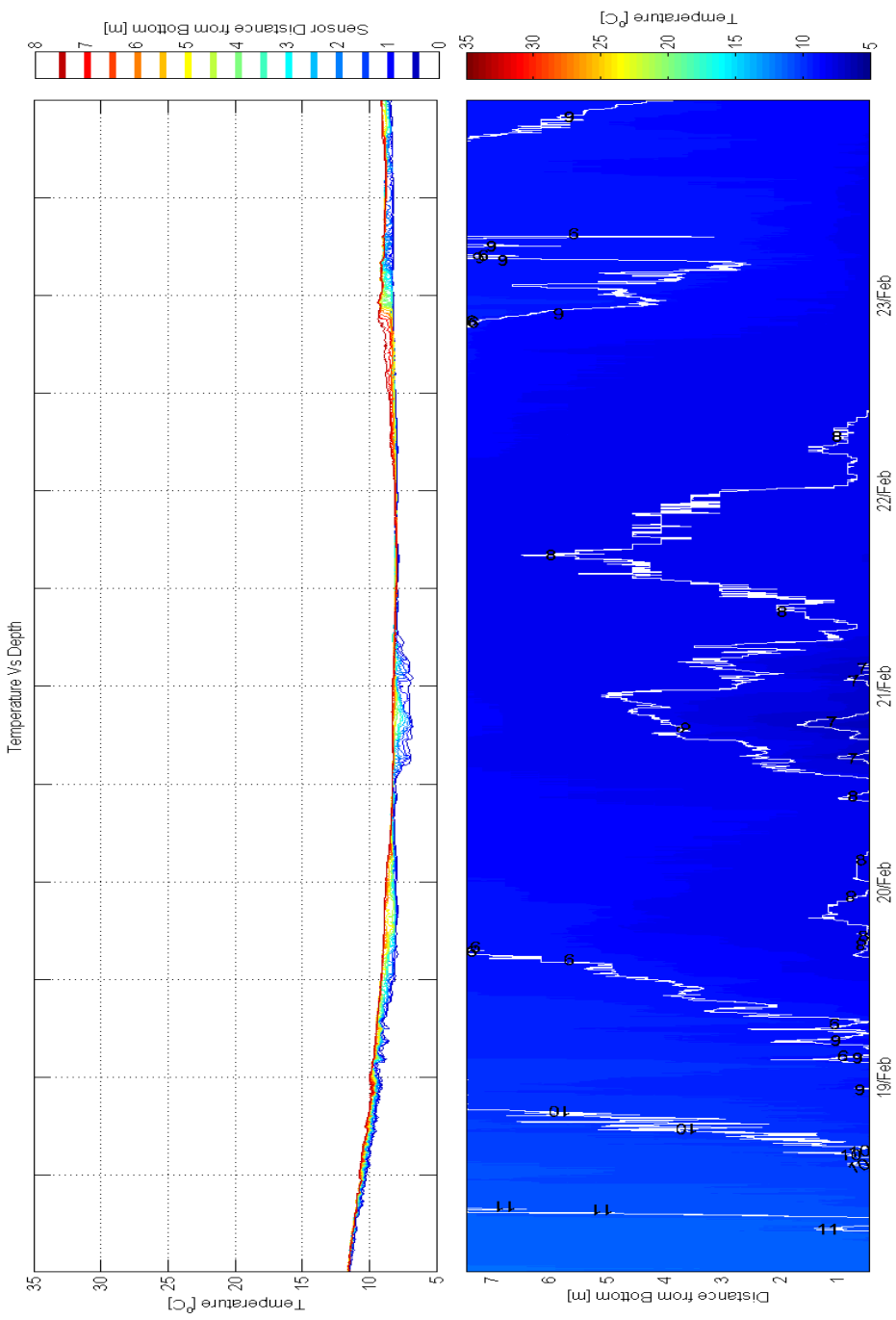

Fig A.16 Vertical thermal structure for week four of the study. Top panel is the temperature tracer at multiple depths. Bottom panel is a contour plot of the thermal structure

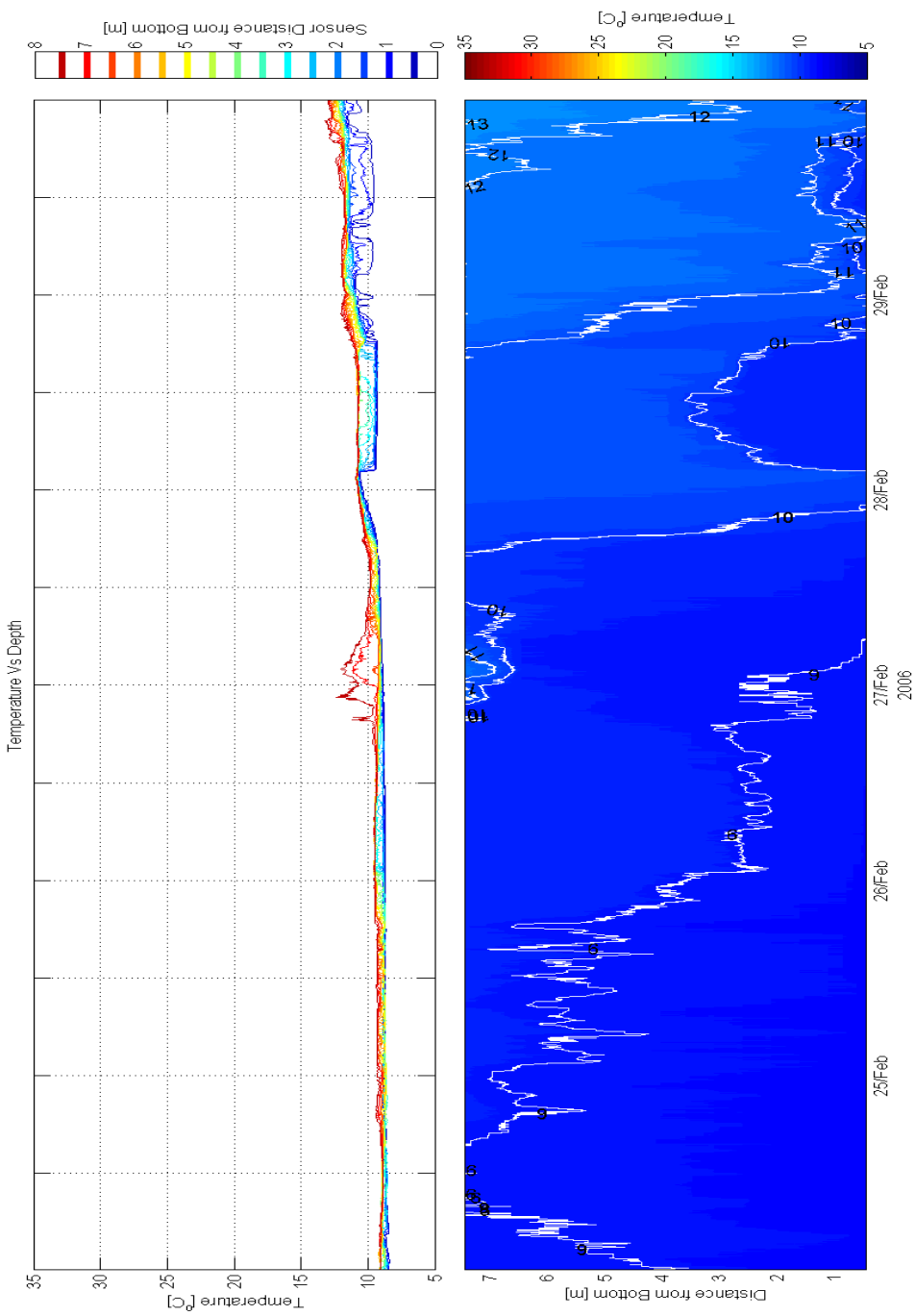

Fig A.17 Vertical thermal structure for week five of the study. Top panel is the temperature tracer at multiple depths. Bottom panel is a contour plot of the thermal structure

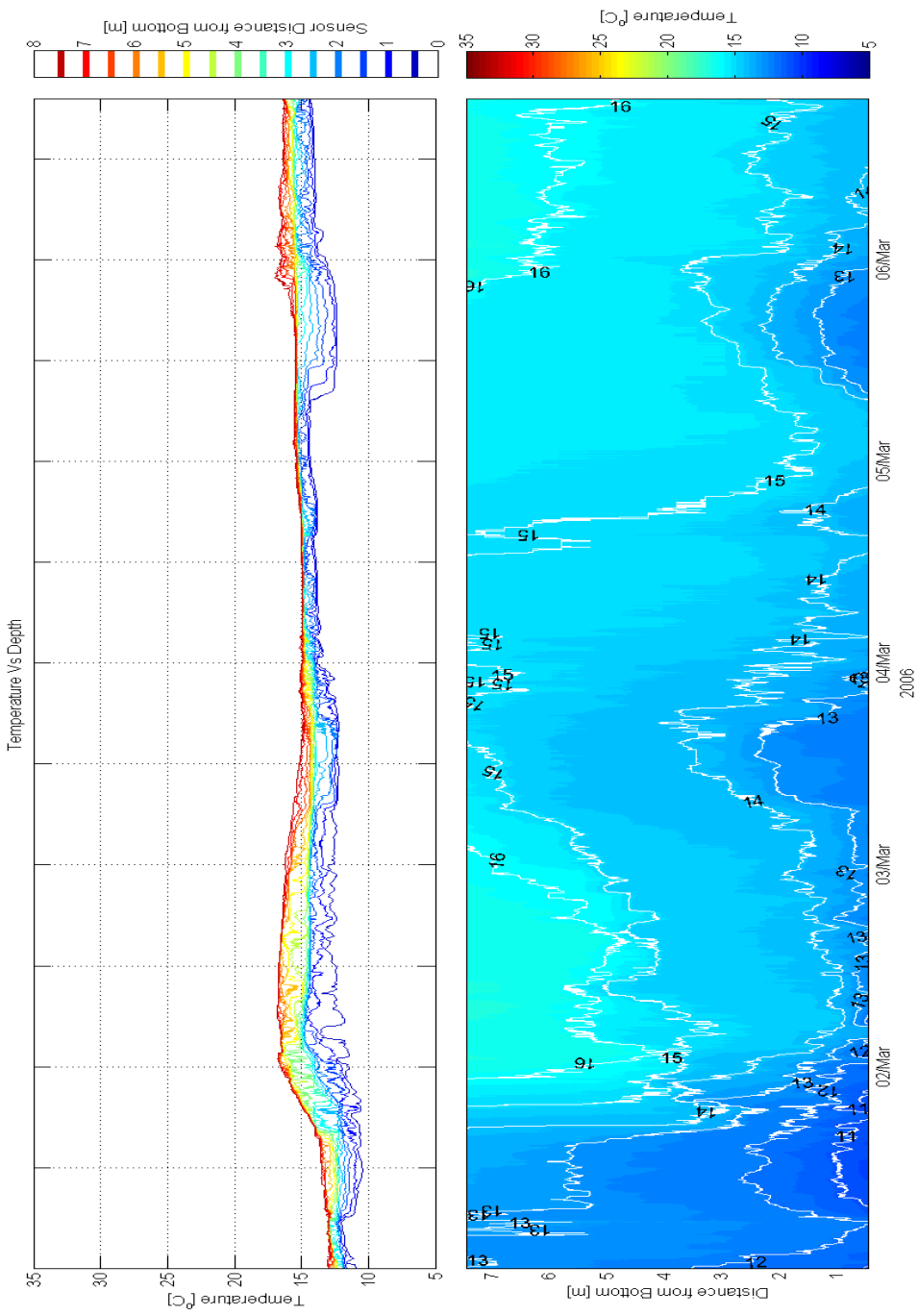

Fig A.18 Vertical thermal structure for week six of the study. Top panel is the temperature tracer at multiple depths. Bottom panel is a contour plot of the thermal structure

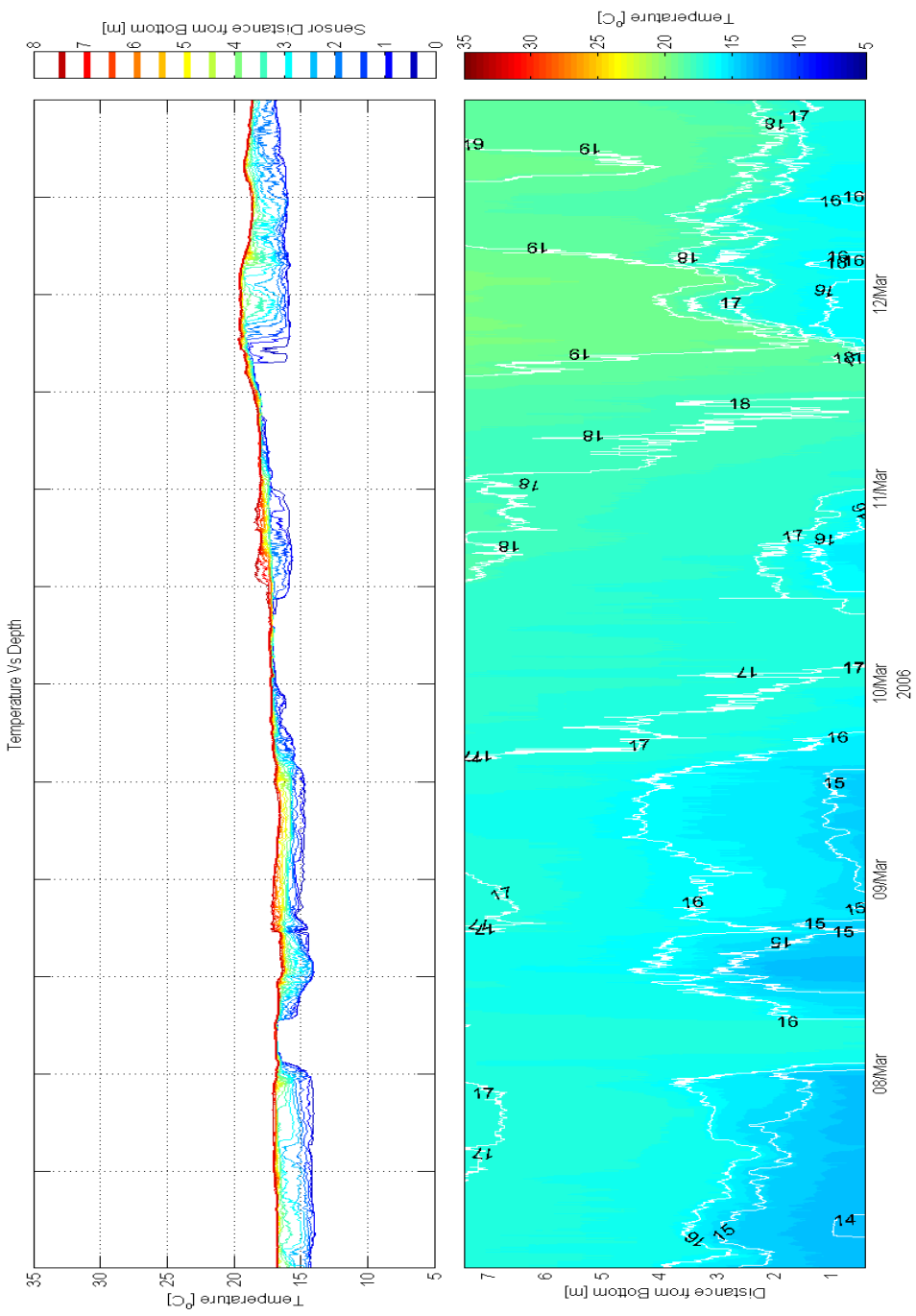

Fig A.19 Vertical thermal structure for week seven of the study. Top panel is the temperature tracer at multiple depths. Bottom panel is a contour plot of the thermal structure

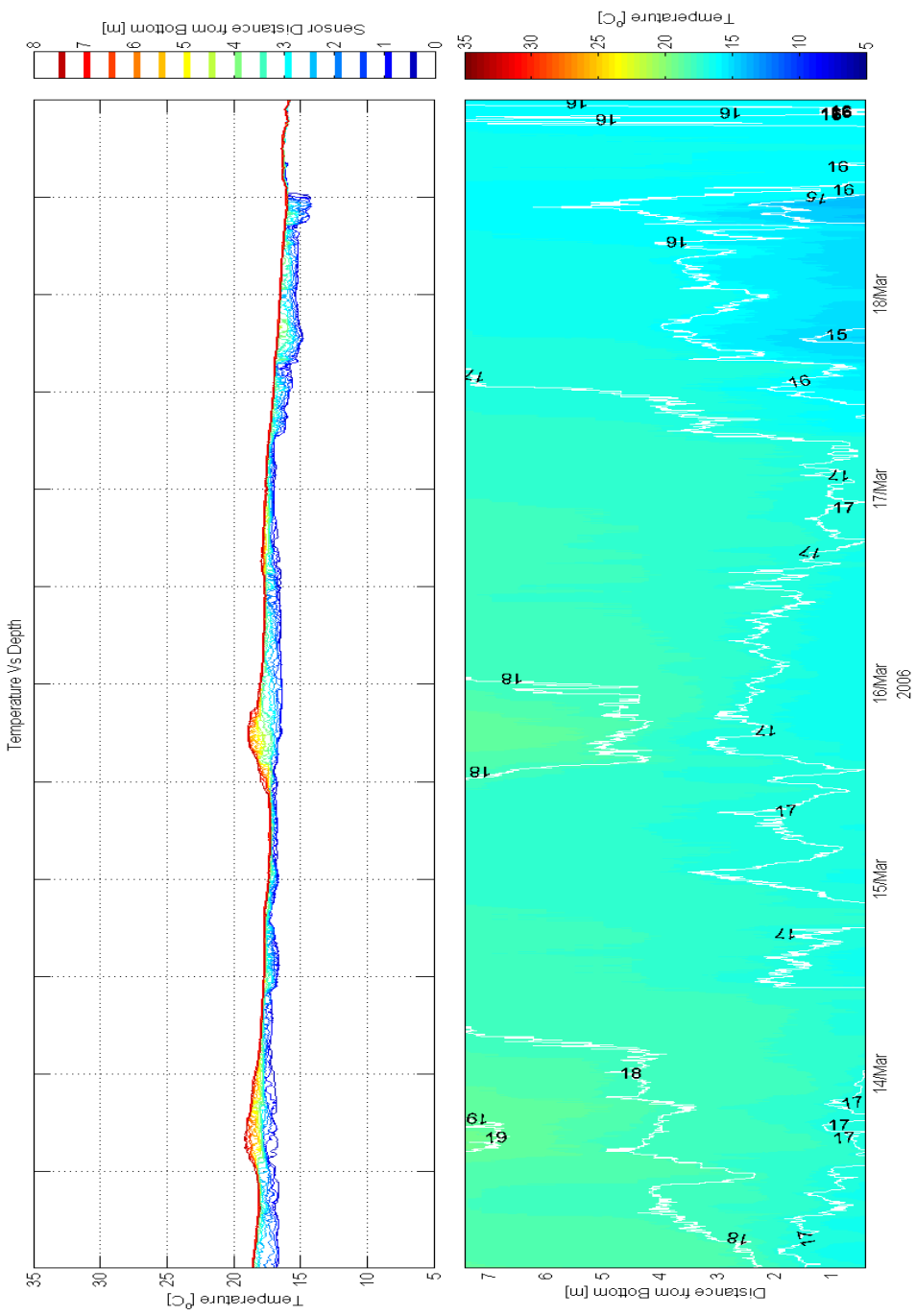

Fig A.20 Vertical thermal structure for week eight of the study. Top panel is the temperature tracer at multiple depths. Bottom panel is a contour plot of the thermal structure

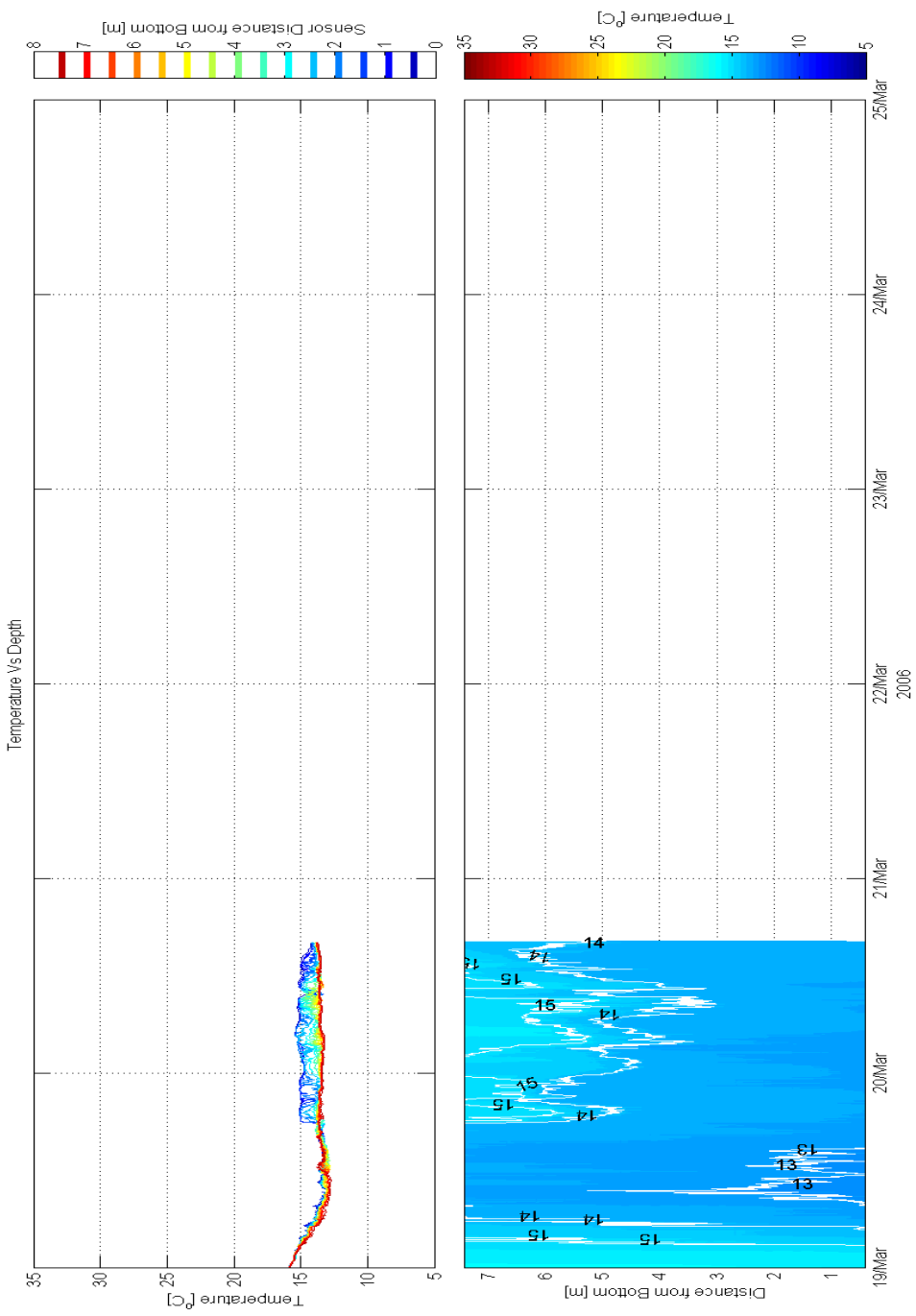

Fig A.21 Vertical thermal structure for week nine of the study. Top panel is the temperature tracer at multiple depths. Bottom panel is a contour plot of the thermal structure

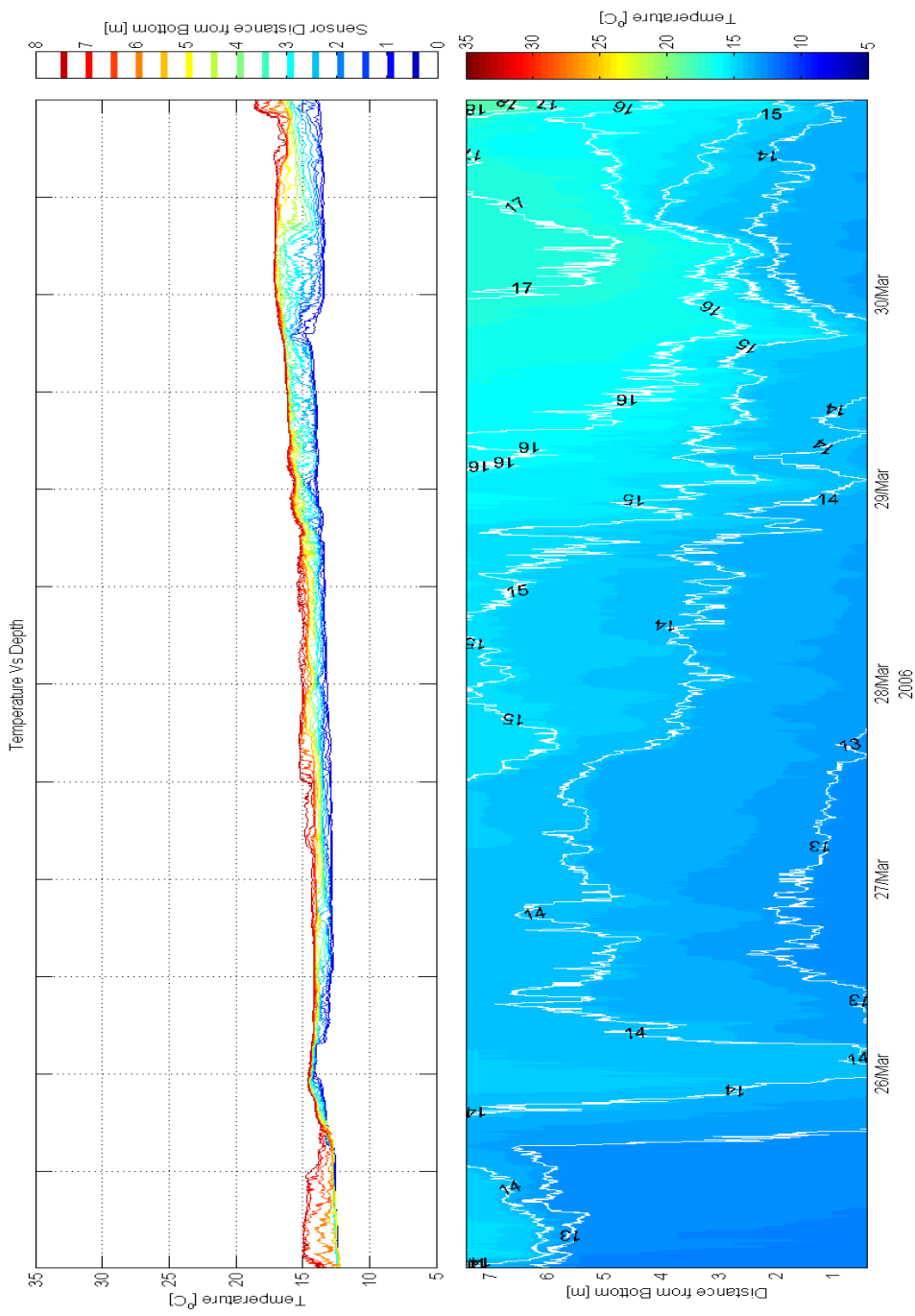

Fig A.22 Vertical thermal structure for week ten of the study. Top panel is the temperature tracer at multiple depths. Bottom panel is a contour plot of the thermal structure

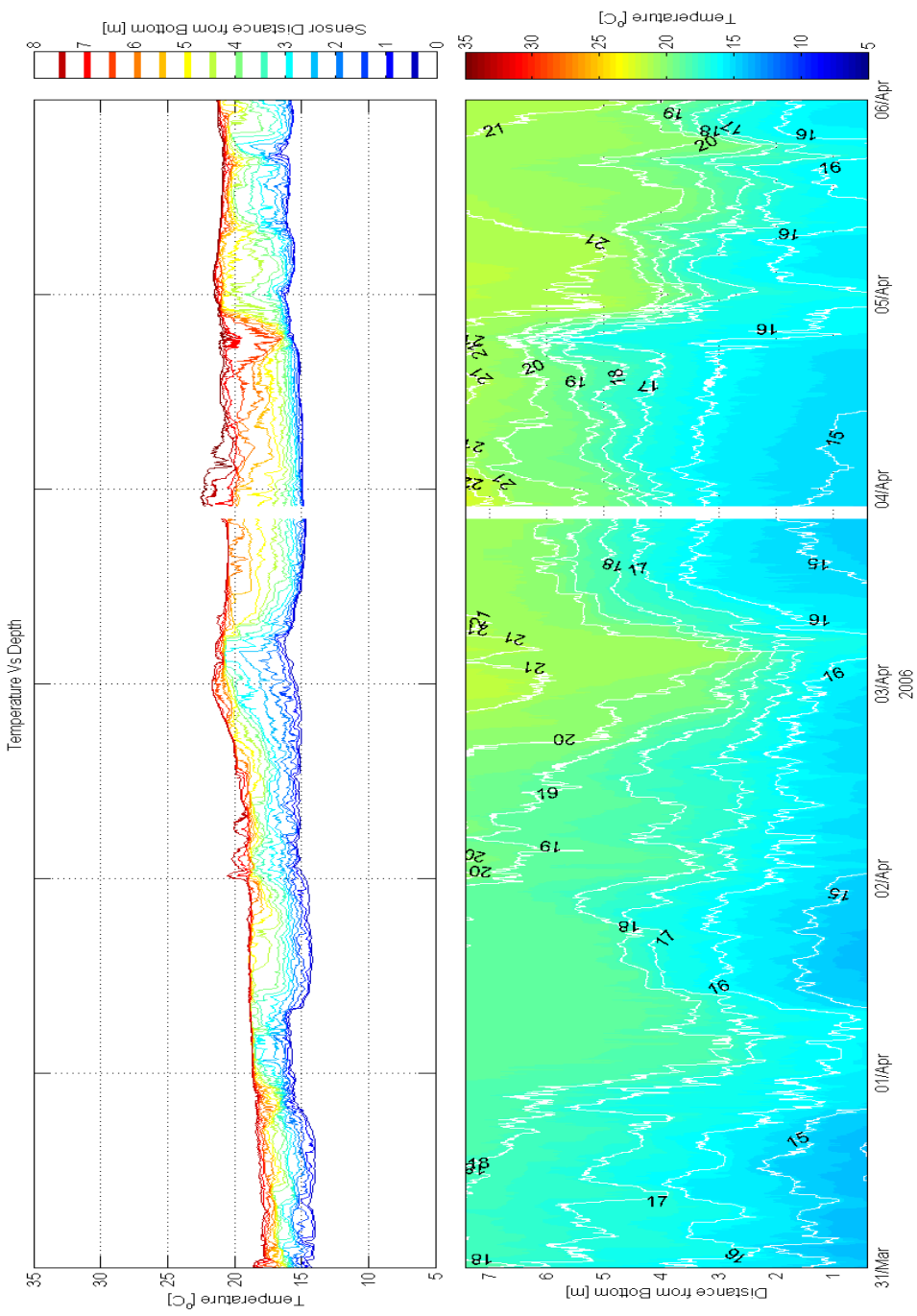

Fig A.23 Vertical thermal structure for week eleven of the study. Top panel is the temperature tracer at multiple depths. Bottom panel is a contour plot of the thermal structure

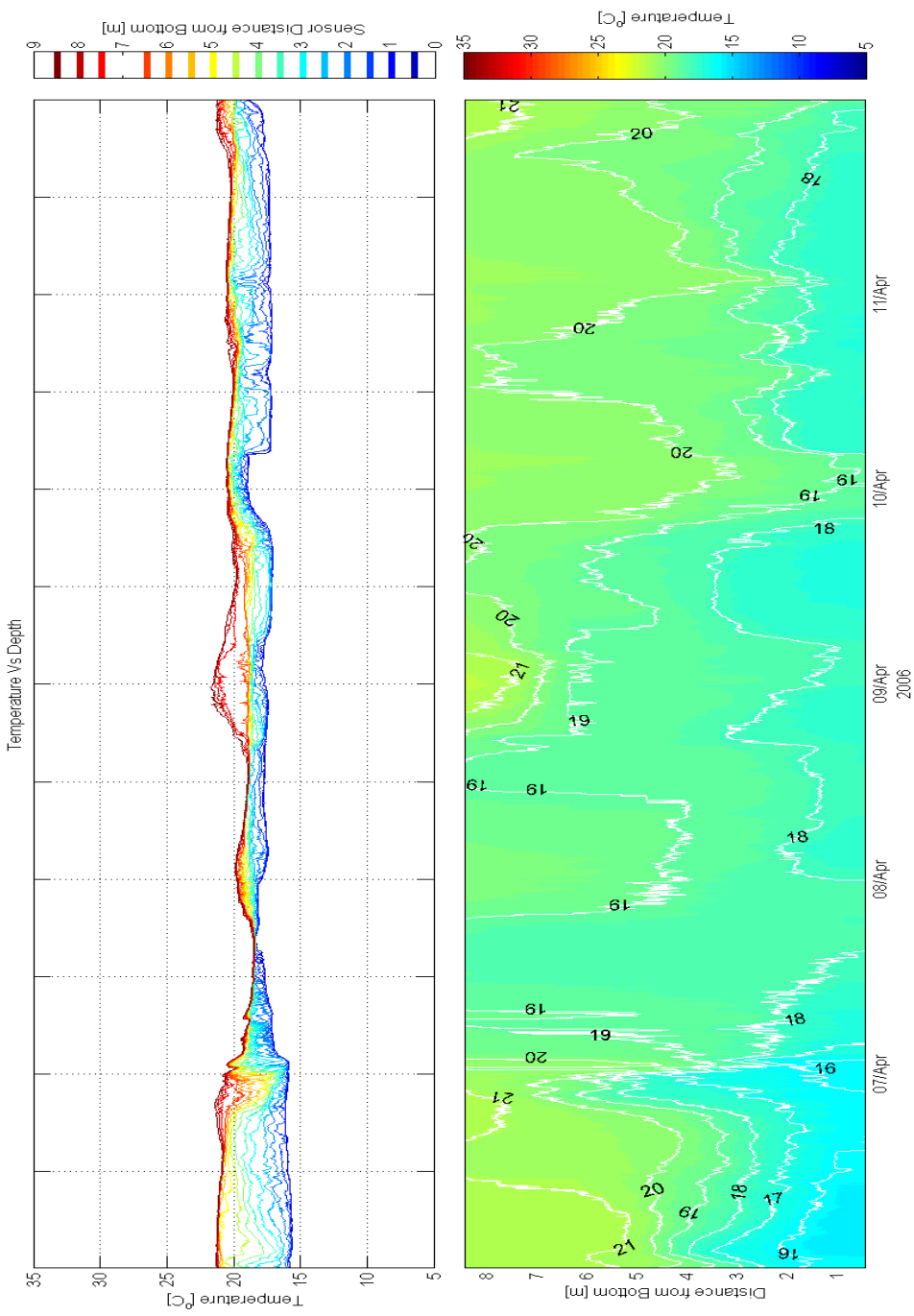

Fig A.24 Vertical thermal structure for week twelve of the study. Top panel is the temperature tracer at multiple depths. Bottom panel is a contour plot of the thermal structure

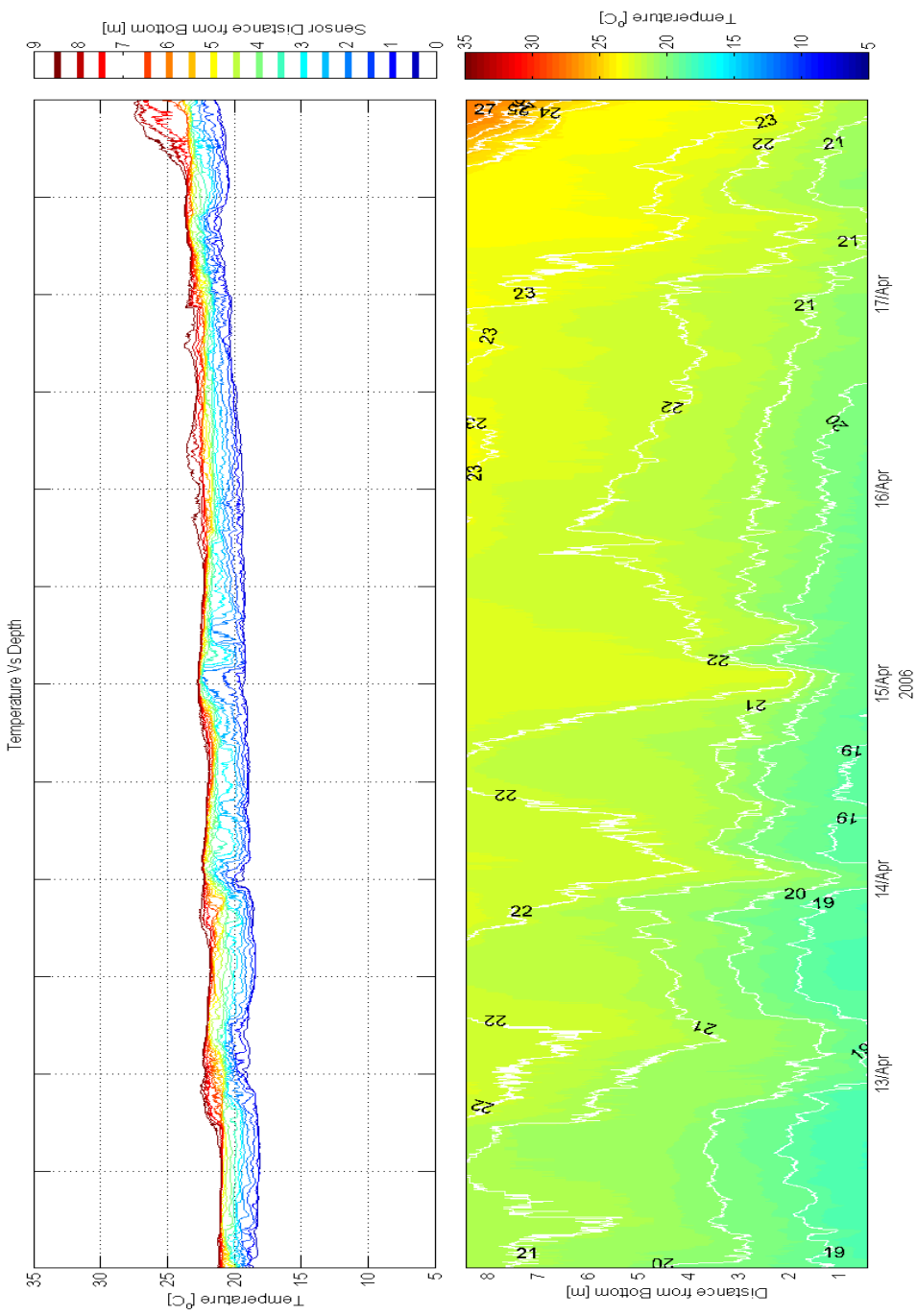

Fig A.25 Vertical thermal structure for week thirteen of the study. Top panel is the temperature tracer at multiple depths. Bottom panel is a contour plot of the thermal structure

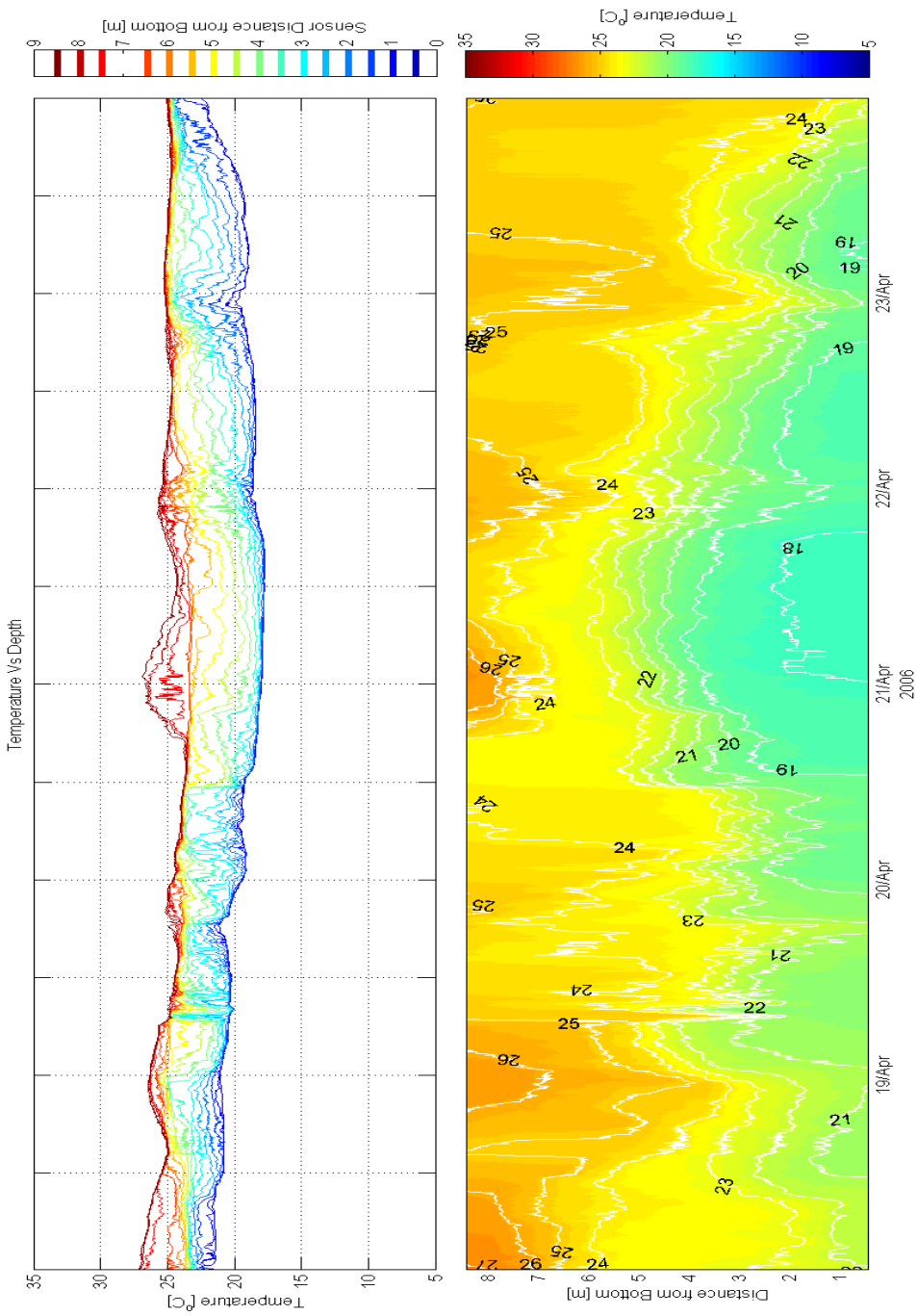

Fig A.26 Vertical thermal structure for week fourteen of the study. Top panel is the temperature tracer at multiple depths. Bottom panel is a contour plot of the thermal structure

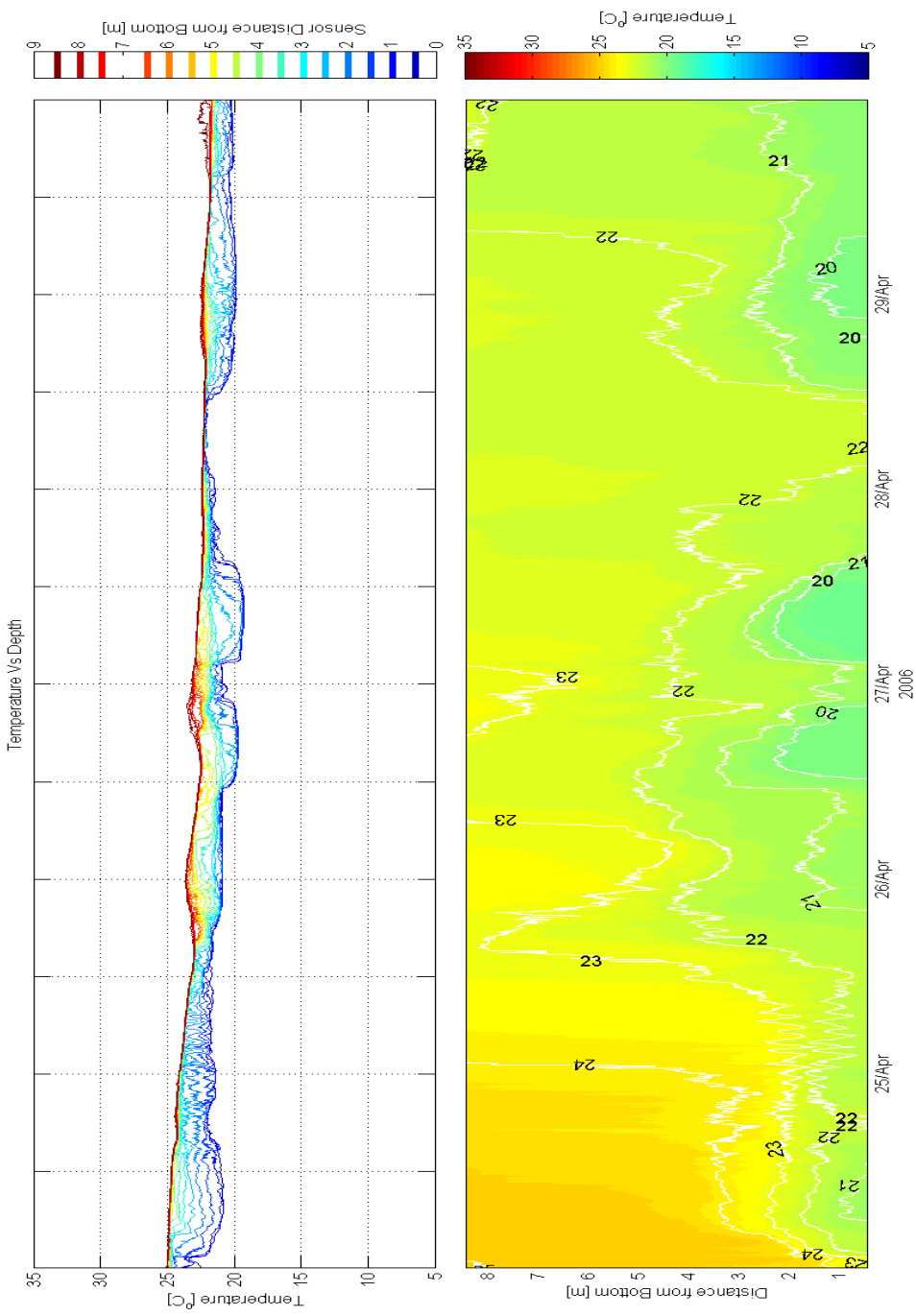

Fig A.27 Vertical thermal structure for week fifteen of the study. Top panel is the temperature tracer at multiple depths. Bottom panel is a contour plot of the thermal structure

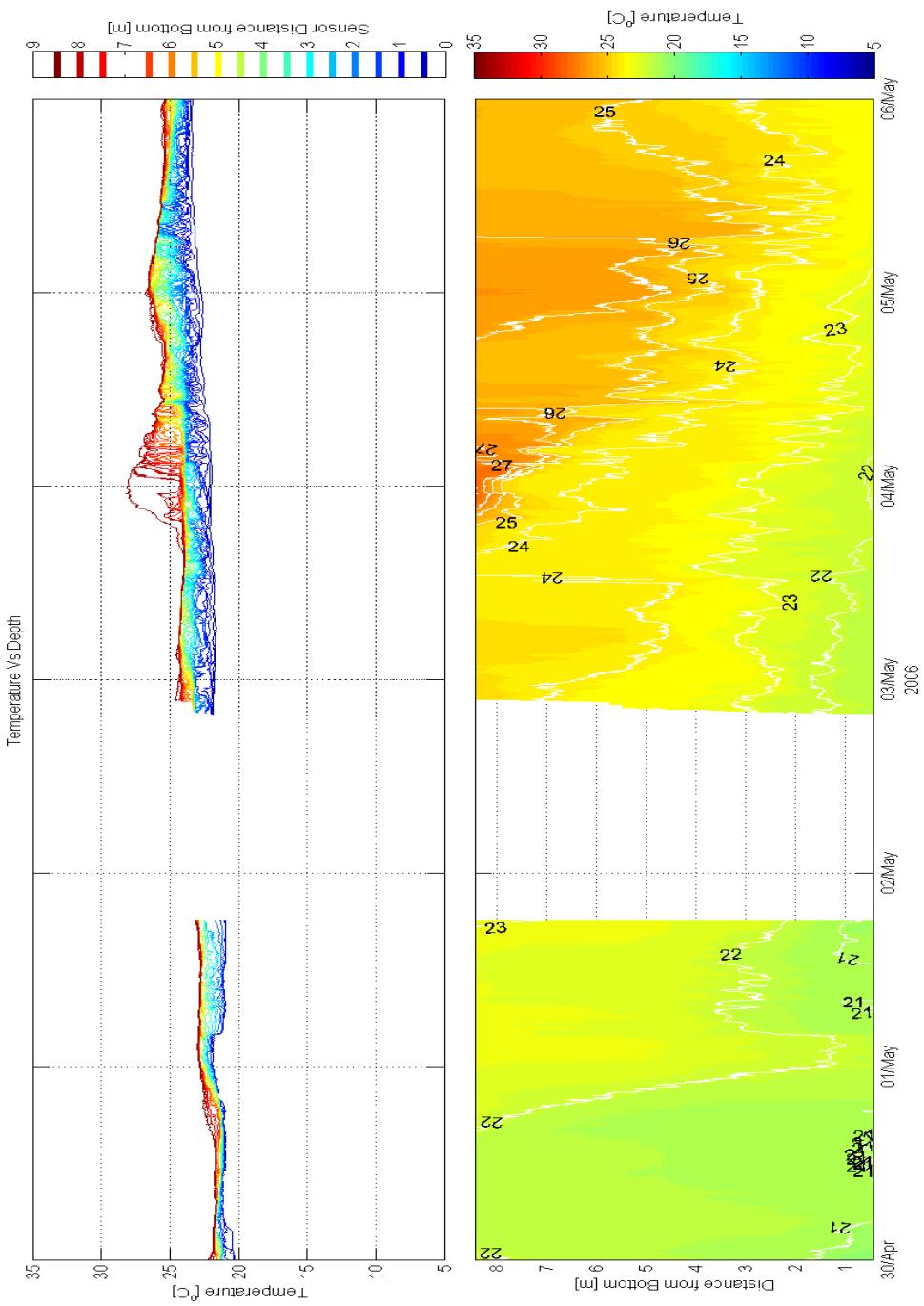

Fig A.28 Vertical thermal structure for week sixteen of the study. Top panel is the temperature tracer at multiple depths. Bottom panel is a contour plot of the thermal structure

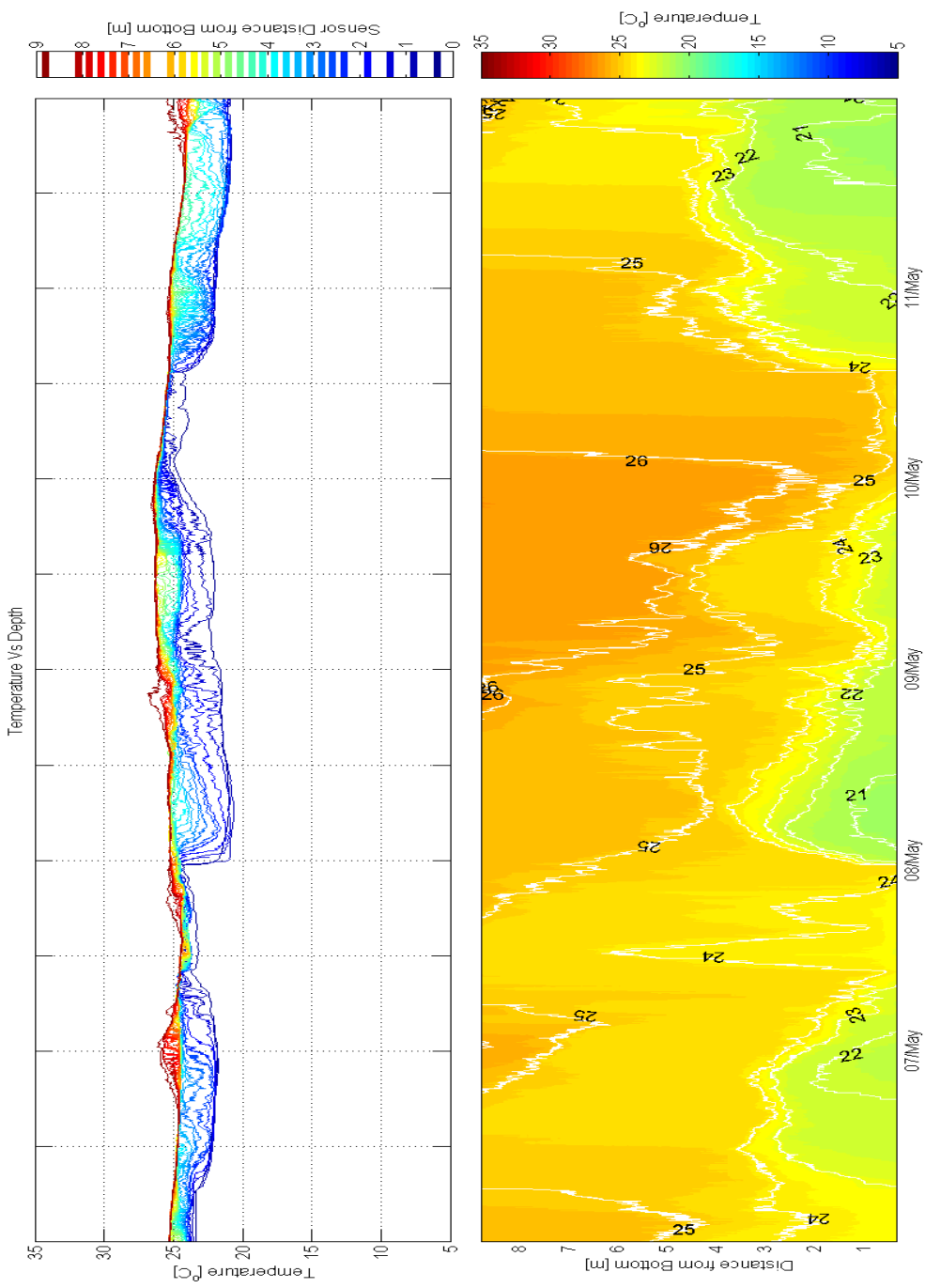

Fig A.29 Vertical thermal structure for week seventeen of the study. Top panel is the temperature tracer at multiple depths. Bottom panel is a contour plot of the thermal structure

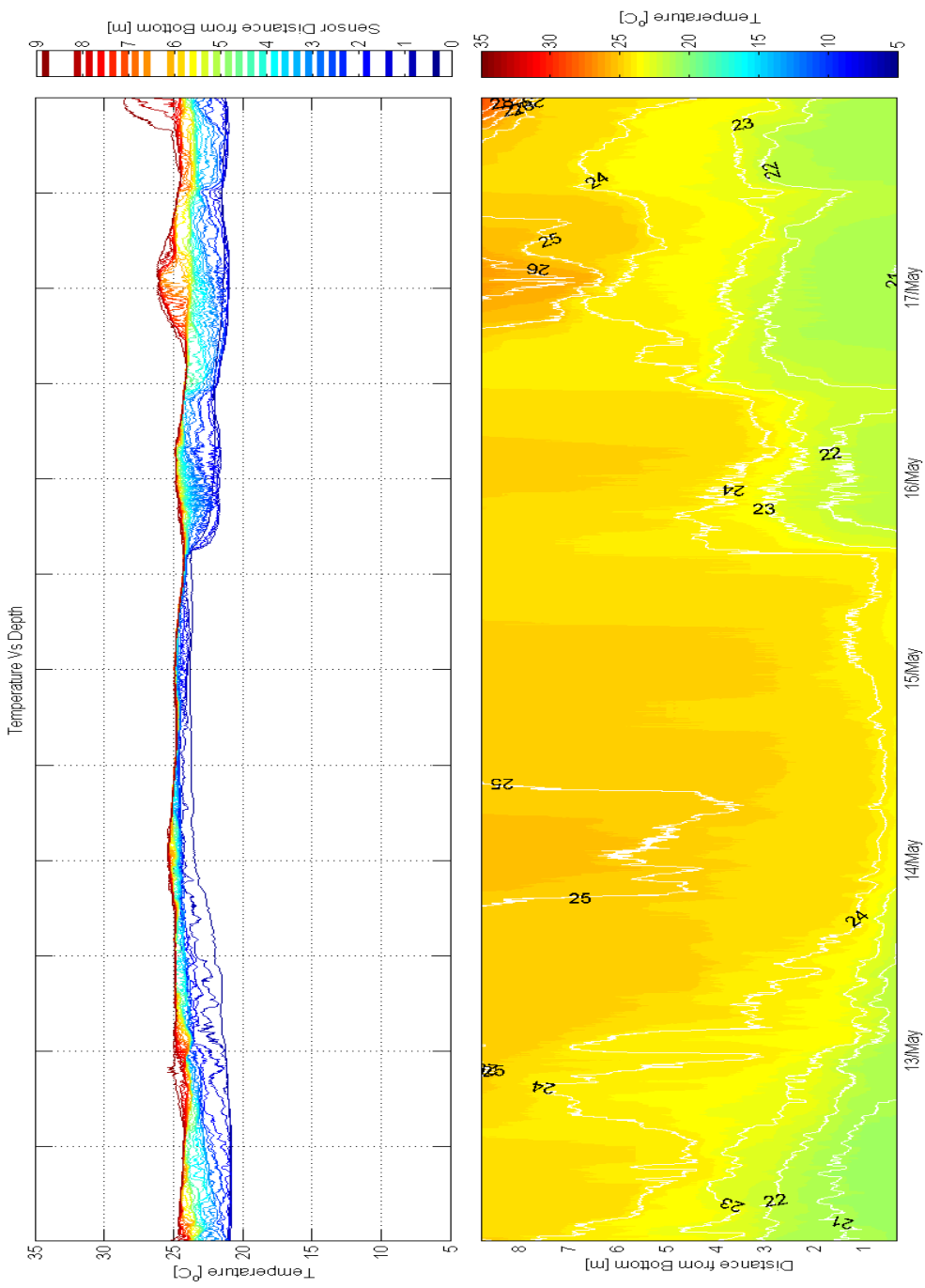

Fig A.30 Vertical thermal structure for week eighteen of the study. Top panel is the temperature tracer at multiple depths. Bottom panel is a contour plot of the thermal structure

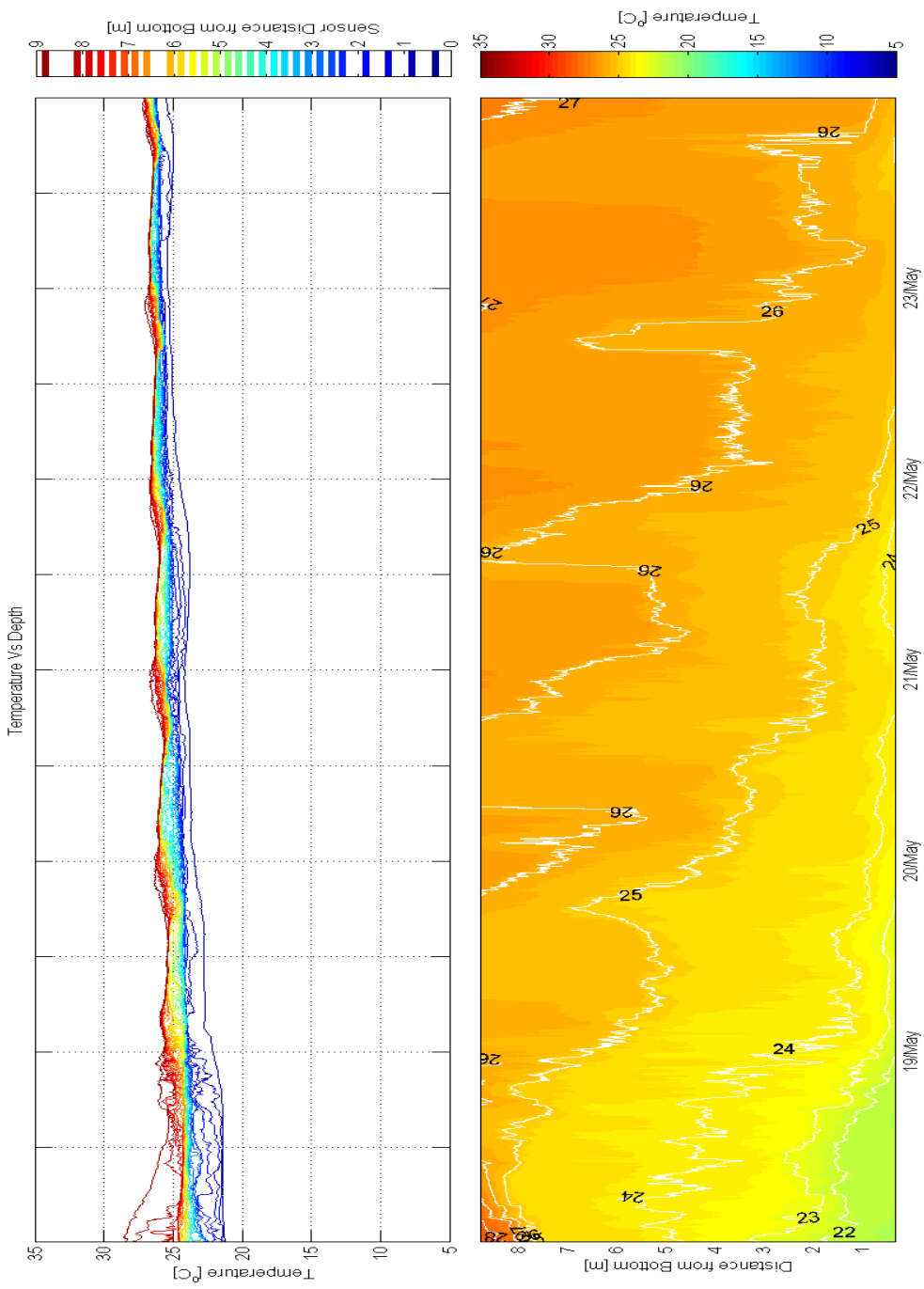

Fig A.31 Vertical thermal structure for week nineteen of the study. Top panel is the temperature tracer at multiple depths. Bottom panel is a contour plot of the thermal structure

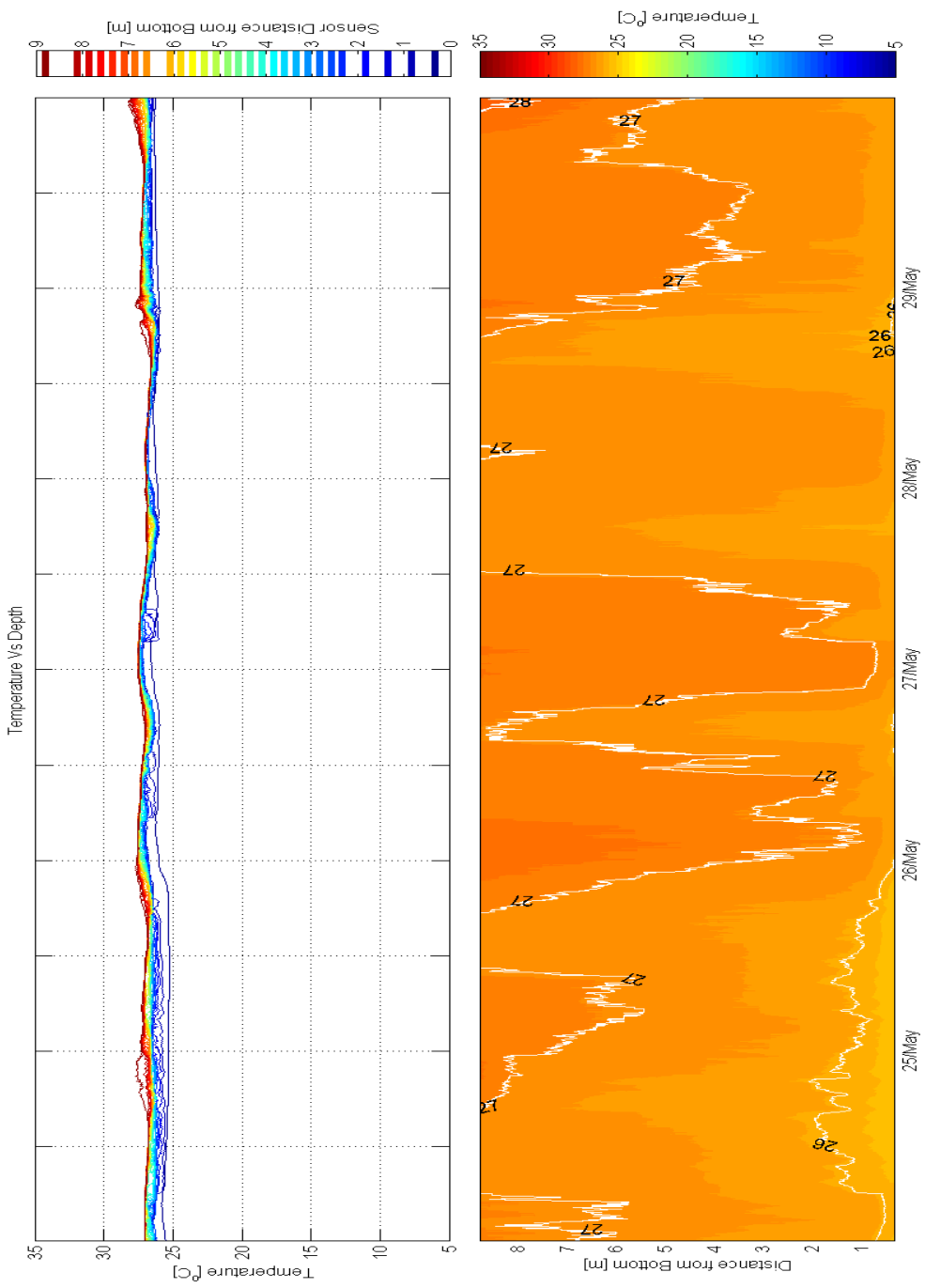

Fig A.32 Vertical thermal structure for week twenty of the study. Top panel is the temperature tracer at multiple depths. Bottom panel is a contour plot of the thermal structure

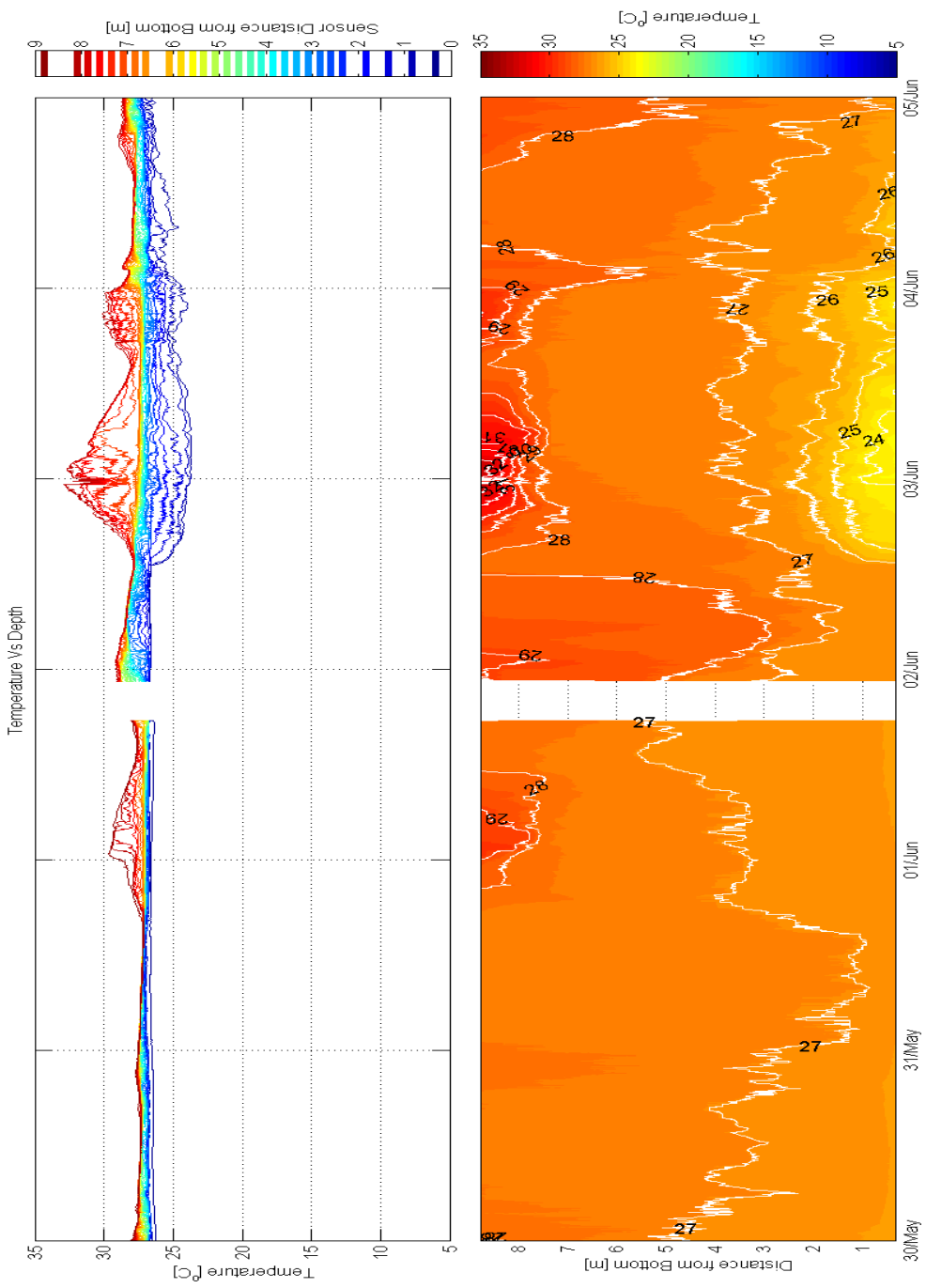

Fig A.33 Vertical thermal structure for week twenty-one of the study. Top panel is the temperature tracer at multiple depths. Bottom panel is a contour plot of the thermal structure

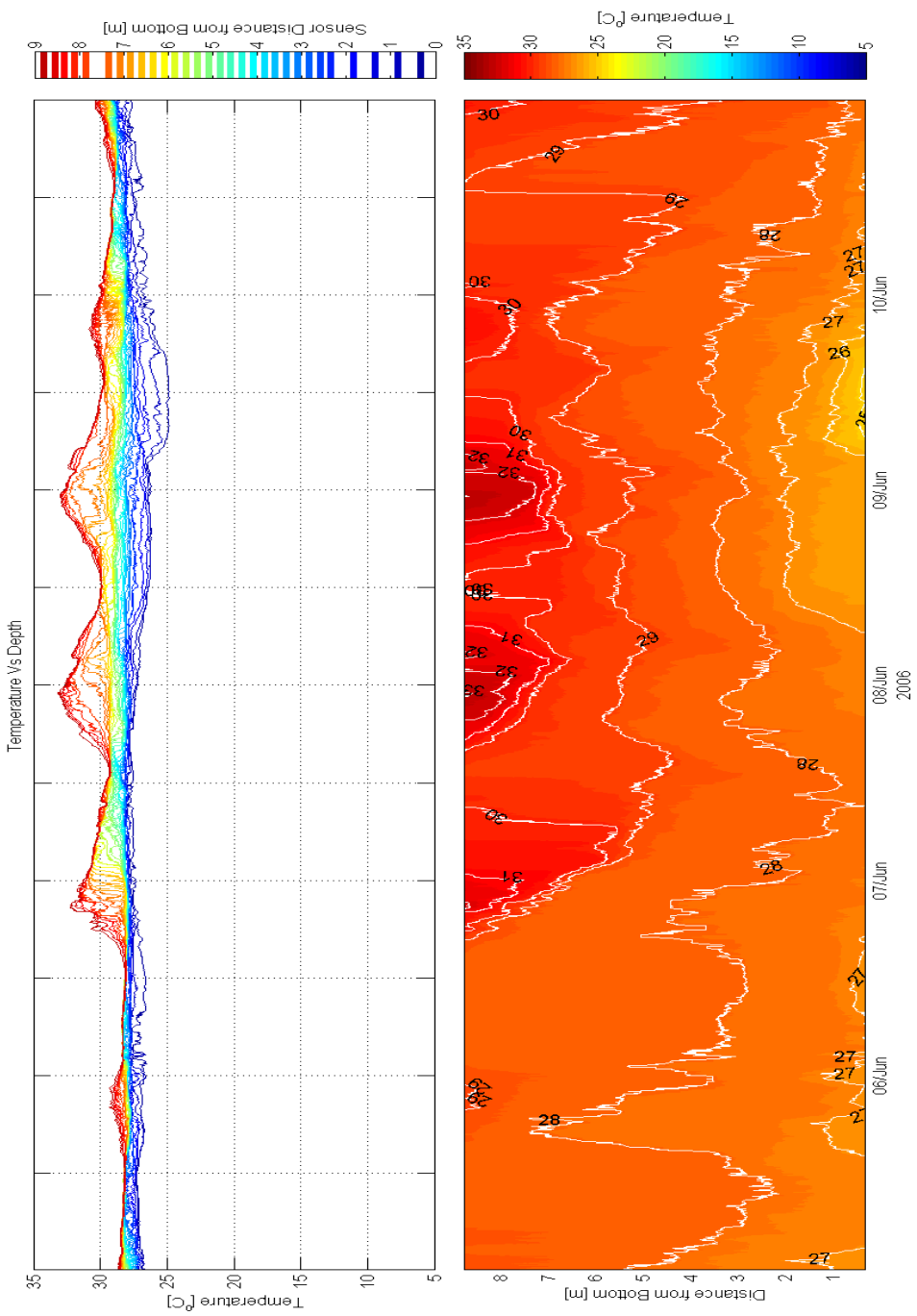

Fig A.34 Vertical thermal structure for week twenty-two of the study. Top panel is the temperature tracer at multiple depths. Bottom panel is a contour plot of the thermal structure

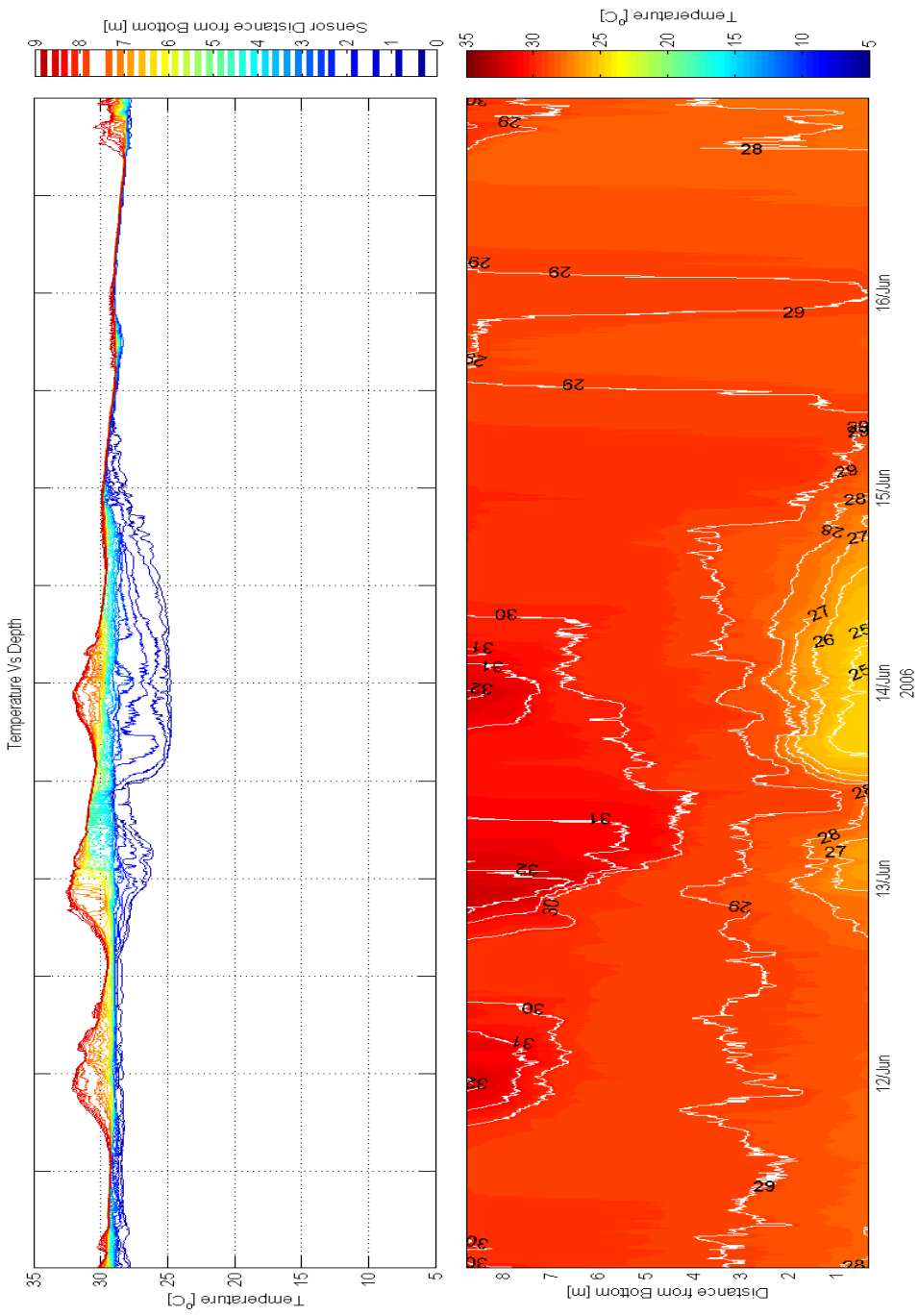

Fig A.35 Vertical thermal structure for week twenty-three of the study. Top panel is the temperature tracer at multiple depths. Bottom panel is a contour plot of the thermal structure

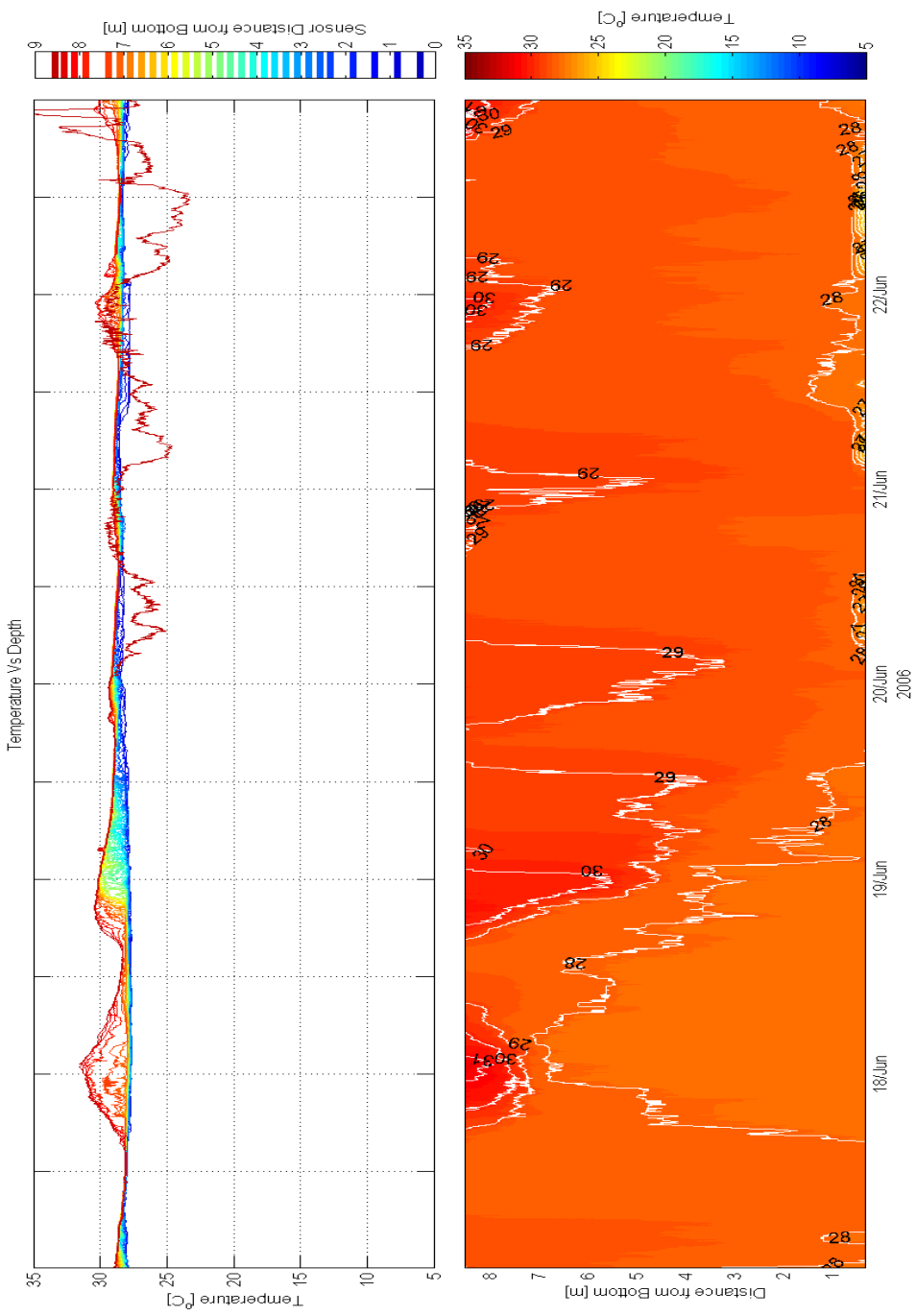

Fig A.36 Vertical thermal structure for week twenty-four of the study. Top panel is the temperature tracer at multiple depths. Bottom panel is a contour plot of the thermal structure

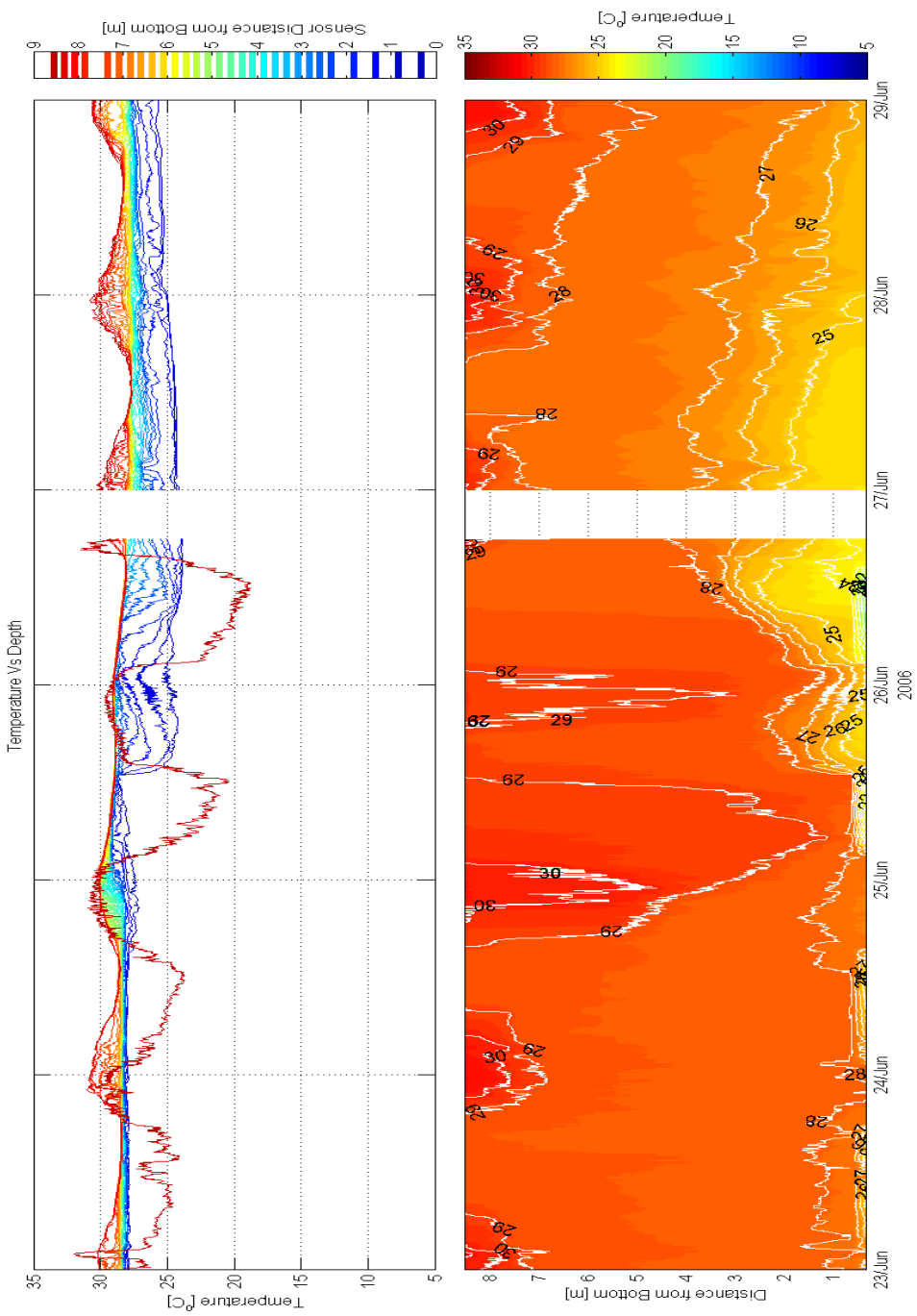

Fig A.37 Vertical thermal structure for week twenty-five of the study. Top panel is the temperature tracer at multiple depths. Bottom panel is a contour plot of the thermal structure

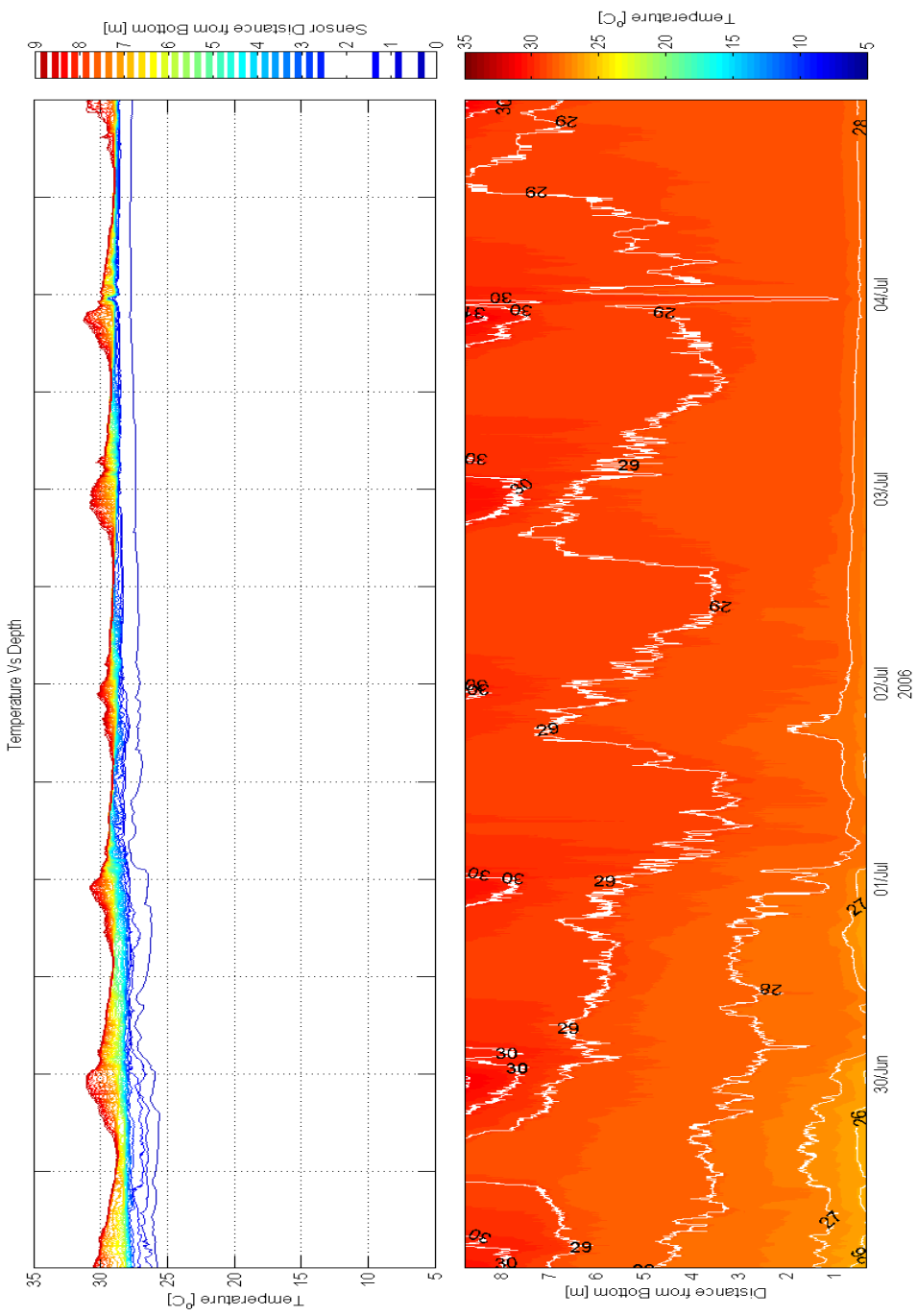

Fig A.38 Vertical thermal structure for week twenty-six of the study. Top panel is the temperature tracer at multiple depths. Bottom panel is a contour plot of the thermal structure

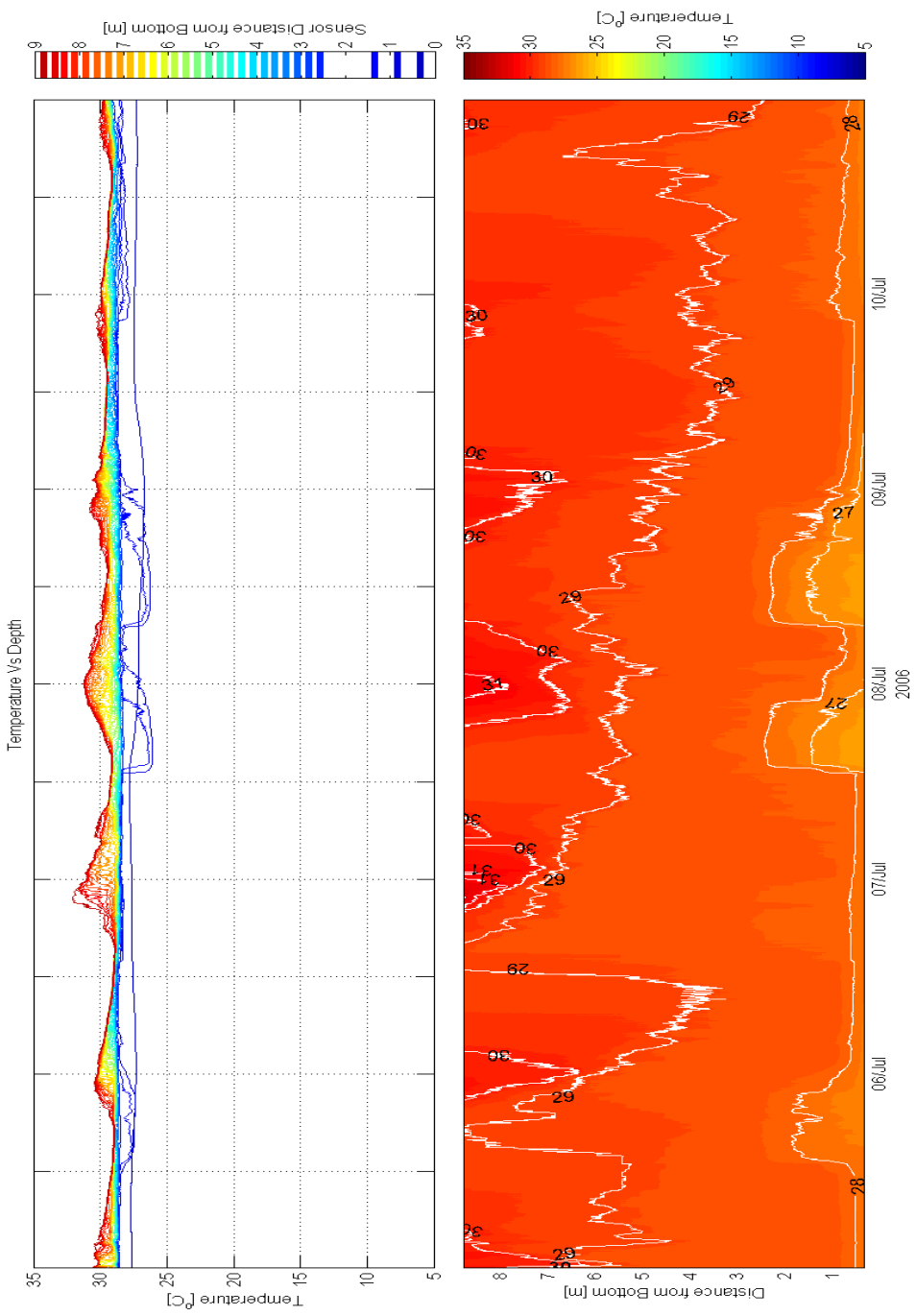

Fig A.39 Vertical thermal structure for week twenty-seven of the study. Top panel is the temperature tracer at multiple depths. Bottom panel is a contour plot of the thermal structure

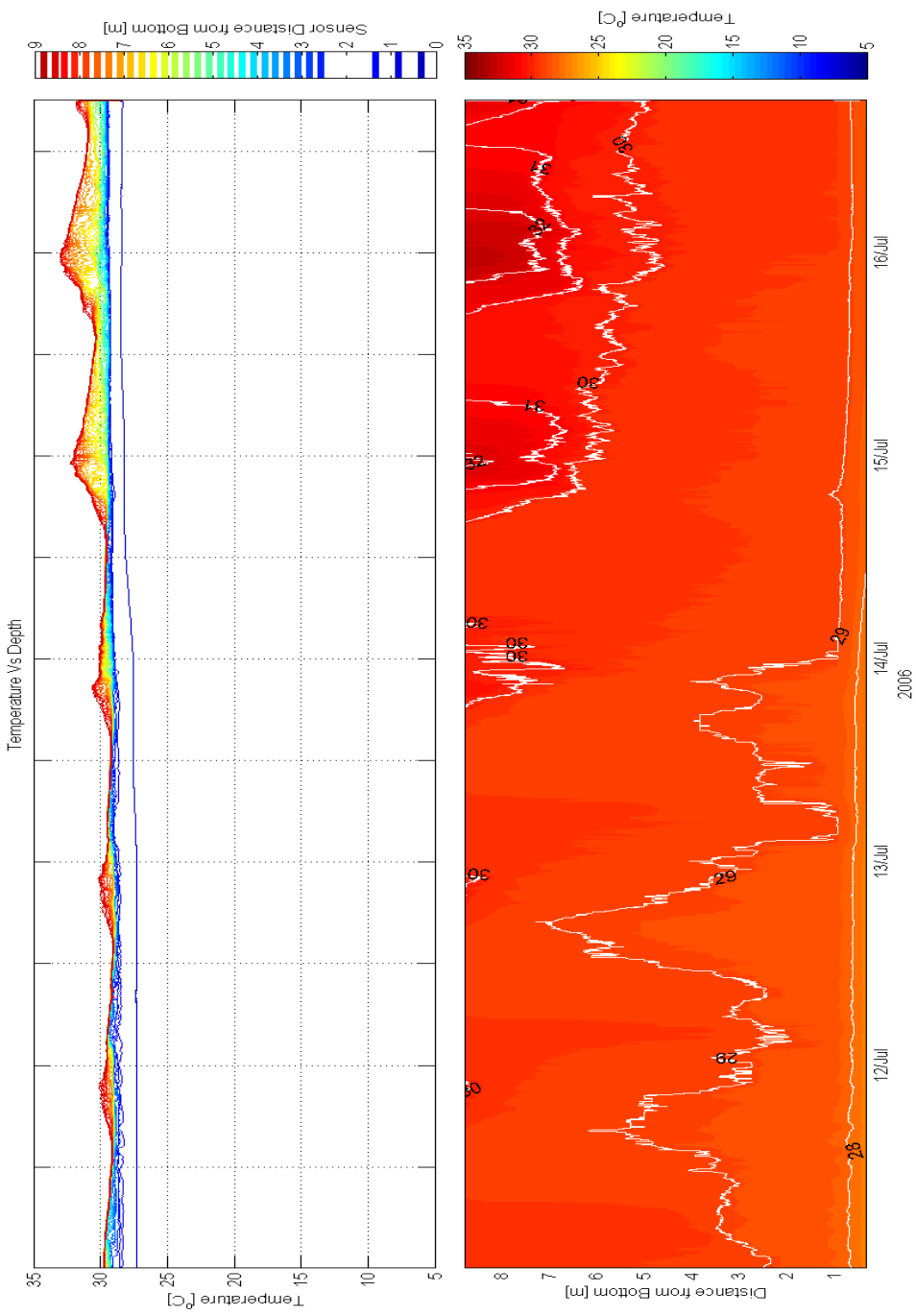

Fig A.40 Vertical thermal structure for week twenty-eight of the study. Top panel is the temperature tracer at multiple depths. Bottom panel is a contour plot of the thermal structure

A.4 Lake Whitney Current Structure

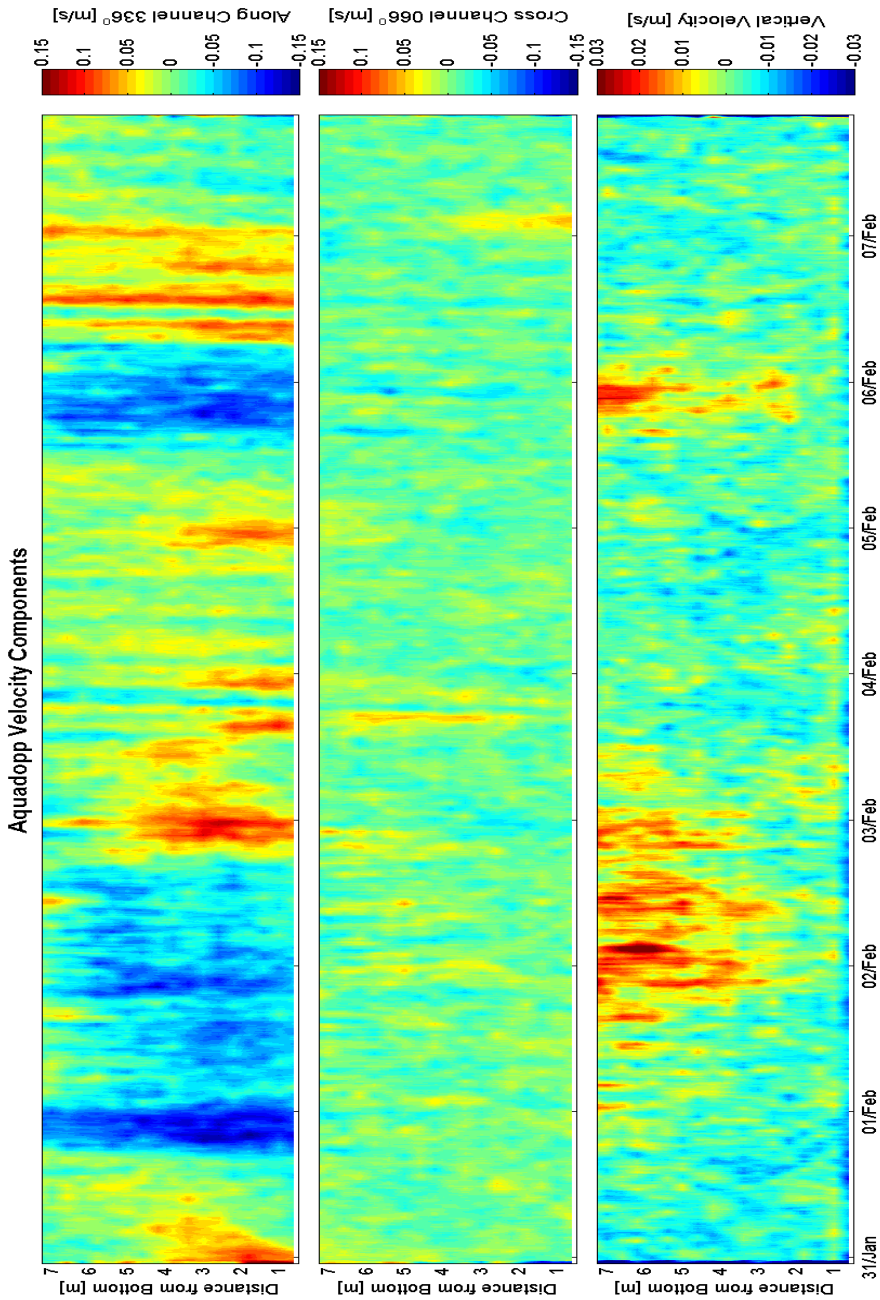

Fig A.41 Vertical velocity structure for week one of the study

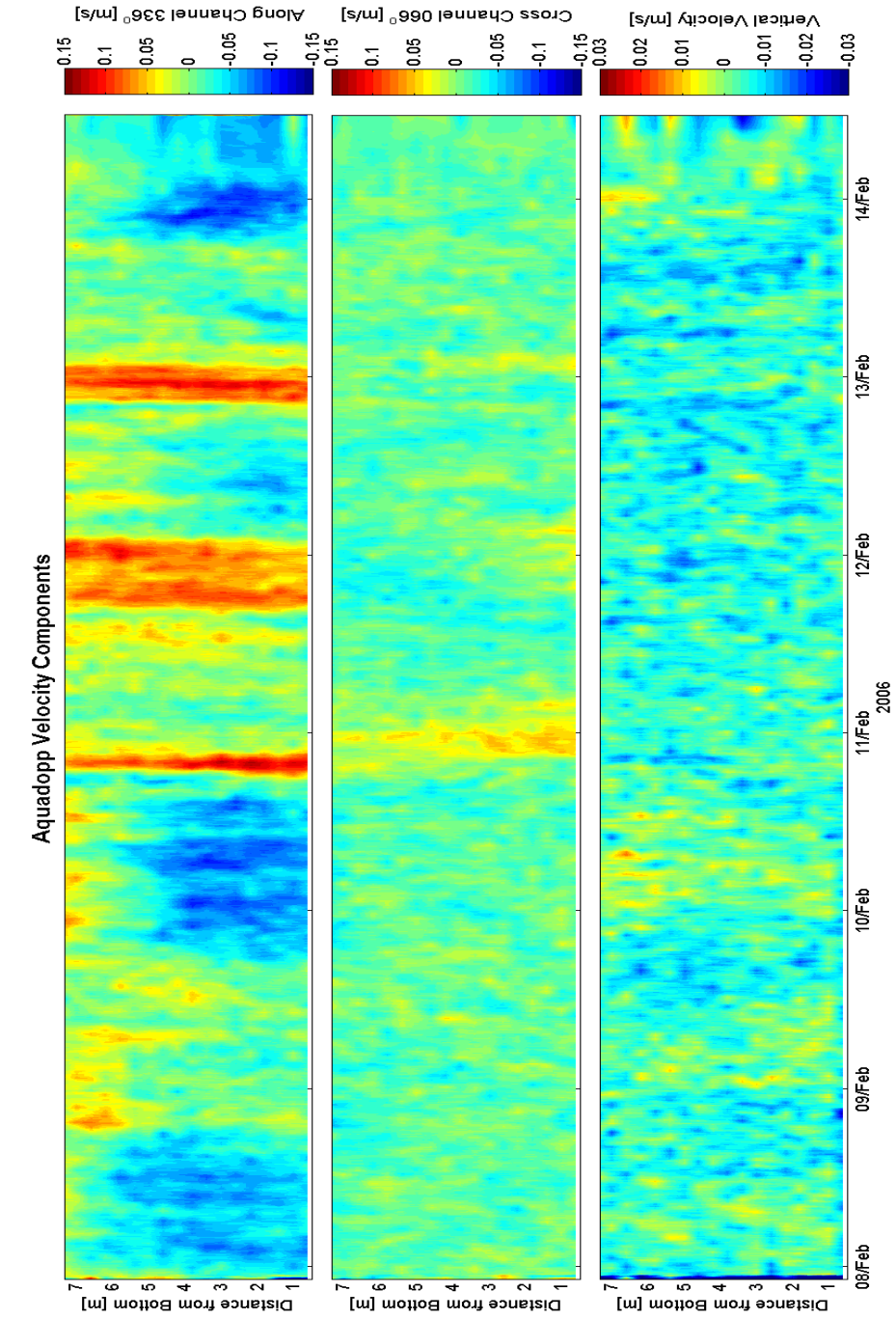

Fig A.42 Vertical velocity structure for week two of the study

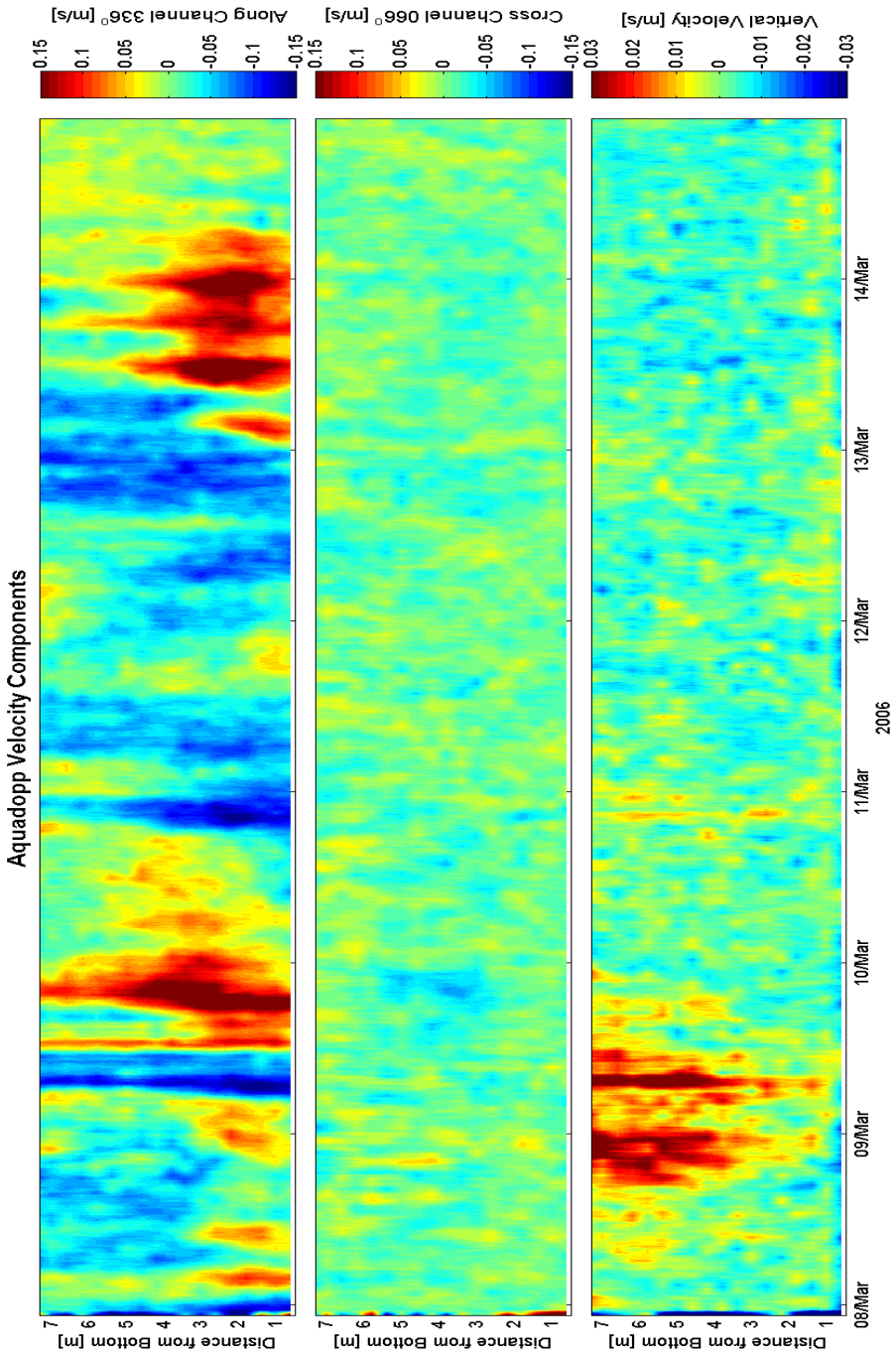

Fig A.43 Vertical velocity structure for week three of the study

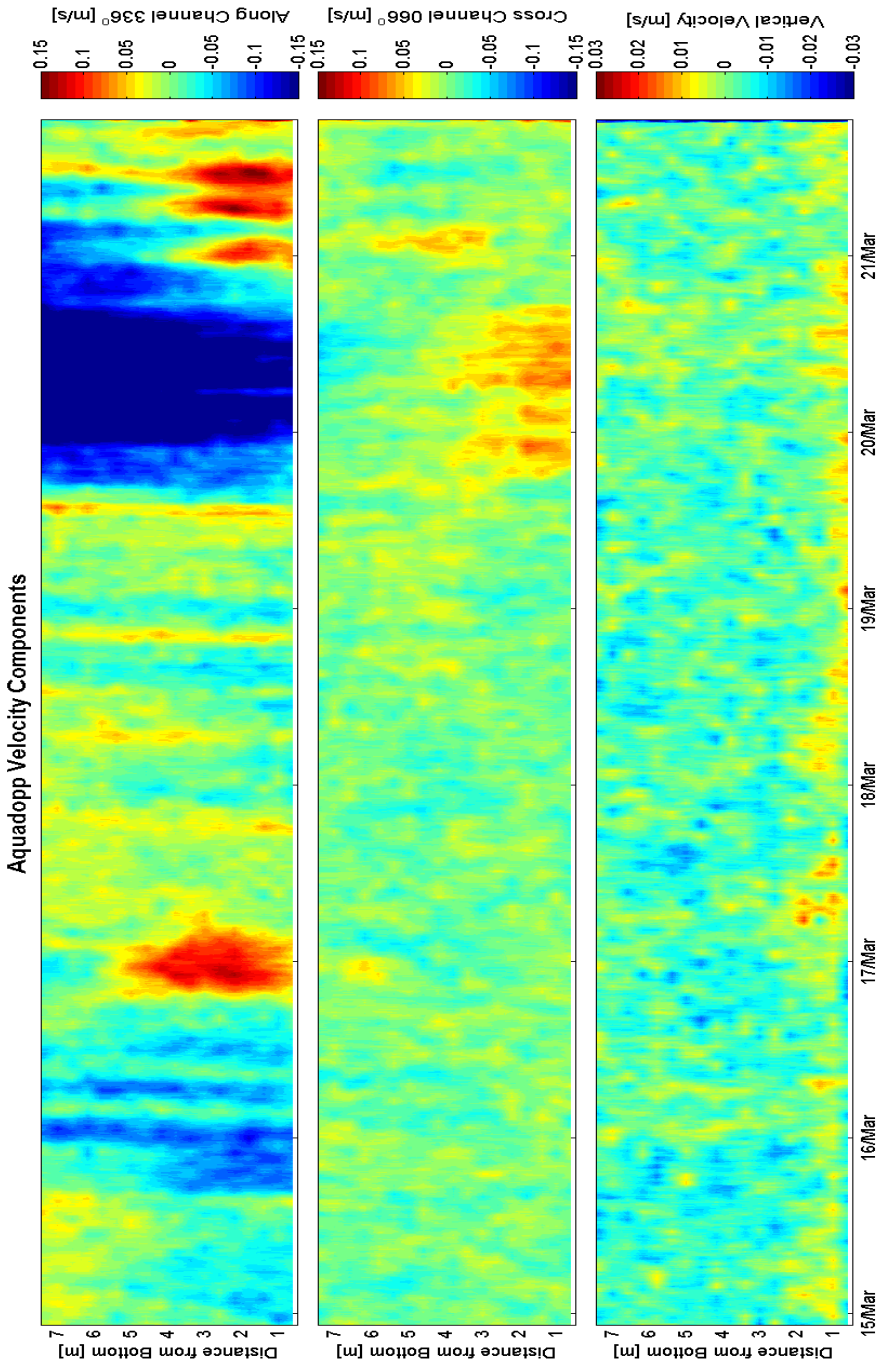

Fig A.44 Vertical velocity structure for week four of the study

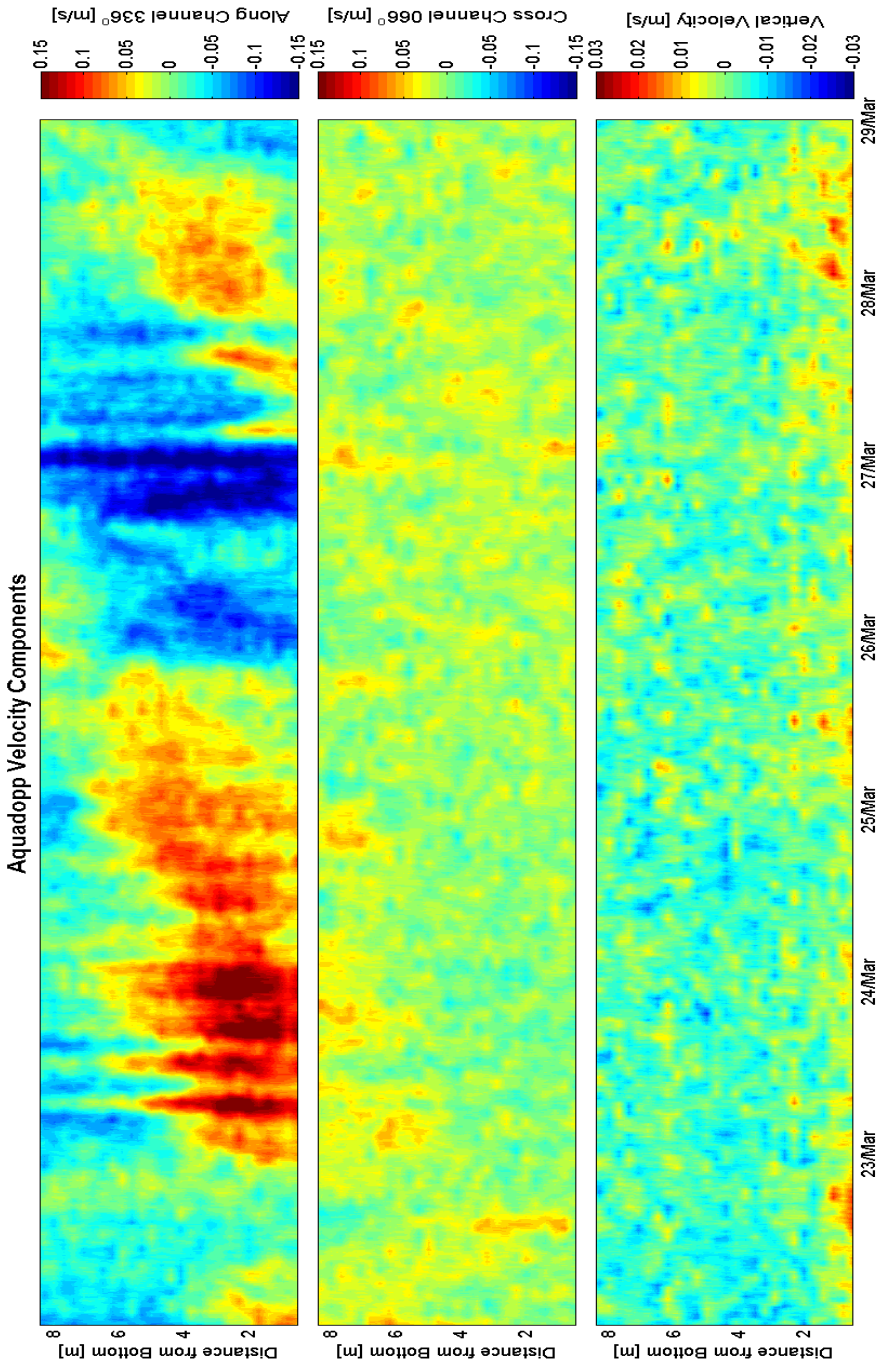

Fig A.45 Vertical velocity structure for week five of the study

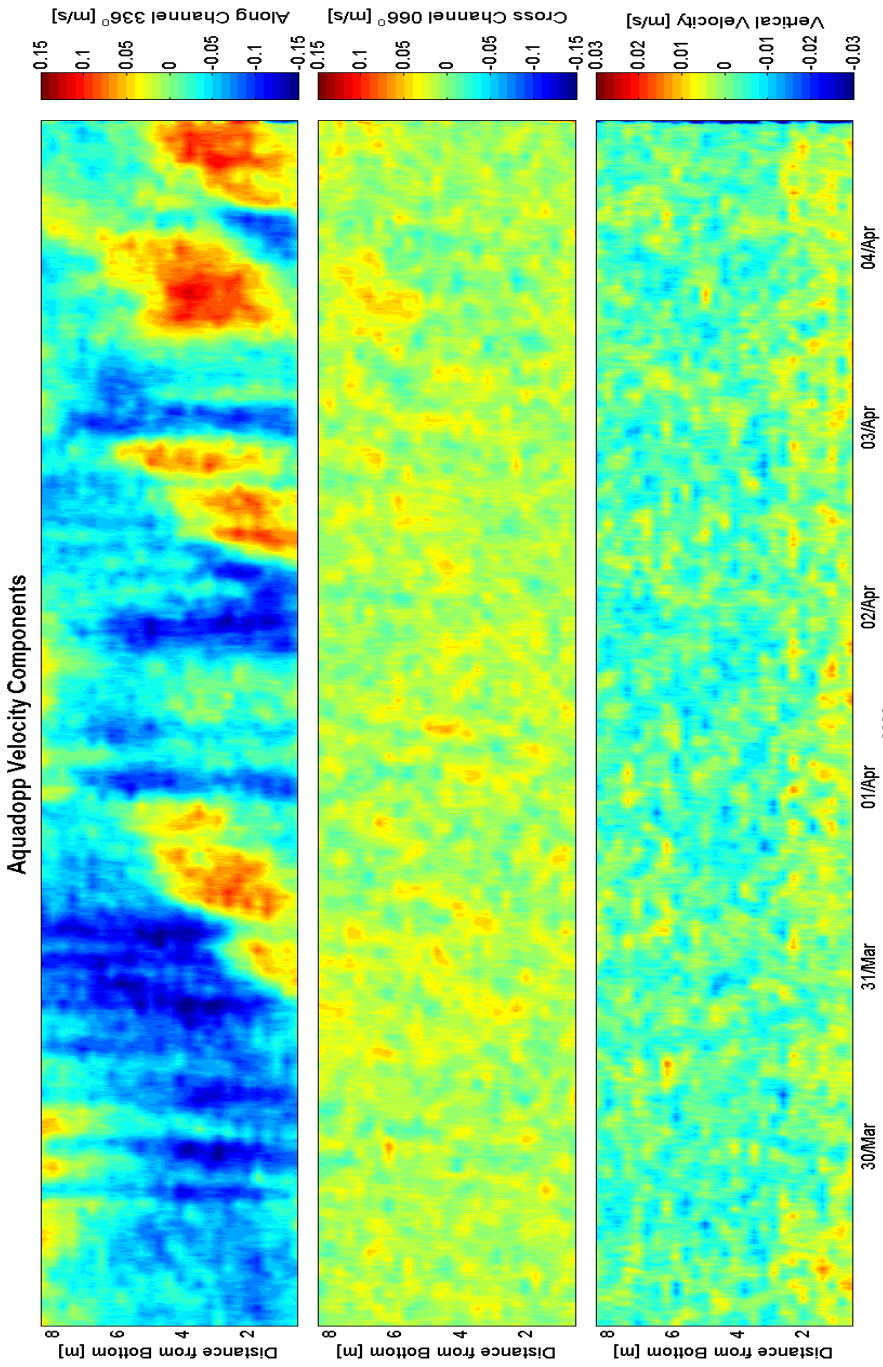

Fig A.46 Vertical velocity structure for week six of the study

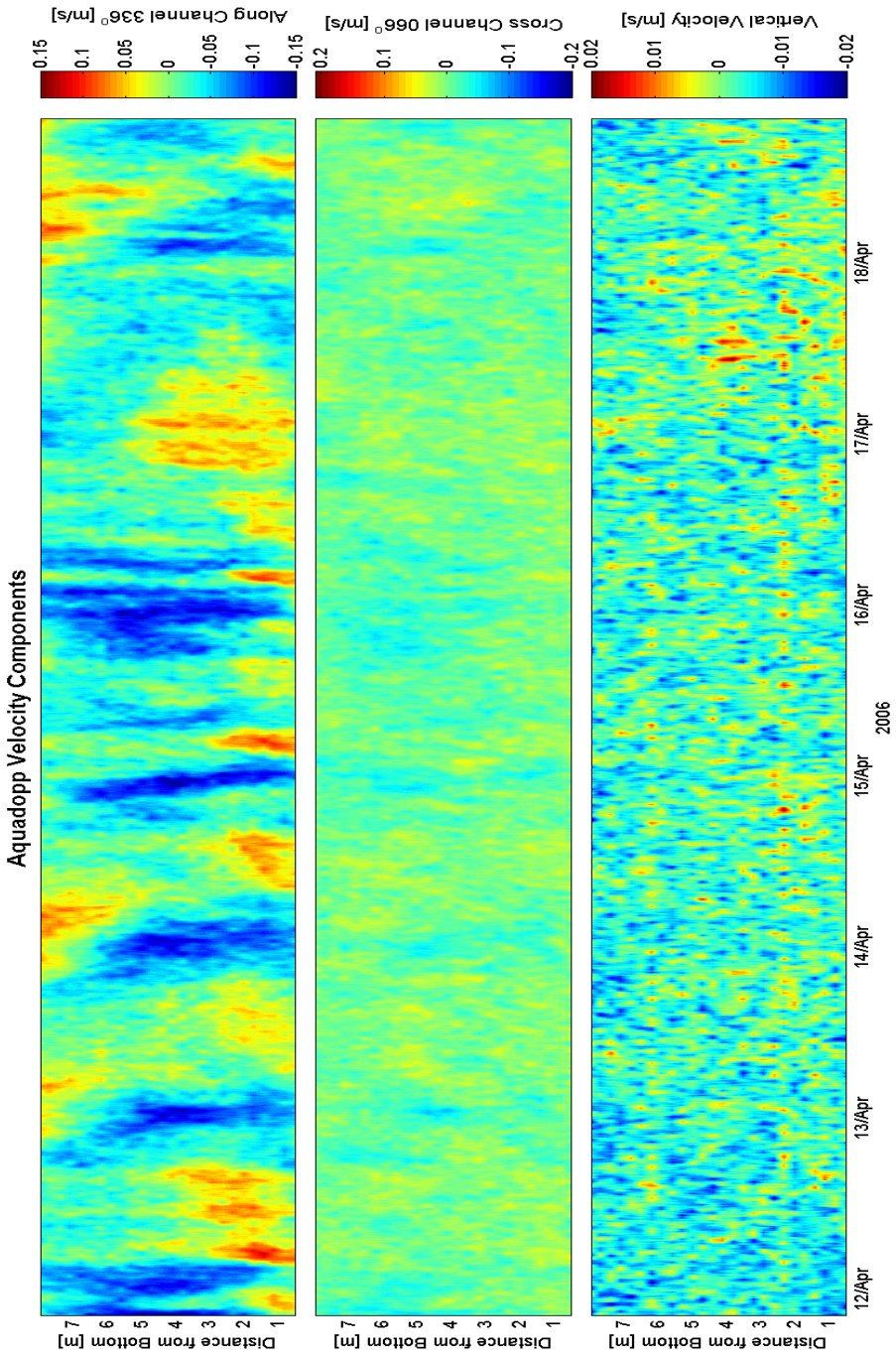

Fig A.47 Vertical velocity structure for week seven of the study

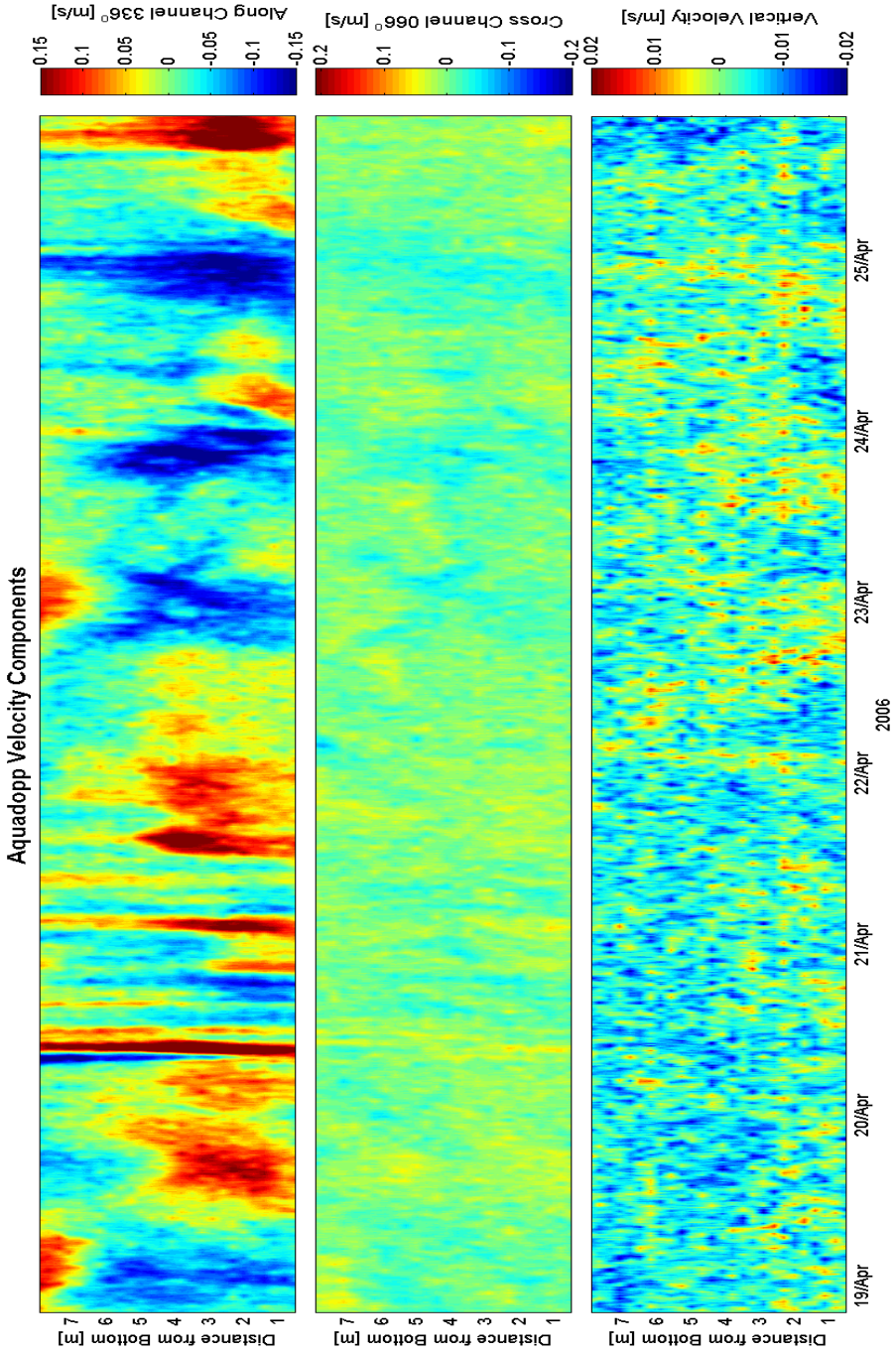

Fig A.48 Vertical velocity structure for week eight of the study

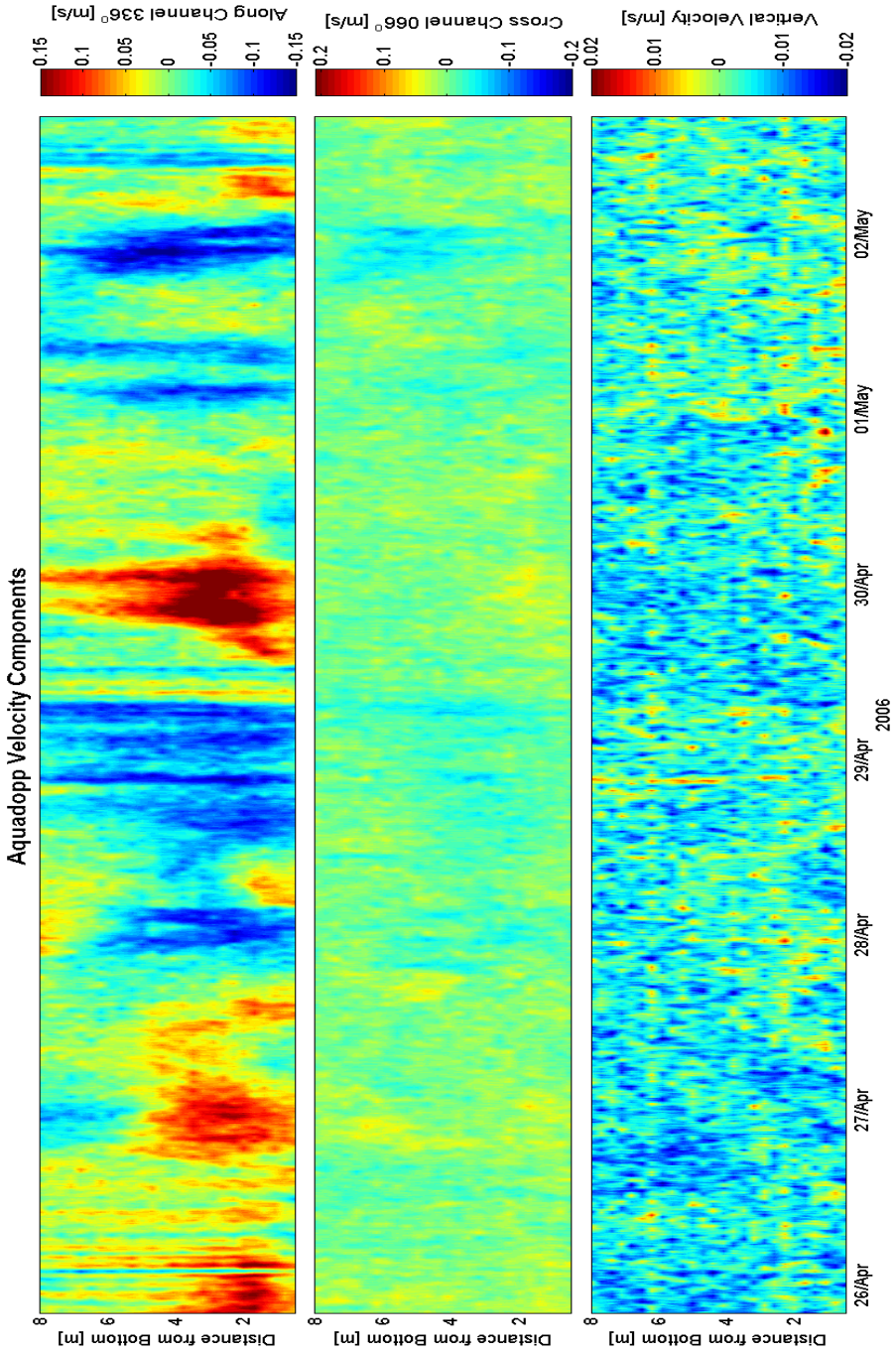

Fig A.49 Vertical velocity structure for week nine of the study

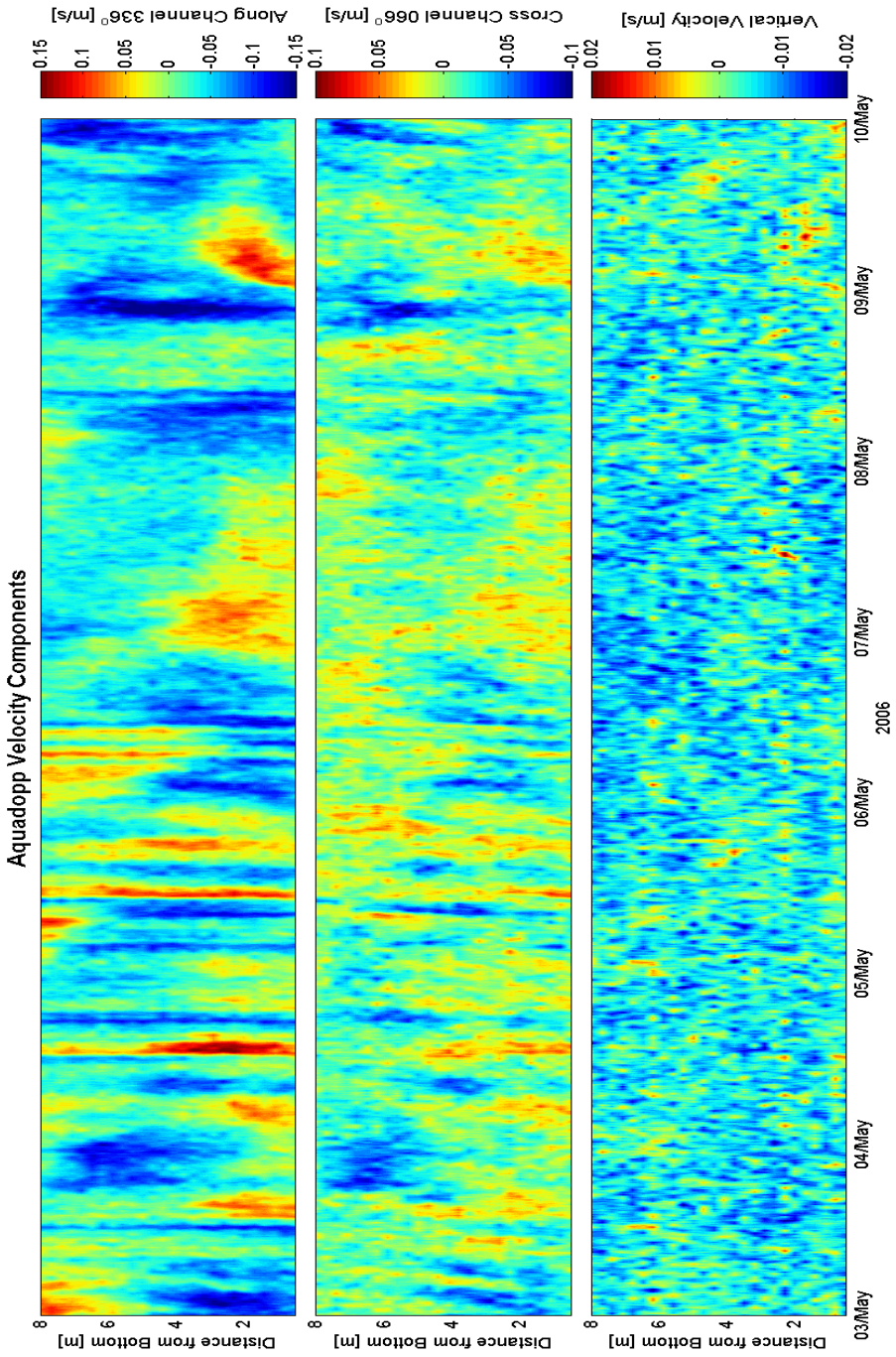

Fig A.50 Vertical velocity structure for week ten of the study

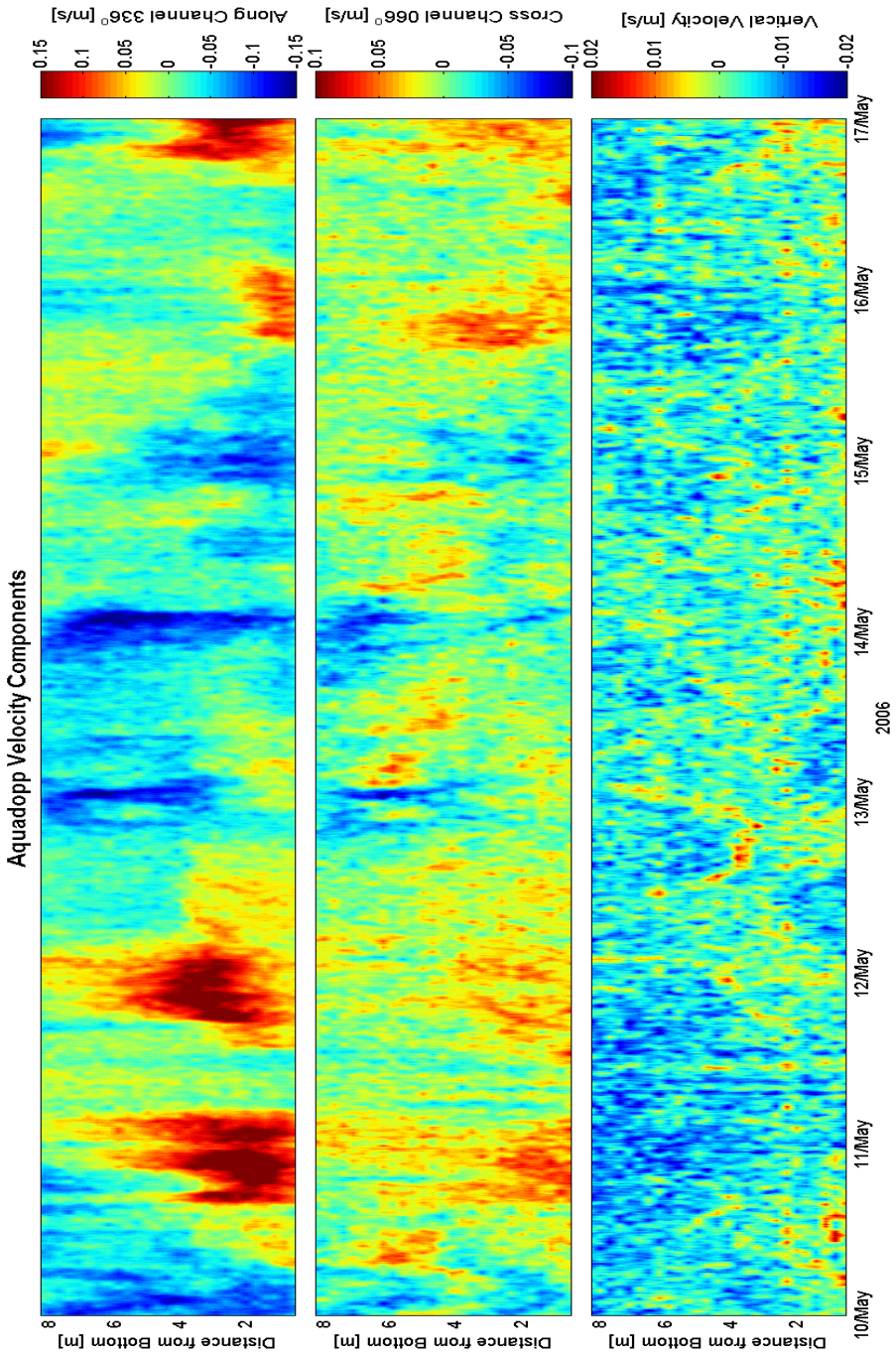

Fig A.51 Vertical velocity structure for week eleven of the study

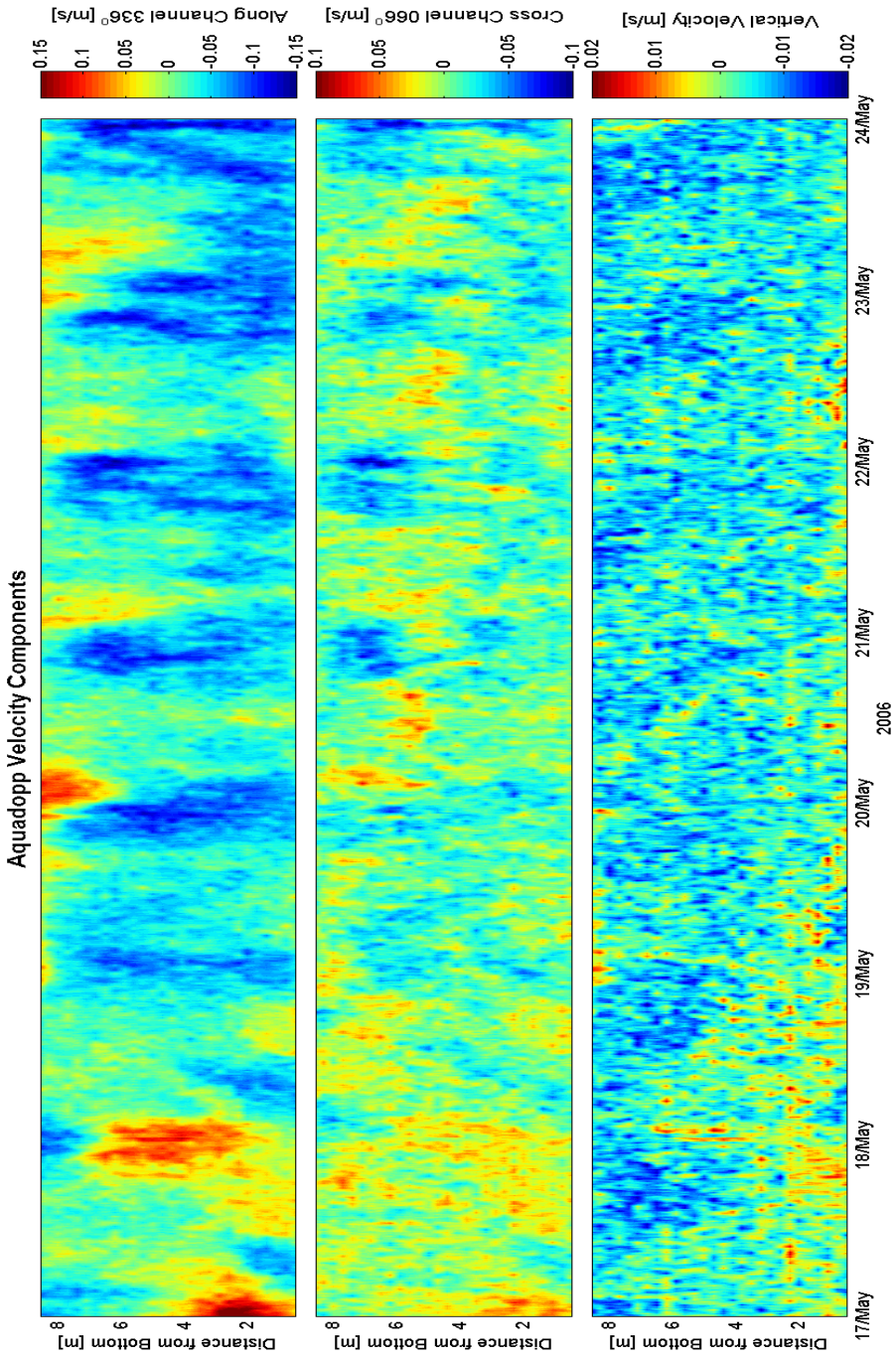

Fig A.52 Vertical velocity structure for week twelve of the study

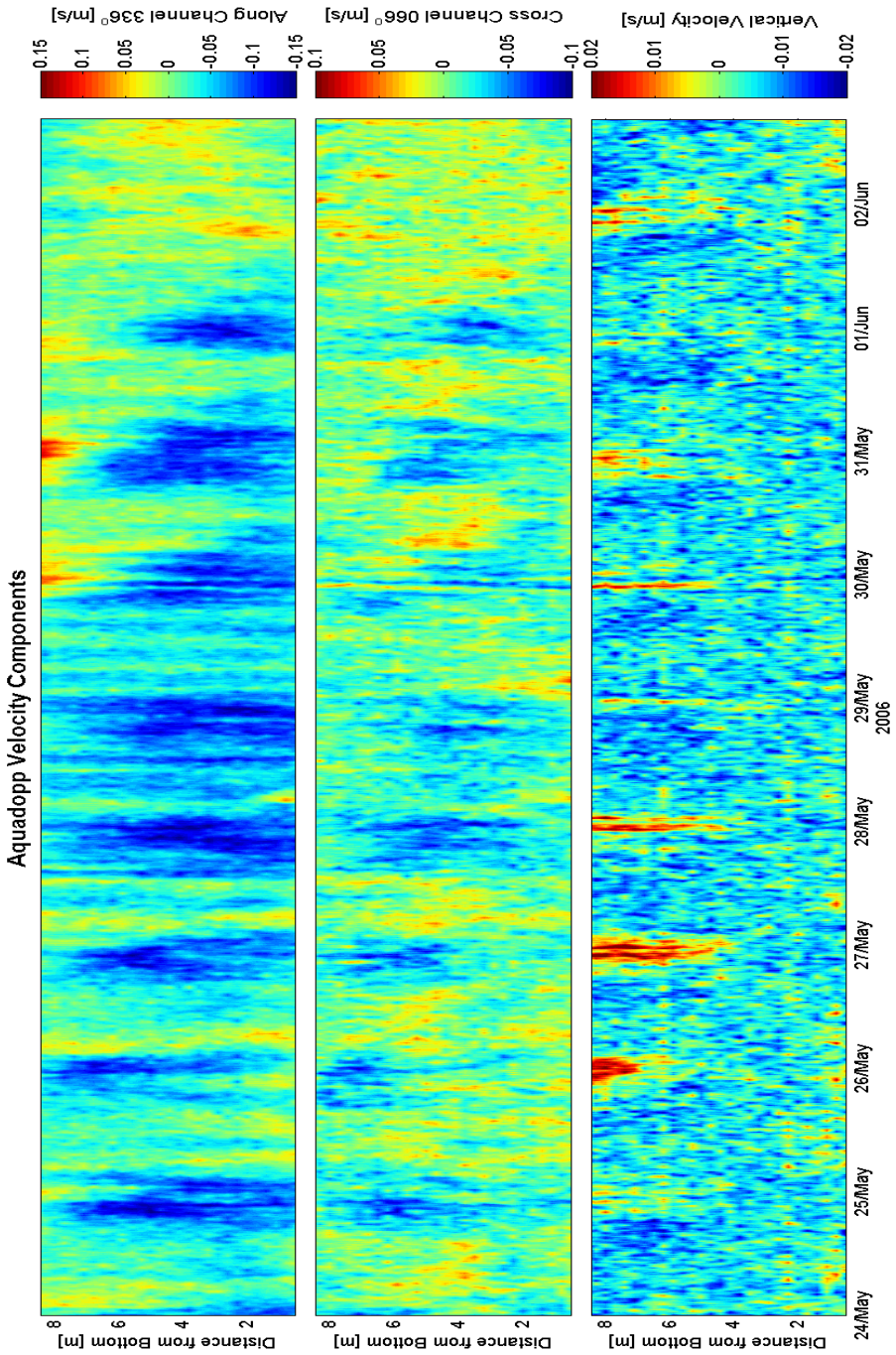

Fig A.53 Vertical velocity structure for week thirteen of the study

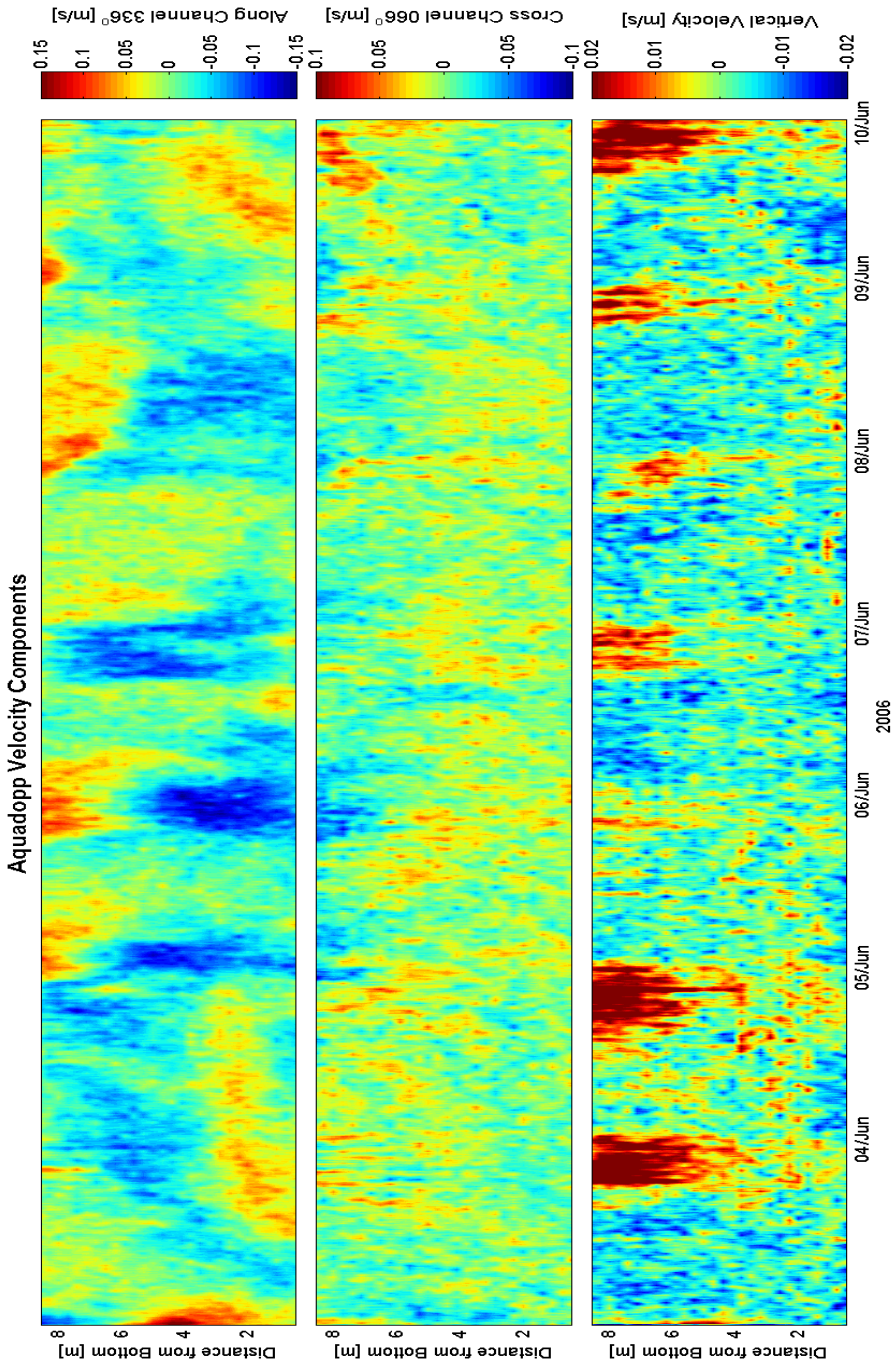

Fig A.54 Vertical velocity structure for week fourteen of the study

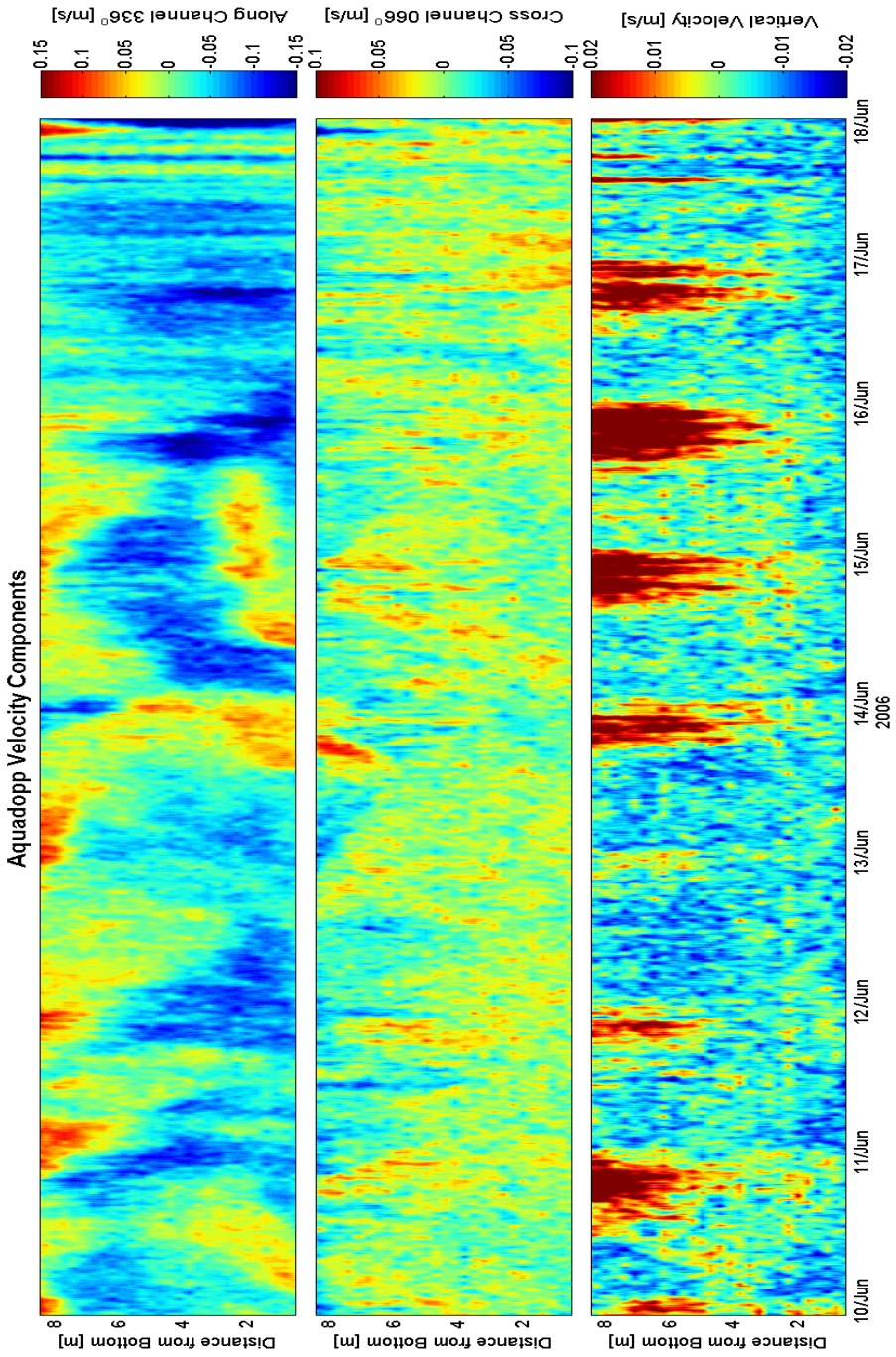

Fig A.55 Vertical velocity structure for week fifteen of the study

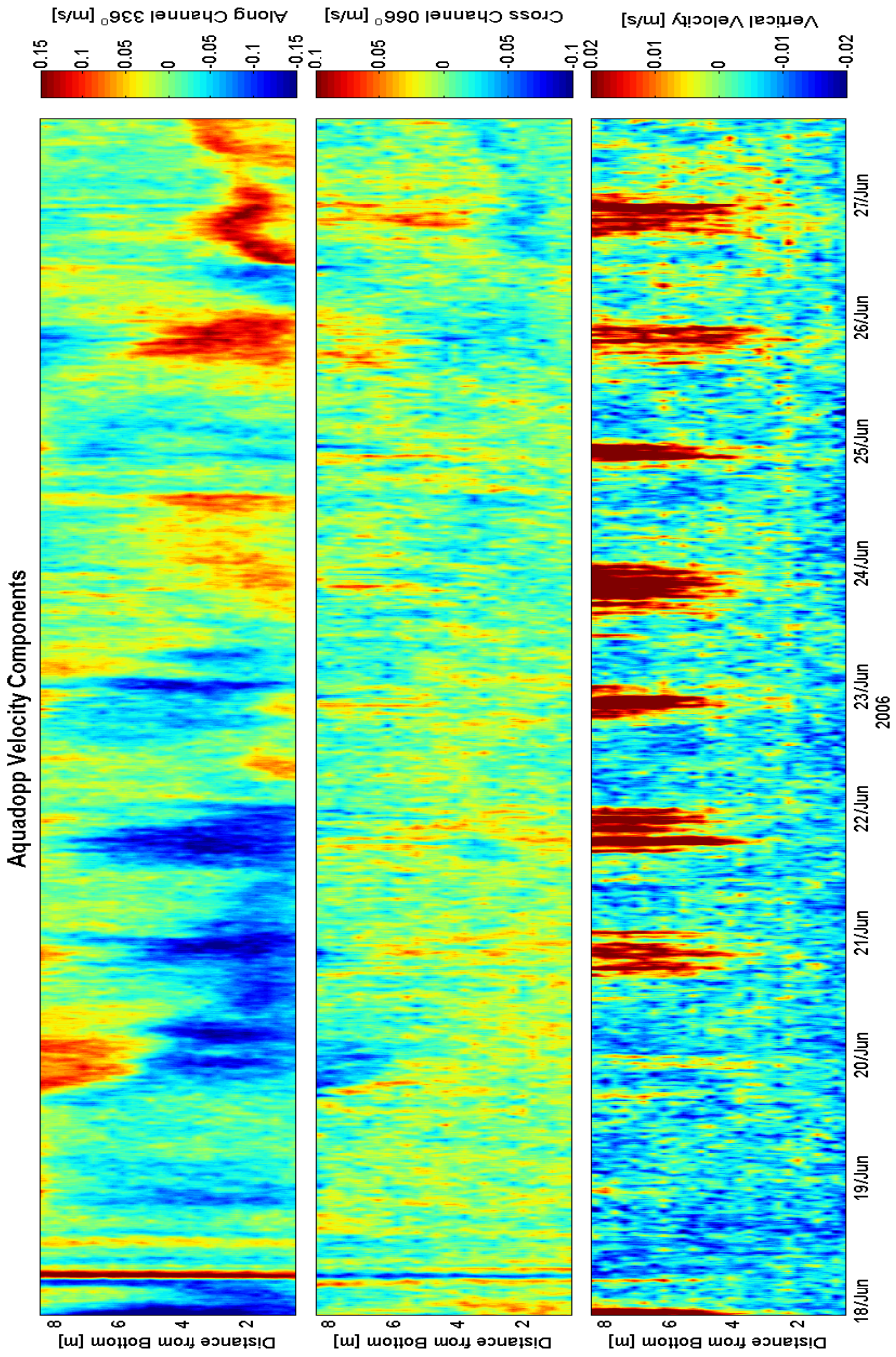

Fig A.56 Vertical velocity structure for week sixteen of the study

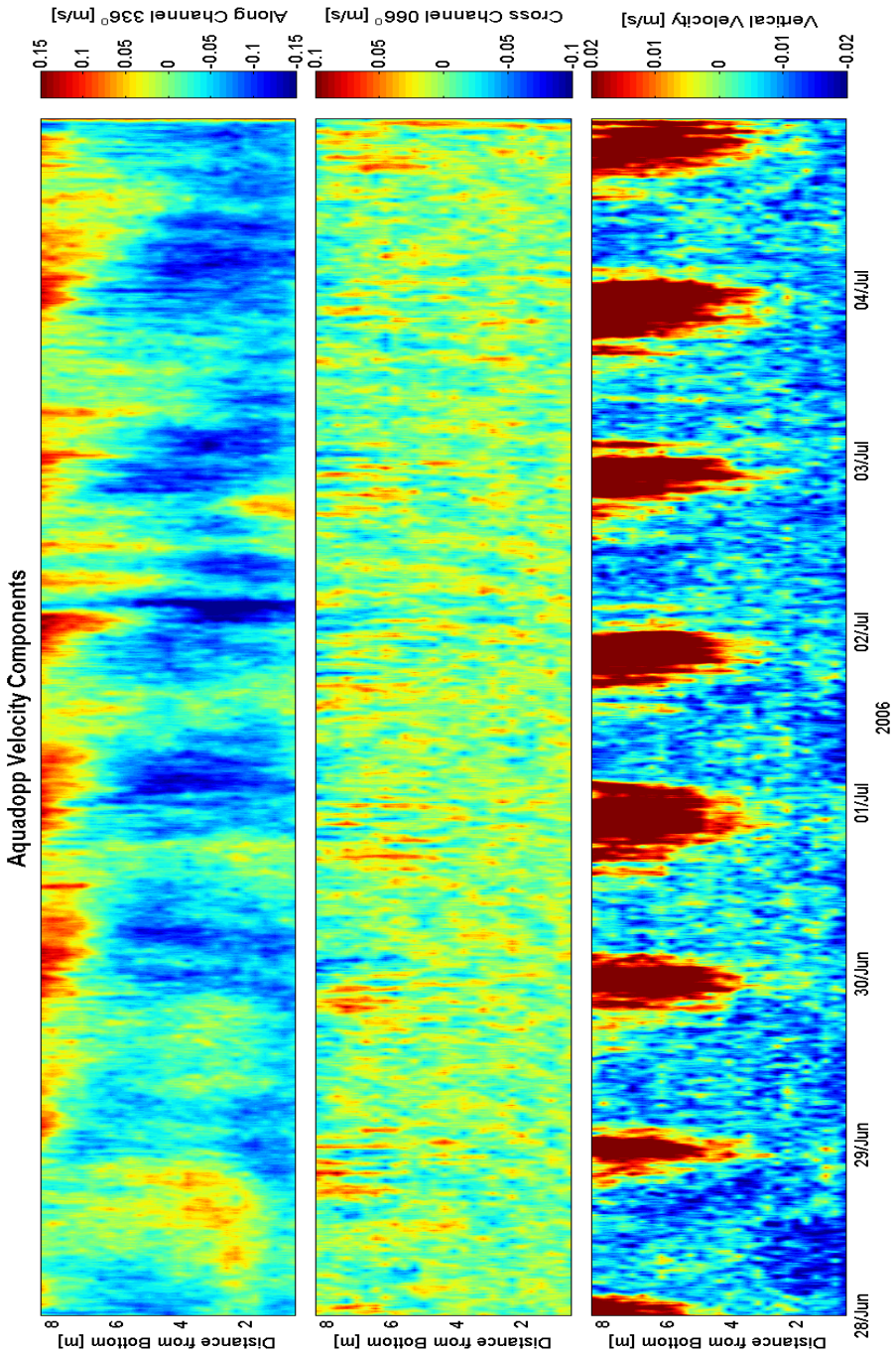

Fig A.57 Vertical velocity structure for week seventeen of the study

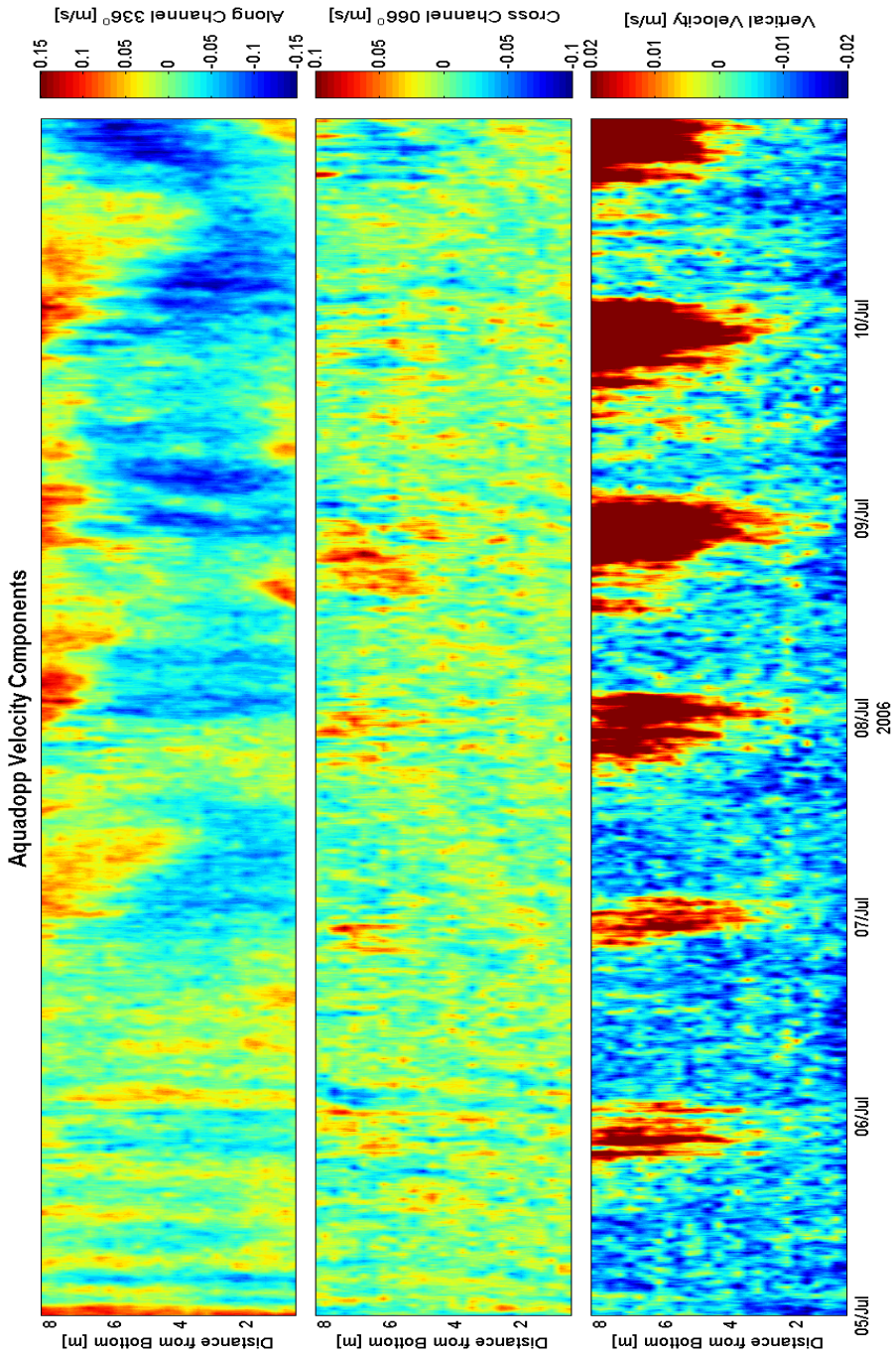

Fig A.58 Vertical velocity structure for week eighteen of the study

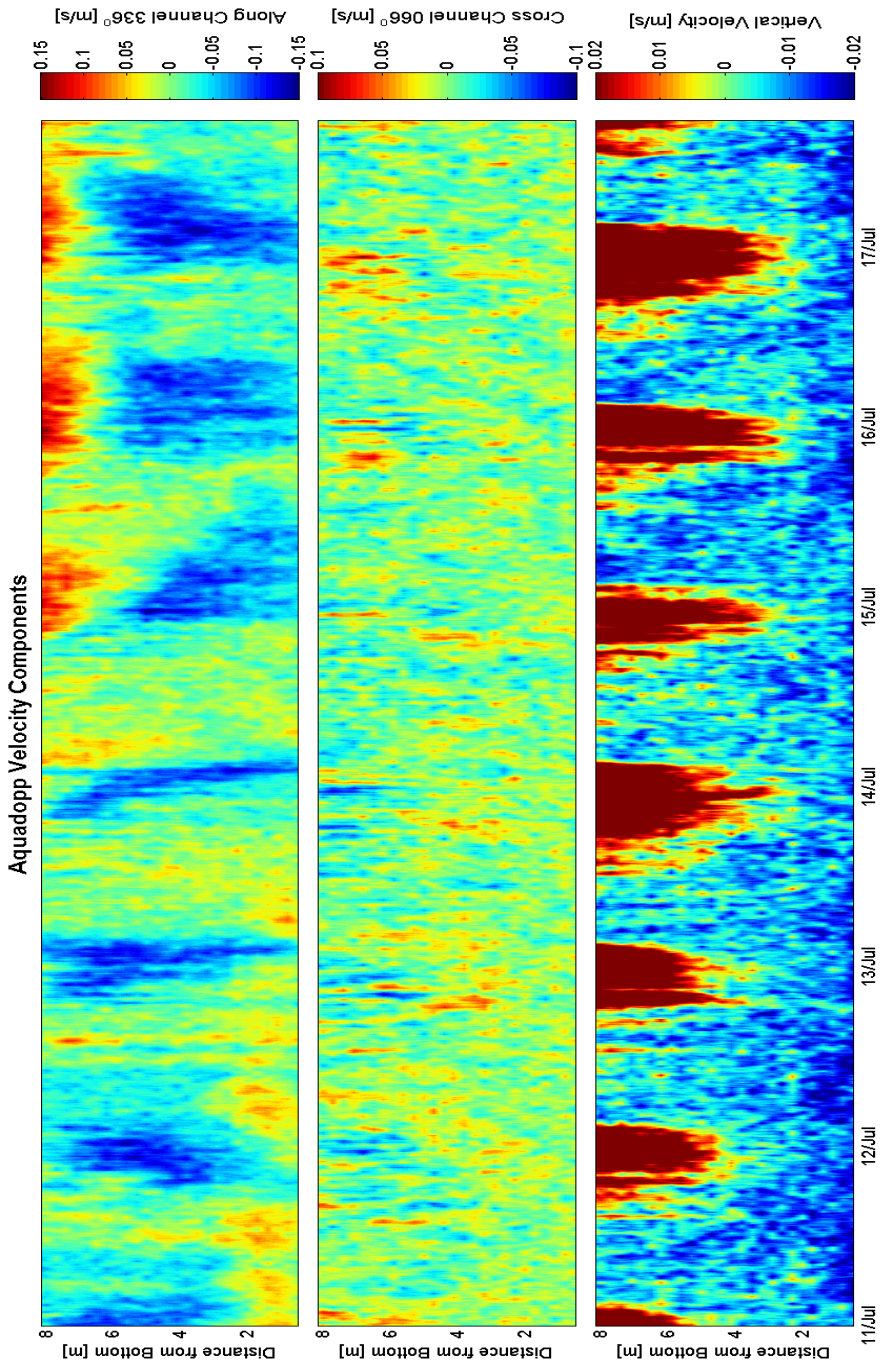

Fig A.59 Vertical velocity structure for week nineteen of the study

APPENDIX B SIMULATION RESULTS

B.1 *k-kl* Model March Simulations

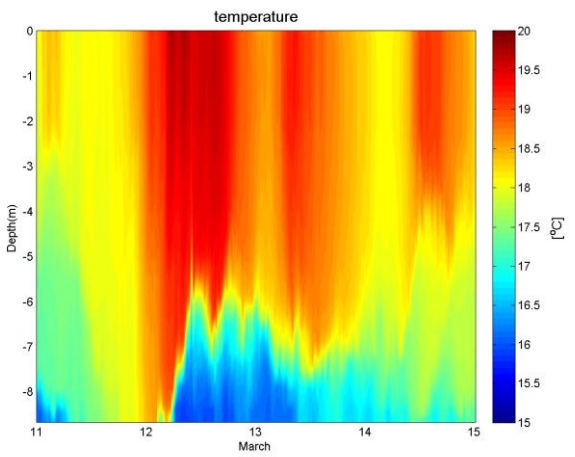

Fig B.1 Simulated thermal structure

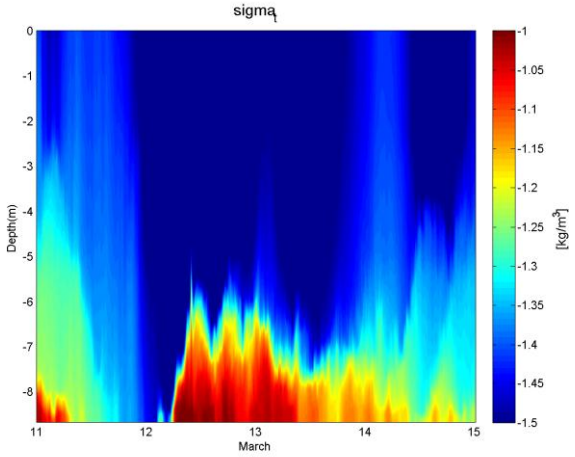

Fig B.2 Simulated density structure

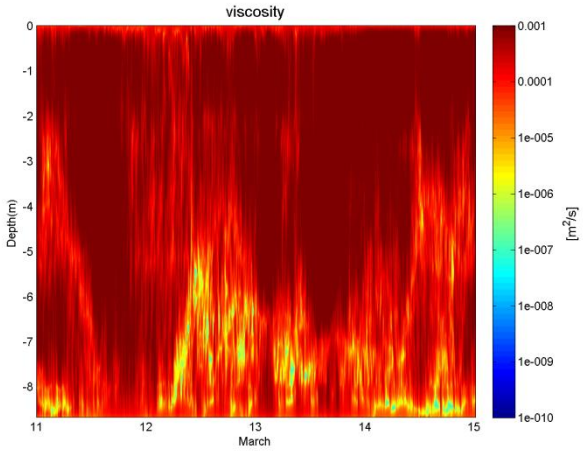

Fig B.3 Simulated viscosity

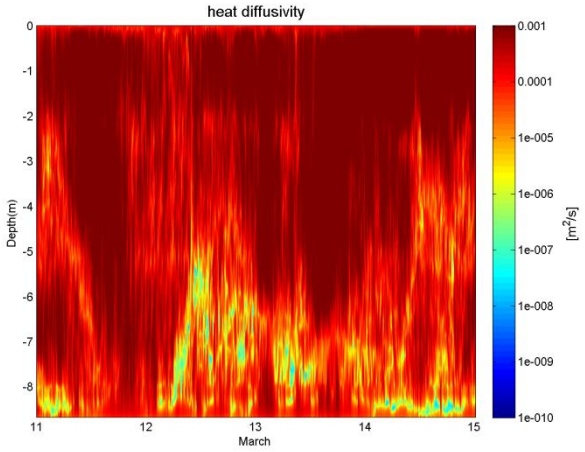

Fig B.4 Simulated heat diffusivity

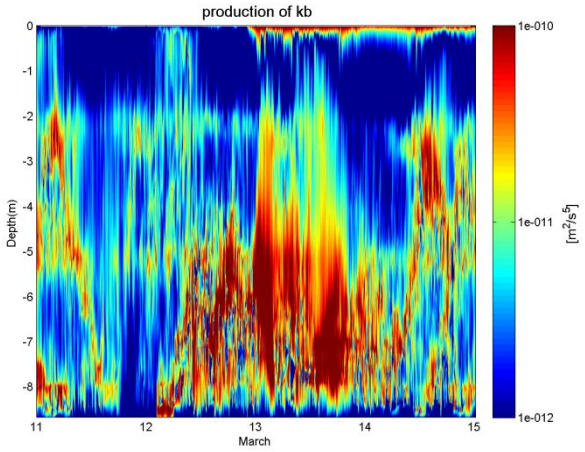

Fig B.5 Simulated production of kb

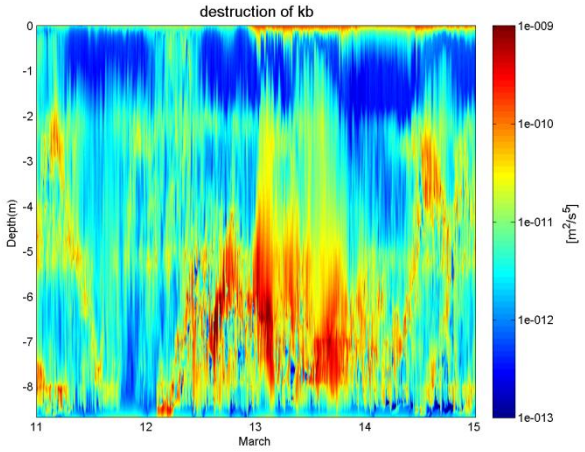

Fig B.6 Simulated destruction of kb

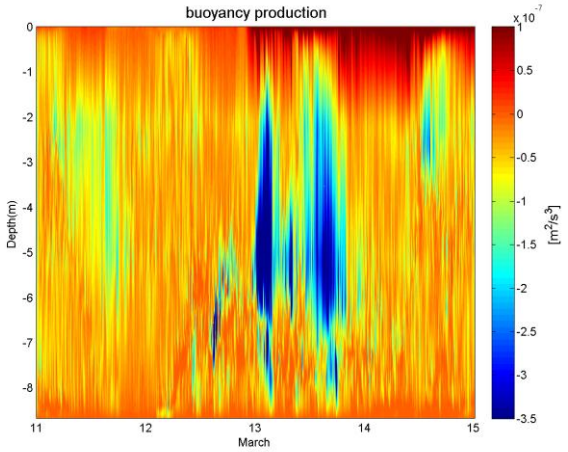

Fig B.7 Simulated buoyancy production

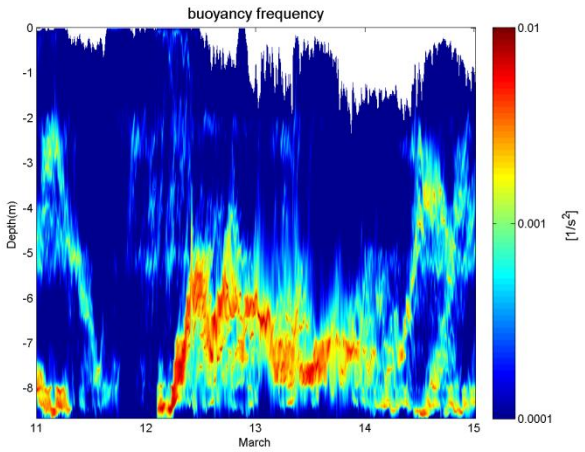

Fig B.8 Simulated buoyancy frequency

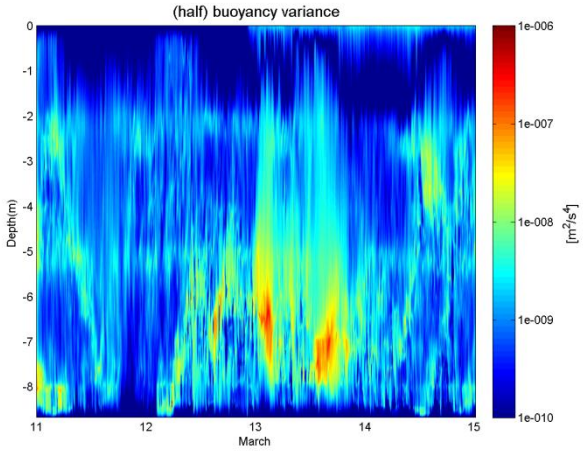

Fig B.9 Simulated buoyancy variance

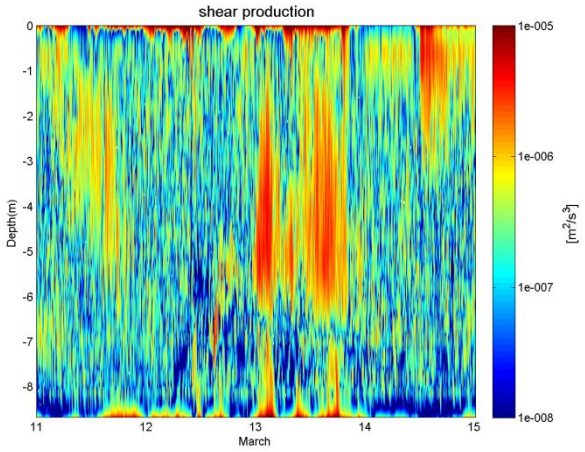

Fig B.10 Simulated shear production

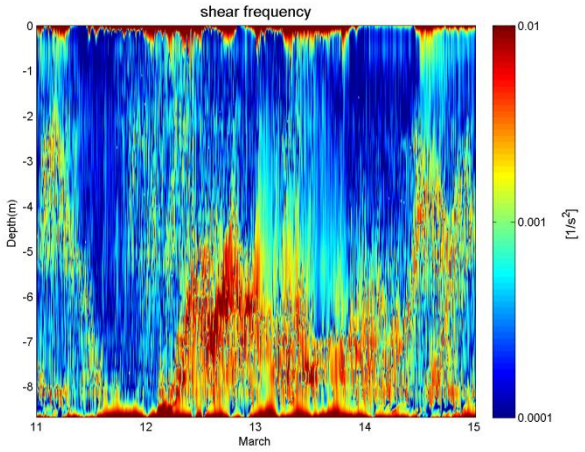

Fig B.11 Simulated shear frequency

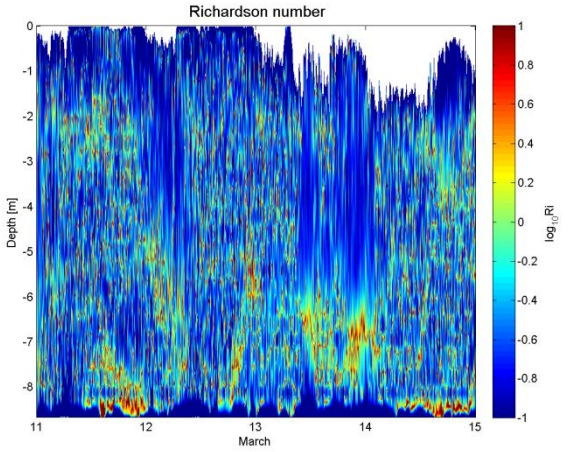

Fig B.12 Simulated Ri number

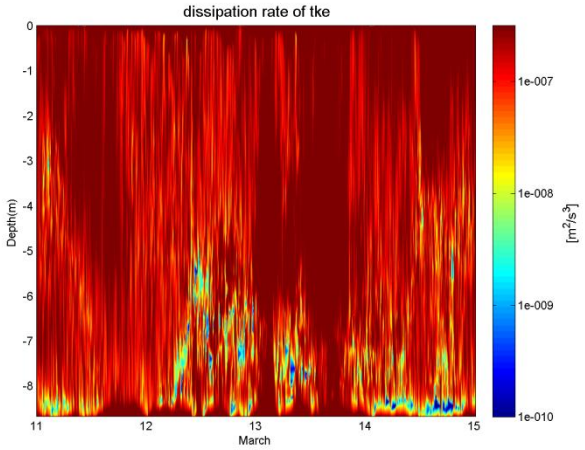

Fig B.13 Simulated ϵ

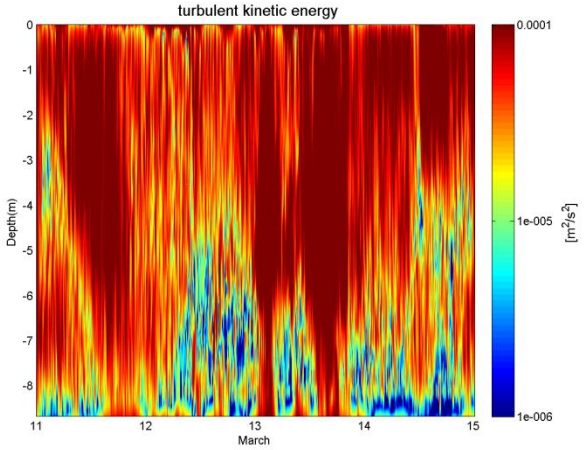

Fig B.14 Simulated TKE

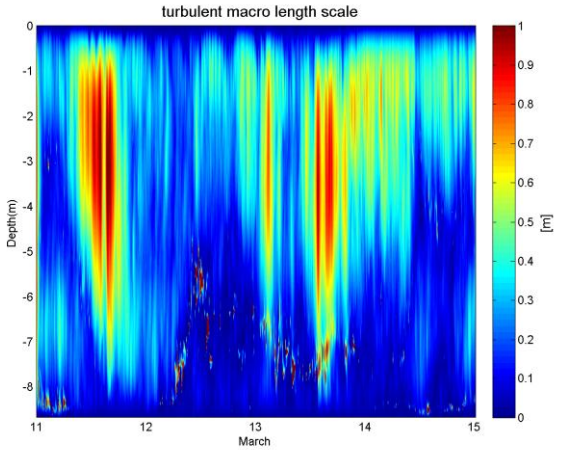

Fig B.15 Simulated turbulent macro length scale

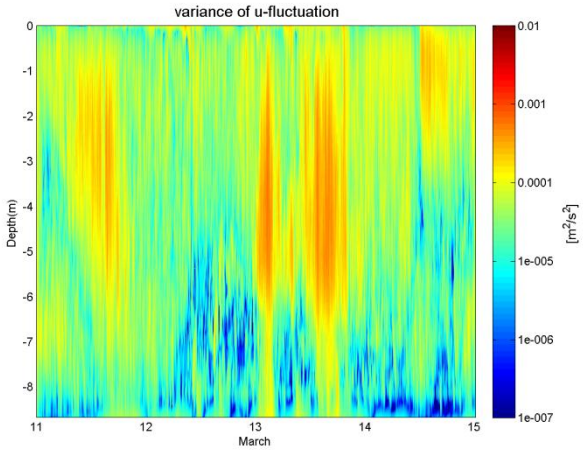

Fig B.16 Simulated variance U

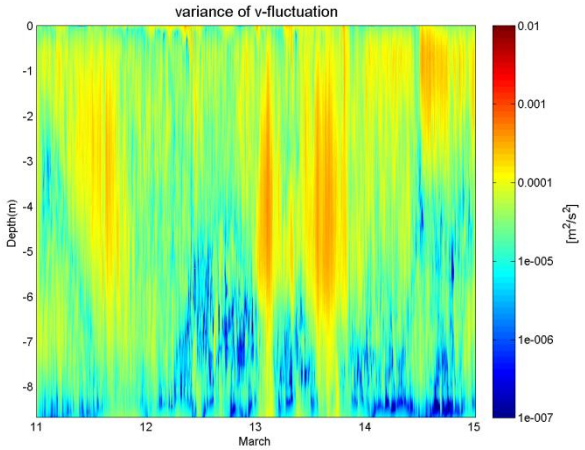

Fig B.17 Simulated variance V

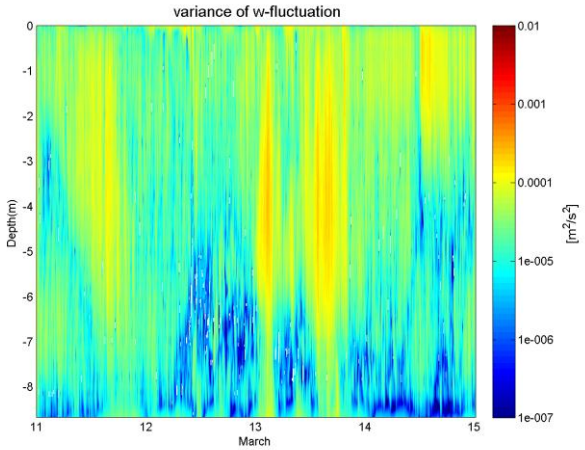

Fig B.18 Simulated variance W

B.2 k-ϵ Model March Simulations

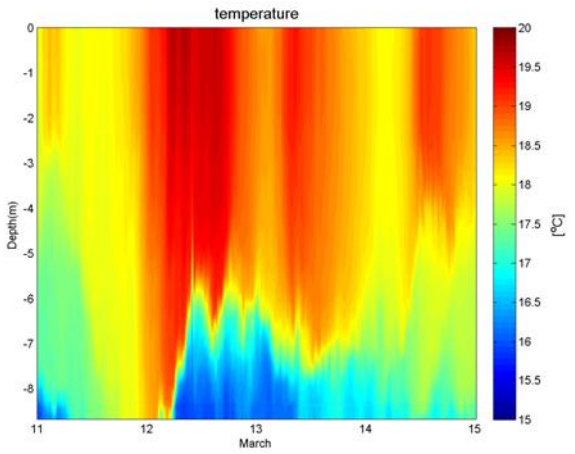

Fig B.19 Simulated thermal structure

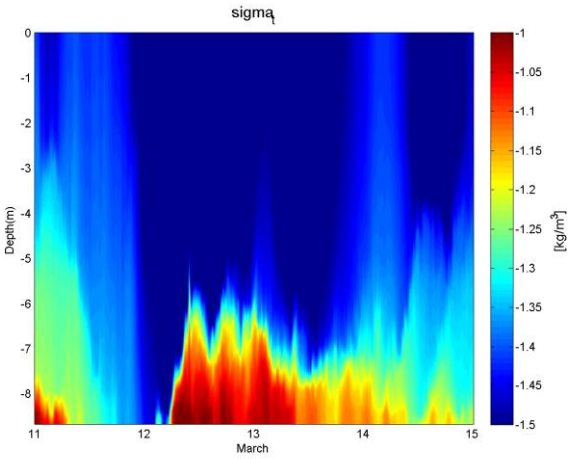

Fig B.20 Simulated density structure

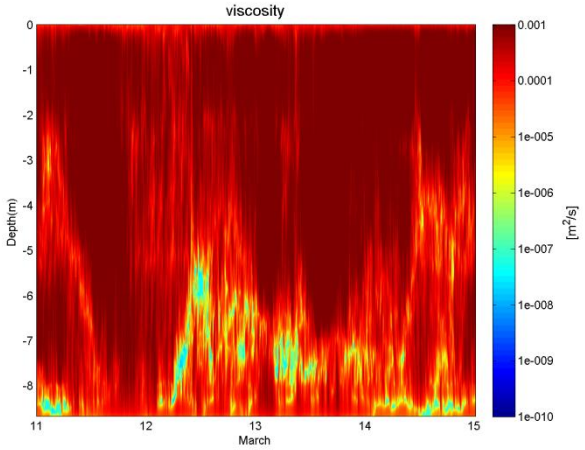

Fig B.21 Simulated viscosity

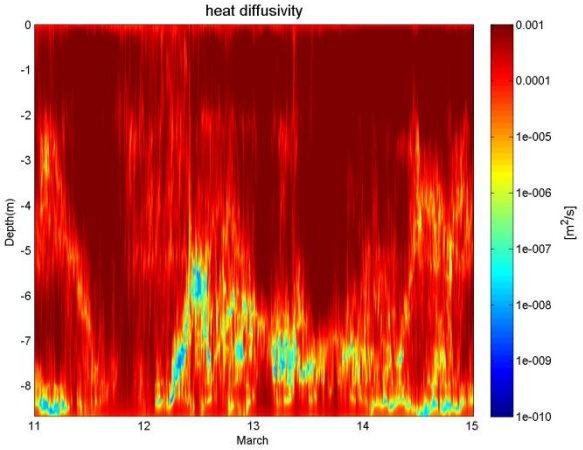

Fig B.22 Simulated heat diffusivity

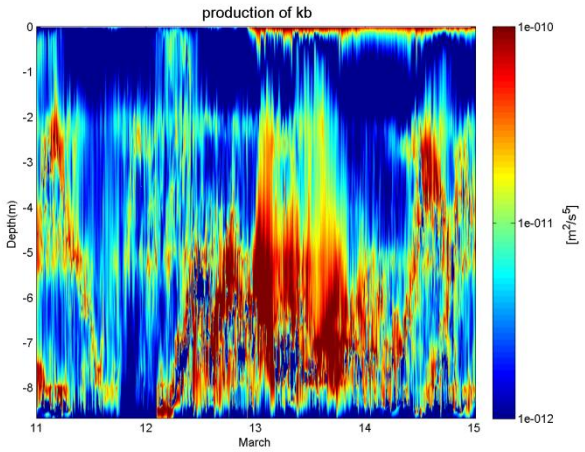

Fig B.23 Simulated production of kb

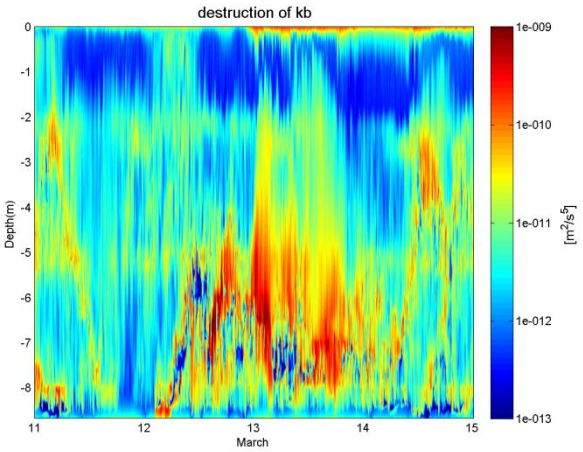

Fig B.24 Simulated destruction of kb

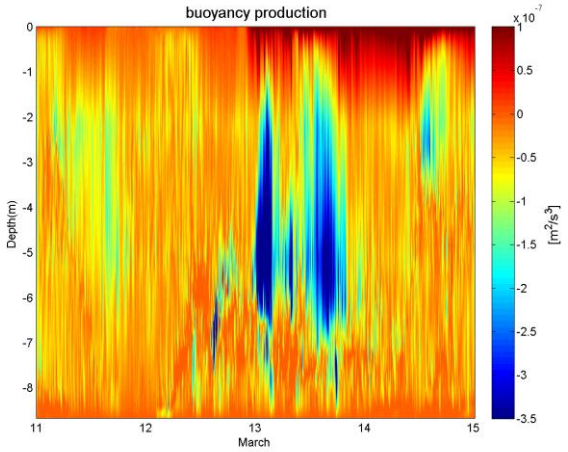

Fig B.25 Simulated buoyancy production

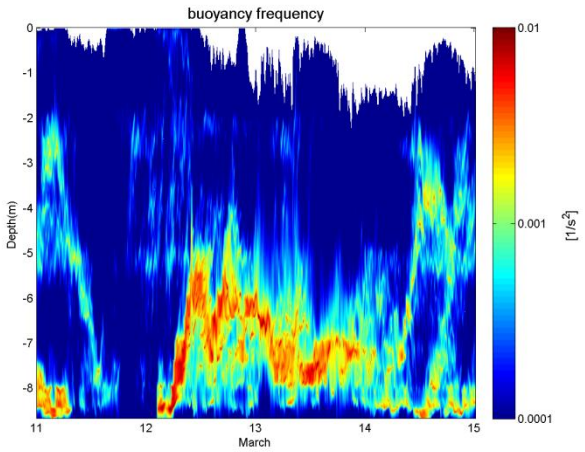

Fig B.26 Simulated buoyancy frequency

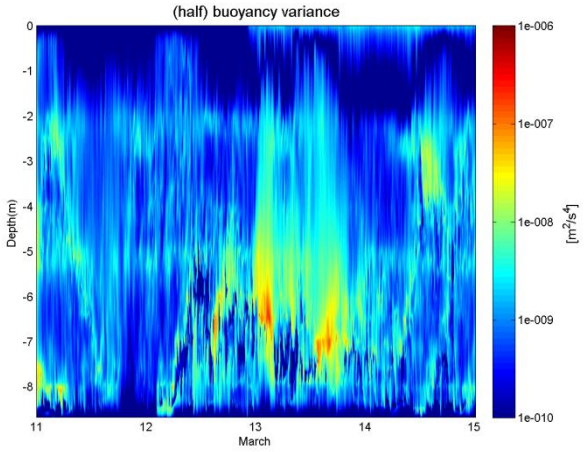

Fig B.27 Simulated buoyancy variance

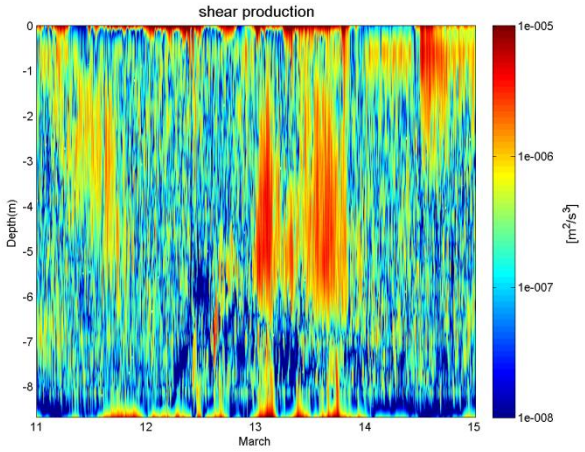

Fig B.28 Simulated shear production

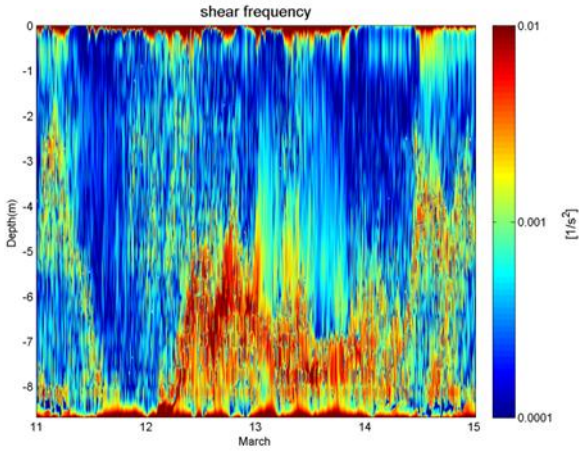

Fig B.29 Simulated shear frequency

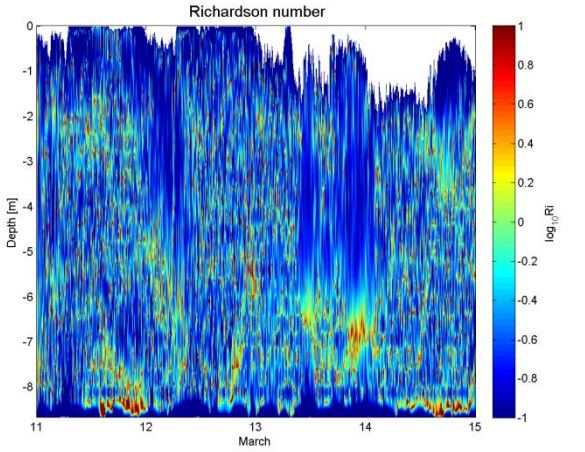

Fig B.30 Simulated Ri number

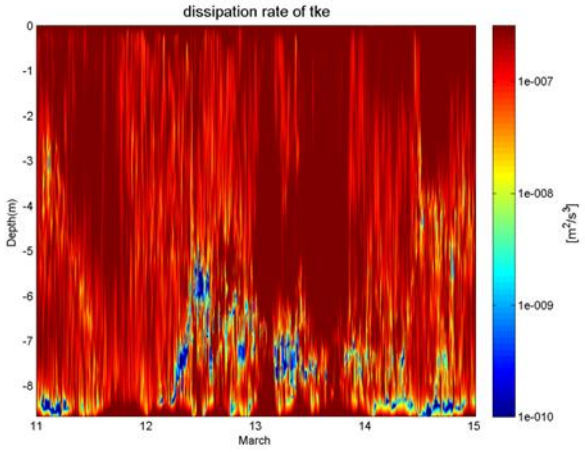

Fig B.31 Simulated ϵ

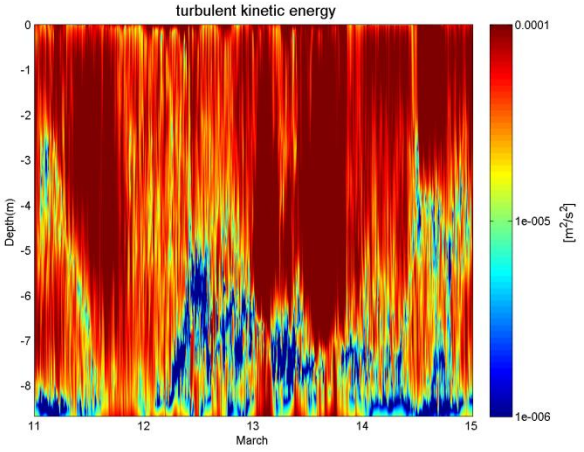

Fig B.32 Simulated TKE

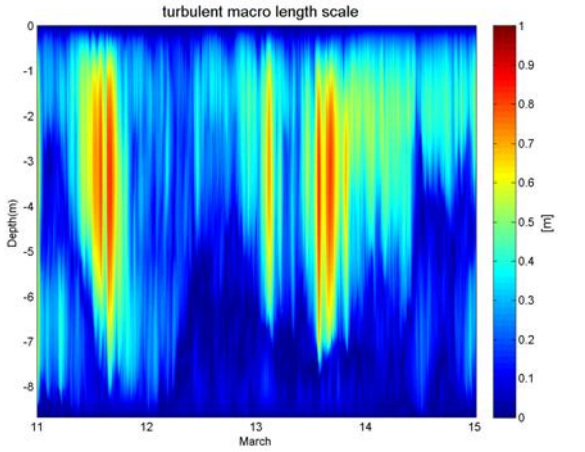

Fig B.33 Simulated turbulent macro length scale

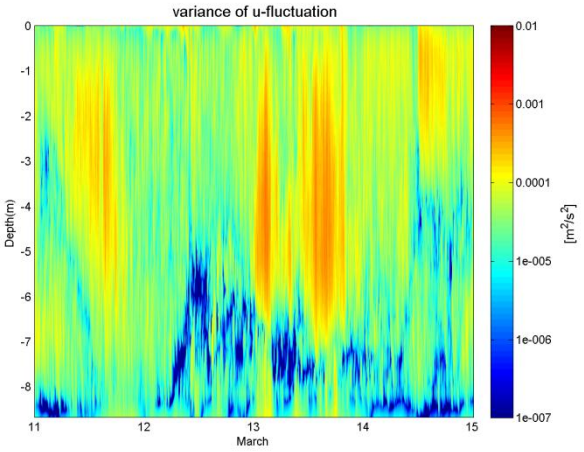

Fig B.34 Simulated variance U

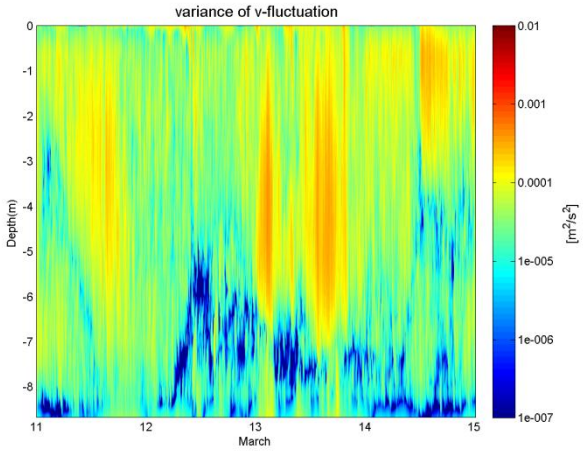

Fig B.35 Simulated variance V

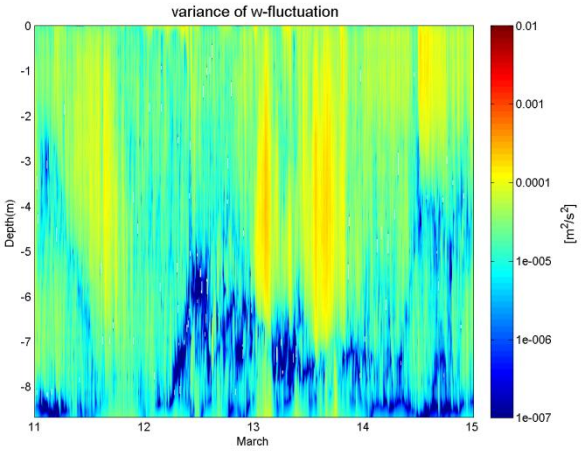

Fig B.36 Simulated variance W

B.3 *k-kl* Model June Simulations

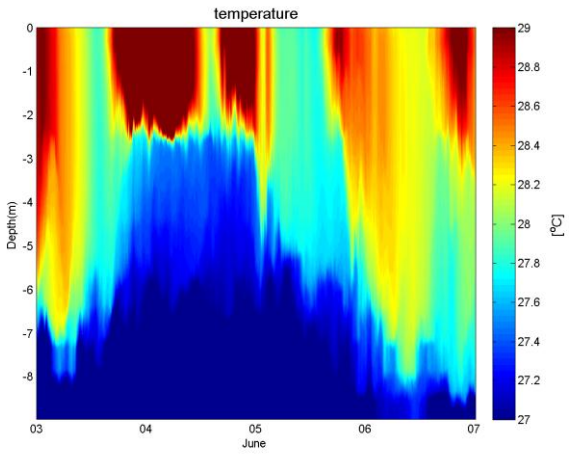

Fig B.37 Simulated thermal structure

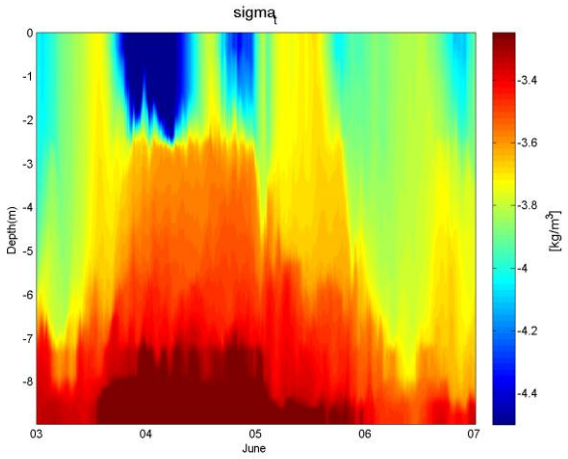

Fig B.38 Simulated density structure

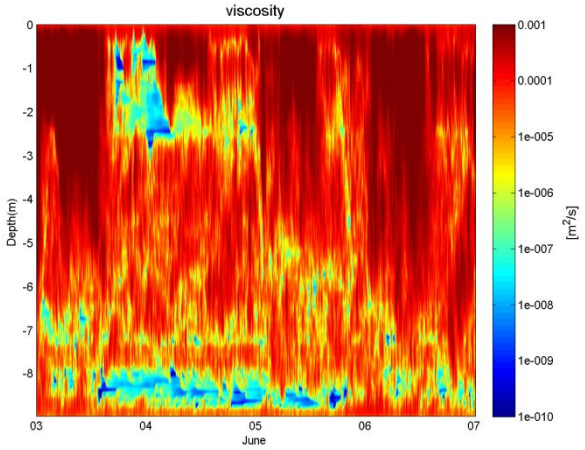

Fig B.39 Simulated viscosity

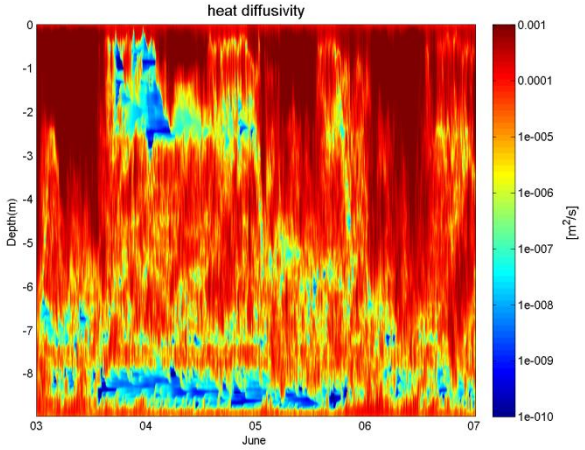

Fig B.40 Simulated heat diffusivity

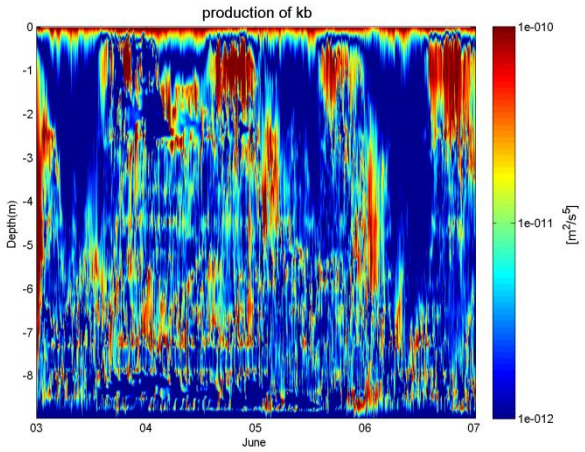

Fig B.41 Simulated production of kb

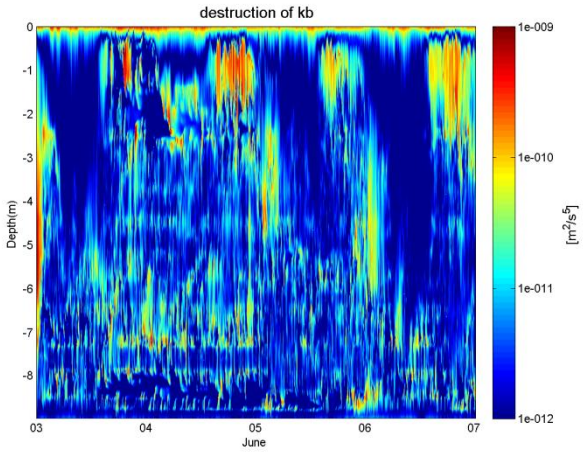

Fig B.42 Simulated destruction of kb

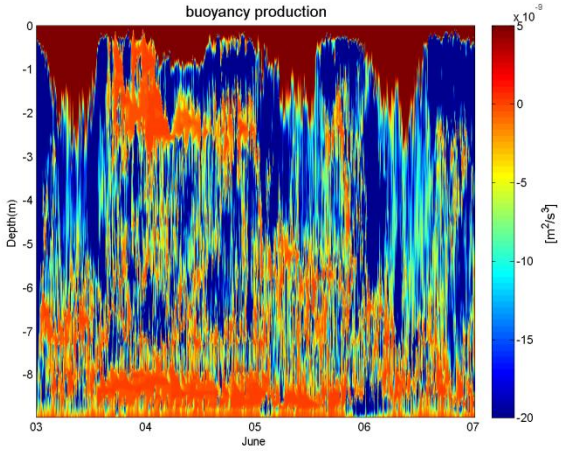

Fig B.43 Simulated buoyancy production

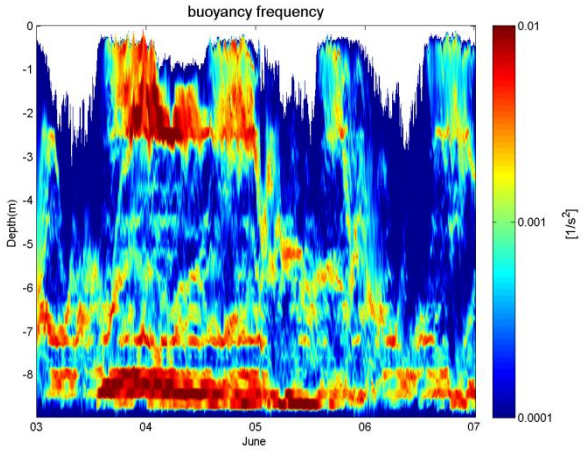

Fig B.44 Simulated buoyancy frequency

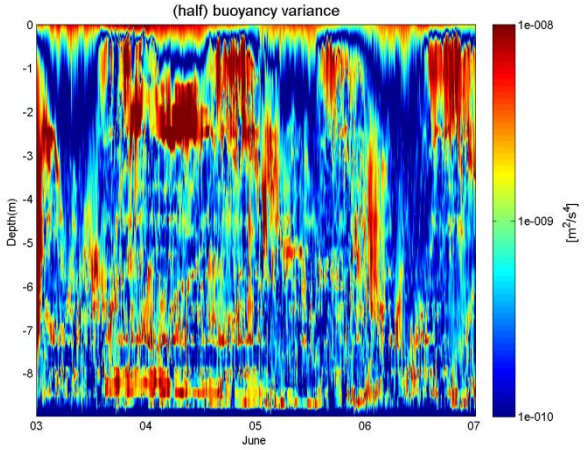

Fig B.45 Simulated buoyancy variance

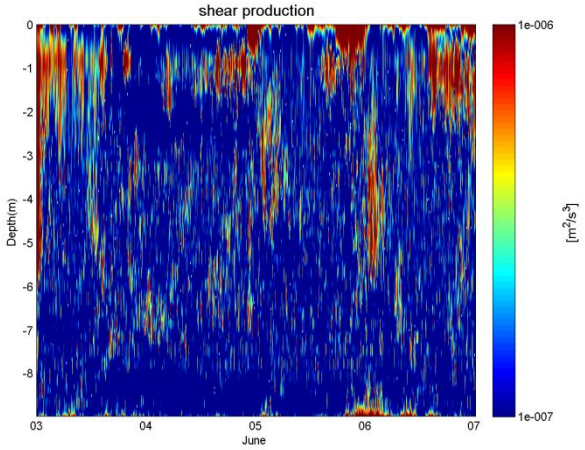

Fig B.46 Simulated shear production

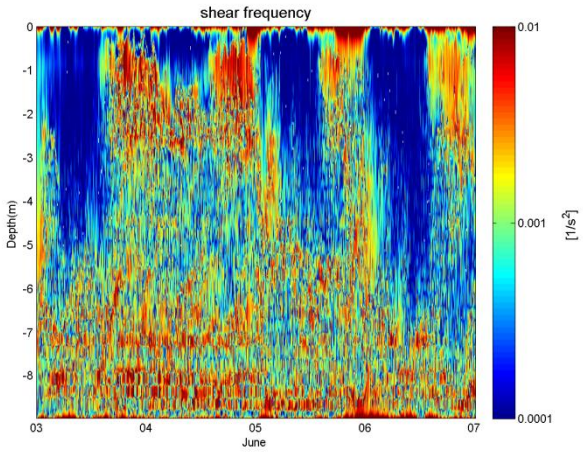

Fig B.47 Simulated shear frequency

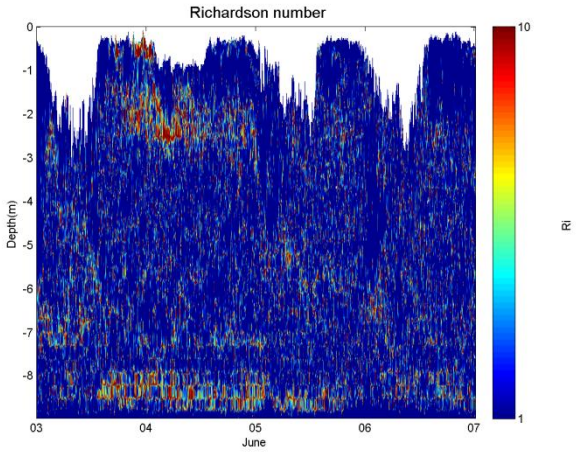

Fig B.48 Simulated Ri number

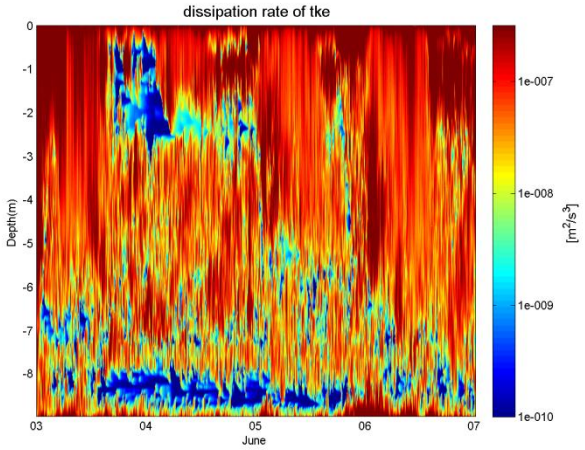

Fig B.49 Simulated ϵ

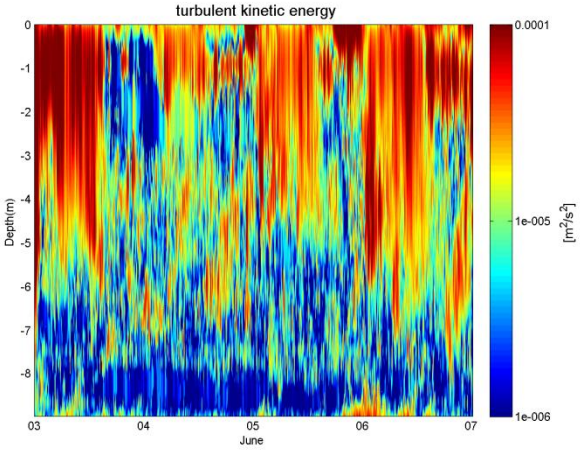

Fig B.50 Simulated TKE

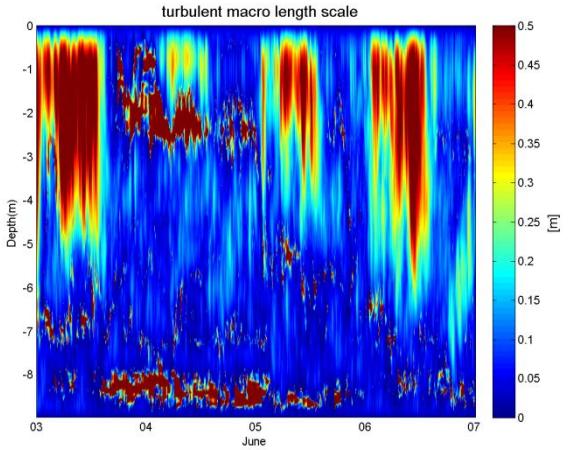

Fig B.51 Simulated turbulent macro length scale

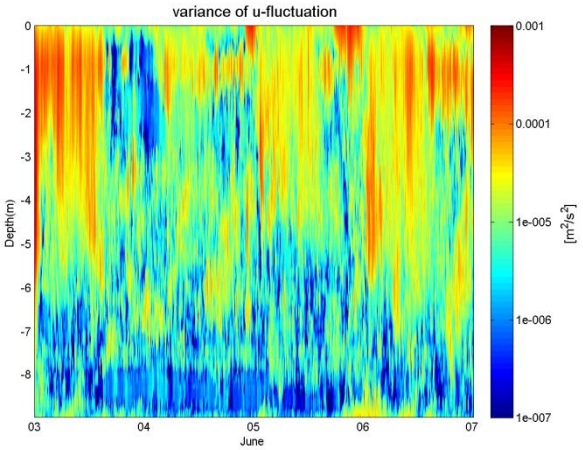

Fig B.52 Simulated variance U

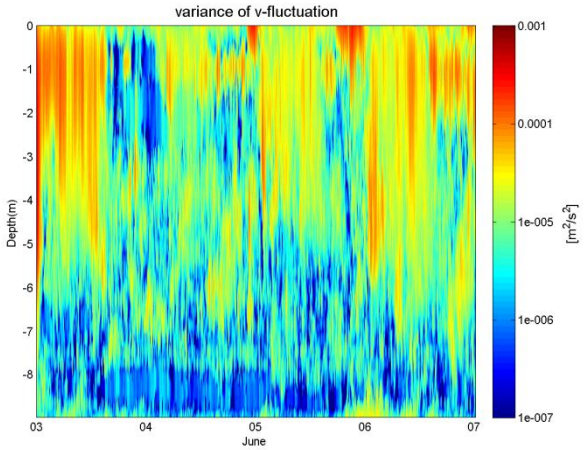

Fig B.53 Simulated variance V

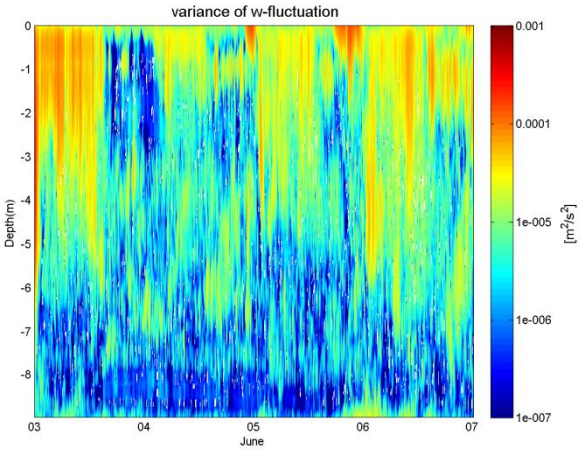

Fig B.54 Simulated variance W

B.4 k-ϵ Model June Simulations

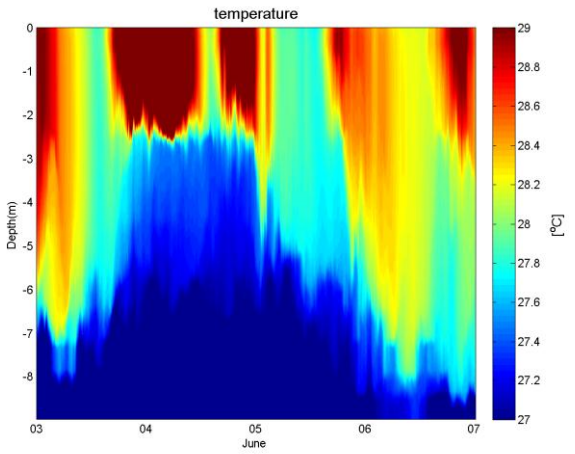

Fig B.55 Simulated thermal structure

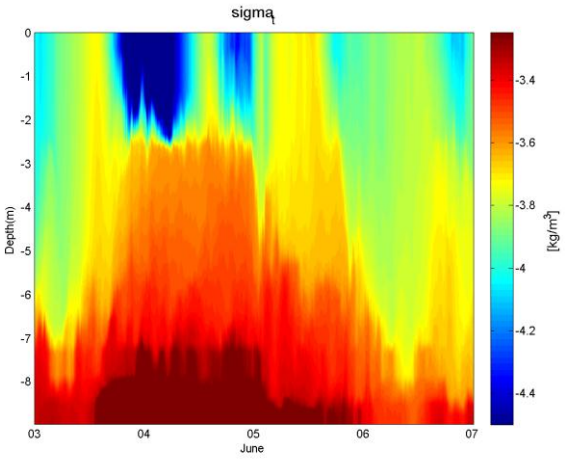

Fig B.56 Simulated density structure

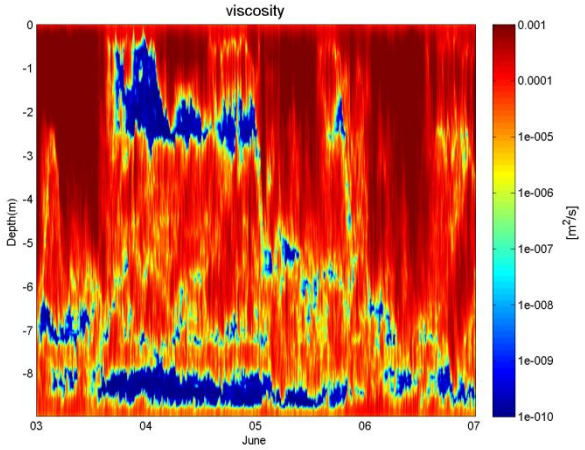

Fig B.57 Simulated viscosity

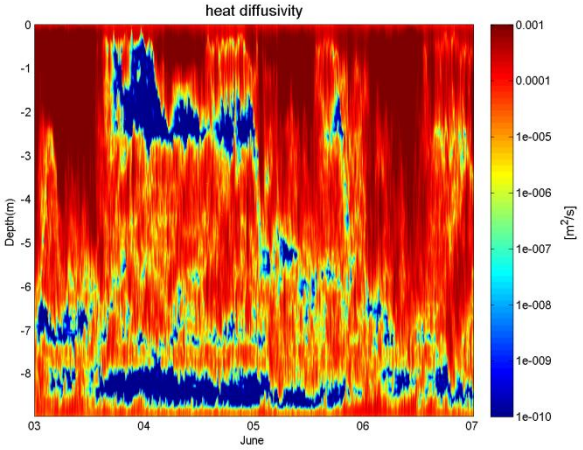

Fig B.58 Simulated heat diffusivity

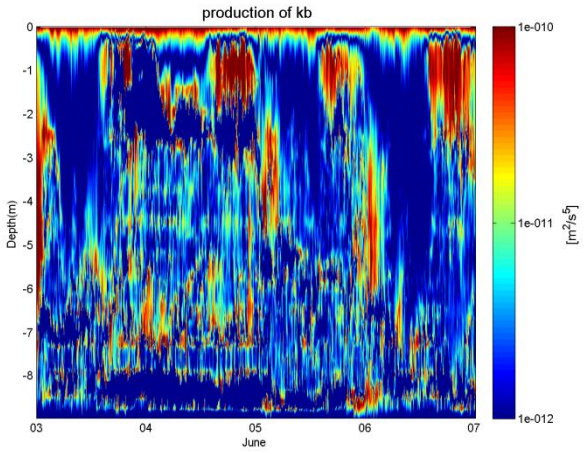

Fig B.59 Simulated production of kb

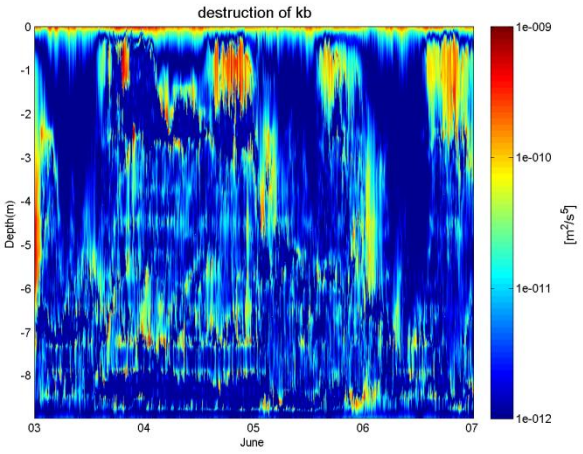

Fig B.60 Simulated destruction of kb

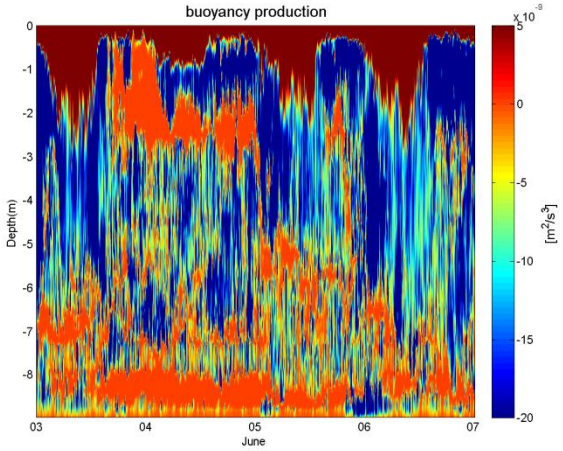

Fig B.61 Simulated buoyancy production

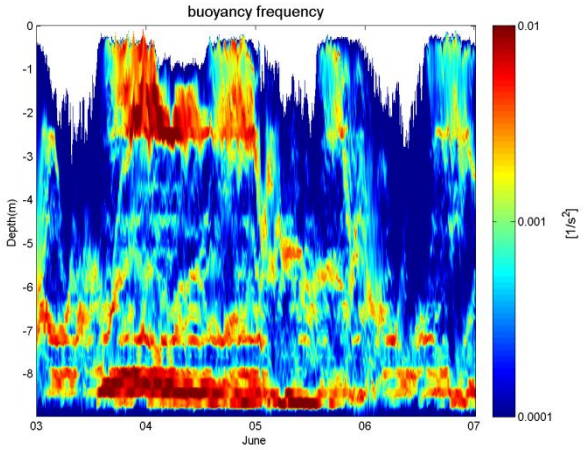

Fig B.62 Simulated buoyancy frequency

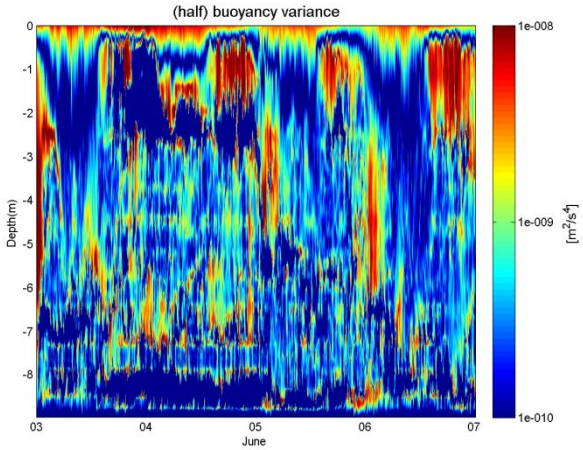

Fig B.63 Simulated buoyancy variance

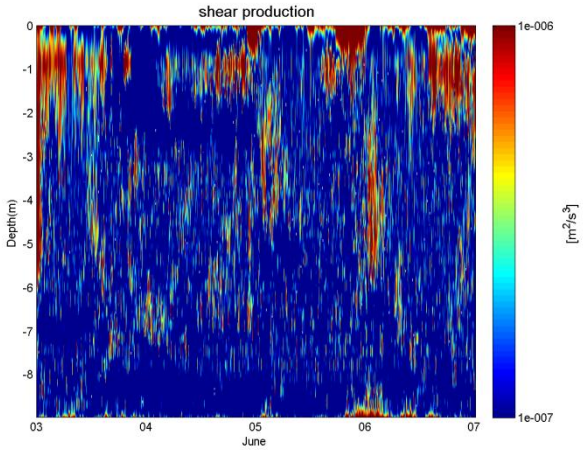

Fig B.64 Simulated shear production

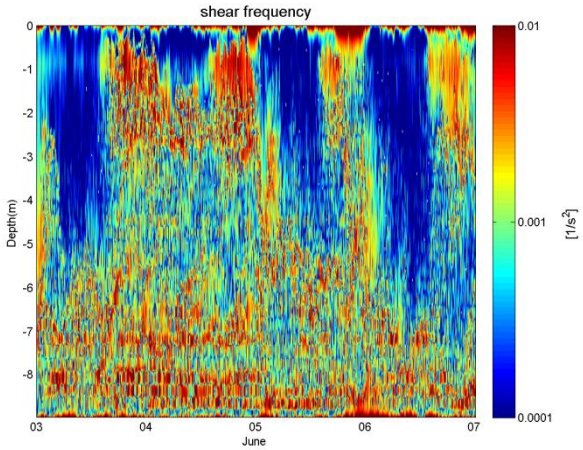

Fig B.65 Simulated shear frequency

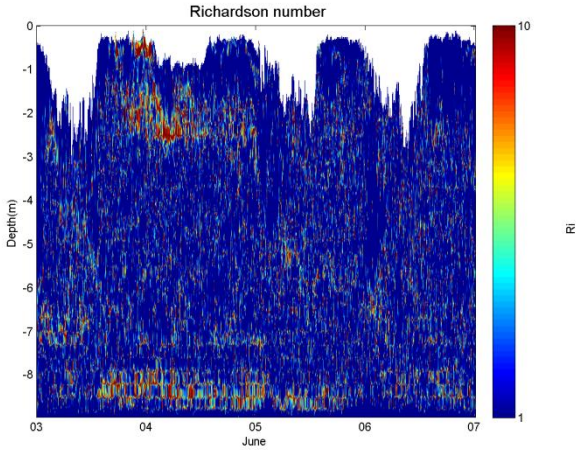

Fig B.66 Simulated Ri number

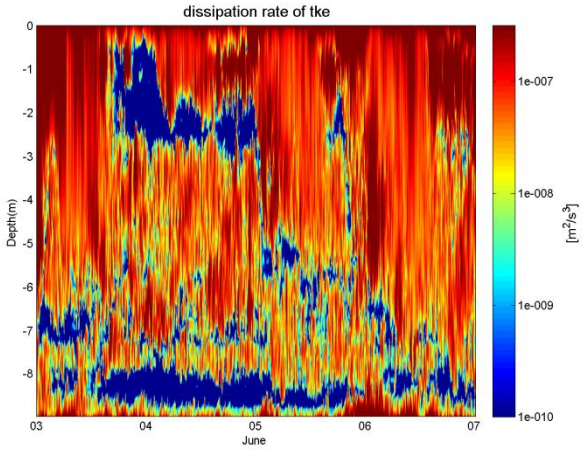

Fig B.67 Simulated ϵ

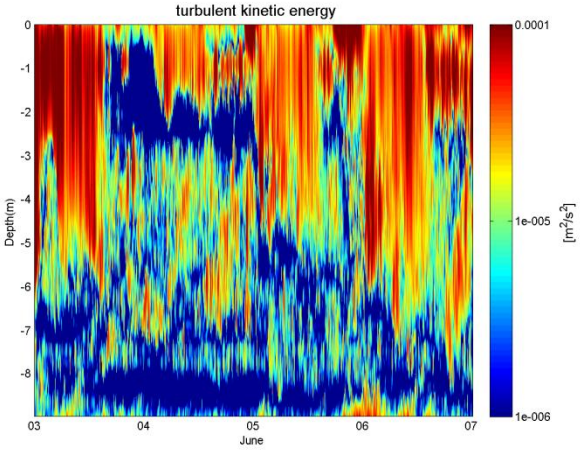

Fig B.68 Simulated TKE

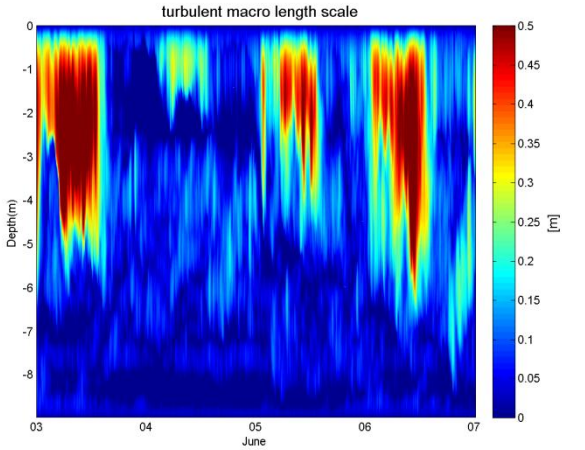

Fig B.69 Simulated turbulent macro length scale

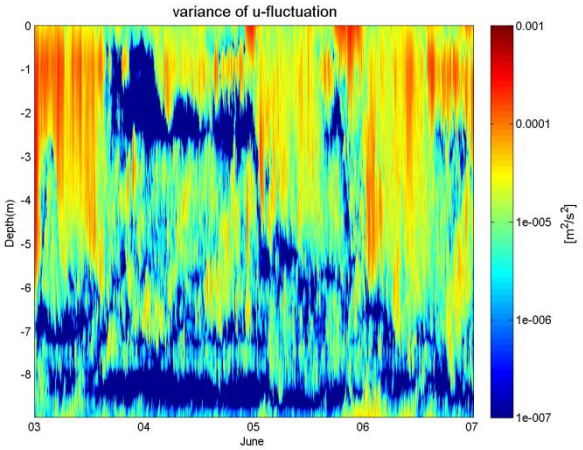

Fig B.70 Simulated variance U

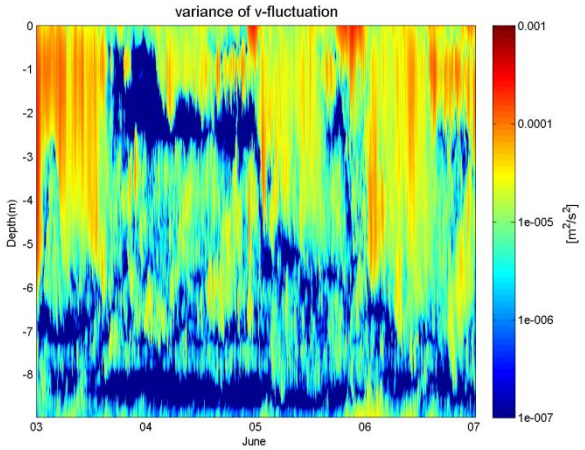

Fig B.71 Simulated variance V

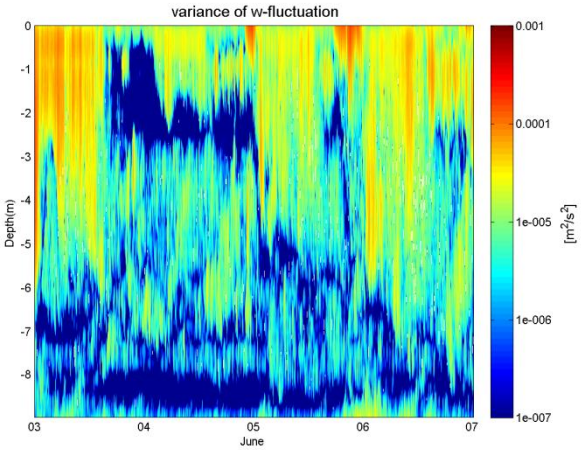

Fig B.72 Simulated variance W

VITA

Fahad Suliman Al Senafi has received his Bachelor of Science degree in Marine Studies from The University of Plymouth at Plymouth, England in 2006. He entered the Physical Oceanography master's program at Texas A&M University in September 2010. His research interests include small scale physical process in coastal oceans and shelves, interactions between internal waves and turbulence. He plans to carry doing research in this field at the Northern Arabian Gulf.

Address: OCSB 3029, 200 Seawolf Parkway, Galveston, Texas, 77553

Email Address: falsenafi@hotmail.com